Geological, geophysical and plate kinematic constraints for models of the India-Asia collision and the post-Triassic central Tethys oceans

Andrew J Parsons, Kasra Hosseini, Richard M Palin, Karin Sigloch

To cite this version:

Andrew J Parsons, Kasra Hosseini, Richard M Palin, Karin Sigloch. Geological, geophysical and plate kinematic constraints for models of the India-Asia collision and the post-Triassic central Tethys oceans. Earth-Science Reviews, 2020, 208, pp.103084. 10.1016/j.earscirev.2020.103084 . hal-03425541

HAL Id: hal-03425541
https://hal.science/hal-03425541

Submitted on 1 Dec 2021

Earth-Science Reviews 208 (2020) 103084

Contents lists available at ScienceDirect

Earth-Science Reviews

journal homepage: www.elsevier.com/locate/earscirev

Invited review

Geological, geophysical and plate kinematic constraints for models of the India-Asia collision and the post-Triassic central Tethys oceans

Andrew J. Parsons [a,*], Kasra Hosseini [a,1], Richard M. Palin [b,2], Karin Sigloch [a]

[a] Department of Earth Sciences, University of Oxford, Oxford OX1 3AN, UK
[b] Department of Geology and Geological Engineering, Colorado School of Mines, Golden, CO 80401, USA

ABSTRACT

In this study, we integrate bedrock datasets, observations of subducted slabs in the mantle, and plate kinematic constraints to constrain models for the India-Asia collision and the central Tethys oceans. To accomplish this, we review: (1) the post-Triassic bedrock record of subduction in Tibet; (2) seismic tomographic imaging of subducted slabs in the mantle; (3) timing of the India-Asia collision; and (4) the pre-collisional size of Greater India. Following the assumption that slabs sink vertically through the mantle, their positions and geometries determined from seismic tomography constrain the locations and kinematics of paleo-subduction zones. Integrating this with bedrock constraints allows us to constrain post-Triassic subduction zone configurations for the central Tethys oceans. Neotethys was consumed by at least two subduction zones since the Jurassic. At the onset of the India-Asia collision at 59 ± 1 Ma, one subduction zone was active along the southern Asian continental margin at ~20°N. At that time, a second may have been active at subequatorial latitudes, but support for this from a bedrock perspective is lacking. This subduction zone configuration allows for three reconstructions for Greater India: The (1) minimum-area; (2) enlarged-area; and (3) Greater India Basin reconstructions. We integrate these reconstructions and subduction zone configurations in a plate kinematic framework to test their validity for the India-Asia collision. No single model is entirely satisfactory and each invokes assumptions that challenge accepted concepts. These include our understanding of suture zones, and the limits of continental subduction. We explore these challenges and their implications for our understanding of the India-Asia collision and continental collisions in general.

1. Introduction

Tectonic models represent hypothesized approximations of past geological events that best fit and explain a pre-defined collection of data points. Incorporation of geological observations with an understanding and consideration of geodynamic concepts, geological processes, and physical properties of geological materials ensures that empirical models are consistent with physics and mechanics, and that numerical models are consistent with field observations and petrological constraints. Integrating these constraints and concepts within a plate kinematic framework ensures that models are consistent with global plate tectonics and the structure of the deep mantle, and reduces the degrees of freedom by which tectonic events can be modelled (i.e., integration of a wider range of constraints in a plate kinematic framework leads to a more tightly constrained tectonic model; e.g. Wu et al., 2016; Sigloch and Mihalynuk, 2017; Chen et al., 2019; van Hinsbergen et al., 2019). Note that here, we use the term ‘plate kinematic framework’ to describe a tectonic model that considers constraints from the geological record in the context of past and present motions and distributions of tectonic plates.

When mutually exclusive models are proposed for the same tectonic event, the details on which they disagree can highlight problems with the assumptions required by each model and discrepancies between, or limitations of, certain data types or interpretations used to support each model (e.g. the channel flow vs. duplexing debate for the Himalayan orogeny: Beaumont et al., 2001; Kohn, 2008; Cottle et al., 2015; Parsons et al., 2016b). In situations where reconciliation of competing models is not possible, such discrepancies may reveal flaws in the underlying model assumptions or may indicate important limitations, gaps or inconsistencies in our understanding of geodynamic processes and how such processes are recorded in the geological record (e.g. on-going debate regarding the accretionary history of the Northern Cordillera: Johnston, 2008; Hildebrand, 2009; Nelson et al., 2013; Sigloch and Mihalynuk, 2017; Parsons et al., 2018; van Staal et al., 2018; Monger and Gibson, 2019). In this study, we consider the post-Triassic history of terrane accretion and assembly of the Tibetan plateau and attempt to reconcile mutually exclusive models for the India-Asia collision.

The India-Asia collision and Himalayan-Tibetan orogeny is one of the most studied tectonic events of Earth history (Fig. 1). It is widely cited as a unique natural laboratory for studying collisional tectonics and is

---

* Corresponding author.
E-mail address: andrew.parsons@earth.ox.ac.uk (A.J. Parsons).

[1] Now at: The Alan Turing Institute, British Library, 96 Euston Road, London NW1 2DB, UK.

[2] Now at: Department of Earth Sciences, University of Oxford, Oxford OX1 3AN, UK.

http://dx.doi.org/10.1016/j.earscirev.2020.103084
Received 12 June 2019; Received in revised form 22 December 2019; Accepted 8 January 2020

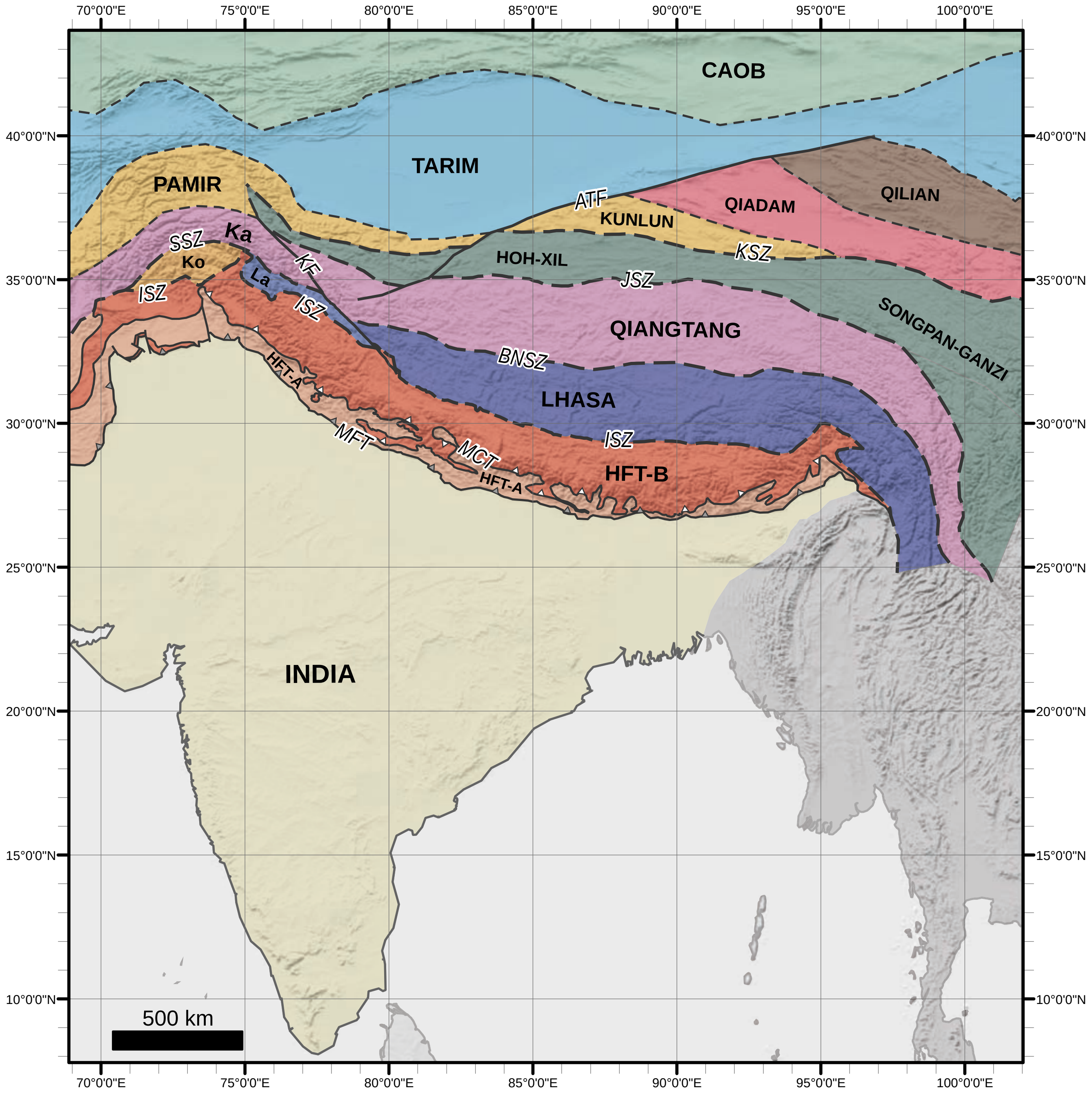

Fig. 1. Terrane map of crustal blocks and bounding structures of the Himalaya-Tibet orogenic system. AFT – Altyn Tagh Fault; BNSZ – Bangong-Nujiang Suture Zone; CAOB – Central Asian Orogenic Belt; HFT-A – Himalaya Fold-and-Thrust Belt, Sequence A (includes Lesser Himalayan Sequence and Subhimalayan Zone; based on Martin, 2017b); HFT-B – Himalaya Fold-and-Thrust Belt, Sequence B (includes Greater Himalayan Sequence and Tethyan Himalayan Sequence; based on Martin, 2017b); ISZ – Indus Suture Zone; JSZ – Jinsha Suture Zone; Ka – Karakoram; KF – Karakoram Fault; Ko – Kohistan; KSZ – Kunlun Suture Zone; La – Ladakh; MFT – Main Frontal Thrust; MCT – Main Central Thrust; SSZ – Shyok Suture Zone. Drawn from Searle et al. (2011), Parsons et al. (2016a), Martin (2017b), Goscombe et al. (2018), Li et al. (2018), and Kapp and DeCelles (2019). Georeferenced overlays (.kml, .kmz) and shapefiles of all points, lines, and polygons presented in our map figures are available for use and editing with global information system software (e.g. Google Earth, GPlates, ArcGIS) in Supplementary Materials 01 and 02.

commonly used as a modern analogue for understanding ancient orogenic events, such as the Caledonian, Trans-Hudson and Northern Cordilleran orogenies (e.g. St-Onge et al., 2006; Streule et al., 2010; Staples et al., 2016). However, the manner in which collision between India and the south margin of central Asian took place remains highly debated. Competing elements of existing models may be considered in terms of the subduction zone configuration of the central Tethys oceans prior to and during the India-Asia collision, and the palaeogeographic reconstruction of the northern margin of India, commonly referred to as Greater India.

Important distinctions between current models include, (1) the locations and lateral migrations of subduction zones in the central Tethys oceans, prior to and during the India-Asia collision (e.g. Stampfli and Borel, 2004; Jagoutz et al., 2015; Kapp and DeCelles, 2019); (2) whether the Himalayan orogeny occured via a single collision between India and Asia (e.g. Gansser, 1966; Hu et al., 2016a; Ingalls et al., 2016), or via collision between India and a Neotethys intra-oceanic arc, followed by collision of India plus its accreted intra-oceanic arc with Asia (e.g. Mahéo et al., 2004; Stampfli and Borel, 2004; Aitchison et al., 2007; Replumaz et al., 2014; Burg and Bouilhol, 2019); (3) the volume of Greater India continental lithosphere subducted and removed from the bedrock record (Ingalls et al., 2016; Rowley and Ingalls, 2017; van Hinsbergen et al., 2017; van Hinsbergen et al., 2019); and (4) the structural continuity between the northern margin of Greater India and the Indian continent, which may or may not have been dissected by an intervening oceanic basin, referred to as the Greater India Basin (e.g. Hu et al., 2016a; Rowley, 2019b; van Hinsbergen et al., 2019; Zhou and Su, 2019).

We evaluate these models for the India-Asia collision and the post-Triassic evolution of the central Tethys oceans by integrating published geological and geophysical datasets in a plate kinematic framework. We use the size, geometry and locations of seismically fast anomalies in the mantle interpreted as subducted lithosphere, to constrain palaeo-trench locations within the central Tethys oceans (e.g. Hafkenscheid et al., 2006; Replumaz et al., 2010; Steinberger et al., 2012; Sigloch and Mihalynuk, 2017; Chen et al., 2019; Clennett et al., 2019). We then integrate this seismic tomography and other geological and geophysical datasets within an existing plate reconstruction model (i.e., our 'plate kinematic framework', provided by Müller et al., 2019) using the palaeo-global information system software, GPlates (Müller et al., 2018), in order to compare and evaluate competing models within the same plate kinematic framework.

Our review and analysis are outlined as follows: First, we present a brief summary of the tectonostratigraphic units and terranes discussed in this article (Section 2). This is followed by a summary of competing models for the central Tethys oceans and the India-Asia collision (Section 3). Readers who are familiar with the Himalayan-Tibetan orogenic system and central Tethys oceans may wish to skip Section 2. In Section 4, we outline our analytical approach, including a description of how we make geological and geodynamic interpretations of subducted slabs from seismic tomography.

In Section 5, we review and evaluate the bedrock, mantle and plate kinematic datasets used to constrain our plate kinematic reconstructions of the central Tethys oceans and the India-Asia collision. This section and its accompanying supplementary files may also be read as a standalone review for reference and evaluation of current understandings, including: (1) the post-Triassic bedrock record of subduction and terrane accretion; (2) seismic tomographic observations from the deep mantle beneath the Indian hemisphere; (3) the timing of onset of the India-Asia collision; (4) the locations of India and the south Asian active margin at the onset of collision; and (5) Himalayan crustal shortening and geophysical imaging of Indian lithosphere beneath the Tibetan plateau as an estimate of the minimum size of Greater India. Georeferenced overlays (.kml, .kmz) and shapefiles of all points, lines, and polygons presented in our map figures are available for use and editing with global information system software (e.g. Google Earth, GPlates, ArcGIS) in Supplementary Materials 01 and 02. Data used in section 5 are catalogued in Supplementary Materials 03, 04, 06, and 07.

Finally, we integrate the datasets presented in Section 5 to constrain our own models for the post-Triassic subduction zone configuration of the central Tethys oceans (Section 6.1), and the plate kinematic evolution of the India-Asia collision (Section 6.2). We evaluate these models and their limitations and discuss their implications for our understanding of the geodynamics and bedrock record of continental subduction and collision (Section 7), with a final comment on future directions of research needed to resolve the remaining unknowns and inconsistencies.

2. Tectono-stratigraphic units

Tectono-stratigraphic units of the Himalayan orogen and Tibetan plateau (Figs. 1–2) are summarized below. Due to the vast amount of research conducted in these areas for over half a century, it is impractical to cite in line, all important contributions to this subject. Instead, we have typically opted to cite a selection of works that are representative of current understandings and/or published review articles that have collated this information previously. However, our study draws on a much larger and comprehensive list of published works (e.g. Fig. 3), which are compiled in Supplementary Materials 03 and 04, and acknowledged in the reference list at the end of this article. This includes individual studies used to build the geochronological evolution of post-Triassic subduction zones displayed in Fig. 3. A detailed description of the post-Triassic subduction history displayed in Fig. 3 is presented in Section 5.1 as one of our primary data sets for testing models of the central Tethys oceans and India-Asia collision. The geological 'events' discussed in the following sections correspond to 'event numbers' displayed on Fig. 3, which are catalogued in Supplementary Materials 04. Georeferenced overlays (.kml, .kmz) and shapefiles of all points, lines, and polygons presented in our map figures are available for use and editing with global information system software (e.g. Google Earth, GPlates, ArcGIS) in Supplementary Materials 01 and 02.

2.1. The Himalayan orogen

The Himalayan orogen can be divided into four broadly continuous tectonostratigraphic units separated by high-strain zones that strike parallel to the orogen (Fig. 2). From south to north, these units are: (1) the Subhimalayan zone; (2) the Lesser Himalayan sequence; (3) the Greater Himalayan sequence; and (4) the Tethyan Himalayan sequence (Le Fort, 1975; Hodges, 2000; Martin, 2017b). The general features of these units are summarized below, although we note that local variations in the thickness, lithology and deformation history of these units do occur. It is beyond the scope of this study to describe these variations detail in, for which the reader is directed to a recent set of reviews (Martin, 2017a, 2017b, Carosi et al., 2018, Dyck et al., 2019, Goscombe et al., 2018).

The Subhimalaya zone (SHZ, Fig. 2) comprises weakly metamorphosed Miocene to Pleistocene synorogenic sedimentary rocks known as the Siwaliks Group, deposited in a wedge-top basin (DeCelles et al., 1998). The SHZ is underlain by the top-to-the-south Main Frontal thrust (MFT), which marks the most southern structural limit of the Himalayan orogen (DeCelles et al., 1998).

The Lesser Himalayan sequence (LHS, Fig. 2) is structurally emplaced over the SHZ by the top-to-the-south Main Boundary thrust (MBT). The LHS comprises Paleoproterozoic to Early Mesozoic, Late Carboniferous to Permian and Cretaceous to Pleistocene sedimentary rocks with Paleoproterozoic igneous intrusions interpreted as the southern part of the Greater India passive margin (Hodges, 2000; Martin, 2017b; Goscombe et al., 2018).

The Greater Himalayan sequence (GHS, Fig. 2) is structurally emplaced over the LHS by the top-to-the-south Main Central thrust zone (MCTZ), which forms a pervasive, kilometre-thick shear zone and the roof thrust to the Lesser Himalayan Duplex (Le Fort, 1975; Robinson and Martin, 2014; Larson et al., 2015). The GHS comprises Neoproterozoic to Cambrian-Ordovician sedimentary rocks with Neoproterozoic, Cambrian-Ordovician and Eocene-Miocene granitic intrusions, interpreted as the northern part of the Greater Indian passive margin (Hodges, 2000; Martin, 2017b; Goscombe et al., 2018; Spencer et al., 2018).

The Tethyan Himalayan sequence (THS, Fig. 2) structurally overlies the GHS, via the South Tibetan detachment system (STDS), a top-down-to-the-north low-angle, brittle-ductile detachment (Burg et al., 1984; Kellett et al., 2019). The THS comprises Cambrian to Eocene sedimentary rocks with Permian, Triassic and Early Cretaceous igneous intrusions that form the distal passive margin sequence of Greater India (Hodges, 2000, Martin, 2017b, Goscombe et al., 2018). The northern limit of the THS is defined by the Indus-Yarlung-Tsangpo suture zone, which contains deformed marine sediments and ophiolitic mélange (see section 2.2.4).

Metamorphic discontinuities within and between the THS, GHS and LHS record near-continuous burial, underplating and accretion of material via progressive in-sequence thrusting during: (1) high-pressure (HP) and ultrahigh-pressure (UHP) metamorphism of the THS in the NW Himalaya (Kaghan and Tso Morari, Fig. 2) between ~56–43 Ma (de Sigoyer et al., 2000; Leech et al., 2005; Parrish et al., 2006; Donaldson et al., 2013; Rajkumar, 2015; Rehman et al., 2016; Bidgood et al., 2019a, 2019b); (2) burial and accretion of the GHS beneath the THS along a thrust-sense shear zone (later reactivated ast the STDS: Herren, 1987, Kellett et al., 2019), recorded by the North Himalaya gneiss domes (Fig. 2) during 56–54 Ma (Smit et al., 2014; Ding et al., 2016) and along the High

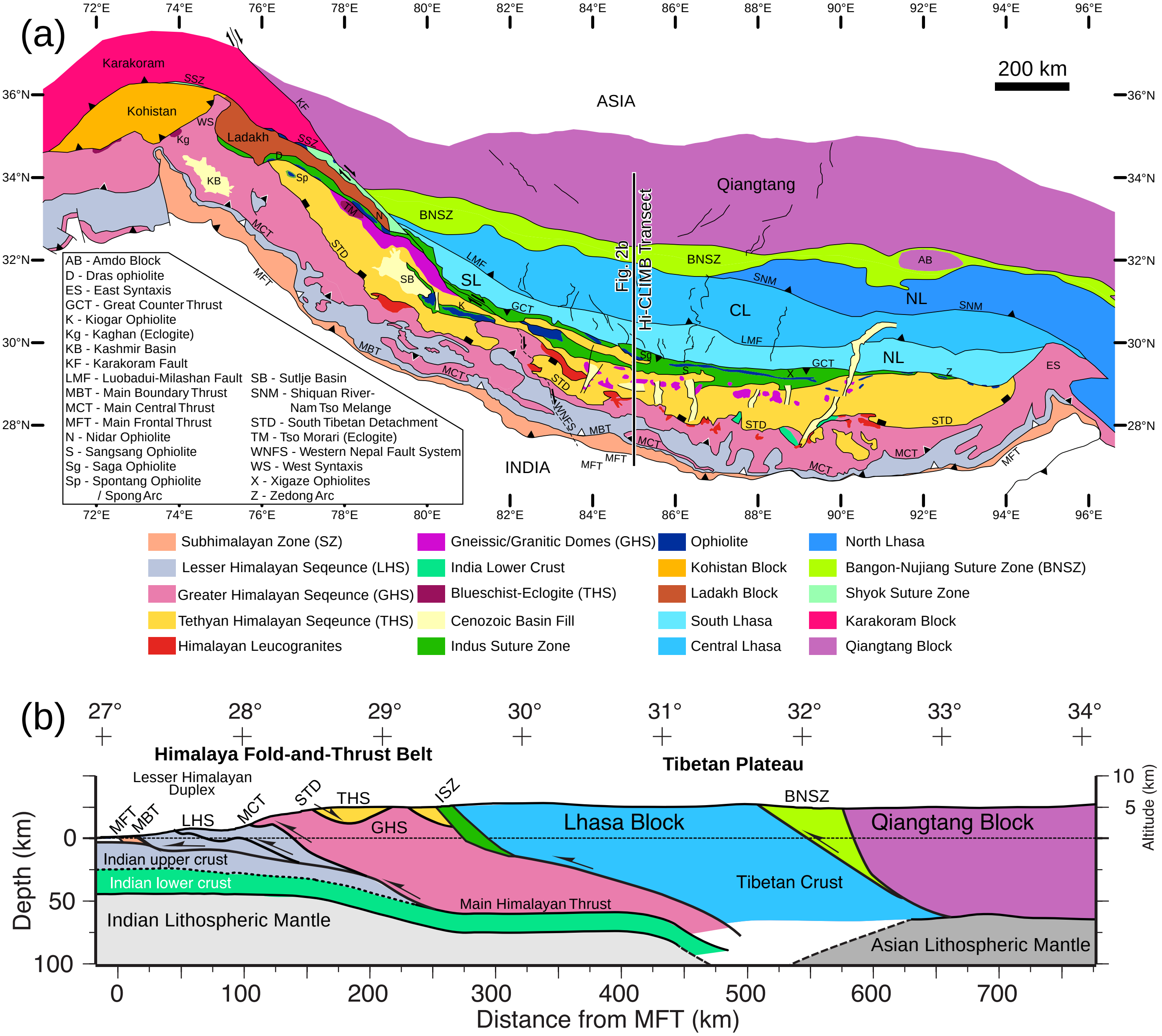

Fig. 2. Geological map and cross section of the Himalaya-Tibet orogenic system. (a) Geological map based on Yin and Harrison (2000), Searle et al. (2011), Parsons et al. (2016a), Martin (2017b), Goscombe et al. (2018), Li et al. (2018), and Kapp and DeCelles (2019). (b) Lithospheric sketch cross-section after Godin and Harris (2014), based on the Hi-CLIMB receiver function profile of Nábělek et al. (2009). Georeferenced overlays (.kml, .kmz) and shapefiles of all points, lines, and polygons presented in our map figures are available for use and editing with global information system software (e.g. Google Earth, GPlates, ArcGIS) in Supplementary Materials 01 and 02.

Himalaya between the MCTZ and STDS during ~51–30 Ma (Catlos et al., 2001; Carosi et al., 2010; Wang et al., 2013; Ambrose et al., 2015; Carosi et al., 2015; Iaccarino et al., 2015; Larson and Cottle, 2015; Parsons et al., 2016c; Braden et al., 2017; Goscombe et al., 2018); (3) accretion and crustal thickening of the GHS accommodated by one or more internal thrust-sense shear zones including the High Himalayan discontinuity during ~41–17 Ma (Ambrose et al., 2015; Carosi et al., 2016; Carosi et al., 2018; Goscombe et al., 2018; Mottram et al., 2019; Waters, 2019); (4) earliest burial and metamorphism of Indian continental lower crust (structurally lowest crustal unit beneath GHS, Fig. 2) at ~38 Ma (Kellett et al., 2014); and (5) accretion and crustal thickening of the GHS and LHS during in-sequence thrusting within the MCTZ and Lesser Himalayan duplex since ~15 Ma (e.g. Robinson and Martin, 2014; Larson et al., 2015; Goscombe et al., 2018).

2.2. The Tibetan plateau

The Tibetan plateau represents a collage of fault-bounded crustal blocks (Fig. 1) that progressively accreted to the southern margin of Asia throughout the Paleozoic to Mesozoic (Yin and Harrison, 2000; Zhang et al., 2012a; Kapp and DeCelles, 2019). In this study, we focus on the Lhasa, Kohistan and Ladakh blocks, and to a lesser extent the Qiangtang and Karakoram blocks (Fig. 2), which preserve a geological record of the India-Asia collision. The Lhasa, Qiangtang, Karakoram, and Ladakh blocks (Fig. 2) are continental fragments of Gondwanan affinity, comprising Ordovician to Triassic continent shelf deposits overlying Cambrian or older basement gneiss. These strata are intruded and overlain by Mesozoic to Cenozoic subduction-related plutonic rocks and volcano-sedimentary sequences (Fig. 3) (Yin and Harrison, 2000; Zhang et al., 2012a). In contrast, the

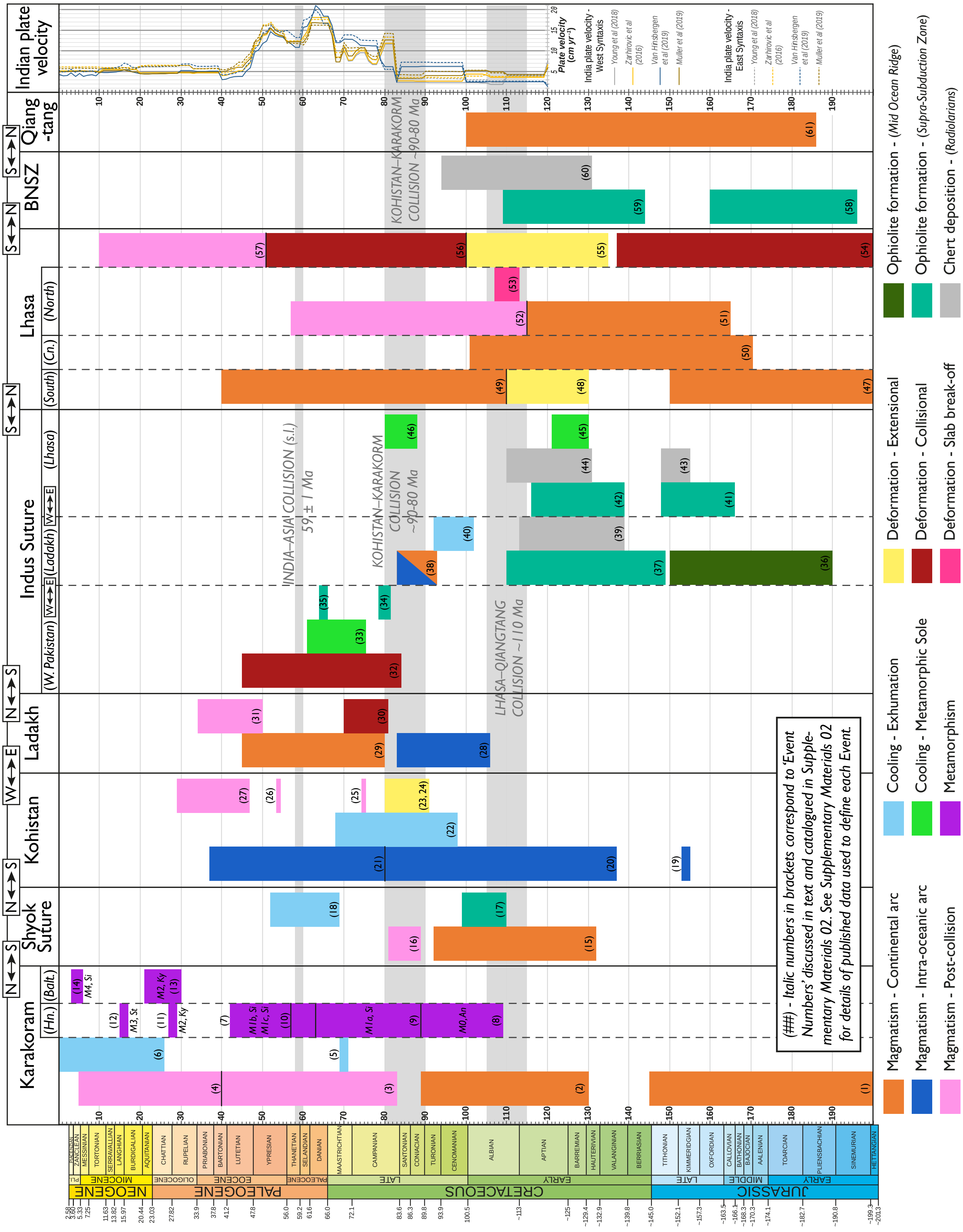

(caption on next page)

Kohistan block is an intra-oceanic arc with no continental crustal components (e.g. Burg, 2011).

2.2.1. Qiangtang-Karakoram blocks

The Qiangtang block records Early Jurassic to Early Cretaceous calc-alkaline magmatism associated with northward subduction of the Bangong-Tethys Ocean, which separated it from the Lhasa block (Event 61: Fig. 3) (e.g. Kapp et al., 2005; Zhang et al., 2012b; Li et al., 2018; Li et al., 2019; Kapp and DeCelles, 2019 and references therein). Closure of the Bangong-Tethys Ocean was followed by a marine transgression, which covered most of Qiangtang with a carbonate platform (Zhang et al., 2012a).

To the west, the Karakoram block (Fig. 2) comprises Late Triassic to Miocene plutonic phases of the Karakoram batholith (Events 1–4: Fig. 3) and Paleozoic sedimentary rocks of Gondwanan affinity that are continuous into the southern Pamir (Searle et al., 1989; Heuberger et al., 2007; Ravikant et al., 2009; Searle et al., 2010; Phillips et al., 2013; Borneman et al., 2015; Searle and Hacker, 2019). Orogenic events are recorded between the Early to Middle/Late Jurassic and between the Early to Late Cretaceous (Gaetani et al., 1990; Gaetani et al., 1993). The Karakoram block is considered the western extension of the Qiangtang block after restoration of the Karakoram fault zone (KFZ) (Fig. 2) (e.g. Robinson, 2009; Kumar et al., 2017).

2.2.2. Lhasa block

The North and Central Lhasa block (Fig. 2) record Middle Jurassic to Early Cretaceous calc-alkaline magmatism associated with southward subduction of the Bangong-Tethys Ocean (Events 50–51: Fig. 3) (Chiu et al., 2009; Zhu et al., 2009b; Li et al., 2018; Kapp and DeCelles, 2019; Li et al., 2019). Closure of this ocean occurred during collision between Lhasa and Qiangtang between ~130–110 Ma, resulting in formation of the Bangong-Nujiang suture zone (BNSZ), which contains Early Jurassic to Early Cretaceous supra-subduction zone (SSZ) ophiolites and associated ocean basin sedimentary rocks (Events 53–60: Fig. 3) (e.g. Baxter et al., 2009; Zhang et al., 2012a; Zhang et al., 2014; Li et al., 2018; Zeng et al., 2018; Kapp and DeCelles, 2019). South Lhasa (Fig. 2) is dominated by the Gangdese arc which records subduction-related calc-alkaline magmatism from the latest Triassic to Eocene, with a magmatic lull between ~150 Ma and ~110 Ma (Events 47–49: Fig. 3) (e.g. Ji et al., 2009; Li et al., 2018; Zhu et al., 2018). The Gangdese arc formed the northern active margin of the Neotethys Ocean, which closed during the India-Asia collision along the intervening Indus-Yarlung-Tsangpo suture zone (ISZ) (Yin and Harrison, 2000; Kapp and DeCelles, 2019).

Convergent deformation of Lhasa is recorded during the Early to Late Jurassic; this was followed by extensional deformation and a marine transgression during closure of the Bangong-Tethys Ocean in the Early Cretaceous, which covered most of the north and central Lhasa block with a carbonate platform (Murphy et al., 1997; Zhu et al., 2009b; Zhang et al., 2012a; Kapp and DeCelles, 2019). Between the Late Cretaceous and Early Eocene, convergent deformation of the Lhasa block resumed, shortening it by ~50% (Kapp et al., 2007; Zhu et al., 2009b; van Hinsbergen et al., 2011).

2.2.3. Ladakh block

West of the Lhasa block lie the Ladakh and Kohistan blocks (Fig. 2), which are dominated by subduction-related Mesozoic to Cenozoic plutons and volcanic sequences (Fig. 3) (Burg, 2011; Searle et al., 2011). These blocks are bounded to the south by the Indus-Yarlung-Tsangpo suture and to the north by the Shyok suture zone (Rolland et al., 2000; Bhutani et al., 2009).

The Ladakh block is typically considered the westward continuation of the Lhasa block (e.g. Raz and Honegger, 1989; Robertson and Degnan, 1994; Weinberg et al., 2000; Searle, 2019). Structural and petrogenetic ties between the Ladakh block and the Kohistan block are frequently made, however, the timing and duration of such links are uncertain, given that the Kohistan and Lhasa blocks were at different latitudes during the Cretaceous (e.g. Burg, 2011).

The Ladakh block comprises the Ladakh batholith and the Dras 1, Dras 2 and Khardung volcano-sedimentary sequences. The Dras 1 volcanics were deformed between ~80–70 Ma, whereas the younger Dras 2 volcanics are undeformed (e.g. Fuchs, 1982; Reuber, 1989; Reuber et al., 1989). This deformation may have occurred in response to collision between neighbouring Kohistan and the Karakoram block.

Previous studies proposed that magmatic assemblages of the Ladakh block formed along the Dras arc between the late Albian to Eocene (Events 28–29: Fig. 3), and represent the eastward continuation of the Gangdese arc (Fuchs, 1982; Honegger et al., 1982; Schärer et al., 1984; Reuber, 1989; Dunlap and Wysoczanski, 2002; Bhutani et al., 2009; Ravikant et al., 2009; White et al., 2011). Alternatively, it has been proposed that the intra-oceanic assemblages of the Dras and Nindam formations are unrelated to the Ladakh batholith and formed above a different subduction zone, equivalent to the Spong arc (Robertson and Degnan, 1994; Buckman et al., 2018; Walsh et al., 2019). To avoid confusion, we use the term 'Dras arc' to refer to the Albian to Santonian intra-oceanic Dras and Nindam formations and 'Ladakh arc' to refer to the Late Cretaceous to Eocene Ladakh batholith.

2.2.4. Kohistan block

The Kohistan block (also referred to as the Kohistan intra-oceanic arc) comprises a near-complete lower to upper crustal intra-oceanic arc magmatic sequence and the younger, more compositionally evolved Kohistan batholith (Fig. 3) (Burg, 2011; Jagoutz et al., 2019). It records subduction-related magmatism in an intra-oceanic setting between the Late Jurassic and Eocene (Events 19–21: Fig. 3) (Dhuime et al., 2009; Burg, 2011; Bouilhol et al., 2013; Jagoutz et al., 2019; Zhuang et al., 2018). Between ~90–80 Ma, the Kohistan intra-oceanic arc underwent a phase of extension ('arc-splitting') (Treloar et al., 1996; Dhuime et al., 2009; Burg, 2011), followed by backward migration of the arc front away from the subduction interface and generation of the bulk of the Kohistan batholith and the associated Teru and Utror volcanics between the Late Cretaceous and Oligocene (Events 21–24: Fig. 3) (Clift et al., 2002; Burg, 2011; Bouilhol et al., 2013; Jagoutz et al., 2019; Zhuang et al., 2018). The petrogenetic relationship between the Kohistan intra-oceanic arc and the Gangdese arc is disputed. Some authors propose that the Kohistan intra-oceanic arc formed along an intra-oceanic subduction zone unrelated to the Gangdese arc (e.g. Aitchison et al., 2007; Burg and Bouilhol, 2019), whereas other propose that the Kohistan intra-oceanic arc formed the westward continuation of the Gangdese arc, similar to the westward transition of the present-day Aleutian arc from continental Alaska to the Bering Sea (e.g. Rolland et al., 2000; Searle, 2019; Kapp and DeCelles, 2019).

Fig. 3. Jurassic to recent history of subduction, magmatism and accretion of crustal blocks of the Tibetan Plateau (See Fig. 1 for crustal block locations). Coloured bars show type and duration of geological events. Italicised numbers are 'Event Numbers' used to match each geological event to their corresponding description in Supplementary Materials 04. Lengths of events are defined by a collection of overlapping published ages plus and minus their errors. Data sources for all Event Numbers are listed in Supplementary Materials 04. India plate velocity profiles are calculated for the East and West syntaxes using a variety of published plate reconstructions (see figure), relative to a fixed mantle reference frame using the GPlates velocity tool. Metamorphism on the Karakoram block is divided into previously defined metamorphic events, M0 to M4; M1 is divided into M1a, M1b M1c (See Supplementary Materials 03 and 04 for description). Abbreviations: An – andalusite grade; Balt. – Baltoro region, Karakoram; BNSZ – Bangong-Nujiang suture zone; Cn. – Central Lhasa; Hn. – Hunza region, Karakoram; Ky – kyanite grade; Si – sillimanite grade; W. Pakistan – West Pakistan. Time scale based on Geological Society of America stratigraphic chart.

2.2.5. Indus suture zone

The Indus-Yarlung-Tsangpo suture zone, referred to hereafter as the Indus suture zone (ISZ), forms a ≤ 50 km wide zone of deformed sedimentary rocks of both Asian and Indian affinity, obducted ophiolites and HP/UHP domains of metamorphosed THS (Fig. 2) (de Sigoyer et al., 2000, Hébert et al., 2012, DeCelles et al., 2014, Laskowski et al., 2016, Bidgood et al., 2019a, 2019b). The ISZ contains latest Middle Jurassic to Early Cretaceous supra-subduction zone (SSZ) ophiolites and volcano-sedimentary sequences with intra-oceanic arc geochemical signatures that formed during the magmatic lull on the Gangdese arc at ~150–110 Ma (Events 37, 39, 41–44: Fig. 3) (Hébert et al., 2012; Chan et al., 2015; Kapp and DeCelles, 2019). Notable ophiolite occurrences south of the Lhasa block include the Zedong and Bainang terranes, and Xigaze, Jungbwa, Sangsang, Saga, Luobusa, Kiogar, and Dazhuqu ophiolites (Fig. 2) (e.g. Malpas et al., 2003; Dubois-Côté et al., 2005; Bédard et al., 2009; Guilmette et al., 2009; Guilmette et al., 2012; Chan et al., 2015). South of Lhasa, the Xigaze forearc contains Early Cretaceous to Eocene sedimentary rocks (the Xigaze Group), which in some places are in depositional contact with the underlying Xigaze and Sangsang ophiolites (Nicolas et al., 1981; Einsele et al., 1994; An et al., 2014; Maffione et al., 2015; Orme et al., 2015). Pre-85 Ma strata from the Xigaze forearc contain detrital zircon signatures indicative of a Lhasa-derived sedimentary province (Orme et al., 2015; Orme and Laskowski, 2016; Kapp and DeCelles, 2019). The transition from a marine to non-marine depositional environment recorded in the Xigaze forearc between 58 Ma and 54 Ma, with deposition cessing by ~51 Ma is interpreted as a record of collision with Greater India (Orme et al., 2015; Kapp and DeCelles, 2019).

Notable occurrences of Early Cretaceous SSZ ophiolites south of the Ladakh block include the Spontang, Nidar, and Dras ophiolites (Fig. 2) (e.g. Reuber et al., 1989; Linner et al., 2001; Pedersen et al., 2001; Mahéo et al., 2004; Ziabrev et al., 2008; Baxter et al., 2010; Buchs et al., 2018; Buckman et al., 2018). Wehrlite in the Dras ophiolite yields an age of 176 ± 10 Ma (KAr, amphibole), however, it is unknown whether those samples formed in an SSZ setting or a mid ocean ridge (MOR) setting (Reuber et al., 1989). In the Spontang ophiolite, Early Cretaceous intra-oceanic arc gabbros (island arc tholeiite composition) intrude Early Jurassic N-MORB (normal mid-ocean ridge basalt) assemblages (Events 36–37: Fig. 3) (Reuber et al., 1989; Pedersen et al., 2001; Buckman et al., 2018). Above this ophiolite, a calc-alkaline andesite from a volcano-sedimentary unit with a mean UPb zircon age of 88 ± 5 Ma has been interpreted as an intra-oceanic arc built upon the Spontang ophiolite, referred to as the Spong arc (Event 38: Fig. 3) (Pedersen et al., 2001; Mahéo et al., 2004; Searle, 2019).

Collectively, the Middle Jurassic to Late Cretaceous intra-oceanic arc assemblages in the ISZ have been referred to as the Neotethys intra-oceanic arc. Some studies argue that the distribution of intra-oceanic SSZ assemblages within the ISZ suggests that there was more than one Neotethys intra-oceanic arc active between the Jurassic and Cretaceous (Mahéo et al., 2004; Guilmette et al., 2009; Guilmette et al., 2012; Hébert et al., 2012). South of the Kohistan block, the ISZ is devoid of rocks derived from the subducting Neotethys Ocean plate (e.g. Scholl and von Huene, 2007, 2010; Burg, 2011). Several lesser-studied SSZ ophiolites have been reported from the suture zone between India and the Kabul block in western Pakistan (Events 32–35: Fig. 3), southwest of the Kohistan block; these include the Bela, Dargai, Khost, Muslim Bagh, Waziristan and Zhob ophiolites, which have Early to Late Cretaceous formation ages and Late Cretaceous to Eocene obduction ages (e.g. Ahmed, 1993; Mahmood et al., 1995; Beck et al., 1996; Gnos et al., 1997; Khan et al., 2009; Kakar et al., 2012). Previous studies have suggested that the West Pakistan ophiolites were obducted during the West India orogeny sometime between the Campanian to Eocene, via collision between northwest India and the Kabul block (e.g. Beck et al., 1996; Gnos et al., 1997; Gaina et al., 2015; van Hinsbergen et al., 2019).

3. Competing tectonic models for the India-Asia collision

For the purpose of this study, we distinguish between *sensu-lato* (*s.l.*) and *sensu-stricto* (*s.s.*) forms of the India-Asia. The former (*sensu-lato, s.l.*) refers to the onset of the Himalayan orogeny, recorded by the THS, regardless of whether this corresponds to collision with an intra-oceanic arc or the Asian active margin. The latter (*sensu-stricto, s.s.*) refers specifically to collision between Greater India and the Asian active margin. All further mention of the India-Asia collision will be with reference to the *sensu-lato* definition, unless otherwise specified.

Within a plate kinematic framework, distinctions between models for the India-Asia collision (*s.l.*) can be made based on their considerations of (1) the temporal and spatial arrangement of plate boundaries prior to and during collision (Fig. 4) (e.g. Stampfli and Borel, 2004; Hafkenscheid et al., 2006; Jagoutz et al., 2015; Hu et al., 2016a; Kapp and DeCelles, 2019); and (2) the paleogeographic evolution and structure of Greater India (Fig. 5) (e.g. Hu et al., 2016a; van Hinsbergen et al., 2019; Zhou and Su, 2019), which we define as all Indian continental lithosphere north of the MBT. These model considerations are inherently linked because the position of India through time places an important constraint on the viable locations of subduction zones and the maximum and minimum sizes of Greater India. Distinctions between existing models for the India-Asia collision (*s.l.*) based on their treatment of plate boundaries and Greater India are outlined as follows:

3.1. Plate boundary configurations for models of the India-Asia collision (s.l.)

3.1.1. Single subduction zone configurations

Early models proposed that the India-Asia collision (*s.l.*) was facilitated by northward subduction of the Indian plate beneath the Asian plate; collision occurred between the Tethyan Himalaya Sequence on the northern edge of Greater India, and the Lhasa and Kohistan-Ladakh terranes located along the southern Asian margin (Gansser, 1966; Le Fort, 1975; Şengör and Natal'in, 1996) (Fig. 4a-f). Some studies argue that only one suture zone is preserved in the bedrock record between India and Asia, which implies that the Neotethys Ocean was subducted from a single subduction zone that produced a single slab (e.g. Hu et al., 2016a), as reflected by the *Single Subduction – A* configuration (Fig. 4a-c). Alternatively, subduction of the Neotethys Ocean was partly accommodated by an intra-oceanic arc which terminated before the India-Asia collision (Guilmette et al., 2009), as reflected by *the Single Subduction – B* configuration (Fig. 4d-f). This latter situation implies that two sutures exist between India and the Lhasa block (e.g. Guilmette et al., 2009). Within a plate kinematic framework, the single subduction zone configuration places a fundamental constraint on the paleogeographic restoration of Greater India, because at the onset of collision (*s.l.*), northern India was located at the equator, whilst the southern Asian margin was located >3000 km to the north (e.g. van Hinsbergen et al., 2012, 2019).

3.1.2. Double subduction zone configurations

Double subduction zone models suggest that the India-Asia collision (*s.l.*) and Himalayan orogeny involved the suturing of two subduction zones (Fig. 4g-o). In the NW Himalaya, some studies model suturing between Greater India and the Kohistan intra-oceanic arc at ~65–50 Ma, followed by suturing between the Kohistan and Karakoram blocks at ~45–30 Ma (e.g. Khan et al., 2009; Bouilhol et al., 2013; Replumaz et al., 2014; Jagoutz et al., 2015; Burg and Bouilhol, 2019). Alternatively, other studies of the NW Himalaya model first collision between Greater India and the Spong intra-oceanic arc, and second collision between Greater India and the Kohistan arc (e.g. Mahéo et al., 2004; Stampfli and Borel, 2004; Hafkenscheid et al., 2006; Aitchison et al., 2007; Buckman et al., 2018; Searle, 2019). In the central Himalaya, double subduction models argue for first collision between Greater India and the Xigaze/Zedong intra-oceanic arc and second collision between Greater India (plus the accreted Xigaze/Zedong arc) and Lhasa block along the southern Asian margin (e.g. Aitchison et al., 2000; Aitchison et al., 2007; Hébert et al., 2012) These latter two models imply that the Indus suture zone comprises two sutures (e.g. Aitchison et al., 2000; Mahéo et al., 2004; Guilmette et al., 2009; Guilmette et al., 2012; Hébert et al., 2012; Searle, 2019).

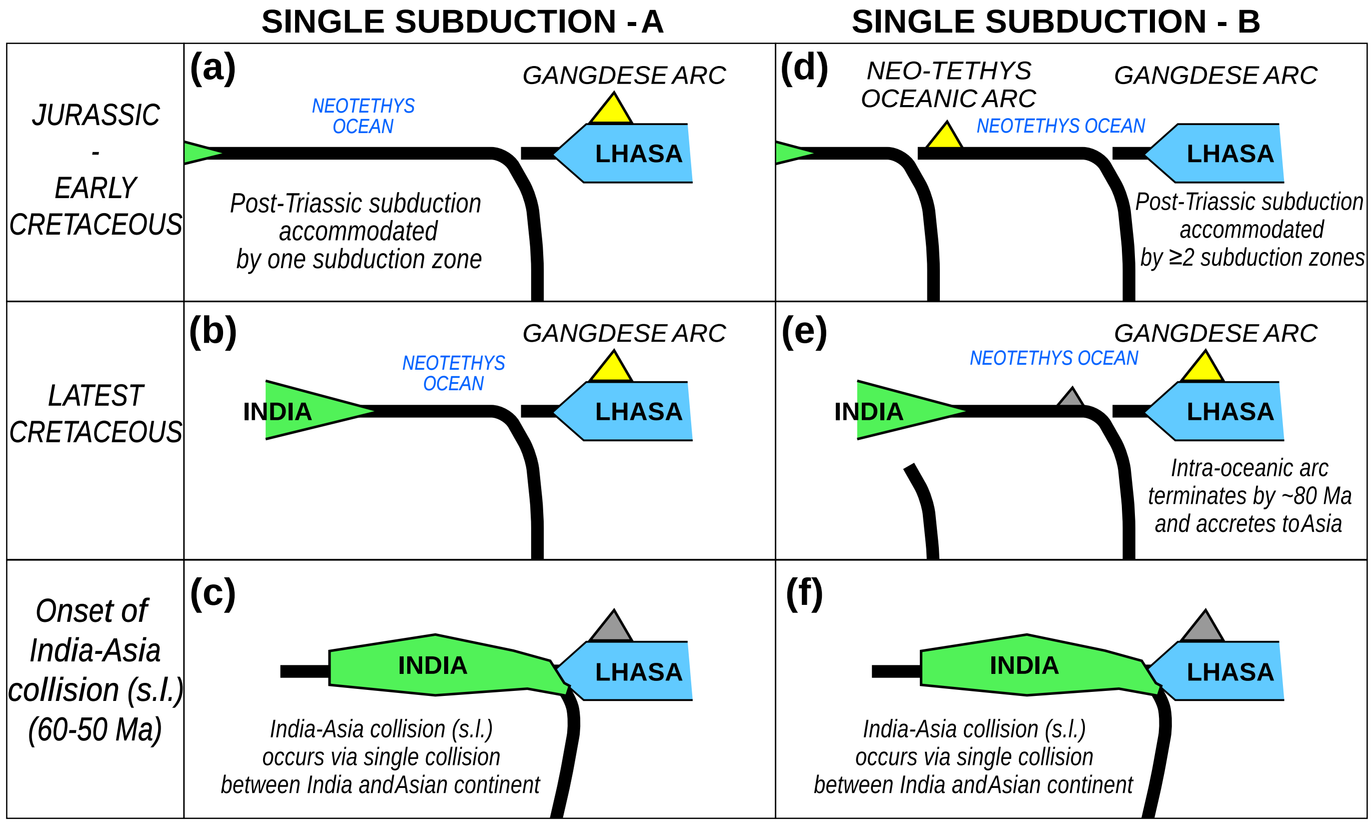

Fig. 4. Subduction zone configurations for models of the India-Asia collision. (a-c) Single subduction configuration – A. (d-e) Single subduction configuration – B. (g-i) Double subduction configuration with fixed (i.e. stationary) trenches. (j-l) Double subduction configuration with a north-migrating southern trench. (m-o) Two stage double subduction configuration in which the first trench migrates south towards India, followed by collision with India and initiation of a new subduction zone to the north. Yellow triangles show active volcanic arcs, and grey triangles show extinct volcanic arcs. Arrows show direction of trench migration.

Many studies favour a double subduction configuration based on plate kinematic reconstructions of the Indian and Asian continents (e.g. Stampfli and Borel, 2004; Replumaz et al., 2010; Guillot and Replumaz, 2013; Replumaz et al., 2014; Jagoutz et al., 2015). These studies argue that the large distance between northern India and southern Asia at the onset of collision (*s.l.*), necessitates collision with a subequatorial Neotethys intra-oceanic arc. The double subduction zone configuration has been used to explain temporal variations in pluton isotope geochemistry in Ladakh and Kohistan (Bouilhol et al., 2013; Jagoutz et al., 2019) and the persistence of oceanic sedimentation north of Everest until ~34 Ma (Aitchison et al., 2000; Aitchison et al., 2007). Furthermore, paleomagnetic studies argue that (1) the Kohistan and Ladakh blocks were located at equatorial latitudes in the Paleocene (e.g. Klootwijk et al., 1984; Zaman and Torii, 1999; Ahmad et al., 2000; Khan et al., 2009); and that (2) two phases of Indian plate deceleration since the Late Cretaceous reflect two separate collisional events (e.g. Bouilhol et al., 2013; Replumaz et al., 2014; Jagoutz et al., 2015).

Some double subduction zone models assume that the subequatorial subduction zone was either fixed or *southward* migrating (Fig. 4 g-i), and active simultaneously with a subduction zone along the south Asian margin (e.g. Stampfli and Borel, 2004; Replumaz et al., 2010, 2014; Guillot and Replumaz, 2013; Searle et al., 1997). In contrast, Jagoutz et al. (2015) argued for a double subduction zone model in which the subequatorial subduction zone migrated *northwards* (Fig. 4j-l), as the cause of rapid Indian plate motion in the Late Cretaceous and Cenozoic. Hafkenscheid et al. (2006) and Kapp and DeCelles (2019) proposed a two-stage variant of the double subduction zone configuration in which the north and south subduction zones were active sequentially (Fig. 4 m-o). In this model, a subduction zone located along the Asian margin, which included the Xigaze forearc, migrated southwards via back-arc spreading (Fig. 4 m) and collided with Greater India at a subequatorial latitude at ~60–50 Ma (Fig. 4n). This was immediately followed by initiation of a new subduction zone along the Asia margin, which facilitated collision between Greater India and Asia at ~40–30 Ma (Fig. 4n-o). Importantly, this model explains how the Xigaze forearc can contain pre-85 Ma sediments sourced from Lhasa, and yet be located at a sub-equatorial at the onset of collision (*s.l.*) (Kapp and DeCelles, 2019).

3.2. Paleogeographic reconstructions of Greater India for models of the India-Asia collision (s.l.)

Several paleogeographic reconstructions of Greater India have been proposed (Fig. 5a-c), which are consistent with either a single or double subduction zone configuration for the India-Asia collision (*s.l.*). We classify these as: (1) Minimum-area reconstructions; (2) Enlarged-area reconstructions; and (3) Greater India Basin reconstructions.

3.2.1. Minimum-area reconstructions

Minimum-area reconstructions (Fig. 5a) assume that Greater India was contiguous with the rest of India and had a pre-collisional north-south width of <1000 km, estimated from crustal shortening estimates, mass-balance calculations and subsurface imaging of Indian continental lithosphere beneath southern Tibet (e.g. Replumaz et al., 2010; van Hinsbergen et al., 2011a; Yakovlev and Clark, 2014; van Hinsbergen et al., 2019). These restorations assume that most, if not all of Greater

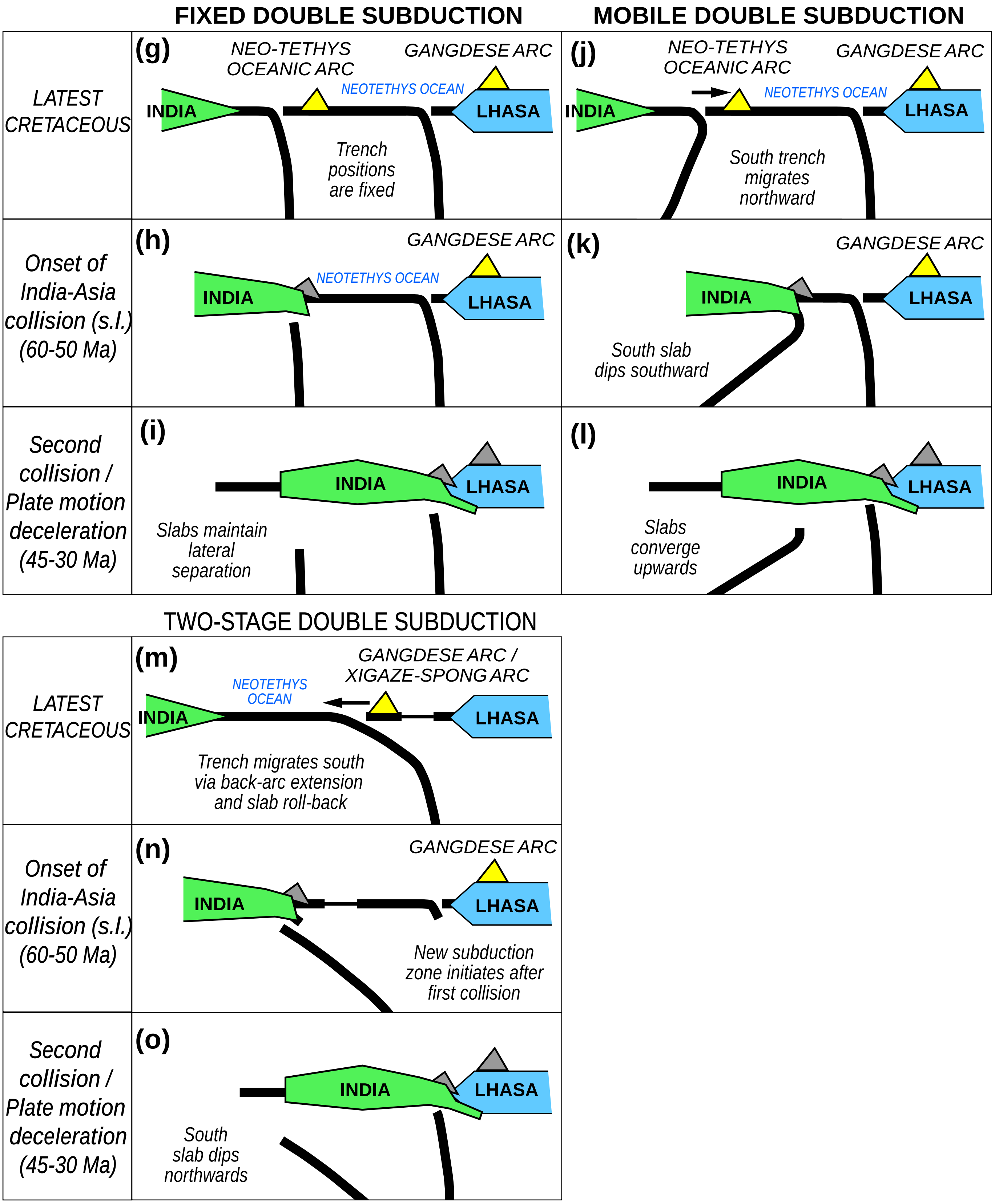

Fig. 4 (*continued*).

India's continental crust is preserved in the bedrock record and overlying sediments (e.g. Yakovlev and Clark, 2014). At the onset of collision (*s.l.*) at ~60–50 Ma, minimum-area restorations within a plate kinematic framework position the leading edge of Greater India >2000 km south of the Asian margin and assume that the intervening area was occupied by Neotethys oceanic lithosphere. Consequently, minimum-area Greater India restorations invoke a double subduction zone configuration to remain valid and assume that the onset of the India-Asia collision (*s.l.*)

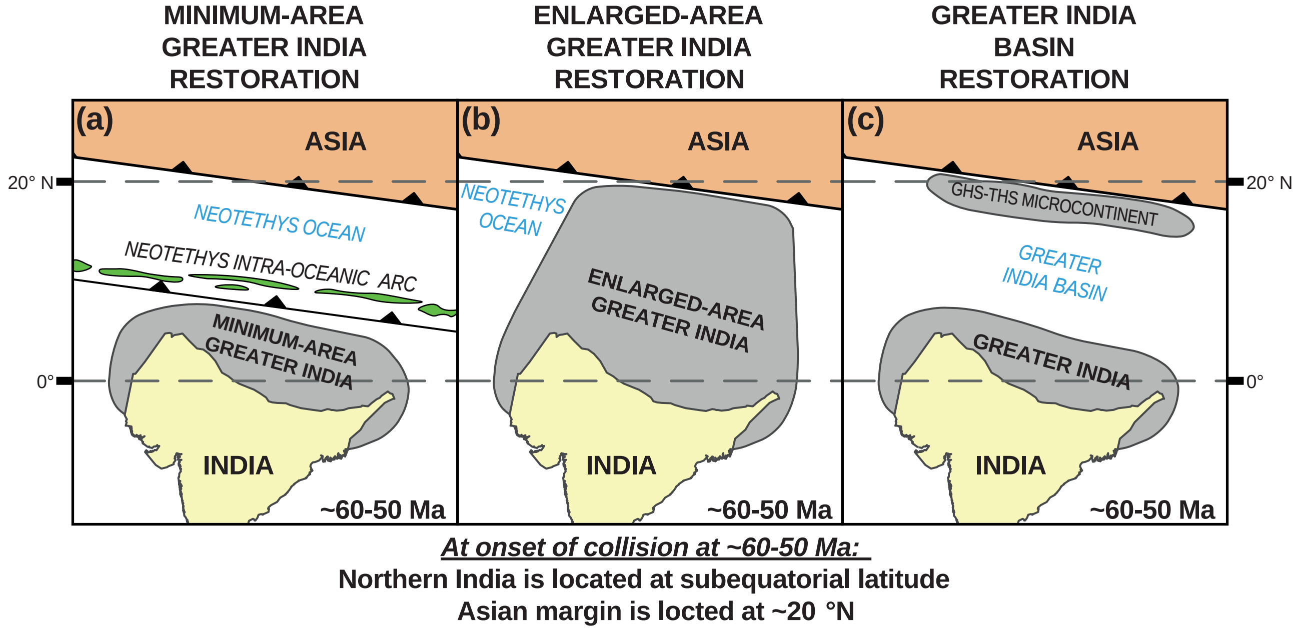

Fig. 5. Greater India restorations for models of the India-Asia collision. (a) Minimum-area restoration. (b) Enlarged-area reconstruction. (c) Greater India Basin reconstruction. GHS – Greater Himalayan Sequence; THS – Tethyan Himalayan Sequence.

occurred between Greater India and a Neotethys intra-oceanic arc (e.g. Replumaz et al., 2010, 2014; Zahirovic et al., 2016; Zhou and Su, 2019). In some studies, the assumption of a minimum-area Greater India forms the central justification for the double subduction zone configuration.

3.2.2. Enlarged-area reconstructions

Enlarged-area reconstructions of Greater India (Fig. 5b) are based on the premise that (1) Greater India was contiguous with the rest of the Indian continent; and that (2) the India-Asia collision (*s.l.*) had a single subduction zone configuration (e.g. Hu et al., 2016a; Ingalls et al., 2016). When incorporated into a plate kinematic framework, the enlarged-area Greater India restoration has a north-south width of at least 3000 km (e.g. Ingalls et al., 2016; Rowley, 2019a; van Hinsbergen et al., 2019), which is at least ~2000 km in excess of restorations based on crustal shortening estimates (i.e. minimum-area reconstruction). Mass-balance exercises argue that erosion can account for some of the missing upper crustal material, but these calculations indicate that the missing middle and lower crust and lithospheric mantle is unaccounted for by the present-day lithosphere (e.g. Yakovlev and Clark, 2014; Ingalls et al., 2016). As such, studies which model the India-Asia collision (*s.l.*) with a single subduction zone configuration and an enlarged-area reconstruction of Greater India must assume (albeit sometimes implicitly) that a 2000 km-wide portion of continental crust and lithospheric mantle has been subducted and/or delaminated into the mantle without returning to the surface (Hu et al., 2016a; Ingalls et al., 2016; Rowley and Ingalls, 2017; van Hinsbergen et al., 2017; van Hinsbergen et al., 2019).

3.2.3. Greater India Basin reconstructions

Greater India Basin reconstructions (Fig. 5c) are based on the premise that (1) collision at ~60–50 Ma occurred between Greater India rocks of THS and the Asian continental margin; that (2) Greater India had a north-south width (present-day coordinates) of <1000 km before India rifted from Gondwana (Huang et al., 2017a; Huang et al., 2017b; van Hinsbergen, 2019; van Hinsbergen et al., 2019); and that (3) wholesale subduction of a ~2000 km-wide portion of Greater India predicted by the enlarged-area reconstruction (e.g. Ingalls et al., 2016; Hu et al., 2016a, 2016b), is geodynamically unfeasible (van Hinsbergen et al., 2012, 2019; van Hinsbergen et al., 2017). This reconstruction argues that a microcontinent of Greater India continental lithosphere comprising the THS and GHS rifted from the LHS during the Early Cretaceous, leading to ocean spreading of the intervening Greater India Basin (Sinha Roy, 1976; Hsü et al., 1995; van Hinsbergen et al., 2012, 2019; Zhou and Su, 2019). In this scenario, the onset of the India-Asia collision (*s.l.*) at ~60–50 Ma occurred between the GHS-THS microcontinent and the south Asian margin. This was followed by northwards subduction of Greater India Basin oceanic lithosphere, which closed at ~30–20 Ma during collision between Indian (including the LHS at its leading edge) and the GHS-THS microcontinent (van Hinsbergen et al., 2012, 2019; Zhou and Su, 2019).

An important implication of this reconstruction is that the Greater Indian Basin closed between the GHS and LHS. This implies that the MCT must have thrusted the GHS over the Greater Indian Basin suture zone and its Eocene to Oligocene forearc and foreland basin. This provides an explanation for the scarcity of late Eocene-Oligocene foreland basin strata in the Himalayan orogen, but it also re-defines the MCT as a paleo-plate boundary between the GHS and LHS, in effect, equating it to a cryptic suture zone (e.g. Burke et al., 1977; Dewey, 1977). This proposition has been met with strong opposition from many workers who argue that over half a century's worth of field and laboratory analyses provide no lithological evidence for a suture zone ever existing between the GHS and LHS (e.g. Hu et al., 2016a; Searle, 2019).

3.3. Moving forward

Several mutually exclusive hypotheses for the India-Asia collision (*s.l.*) have been proposed based on the outlined subduction zone configurations and Greater India reconstructions (Fig. 4–5). Little progress has been made to resolve the differences between these models, yet it has become commonplace for recent studies to interpret their data in the context of just one of these three models (e.g. Gibbons et al., 2015; Hu et al., 2016a; Zahirovic et al., 2016; Buckman et al., 2018; Burg and Bouilhol, 2019), with little discussion of the validity of alternative models, and little to no consideration of the geodynamic assumptions, both explicitly and implicitly imposed by each model on their own interpretations. To address this issue, we present a critical evaluation of the different subduction zone configurations and Greater India reconstructions using a synthesis of geological and geophysical constraints integrated within a plate kinematic framework.

4. Methods: data synthesis and evaluation

Our analysis requires the integration of (1) bedrock observations; (2) plate kinematic constraints; and (3) geophysical observations of the Tibetan lithosphere and the distribution of subducted slabs in the deep mantle. Methods and decisions used to evaluate and interpret bedrock observations and kinematic constraints are generally well understood and are therefore described in Supplementary Materials 05. The geological and geodynamic interpretation of subducted slabs made from seismic tomographic observations, especially in the context of plate kinematics and bedrock observations, is less widely practiced. Therefore, we outline below, the geophysical datasets used in our study, and the concepts and understandings on which we ground our interpretations of these data.

4.1. Geophysical constraints

The structure and composition of the deep mantle is spatially and temporally variable; a first-order reason for this variability is the presence of subducted lithosphere in certain parts of the mantle but not in others. Removal of palaeo-ocean basins via subduction is one of the most important obstacle to reconstructing the palaeogeographies of collisions and accretions from the bedrock record alone. However, the surface (i.e. bedrock) and subsurface (i.e. mantle) records of subduction are directly linked, and geophysical observations of subducted slabs have the same immediate relevance to our understanding of the geological past as the bedrock record. Differences between the mantle and bedrock records relate to the scales and techniques with which they are observed and interpreted, but both form an integral part of our planet's geological record. Integration of bedrock and mantle records thus provides a more holistic account of Earth’s tectonic evolution than that which can be determined from looking at either record in isolation. In our analysis, geophysical observations of the subsurface lithosphere and deep mantle serve two purposes:

(1) We use regional-scale seismic tomography models and receiver function analyses to investigate the lithospheric and upper mantle structure of the Tibetan Plateau (Section 5.5.3) (e.g. Nábělek et al., 2009; Agius and Lebedev, 2013; Zhang et al., 2015; Liang et al., 2016; Xu et al., 2017). Those analyses constrain the extent and geometry of Indian lithosphere underthrusting and/or subducting beneath the Tibetan Plateau, which is relevant to reconstructions of Greater India (e.g. Replumaz et al., 2010; van Hinsbergen et al., 2019).

(2) We use global seismic tomography models to constrain the size, geometry, depth and location of subducted slabs in the deep mantle (-Section 5.2), from which we infer the locations, duration and timing of paleo-subduction zones (e.g. Van der Voo et al., 1999; Hafkenscheid et al., 2006; Sigloch and Mihalynuk, 2013; Domeier et al., 2016; Wu et al., 2016; Sigloch and Mihalynuk, 2017; van der Meer et al., 2018; Chen et al., 2019). Our methods and assumptions used to interpret seismically fast tomographic anomalies are outlined below.

4.1.1. Geological interpretation of seismically fast anomalies in the deep mantle

Seismic tomography reveals regions of mantle with seismic velocities that are either faster or slower than a laterally averaged reference model (e.g. PREM - the Preliminary reference Earth model; Dziewonski and Anderson, 1981, IASP91 - Kennett and Engdahl, 1991, AK135 - Kennett et al., 1995). Subducting slabs of lithosphere are colder and denser than the surrounding peridotite mantle and thus produce seismic anomalies that are faster than the reference model. This is confirmed from observations of active subduction zones, in which the size, geometry and location of seismically fast anomalies closely correlates with the locations of the overlying subduction zone trenches and earthquake hypocentres within the Wadati-Benioff zone of subduction megathrusts (e.g. Grand et al., 1997; van der Hilst et al., 1997).

Interpretation of seismically faster-than-average regions of the mantle as slabs of subducted lithosphere that have detached from their subduction zones requires additional criteria to rule out that they are artefacts of the tomographic inversion process (e.g. Foulger et al., 2013):

Firstly, one must consider if the seismically fast anomaly in question has a 3D morphology expected for a sinking slab. In the upper mantle, the geometry of a detached slab should retain a large aspect ratio in the form of a sub-vertical wall or ramp with a linear to curvilinear horizontal trace. The geometries of slabs within the mantle transition zone (MTZ) and lower mantle are more complex due to the viscosity and density contrasts across the MTZ, which can cause the slab to buckle and fold as it sinks (Fig. 6) (e.g. Ribe et al., 2007; Sigloch and Mihalynuk, 2013; Goes et al., 2017; Čížková and Bina, 2019). Still, when viewed in the horizontal plane, the slab should retain the linear shape of the subduction zone from which it detached. Larger anomalies are more confidently imaged than small ones. Hence, isolated and relatively smaller seismically fast anomalies with small, ‘blobby’ aspect ratios in both the vertical and horizontal planes are questionable and their geological interpretation should be treated with caution. One possible exception is where localized removal of subcontinental lithospheric mantle is suspected (e.g. Houseman and Molnar, 1997; Göğüş et al., 2017; Kelly et al., 2019), which could produce relatively small and ellipsoidal, fast anomalies within the upper mantle.

For a seismically fast anomaly to be interpreted as a detached slab of subducted lithosphere, one must then consider whether bedrock datasets support that conclusion. This has been central to the development of recent global plate reconstruction models, which demonstrate a close fit between the locations of seismically fast anomalies with slab-like geometries and the reconstructed locations of paleo-subduction zone trenches (e.g. van der Meer et al., 2010; Steinberger et al., 2012; Domeier et al., 2016; Müller et al., 2019). Support from the bedrock record becomes more difficult where its interpretations are contested (e.g. Nelson et al., 2013; Sigloch and Mihalynuk, 2017; Parsons et al., 2018; Clennett et al., 2019; Monger and Gibson, 2019), and for the deepest seismically fast anomalies in the lower mantle, which subducted in the distant past and are thus harder to spatially correlate with the bedrock record in a kinematic reference frame (e.g. Shephard et al., 2012; Torsvik and Cocks, 2017).

Before attempting the interpretation of any slab, one should consider the results of tomographic resolution tests in the mantle area in question, as conveyed by the original publication of a tomographic model. A poorly defined seismic anomaly with an unexpected size and/or geometry may indicate the general presence of slab in the area, without resolving details such as strike or true spatial extent. Some tomographic studies include hypothesis-driven resolution tests, featuring the hypothesized geometries of a slab of interest as a model input in the reference model (e.g. Ritsema et al., 2007; Foulger et al., 2013; Zhao et al., 2014; Liang et al., 2016). These hypothesis-driven resolution tests represent the most effective and robust way to determine whether a fast anomaly can be attributed to a region of seismically fast material in the mantle or an artefact of the tomographic inversion process. In the event of the former, these tests may also constrain the size and shape of the physical manifestation (i.e. slab geometry) responsible for the seismically fast velocity anomaly (e.g. Zhao et al., 2014; Liang et al., 2016).

Global body-wave tomography models (e.g. Amaru, 2007; Hosseini et al., 2020) provide the most comprehensive resolution in the middle third of the mantle, and in the upper mantle beneath seismically instrumented regions. P-wave models have been preferred over S-wave models for slab interpretations, as the shorter wavelengths and greater abundance of P-wave measurements can better resolve slab-sized anomalies. However, there should still be a general agreement between P- and S-wave models. In the upper mantle, surface-wave tomography models (e.g. Ceylan et al., 2012; Agius and Lebedev, 2013; Schaeffer and Lebedev, 2013) provide better vertical resolution and may sample an area more extensively than body waves, especially in the vast areas that are sparsely instrumented (including all of the oceans). However, mantle-penetrating surface waves have much longer wavelengths than body waves (hundreds of kilometres). In combination with sparse instrumentation, these models can become too laterally averaged to resolve a subducted slab on the length scale of an arc segment.

Differences exist between models that use the same seismic phases because of differences in how they are constructed and processed, or in the

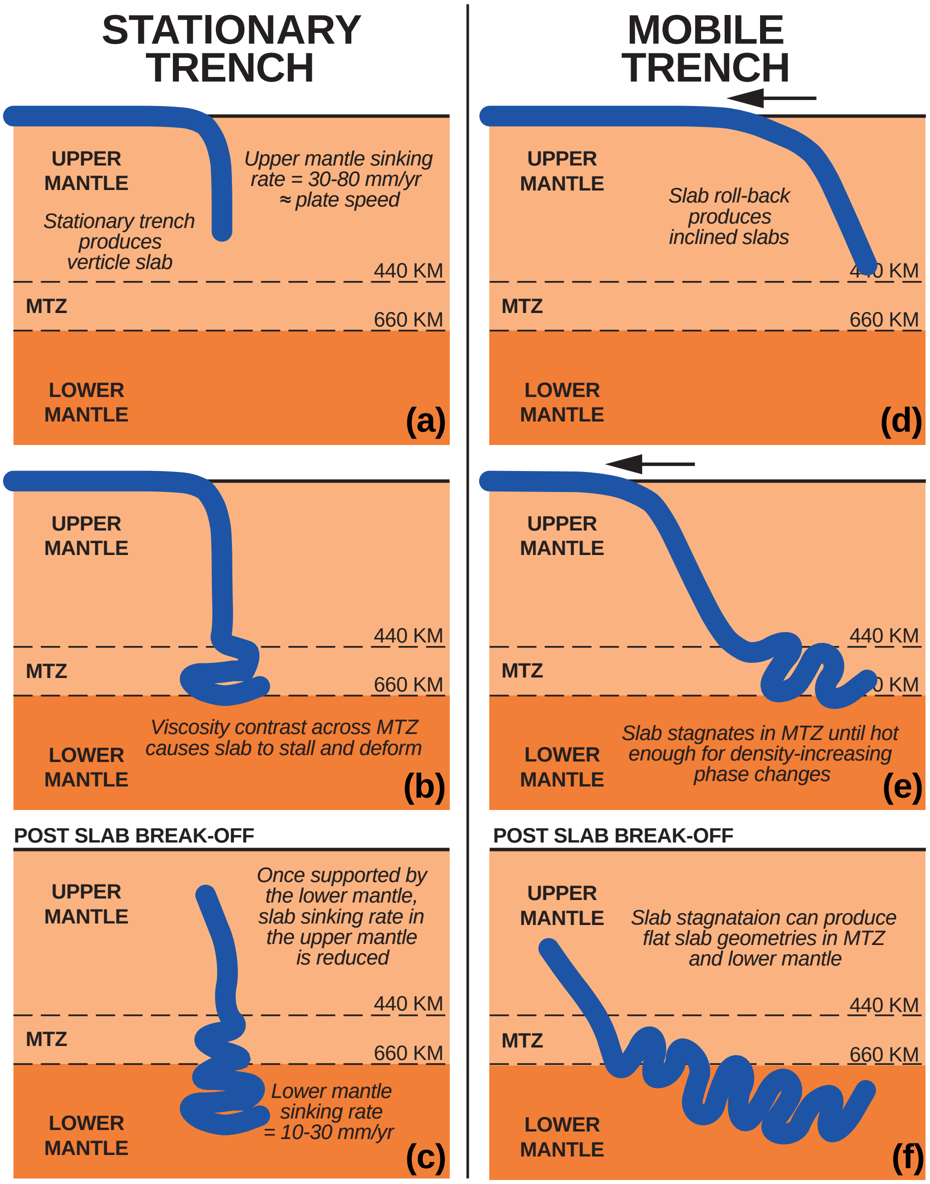

Fig. 6. Cartoon representation of modes of sinking for subducted slabs (blue) in the upper and lower mantle for (a-c) stationary trenches; and (d-f) mobile trenches. The viscosity contrast across the mantle transition zone (MTZ) causes slab to decelerate and deform. (For interpretation of the references to colour in this figure legend, the reader is referred to the web version of this article.)

spatial coverage of the earthquake datasets used to populate them (e.g. Foulger et al., 2013). Consequently, it is good practice to compare and contrast the size, shape and position of a given seismic anomaly in different tomographic models. The recent development of 'Vote Maps', which overlay the results of multiple seismic tomography models via the SubMachine tool, provides a quick and effective way of comparing anomalies in different tomographic models (e.g. Lekic et al., 2012; Shephard et al., 2017; Hosseini et al., 2018), but the user must not be lulled by their largest common denominator effect. Agreement between models is comforting, but progress in geophysical imaging results from methodological innovations, which inevitably provide the basis for certain features being correctly resolved in a new model for the first time (producing disagreement with vote maps of existing models).

There are no simple criteria for defining the physical limits of a subducted slab from its corresponding seismic anomaly. Finite wavelength and limited wave coverage produce a spatial imaging blur even for mantle anomalies that have sharp boundaries, such as subducted lithosphere. Regularization during the inversion process can lead to smearing or dampening of anomalies such that they are larger or smaller than the physical body, which they represent. In the lower mantle, P-wave tomographies tend to feature maximum velocity perturbations of around +1% faster-than-reference. In regions of good tomographic resolution, previous studies have defined the outlines of subducted slabs by the steepest gradient in seismic velocity contours, which tends to coincide with perturbation levels of 0.20–0.35% faster-than-reference (Hafkenscheid et al., 2006; Wu et al., 2016; Sigloch and Mihalynuk, 2017; Chen et al., 2019). Those magnitudes of velocity perturbation can serve as threshold criteria for defining the physical limits of poorly defined seismically fast anomalies, which are not surrounded by a steep gradient of velocity contours. This approach is supported by the degree of fit in mass-balance restorations that restore volumes of the seismically fast anomalies back to equivalent volumes of oceanic lithosphere at the Earth's surface (Wu et al., 2016; Chen et al., 2019). However, it is important to understand that the same physical velocity anomaly can appear differently in different tomography models, in terms of both its geometry and the magnitude of its relative velocity perturbation, because the tomographies feature different data coverage, regularisation parameters or 1-D reference models (e.g. Foulger et al., 2013).

The recent development of the web-based tool, ‘SubMachine’ (Hosseini et al., 2018) now allows for rapid and easy display and comparison of global tomographic models for specific regions of the mantle. Such tools dramatically lower the technical entry hurdle needed to integrate observations from the bedrock and mantle geological record and provide an important avenue for the union of geological and geophysical sciences. After following the steps outlined above, a user should be able to identify a selection of seismically fast tomographic anomalies, which they can interpret as slabs of subducted lithosphere with variable but well-reasoned degrees of confidence. The next step is to consider whether the position, size and geometry of those anomalies is *geodynamically* consistent with global plate reconstruction models and bedrock datasets.

4.1.2. Geodynamic interpretation of tomographically imaged slabs in the deep mantle

The locations of tomographically imaged subducted slabs mark the positions of their paleo-subduction zones (Van der Voo et al., 1999; Hafkenscheid et al., 2006; Replumaz et al., 2010; Replumaz et al., 2014; van Hinsbergen et al., 2019), based on the assumption that slabs sink vertically from the point at which they enter the mantle, and migrate laterally by only ~1–2° every 100 Myr (Steinberger et al., 2012). This assumption is consistent with current understandings of mantle rheology and convection (e.g. Ribe et al., 2007; Čížková and Bina, 2013; Agrusta et al., 2017; Čížková and Bina, 2019) and supported by a general agreement, at least for the past 130 Myr, between the predicted mantle structure from global plate reconstructions and mantle convection models with the imaged mantle structure via tomographic techniques (e.g. Steinberger et al., 2012; Domeier et al., 2016).

Application of the vertical sinking hypothesis has produced well-constrained tectonic models for the evolution of SW Pacific and North and South American Cordilleran margin, in which seismic tomography of subducted slabs has been robustly integrated with plate circuits and bedrock geological data in a comprehensive and consistent manner (Sigloch and Mihalynuk, 2013; Wu et al., 2016; Sigloch and Mihalynuk, 2017; Chen et al., 2019; Clennett et al., 2019). In these studies and others, the depths of the bottom and top surfaces of each anomaly are related respectively to subduction initiation and slab break-off events with given ages, which allows the rate at which slabs sink in the mantle to be calculated. In general, this approach yields a whole-mantle average sinking rate of ~10–20 mm/yr, which is consistent with geodynamic modelling (e.g. Sigloch and Mihalynuk, 2013; Butterworth et al., 2014; Wu et al., 2016; van der Meer et al., 2018; Chen et al., 2019).

Viscosity and density contrasts across the MTZ show that the velocity of a sinking slab will vary as it transitions from the upper mantle into the MTZ and lower mantle (e.g. Čížková and Bina, 2013; Agrusta et al., 2017; Čížková and Bina, 2019). Upon entering the upper mantle, the sinking rate of a subducting slab should reflect the velocity of lithospheric plate to which it is attached (Fig. 6a, d), based on the interpretation that subduction is the dominant driving force of tectonic plate motions (e.g. Forsyth and Uyeda, 1975). Previous studies suggest that sinking rates of slabs in the upper mantle are 30–80 mm/yr (e.g. Steinberger et al., 2012; Sigloch and Mihalynuk, 2013; Wu et al., 2016; Zahirovic et al., 2016; van der Meer et al., 2018). At the point of reaching the MTZ, the subducting slab may stagnate in the MTZ due to the density contrast across the 660 km discontinuity (Fig. 6b, e), and/or continue into the lower mantle at a reduced velocity, due to the increased viscosity of the lower mantle relative to the upper mantle (Fig. 6c, f) (Goes et al., 2017, Čížková and Bina, 2019). A slab stagnating in the MTZ will remain there until it is hot enough to facilitate the density-increasing endothermic ringwoodite to bridgmanite + magnesiowüstite transition, at which point it will sink into the lower mantle (Goes et al., 2017). In either case, once a subducting slab reaches the base of the upper mantle, the increased viscosity of the lower mantle resists further descent of the slab in such a way to reduce its sinking velocity, causing the slab to buckle and fold (Fig. 6b-c, e-f) (e.g. Ribe et al., 2007; Goes et al., 2017). This has been confirmed by seismic tomography and synthetic seismic tests of the subducting Australian plate and Farallon plate, which display dramatic increases in thickness across the MTZ and into the lower mantle (Ribe et al., 2007; Sigloch et al., 2008). Once in the lower mantle, slab-sinking rate estimates are 10–30 mm/yr, comparable to whole-mantle average sinking rates (e.g. Steinberger et al., 2012, Sigloch and Mihalynuk, 2013, Wu et al., 2016, Zahirovic et al., 2016, van der Meer et al., 2018).

If a subduction zone trench remains stationary then its slab is likely to have a vertical wall geometry that thickens in the lower mantle (Fig. 6a-c) (e.g. Ribe et al., 2007; Sigloch and Mihalynuk, 2017; Čížková and Bina, 2019). If a trench migrates via roll-back during subduction, then its slab will have a ramp geometry that dips away from the direction of trench migration in the upper mantle (Fig. 6d). In the MTZ and/or lower mantle, a slab subducted from a migrating trench is likely to thicken, and will have a sub-horizontal to dipping geometry (Fig. 6e-f), depending on how fast the trench retreated and how long the slab stagnated in the MTZ before entering the lower mantel (Goes et al., 2008; Agrusta et al., 2017; Čížková and Bina, 2019). Alternatively, if the subduction zone advances towards the direction of subduction then some studies have proposed that the subducting slab may be overturned or dragged in the direction of trench motion (e.g. Advokaat et al., 2018; Spakman et al., 2018).

Final consideration should be given to the possibility of lateral variations in mantle viscosity. The presence of antipodal large low velocity provinces beneath Africa and the Pacific Ocean indicate that at the largest scale, mantle viscosity must vary laterally (Steinberger et al., 2012; Garnero et al., 2016; Niu, 2018). However, the magnitude of variation at the scale of hundreds to thousands of kilometres is unclear (Steinberger et al., 2012). Local variations in sinking rates of slabs from the same region may indicate that small-scale lateral variations in viscosity exist (e.g. van der Meer et al., 2010; Steinberger et al., 2012; van der Meer et al., 2018). However, such variations may be equally explained by uncertainty related to the tomographic interpretation of the size and positions of the slabs, and/or the timing and duration of subduction. Understanding the scales and magnitudes at which mantle viscosity varies laterally represents a major scientific challenge that must be overcome in order to elucidate the significance of variable slab sinking rates (Steinberger et al., 2012, van der Meer et al., 2018).

5. Synthesis of constraints for models of the India-Asia collision (*s.l.*)

To evaluate the competing subduction zone configurations and Greater India reconstructions for models of the India-Asia collision (*s.l.*), we must determine the following: (1) the post-Triassic subduction zone configuration of the central Tethys oceans; (2) the timing of India-Asia collision (*s.l.*); (3) the locations of the Indian continent and paleo-trenches within the Neotethys Ocean prior to, and during the onset of collision; and (4) the size of Greater India at the onset of collision. In the following sections, we describe and interpret the data and observations used to constrain these geological elements and events. We will then integrate this information in a plate kinematic framework in section 6, to test subduction zone configurations and Greater India reconstructions for the India-Asia collision (*s.l.*) and the post-Triassic evolution of the central Tethys oceans.

5.1. Post-Triassic record of subduction in central and southern Tibet

This section interprets the existing geochronological and geochemical datasets summarized in Fig. 3 to constrain the post-Triassic subduction history of the central Tethys oceans (Fig. 7). Here, we define “accretion” as the sequential addition of material from a subducting lower plate to an overriding upper plate or vice versa, via underplating, obduction or transform faulting. In general, this requires down-cutting of the subduction interface into the lower plate via in-sequence thrusting (subduction-accretion). Subduction-erosion describes a special case of accretion where upper plate material is accreted to the lower plate via out-of-sequence thrusting during subduction. An extended summary of modes of accretion, with references, is given by Parsons et al. (2018). Full descriptions of the supporting geochronological

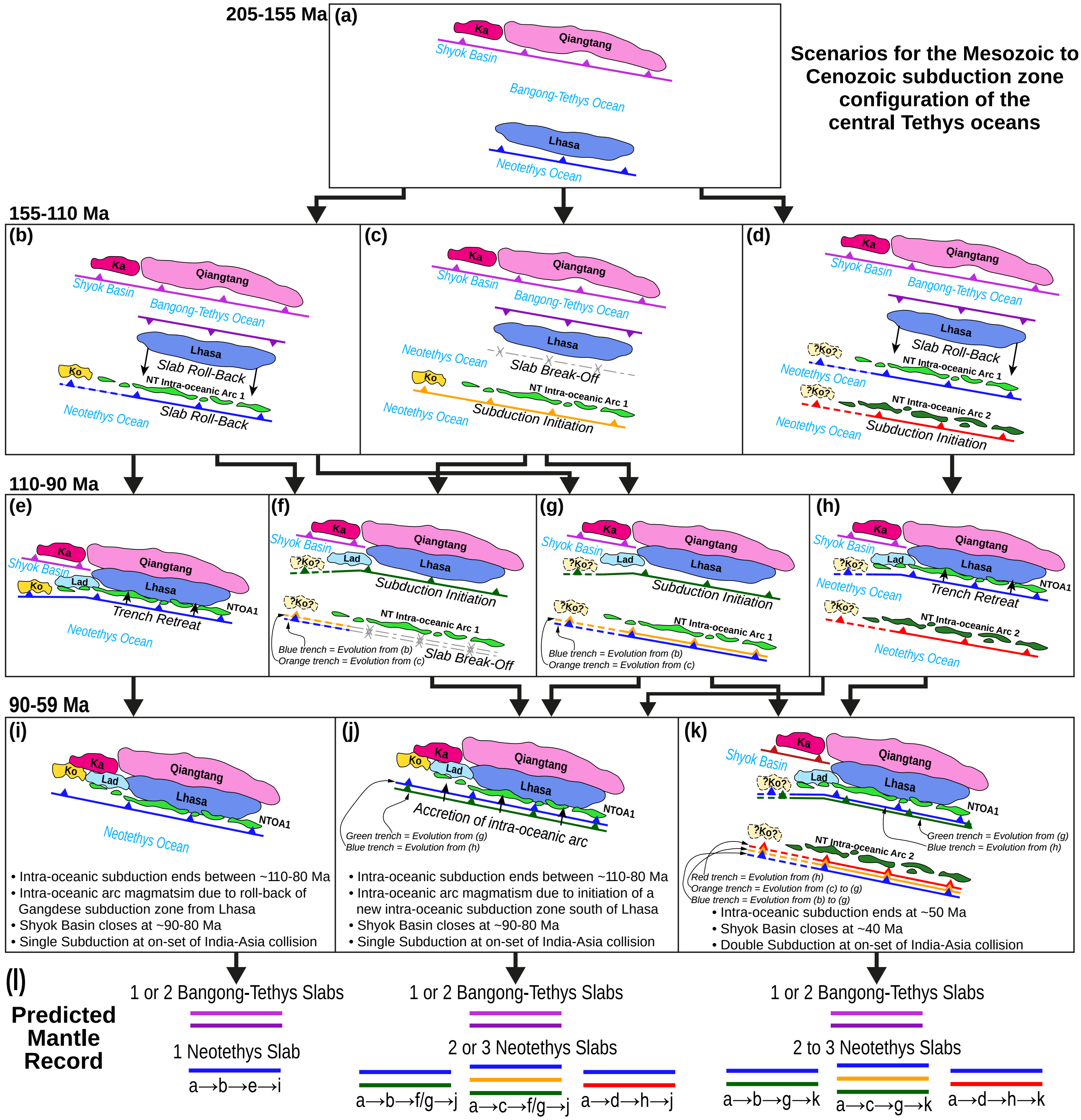

(i)
- Intra-oceanic subduction ends between ~110-80 Ma
- Intra-oceanic arc magmatsim due to roll-back of Gangdese subduction zone from Lhasa
- Shyok Basin closes at ~90-80 Ma
- Single Subduction at on-set of India-Asia collision

(j)
- Intra-oceanic subduction ends between ~110-80 Ma
- Intra-oceanic arc magmatism due to initiation of a new intra-oceanic subduction zone south of Lhasa
- Shyok Basin closes at ~90-80 Ma
- Single Subduction at on-set of India-Asia collision

(k)
- Intra-oceanic subduction ends at ~50 Ma
- Shyok Basin closes at ~40 Ma
- Double Subduction at on-set of India-Asia collision

Fig. 7. (a-k) Mesozoic to Cenozoic subduction zone configuration for central Tethys region, based on published constrains (See Fig. 3 & Supplementary Materials 03 and 04). Arrows between diagrams mark potential evolutionary scenarios for different subduction zone configurations. Subduction zones colours define distinct subducted slabs. Abbreviations: Ka – Karakoram; Ko – Kohistan; Lad – Ladakh; NTOA1 – Neotethys intra-oceanic arc 1. Dashed subduction zones and pale yellow dashed block labelled “?Ko?” correspond to equally plausible restorations of the Kohistan block for a given time period, based on the limited constraints. (l) Predicted number of slabs of subducted Bangong-Tethys and Neotethys ocean lithosphere, based on possible scenarios. Coloured lines for each slab match to specific colour-coded subduction zones in (a-k).

and geochemical constraints used by our study (as presented in Figs. 3 and 7) are compiled in Supplementary Materials 03 and 04.

5.1.1. Closure of the Bangong-Tethys Ocean and Shyok basin via suturing of the Lhasa-Ladakh-Kohistan block with the Qiangtang-Karakoram block

During the Jurassic, the Qiangtang-Karakoram and Lhasa blocks were separated by the Bangong-Tethys Ocean (Kapp and DeCelles, 2019; Li et al., 2019). South of the Karakoram block, this ocean is referred to as the Shyok basin (Fig. 7a). Late Triassic to Early Cretaceous subduction beneath south Qiangtang and Late Jurassic to Early Cretaceous subduction beneath north Lhasa (Fig. 7a-e) sutured these blocks at ~130–110 Ma, accompanied by extensional deformation of the Lhasa block, and a marine transgression which covered both Lhasa and Qiangtang (Events 52–56, 61: Fig. 3) (Kapp et al., 2005; Zhang et al., 2012a; Li et al., 2018; Kapp and DeCelles, 2019; Li et al., 2019). To the west, northward subduction continued beneath the Karakoram block (Fig. 3) till at least the Late Cretaceous, although calc-alkaline magmas continued to be emplaced within the Karakoram block until ~40 Ma (Events 1–4: Fig. 3) (e.g. Searle et al., 1989; Heuberger et al., 2007; Ravikant et al., 2009; Searle et al., 2010; Phillips et al., 2013; Borneman et al., 2015).

The timing of suturing of the Shyok basin via collision between the Karakoram and Kohistan blocks is contested. Some studies, which favour a double subduction configuration for the India-Asia collision (*s.l.*) (e.g. Bouilhol et al., 2013; Jagoutz et al., 2015; Burg and Bouilhol, 2019), propose that the Kohistan and Ladakh blocks collided with Karakoram at ~40 Ma (Fig. 7 k). However, Najman et al. (2017) demonstrated that at 54 Ma, sediments derived from the Lhasa block were deposited on northwest Greater India, south of the Ladakh block; this suggests the Ladakh block had accreted to Asia by that time, in order to allow sediment transport from Lhasa to Greater India.

Other studies argue that suturing between Karakoram and the Kohistan and Ladakh blocks occurred at 90–80 Ma (Fig. 7i-j) (e.g. Debon et al., 1987; Treloar et al., 1996; Clift et al., 2002; Burg, 2011; Borneman et al., 2015). This is supported by (1) burial-related sillimanite-grade metamorphism and partial melting (metamorphic phase M1a) within the Karakoram metamorphic complex, followed by cooling of the Karakoram, Kohistan and Ladakh blocks and an associated influx of detrital zircons during ~89–60 Ma (Events 5, 9, 18, 22, 30: Fig. 3) (e.g. Reuber et al., 1989; Burg, 2011; Palin et al., 2012; Zhuang et al., 2018), which is consistent with Late Cretaceous collision between Karakoram and the Kohistan and Ladakh blocks; (2) continued prograde sillimanite-grade metamorphism of the Karakoram block between ~57–42 Ma (metamorphic phase M1b-c, Event 10: Fig. 3) (e.g. Palin et al., 2012), which is consistent with Paleogene collision between India and Asia and inconsistent with a ~40 Ma collision between Kohistan and Karakoram; (3) an Early to Late Cretaceous erosional unconformity overlying strongly folded and faulted strata on the Karakoram block (Gaetani et al., 1990; Gaetani et al., 1993); (4) the age of undeformed dykes (~89–75 Ma) that cross-cut rocks of the Shyok suture zone, and deformed intrusive rocks in the Kohistan block (Events 16, 25: Fig. 3) (Petterson and Windley, 1992; Weinberg et al., 2000; Yamamoto et al., 2005; Borneman et al., 2015); (5) the Late Cretaceous age of undeformed Dras 2 dykes which cross cut deformed Dras 1 volcaniclastics on the Ladakh block (Fuchs, 1982; Reuber, 1989; Reuber et al., 1989); and (6) the Albian-Cenomanian minimum age of volcano-sedimentary units within the Shyok suture (Events 15–17: Fig. 3) (Rolland et al., 2000; Bhutani et al., 2009; Borneman et al., 2015; Kumar et al., 2017). These studies propose that post-90 Ma subduction-related magmatism in the Karakoram block was produced by northward subduction of Neotethys beneath the Kohistan-Ladakh blocks after they accreted to the Asian margin; this is supported by a change in isotope geochemistry of magmas intruded into the Karakoram block after 90 Ma (e.g. Heuberger et al., 2007; Ravikant et al., 2009; Burg, 2011; Phillips et al., 2013; Borneman et al., 2015; Kumar et al., 2017). Further details and additional arguments for closure of the Shyok basin between 90 and 80 Ma are discussed in Supplementary Materials 03.

In summary, the above constraints are consistent with termination of subduction and suturing of the Bangong-Tethys Ocean along the southern Qiangtang margin and northern Lhasa margin during the Early Cretaceous (Fig. 7a-d) (e.g. Li et al., 2018). Most observations suggest that northward subduction beneath the southern Karakoram margin ended in the Late Cretaceous (Fig. 7e-h), but some studies argue that it continued to the Eocene (Fig. 7 k) (e.g. Borneman et al., 2015; Burg and Bouilhol, 2019).

5.1.2. Neotethys subduction beneath the Lhasa-Ladakh-Kohistan blocks

Subduction-related magmatism within the Lhasa-Ladakh-Kohistan blocks can be explained by many scenarios (Fig. 7b-k). Some studies propose continuous northward subduction of the Neotethys Ocean was facilitated by a single subduction zone (Fig. 7a-b, e, i), active along the south margin of all three blocks from the latest Triassic to Eocene (Zhang et al., 2012a; Li et al., 2018; Zhu et al., 2018; Kapp and DeCelles, 2019). In such hypotheses, magmatic lulls recorded by the Gangdese arc between ~150–110 Ma are explained by southwards slab roll-back during a phase of extension and marine transgression on the Lhasa block (Fig. 7b, d), leading to periods of intra-oceanic arc magmatism responsible for the formation of the Zedong terrane and SSZ ophiolites observed throughout the ISZ (Events 37, 41–52: Fig. 3) (e.g. Zhu et al., 2009b; Zhang et al., 2012a; Dai et al., 2013; Maffione et al., 2015; Wang et al., 2017; Kapp and DeCelles, 2019). Subsequent subduction-erosion, during convergent deformation of the Lhasa block (Events 30, 56: Fig. 3) may then explain how the trench and slab migrated back towards the Lhasa and Ladakh block (Fig. 7e), so as to revive magmatism within the Gangdese arc at ~110 Ma (Kapp et al., 2007; White et al., 2011; Li et al., 2018; Zhu et al., 2018). In this model, the Kohistan intra-oceanic arc and Dras arc could have initiated along-strike of the Zedong terrane during the first pulse of southward slab roll-back and intra-oceanic magmatism, allowing them to migrate with the southward retreating trench (Fig. 7b, d). This model is consistent with the deposition, in the Xigaze forearc, of Lhasa-derived sediments on top of the Xigaze and Sangsang ophiolites, which requires that these ophiolites be located close to the Lhasa block and not separated from the Lhasa block by an intervening trench (e.g. Burg and Chen, 1984; Einsele et al., 1994; Maffione et al., 2015; Orme and Laskowski, 2016; Kapp and DeCelles, 2019).

Consideration of the Spontang ophiolite, which forms an isolated klippe above the ISZ, south of Ladakh (Fig. 2), suggests that an alternative model is needed to explain the subduction configuration of the Neotethys ocean. The presence of Early Cretaceous SSZ gabbro emplaced into Early Jurassic N-MORB oceanic crust in the Spontang ophiolite (Events 36–37: Fig. 3) is hard to reconcile with models of Late Jurassic to Early Cretaceous roll-back and forearc spreading of the Gangdese arc (e.g. Fig. 7b) (e.g. Maffione et al., 2015; Kapp and DeCelles, 2019); that process should generate new oceanic crust in the upper plate with Late Jurassic forearc basalt, and boninite compositions (e.g. Stern and Bloomer, 1992; Stern and Gerya, 2018), rather than the observed Early Jurassic N-MORB compositions (Pedersen et al., 2001). Instead, the recorded petrogenetic relationship is more readily explained by Late Jurassic to Early Cretaceous subduction initiation (i.e. a new subduction zone, south of the Gangdese subduction zone) within Early to Middle Jurassic MORB oceanic crust (e.g. Fig. 7c) (e.g. Hébert et al., 2012). As such, magmatic lulls recorded by the Gangdese arc may correspond to initiation of a new, more southerly positioned intra-oceanic subduction zone at ~160–150 Ma within the Neotethys Ocean (Fig. 7c) (e.g. Guilmette et al., 2012; Hébert et al., 2012; Chan et al., 2015). In this situation, revival of the Gangdese arc at ~110 Ma was facilitated by subduction initiation beneath Lhasa, in the back-arc region of the Neotethys intra-oceanic arc (Fig. 7f-g). This subduction initiation may have occurred in response to contemporaneous collision and suturing between Qiangtang and Lhasa (i.e. induced subduction initiation via subduction polarity reversal: e.g. Stern and Gerya, 2018, Parsons et al., 2018), although further investigation is required to validate this hypothesis.

In the ISZ, fragmented metamorphic soles with SSZ protoliths and melange units with SSZ-derived detrital material, located in the footwalls to the overlying Xigaze, Sangsang, and Dras SSZ ophiolites, requires the presence of at least two intra-oceanic arcs. This structural arrangement invokes a situation where the SSZ metamorphic soles and SSZ melange units were formed in the upper plate of a southern intra-oceanic subduction zone, and were then subducted/accreted as part of the lower plate to a northern subduction zone, (e.g. Fig. 7d), in a similar configuration to the present-day Philippine Sea plate between the Ryukyu and Izu-Bonin-Mariana subduction zones (e.g. Mahéo et al., 2004; Mahéo et al., 2006; Guilmette et al., 2009; Guilmette et al., 2012; Hébert et al., 2012).

The Neotethys intra-oceanic arc(s) terminated either at ~116–110 Ma (Fig. 7e-f) (e.g. Dai et al., 2013; Chan et al., 2015), at ~90–80 Ma (Fig. 7 g, j) (Corfield et al., 2001; Pedersen et al., 2001; Searle, 2019; Walsh et al., 2019), or during collision with Greater India in the Paleocene or Eocene (Fig. 7 k) (Aitchison et al., 2007; Hébert et al., 2012; Guillot and Replumaz, 2013; Buckman et al., 2018; Burg and Bouilhol, 2019). Many observations support termination between ~116–110 Ma or ~90–80 Ma (Fig. 7f-g, j), including: (1) the absence of evidence for intra-oceanic magmatism from the ISZ east of Kohistan after ~110–80 Ma (Fig. 3); (2) cooling at 102–92 Ma recorded by blueschist-facies SSZ ophiolitic melange in the ISZ south of Ladakh, corresponding to subduction and exhumation of an intra-oceanic arc by 92 Ma (Event 40: Fig. 3) (Honegger et al., 1989; Mahéo et al., 2004; Mahéo et al., 2006); (3) cooling at 88–80 Ma recorded by ophiolite metamorphic soles in the ISZ south of Lhasa (Event 46: Fig. 3) (Malpas et al., 2003; Bao et al., 2013; Chan et al., 2015); (4) compressional deformation recorded on the Lhasa block between ~100 Ma and 50 Ma (Event 56, Fig. 4) (e.g. van Hinsbergen et al., 2011a, 2012; Zhang et al., 2012a); and (5) the supporting evidence for accretion of Kohistan to Karakoram between ~90–80 Ma (see previous section).

Detrital zircons from the Nindam Formation may indicate that intra-oceanic subduction continued until 84 ± 1 Ma (Event 28: Fig. 3), if the Dras arc formed part of the Neotethys intra-oceanic arc (e.g. Robertson and Degnan, 1994); however, this could equally be explained as an east to west transition along a single subduction zone from the continental Gangdese arc to the oceanic Dras arc, similar to the along-strike structure of the Aleutian arc (e.g. Rolland et al., 2000). Southwest of Kohistan, the West Pakistan ophiolites record intra-oceanic magmatism at 80 ± 1.5 Ma to and 65 ± 1 Ma (Events 32–35: Fig. 3) (Ahmed, 1993; Kakar et al., 2012). Previous studies suggest that they formed during an isolated subduction and collisional event (the West India orogeny) between the Kabul block and northwest India sometime during the Campanian to Eocene (Gnos et al., 1997; Gaina et al., 2015; van Hinsbergen et al., 2019). The tectonic relationship between this event and subduction and collisional events between Greater India, the Neotethys intra-oceanic arc and the Gangdese arc is unclear and requires further investigation.

Special consideration should be given to the hypothesized Spong arc. Many studies cite the UPb zircon age of 88 ± 5 Ma (Event 38: Fig. 3) from an andesite that overlies the Spontang ophiolite (the Spong arc; Corfield et al., 2001, Pedersen et al., 2001) as evidence that the Neotethys intra-oceanic arc remained active at least until ~90–80 Ma (e.g. Hébert et al., 2012; Buckman et al., 2018; Searle, 2019). However, we note that (1) the Spong arc andesite has discordant zircon fractions with upper intercept ages suggestive of Precambrian inherited zircon; (2) the Spong arc andesite has an enriched calc-alkaline composition with εNd = −5.4; (3) the petrogenetic correlation between this andesitic volcano-sedimentary sequence and the Spontang ophiolite is not demonstrated, and; (4) other intra-oceanic arc magmatic assemblages reported from the ISZ are no younger than Early Cretaceous (e.g. Corfield et al., 2001; Pedersen et al., 2001; Chan et al., 2015). Based on these observations, we propose that it is equally justifiable to interpret the Spong arc andesite as the volcanic product of the Gangdese arc, deposited on top of the Spontang ophiolite after or during accretion of the Neotethys intra-oceanic arc to the Ladakh and Lhasa blocks by 88 ± 5 Ma.

5.1.3. Summary of subduction configuration scenarios

Possible post-Triassic subduction zone configurations for the Neotethys and Bangong-Tethys oceans, which are consistent with the above constraints, are presented in Fig. 7. Variations between scenarios depend on whether: (1) subduction of the Neotethys Ocean occurred continuously along a single, migrating subduction zone (blue subduction zone on Fig. 7a-b, d-e, h-I, k) or whether the Early Cretaceous magmatic gap (~150–110 Ma) of the Gangdese arc corresponds to termination of subduction beneath south Lhasa at ~150 Ma (slab break-off on Fig. 7c), followed by subduction initiation beneath south Lhasa in the Cretaceous (green subduction zone on Fig. 7f-g), (2) whether the intra-oceanic arcs formed as a result of roll-back of the subducting Neotethys slab beneath Lhasa (blue subduction zone on Fig. 7b, d) or due to subduction initiation of a new Neotethys intra-oceanic subduction zone south of Lhasa (orange subduction zone on Fig. 7c-d), and (3) whether intra-oceanic arcs formed from one or two intra-oceanic subduction zone in the Neotethys Ocean (Fig. 7c-d).

Depending on which scenario is used to explain the post-Triassic subduction configuration of the central Tethys oceans, anywhere between one to three distinct slabs of subducted Neotethys ocean lithosphere and one to two slabs of Bangong-Tethys ocean lithosphere can be expected to reside in the mantle below the Indian hemisphere (Fig. 7l). In Section 6, these predictions of slab distributions within the deep mantle will be tested against seismic tomographic observations (see Section 5.2 below) as a means to test the subduction zone configurations proposed for the India-Asia collision (*s.l.*).

5.2. Mantle structure beneath the Indian hemisphere

Using the web-based 'SubMachine' tool for visualizing and plotting tomographic models of Earth's interior (Hosseini et al., 2018), we have compared the deep mantle structure estimated by 10 different P-wave global tomography models (Table 1) (Montelli et al., 2006; Amaru, 2007; Houser et al., 2008; Li et al., 2008; Simmons et al., 2010; Simmons et al., 2012; Obayashi et al., 2013; Koelemeijer et al., 2016; Tesoniero et al., 2015), including the newly published DETOX-P2 model of Hosseini et al. (2020), which illuminates the lowest third of the mantle especially well. Of these models, four P-wave models and one surface-wave model have been selected to further constrain the geometry and depth of six distinct seismically fast anomalies beneath the Indian hemisphere (Figs. 9–20),

Table 1
List of tomography models analysed in this study.

Model	Data Type	Reference	Notes
DETOX-P2	Body waves	Hosseini et al. (2020)	Combines a large set of multifrequency P and Pdiff measurements (Hosseini and Sigloch, 2015) and analyst-picked arrival times.
GAP-P4	Body waves	Obayashi et al. (2013)	
GyPSuM-P	Body waves	Simmons et al. (2010)	
HMSL-P06	Surface waves, body waves	Houser et al. (2008)	
LLNL_G3Dv3	Body waves	Simmons et al. (2012)	Includes seismic phases with short epicentral distances sensitive to the uppermost mantle, and a 3D background model with laterally variable Moho and mantle transition zone thicknesses to give excellent resolution in the upper mantle.
MITP08	Body waves	Li et al. (2008)	
PRI-P05	Body waves	Montelli et al. (2006)	
SP12RTS-P	Surface waves, body waves, normal modes	Koelemeijer et al. (2016)	
SPani-P	Surface waves, body waves	Tesoniero et al. (2015)	
UU-P07	Body waves	Amaru (2007)	
SL2013sv	Surface waves	Schaeffer and Lebedev (2013)	Upper mantle model. Includes 3500 stations and >20,000 earthquakes. This S wave tomography model has an excellent resolution in the upper mantle.

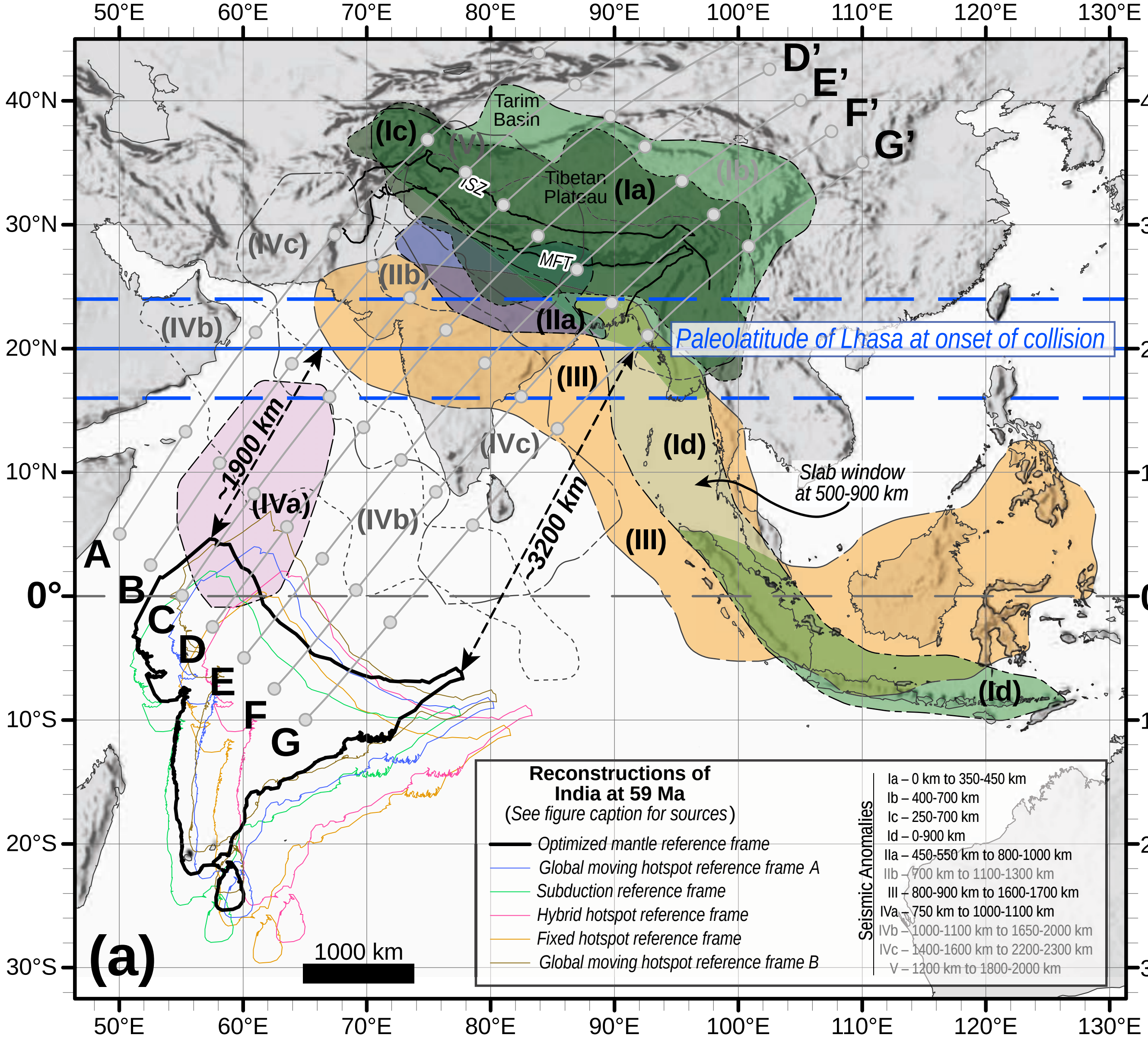

Fig. 8. Kinematic restoration of India and the Asian continental margin at the onset of collision, 59 ± Ma, overlain by the outlines of seismic anomalies I to V at (a) 0–-1700 km depth, and (b) 700–2300 km. Blue thick line corresponds to paleolatitude of the Lhasa block at 20° N ± 4° (errors marked by dashed blue lines) at the onset of collision (see Section 5.4 for discussion). Present day locations of the Main Frontal Thrust (MFT) and Indus Suture Zone (ISZ) are marked with black solid lines. Outlines of seismically fast anomalies I to V approximately corresponds to the largest areas defined by the dv/v = +0.2% contour around each anomaly. Seismic tomography lines of section shown in Figs. 12–20 are drawn with solid grey lines. Distances at 59 Ma of ~1900 km and ~3200 km between South Asian margin and East and West syntaxes of Indian continent are marked by dashed black arrows. Reconstructions of India at 59 Ma are based on different reference frames and reconstruction models: Black line – Optimized mantle reference frame (Müller et al., 2019); Blue line – Global moving hotspot reference frame A (Torsvik et al., 2008; Matthews et al., 2016; Müller et al., 2016; Zahirovic et al., 2016; Young et al., 2018); Green – Subduction reference frame (van der Meer et al., 2010; Shephard et al., 2012); Purple – Hybrid hotspot reference frame (O'Neill et al., 2005; Seton et al., 2012; Shephard et al., 2012); Orange – Fixed hotspot reference frame (Müller et al., 1993; Shephard et al., 2012); Brown line – Global moving hotspot reference frame B (Doubrovine et al., 2012; van Hinsbergen et al., 2019). Georeferenced overlays (.kml, .kmz) and shapefiles of all points, lines, and polygons presented in our map figures are available for use and editing with global information system software (e.g. Google Earth, GPlates, ArcGIS) in Supplementary Materials 01 and 02.

based on their suitability and sensitivity to imaging slabs in the lower mantle (Amaru, 2007; Li et al., 2008; Simmons et al., 2012; Hosseini et al., 2020), and upper mantle (Schaeffer and Lebedev, 2013).

The six fast anomalies are described below and summarized in Table 2. Depth slices from the selected models are presented at depths of 350 km and 600 km (Fig. 9), 800 km (Fig. 10) and 1300 km (Fig. 11). This includes 'vote maps' (e.g. Shephard et al., 2017); one combines the five chosen models (Figs. 9e-f, 10e, 11e) and the other combines 10 P-wave models (Figs. 10f, 11f), into single images that describe their mutual agreement. Additional depth slices at 50 km intervals from 0 km to 2400 km depth are presented in Supplementary Materials 06.

Tomographic cross sections through the six anomalies are presented in Figs. 12–18. Fig. 19 and Supplementary Materials 07 display cross-sections of the outlines of anomalies I to VI, drawn from the +0.2% and +0.3%

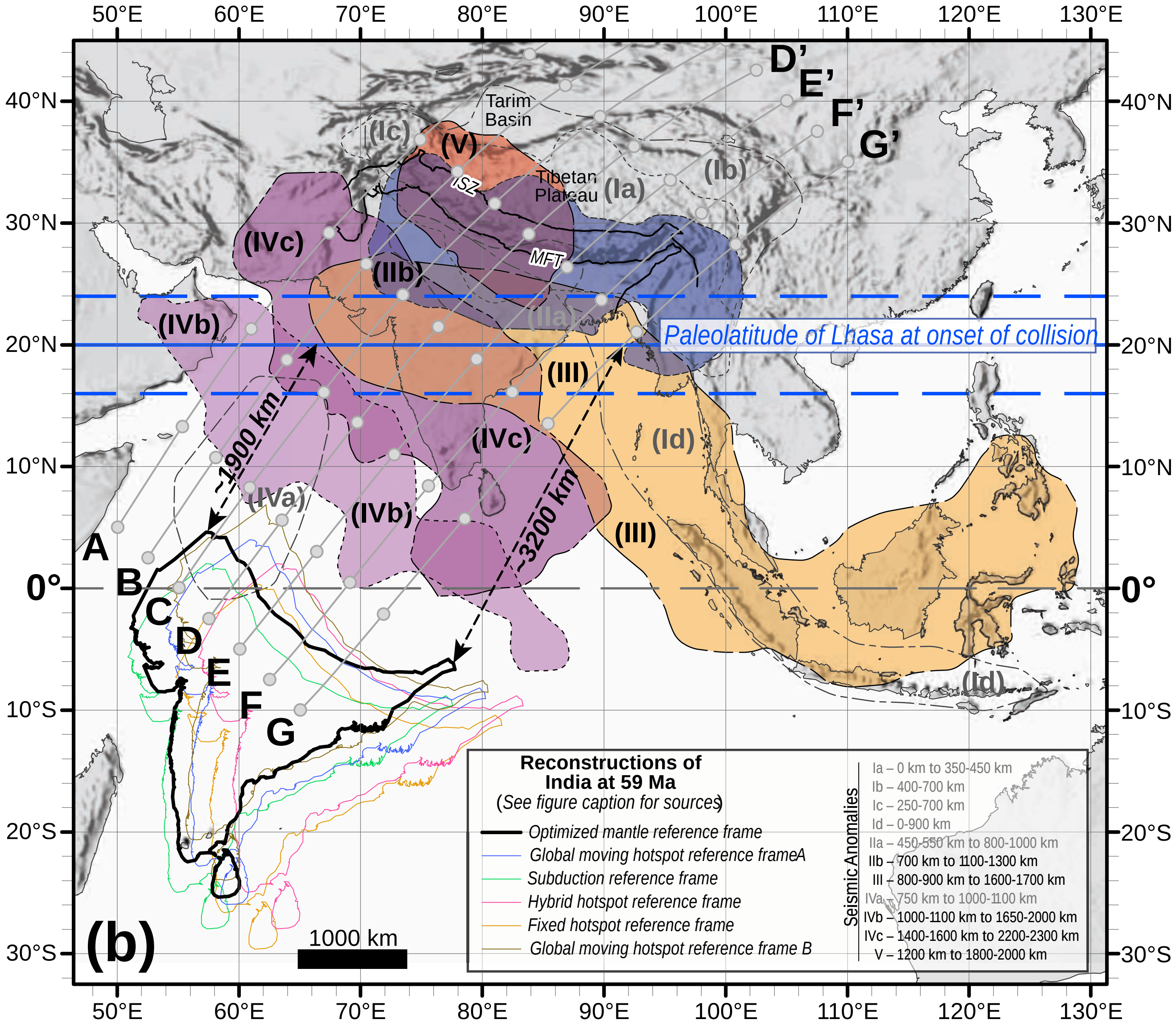

Fig. 8 (*continued*).

velocity perturbation contours from each of the five tomography models. Fig. 20 displays the cross-sectional area of each anomaly based on the combined observations from Figs. 9–13 and Supplementary Materials 06–07.

5.2.1. Anomaly I

Anomaly I is visible in the upper mantle beneath the Tibetan plateau (Figs. 8–9, 12–20). Its size and segmented geometry varies between tomographic models such that it is best described in terms of three connected anomalies (Table 2). Anomaly Ia is visible beneath southern Tibet in all models between 67°E 43°N to 97°E 25°N (Figs. 8–9, 12–20). It is coherent and linear between 0 and 350 km depth, and steeply dips northeast parallel to the ISZ. Between 350 and 450 km depth, Anomaly Ia is only partially visible in tomography models UU-P07, MIT-P08, and DETOX-P2, but well defined in models LLNL-G3Dv3 and SL2013sv, where it is observed directly on top of the upper surface of the underlying Anomaly Ib (Figs. 9, 12–18).

Anomaly Ib is a horizontally extensive anomaly immediately below Anomaly Ia in the MTZ at ~400–700 km depth between 70°E 38°N to 102°E 25°N (Figs. 8–9, 13–20). It is well defined in models LLNL-G3Dv3 and SL2013sv, but poorly defined and only partially imaged in UU-P07, MIT-P08, and DETOX-P2 (Figs. 9, 13–19). Surface-wave models provide better resolution in the upper mantle, which explains why model SL2013sv (Figs. 9a-b, 13–18) detects a much larger volume and depth for Anomaly I than most body-waves models (Schaeffer and Lebedev, 2013). Likewise, the P-wave model LLNL-G3Dv3 (Figs. 9c-d, 13–18) has been constructed to offer a higher resolution of the upper mantle through the use of a 3D background model that includes known lateral variations in Moho and mantle transition zone thicknesses, and a large dataset of *P* and *Pn* arrivals that were re-located using a range of seismic phases including several with short epicentral distances. Therefore, we define the geometry and location of Anomaly Ib from SL2013sv and LLNL-G3Dv3 (Fig. 9, Table 2).

Anomaly Ic is small and localized between 75°E, 38°N and 105°E, 25°N, beneath the Hindu Kush and Pamir regions (Table 2 and Figs. 8–9, 12–13, 19–20). It is well defined in all models except SL2013sv, which cannot distinguish this anomaly from Anomaly Ib and Ia. In all other models,

Table 2
Description of seismic anomalies identified on Figs. 8 to 20.

Anomaly	Description		Also Known As:	Properties	Tomographic Models					Vote Map	Maximum duration of subduction predicted from an assumed sinkingr rate of:		
					DETOX-P2	LLNL-G3Dv3	UU-P07	MIT-P08	SL2013sv3		10 mm/yr	15 mm/yr	20 mm/yr
Anomaly I	The size and geometry of Anomaly I varies with depth and is best described in terms of three connected anomalies (Ia, Ib, and Ic)	**Ia**	CR Anomaly (Replumaz et al., 2014)	**Lateral extent:**	70°E, 41°N to 97°E, 24°N	62°E, 38°N to 103°E, 18°N	63°E, 43°N to 99°E, 25°N	68°E, 39°N to 97°E, 25°N	70°E, 40°N to 100°E, 20°N	67°E, 43°N to 97°E, 25°N	40 Ma to 0 Ma	26 Ma to 0 Ma	20 Ma to 0 Ma
				Top surface:	50 km	0-150 km	0-100 km	0-50 km	0-50 km	0-50 km			
				Top of full linear trace:	50 km	0-150 km	0-200 km	100 km	0-200 km	100 km			
				Bottom surface:	450 km	400 km	400 km	350 km	425 km	350 km			
	Anomaly Ia is well defined by all models		The SE corner of Anomaly Ia is identified as the Burma anomaly (Van der Meer et al. 2018)	**Comments:**	Merges with top of Anomaly Ib and IIa	Slab dips NE from 300 km depth downwards	Anomaly Ia is patchy below 250 km but covers full horizontal area of anomaly outline	Full linear trace of Anomaly Ia is not visible below 250 km	Slab dips NE from 250 km depth downwards	Well defined by Vote Map			
	Anomaly Ia forms a linear anomaly with a WNW-ESE strike and a NE dip				NE corner of Anomaly Ib is not imaged			Lower half of Anomaly Ia is patchy	From 200 km to 425 km depth, Anomaly Ia forms a linear vertical anomaly directly above the central axis of Anomaly Ib				
	Anomaly Ib forms a wide, flat anomaly within the MTZ and base of the upper Mantle												
		Ib	Most of Anomaly Ib has not been formally identified as a subducted slab by previous studies	**Lateral extent:**	77°E, 38°N to 103°E, 28°N	72°E, 42°N to 105°E, 22°N	74°E, 33°N to 108°E, 25°N	98°E, 32°N to 107°E, 24°N	70°E, 38°N to 102°E, 25°N	75°E, 38°N to 105°E, 25°N	70 Ma to 40 Ma	46 Ma to 26 Ma	35 Ma to 20 Ma
	Base of Anomaly Ia merges into the tops of Anomalies Ib and Ic			**Top surface:**	450 km	400-450 km	400 km	350 km	425 km	350 km			
				Top of full linear trace:	-	-	450 km	-	450 km	-			
	LLNL-G3dv and SL2013sv suggest that Anomaly Ib corresponds to large volume of seismically fast material in upper mantle and MTZ; Anomaly Ib is poorly imaged by the other models			**Bottom surface:**	700 km	700 km	700 km	500-600 km	700 km	700 km			
				Comments:	Linear trace not visible	Horizontal area of Anomaly Ib is shifted NE with respect to Anomaly Ia	Anomaly Ib is poorly defined, with patchy appearance	Only the SE margin of Anomaly Ib is imaged by this model	Well defined by this model	Very poorly defined by Vote Map			
			The SE corner of Anomaly Ib is identified as the Burma anaomaly (Van der Meer et al., 2018)		Anomaly Ib dips and widens with depth in a NE direction	Anomaly Ib forms laterally extensive horizontal anomaly between 450-600 km depth	Linear trace not visible		Horizontal area of Anomaly Ib is greatest at 600 km and decreases below this depth				
	Anomaly Ic is a small, isolated anomaly with a east-dipping cylindrical geometry				East corner of Anomaly Ib is not imaged		Horizontal area of Anomaly Ib is same as Anomaly Ia						
		Ic	Hindu Kush anomaly (Van der Meer et al., 2018)	**Lateral extent:**	68°E, 37°N to 75°E, 33°N	68°E, 38°N to 75°E, 33°N	68°E, 36°N to 76°E, 33°N	69°E, 36°N to 73°E, 33°N	Anaomly Ic is indistinguishable from Anomaly Ib in this model	70°E, 37°N to 75°E, 33°N	70 Ma to 0 Ma	46 Ma to 0 Ma	35 Ma to 0 Ma
	Base of Anomaly Ic merges with top of Anomaly IIb			**Top surface:**	0 km	0 km	0 km	0 km		300 km			
				Top of full linear trace:	250 km	250 km	300 km	250 km		300 km			
	Anomaly Ic is well defined by all body wave models		HK Anomaly (Replumaz et al., 2014)	**Bottom surface:**	700 km	700 km	700 km	700 km		700 km			
				Comments:	-	-	-	-					

(continued on next page)

Table 2 (*continued*)

Anomaly	Description		Also Known As:	Properties	Tomographic Models					Vote Map	Maximum duration of subduction predicted from an assumed sinkingr rate of:		
					DETOX-P2	LLNL-G3Dv3	UU-P07	MIT-P08	SL2013sv3		10 mm/yr	15 mm/yr	20 mm/yr
	Anomaly Id is well-defined by all models, with a linear sub-vertical geometry	**Id**	Burma and Sunda anomalies (Van der Meer et al., 2018)	**Lateral extent:**	96°E, 26°N to 126°E, 8°S	97°E, 30°N to 130°E, 8°S	94°E, 24°N to 126°E, 8°S	96°E, 22°N to 126°E, 8°S	94°E, 24°N to 126°E, 8°S	94°E, 24°N to 126°E, 8°S	90 Ma to 0 Ma	60 Ma to 0 Ma	45 Ma to 0 Ma
				Top surface:	0-100 km	0-100 km	0-50 km	0-100 km	0-100 km	0-100 km			
				Top of full linear trace:	300 km	100-150 km	100 km	350-400 km	100-200 km	150-200 km			
	Anomaly Id has a slab window beneath the Andaman Islands		BU & AN Anomalies (Replumaz et al., 2014)	**Bottom surface:**	800-900 km	800-1000 km	900 km	800-900 km	Base of anomaly too deep to be imaged by this model	800-900 km			
	Anomaly Id slab window migrates northwards upsection			**Comments:**	Slab window between 6°N and 15°N at 500-900 km depth	Slab window between 5°N and 20°N at 500-900 km depth	Slab window between 10°N and 20°N at 550-900 km depth	Slab window between 5°N and 16°N at 450-900 km depth	Slab window between 4°N and 16°N at 400-600 km depth	Slab window between 5°N and 20°N at 450-800 km depth			
Anomaly II	Lateral area of Anomaly II increases with depth, best described as two connect anomalies (IIa and IIb)	**IIa**	IV (Van Der Voo et al., 1999)	**Lateral extent:**	74°E, 27°N to 87°E, 29°N	73°E, 28°N to 87°E, 27°N	72°E, 30°N to 87°E, 29°N	75°E, 28°N to 88°E, 28°N	Anomaly IIa is too deep to be imaged by SL2013sv	73°E, 27°N to 87°E, 28°N	110 Ma to 45 Ma	73 Ma to 30 Ma	55 Ma to 22 Ma
			Himalayas anomaly (Van der Meer et al., 2018)	**Top surface:**	400-500 km in E 500-650 km in W	500-600 km	450-550 km in E 750 km in W	450-550 km in E 600-700 km in W		450 km in E 700-800 km in W			
	Anomaly IIa forms a small, well defined linear anomaly in the MTZ			**Top of full linear trace:**	700 km	750 km	750-800 km	750 km		800 km			
				Bottom surface:	900-1000 km	700-800 km	800-900 km	800-1000 km		1000-1050 km			
	Anomally IIb forms a wide, sub-horizontal, poorly defined anomaly beneath the MTZ Shape of Anomaly IIb suggests it subducted from a mobile trench and flattened in the MTZ before sinking into the lower mantle		Hi anomaly (Hafkenscheid et al., 2006) IN Anomaly (Replumaz et al., 2014)	**Comments:**	Upper part of Anomaly IIa is poorly imaged, and poorly differentiated from Anomaly I	Very well defined in this model Top surface plunges to W Slab dips NE	Top surface plunges to W Slab dips NE	Very well defined in this model Top surface plunges to W Slab dips NE		Poorly defined fast anomalies continue between 1000-1300 km			
		IIb	Himalayas anomaly (Van der Meer et al., 2018)	**Lateral extent:**	72°E, 34°N to 100°E, 20°N	73°E, 28°N to 87°E, 27°N	72°E, 34°N to 100°E, 20°N	75°E, 28°N to 88°E, 28°N	Anomaly IIb is too deep to be imaged by SL2013sv	73°E, 27°N to 87°E, 28°N			
				Top surface:	600-700 km	700-800 km	700-800 km	700 km		700 km			
				Top of full linear trace:	1000 km	850-950 km	800-1000 km	950-1050 km		900 km			
	Top of Anomaly IIb forms isolated anomalies that may present pillars of sinking material from MTZ Top of Anomaly II merges into Anomaly I		Anomaly Hi (Hafkenscheid et al., 2006)	**Bottom surface:**	1100-1300 km	1100 km	1000-1100 km	1200-1300 km		1200-1300 km			
				Comments:	Upper part of Anomaly IIb is poorly imaged, and poorly differentiated from Anomaly I	Well defined at 650-900 km depth	Top surface has 'speckled' appearance but covers whole lateral area of Anomaly IIb	Very poorly defined in this model Better defined below 800-950 km Slab dips NE		Top of Anomaly IIb cannot be distinguished from base of Anomaly I			
	In the west, bottom of Anomaly II merges into top of Anomaly V Bottom of anomaly is deeper in west than east		AS Anomaly (Replumaz et al., 2014)		Base of Anomaly IIb is poorly defined and merges with Anomaly III	Poorly defined fast anomalies between 1000-1300 km	At 800-1000 km lateral extent of Anomaly IIb is well defined	Poorly defined fast anomalies continue between 1050-1250 km		Anomally IIb is well defined between 800-1000 km			

(continued on next page)

Table 2 (*continued*)

Anomaly	Description		Also Known As:	Properties	Tomographic Models					Vote Map	Maximum duration of subduction predicted from an assumed sinkingr rate of:		
					DETOX-P2	LLNL-G3Dv3	UU-P07	MIT-P08	SL2013sv3		10 mm/yr	15 mm/yr	20 mm/yr
Anomaly III	Very well defined slab wall		II (Van Der Voo et al., 1999)	**Lateral extent:**	68°E, 25°N to 100°E, 0°N	67°E, 25°N to 100°E, 0°N	66°E, 26°N to 100°E, 0°N	67°E, 23°N to 97°E, 0°N	Anomaly III is too deep to be imaged by SL2013sv	66°E, 25°N to 105°E, 0°N	170 Ma to 90 Ma	113 Ma to 60 Ma	85 Ma to 45 Ma
	No lateral spreading suggests that it did not stagnate in the MTZ		India anomaly (Van der Meer et al., 2018)	**Top surface:**	700-800 km in SE 900 km in NW	700-850 km in SE 950-1000 km in NW	700-800 km in SE 900 km in NW	800-900 km in SE 850-900 km in NW		700-800 km in SE 900-950 km in NW			
	Lateral trace of anomaly suggests derivation from a fixed slightly curved paleo-trench that connected SE to the Sumarta trench (present-day coordinates) and perhaps NW to the Markan trench		Upper half of anomaly IC (Hafkenscheid et al., 2006) TH Anomaly (Replumaz et al., 2014)	**Top of full linear trace:**	1100-1200 km	1050 km	1000 km	950 km		1000 km			
				Bottom surface:	1800-2000 km	1700-1800 km	1700-1800 km	1700-1850 km		1650-1700 km			
	With depth, slab thickens and migrates northward, consistent with southward migration of trench			**Comments:**	Bottom of anomaly is poorly defined Bullseye' anomaly persists to 2500 km but this is likely to be an artefact	Slab folding begins at 1200 km Slab dips NE from 1200 km depth and downwards	Slab folding begins at 1150 km Slab dips NE from 1150 km depth and downwards Poorly defined high velocity anomalies adjacent to main body slab wall anomaly remain visible to 2200-2300 km depth	Slab folding begins at 1100 km Slab dips NE from 1100 km depth and downwards Fast anomalies visible to 2300 km		May continue down to 1900-2000 km			
Anomaly IV	The size, geometry and position of Anomaly IV is very poorly defined. It is therefore possible to interpret Anomaly Iv as 1, 2, or 3 separate slabs, identified as Anomalies IVa, IVb, and IVc	**IVa**	Carlsberg anomaly (Gaina et al., 2015; Van der Meer et al., 2018) Anomaly OC (Hafkenscheid et al., 2006)	**Lateral extent:**	55°E, 5°N to 65°E, 18°N	56°E, 0°N to 65°E, 15°N	57°E, 0°N to 65°E, 18°N	Anomaly IVa is not imaged by MIT-P08	Anomaly IVa is too deep to be imaged by SL2013sv	57°E, 0°N to 67°E, 17°N	110 Ma to 75 Ma	73 Ma to 50 Ma	55 ma to 37 Ma
				Top surface:	950-1050 km	750 km	650-700 km			750-850 km			
				Top of full linear trace:	1150 km	850 km	1000-1100 km			800-900 km			
				Bottom surface:	-	-	-			-			
				Comments:	Poorly imagedby this model	-	Patchy fast anomalies visible from 450 km depth						
	Lateral extent of Anomaly IV suggests these anomalies folded in the MTZ before sinking into the lower mantle	**IVb**	Maldives anomaly (Gaina et al., 2015; Van der Meer et al., 2018)	**Lateral extent:**	57°E, 18°N to 87°E, 7°S	52°E, 25°N to 85°E, 5°S	52°E, 25°N to 85°E, 5°S	52°E, 25°N to 75°E, 0°N	Anomaly IVb is too deep to be imaged by SL2013sv	55°E, 20°N to 87°E, 7°S	200 Ma to 100 Ma	133 Ma to 66 Ma	100 Ma to 50 Ma
				Top surface:	1200-1250 km	1050-1100 km	1100-1150 km	950-1100 km		1050-1100 km			
				Top of full linear trace:	1300 km	1200 km	1300-1400 km	1450 km		1200-1350 km			
			Anomaly OC (Hafkenscheid et al., 2006)	**Bottom surface:**	1900-2000 km	1650-1850 km	1650-1700 km	1650-1800 km		1600-1800 km			
	Anomalies IVb and IVc have a northward dip suggest subduction from a southward migrating trench		III (Van Der Voo et al., 1999)	**Comments:**	Poorly imagedby this model The NW half of Anomaly IVb is not visible in this model	Mid-depth of Anomaly IVb is patchy SE half of Anomaly IVb is very poorly imaged by this model	Base of Anomaly IVa poorly distinguished from Anomaly IVc Poorly defined fast anomalies remain visible in regions adjacent to main body of anomaly IV down to 2200 km depth	Very poorly defined in this model Only visible as small localised anomalies at NW and S margins of Anomaly IVa outline		SE half of Anomlay IVb is poorly imaged May extend down to 2100-2300 km depth			

(*continued on next page*)

Table 2 (*continued*)

Anomaly	**Description**	**Also Known As:**	**Properties**	**Tomographic Models**					**Vote Map**	**Maximum duration of subduction predicted from an assumed sinkingr rate of:**		
				DETOX-P2	**LLNL-G3Dv3**	**UU-P07**	**MIT-P08**	**SL2013sv3**		**10 mm/yr**	**15 mm/yr**	**20 mm/yr**
IVc	Mid-depth of Anomaly IVc has a linear geometry striking NW-SE	Maldives anomaly (Gaina et al., 2015; Van der Meer et al., 2018)	**Lateral extent:**	53°E, 34°N to 83°E, 0°N	61°E, 35°N to 86°E, 5°N	63°E, 34°N to 86°E, 2°N	58°E, 35°N to 78°E, 11°N	Anomaly IVc is too deep to be imaged by SL2013sv	57°E, 34°N to 83°E, 2°N	230 Ma to 140 Ma	153 Ma to 93 Ma	115 Ma to 70 Ma
			Top surface:	1400-1600 km	1400-1600 km	1500-1600 km	1400-1500 km		1400-1600 km			
			Top of full linear trace:	1600-1700 km	1850 km	1800-1900 km	1650 km		1600-1700 km			
			Bottom surface:	2000-2100 km in NW 2200 km in SE	1900 km in NW 2300 km in SE	2000 km in NW 2200 km in SE	2150 km		2000 km in NW 2300 km in SE			
	Anomaly IVc merges with Anomalies III, IVb and V at certain depths	III (Van Der Voo et al., 1999)	**Comments:**	Top of Anomaly IVc is poorly distinguished from Anomalies III and IVa	Top of Anomaly IVc is poorly distinguished from Anomalies III and IVa	Lowest half of anomaly is better defined by this model	Merges with Anomaly III		Upper half of Anomaly IVc is poorly distinguished from Anomalies III, IVa and V			
		Anomly OC and lower half of anomaly IC (Hafkenscheid et al., 2006)		Below 2200 km anomaly continues to 2450 km depth as a vertical cylindrical pillar - possibly a ray path artifact		Top of Anomaly IVc is poorly distinguished from Anomalies III and IVa	SE half of Anomaly IVc not imaged by this model					
Anomaly V	Small, round, localizaed anomaly, with a folded slab geometry	Nepal anomaly (Van der Meer et al., 2018)	**Lateral extent:**	67°E, 42°N to 84°E, 23°N	62°E, 33°N to 91°E, 26°N	76°E, 35°N to 85°E, 29°N	73°E, 35°N to 86°E, 24°N	Anomaly V is too deep to be imaged by SL2013sv	73°E, 35°N to 91°E, 26°N	200 Ma to 120 Ma	133 Ma to 80 Ma	100 Ma to 60 Ma
			Top surface:	1200-1300 km in NW	1300 km	1200 km in NW	1200 km in NW		1200-1250 km in NW			
	Vertical extent of Anomaly V deepens towards ESE		**Top of full linear trace:**	-	-	-	-		-			
		I (Van Der Voo et al., 1999)	**Bottom surface:**	1800-2000 km in SE	2000-2100 km	1900-2000 km in SE	2150 km in SE		1800-2000 km in SE			
	In the west, top of Anomaly V is poorly distinguished from base of Anomaly II		**Comments:**	Top of anomaly is well defined	Top of anomaly is poorly defined	Poorly imaged by this model	Well imaged by this model		Lateral extent of Anomaly V at a given area in Vote Maps is much smaller than mapped outline of anomaly.			
	The size, geometry and position of Anomaly V is poorly defined and varies between tomogrpahy models	Anomlay PT (Hafkenscheid et al., 2006)		Anomaly below 1600 km is poorly defined and poorly distinguished from Anomaly III	Anomaly is well defined and largest below 1500 km	Lateral extent in this model is small when compared to other models	Lateral extent in this model is large when compared to other models					
	Lateral area of Anomaly increase with depth	Part of the AS Anomaly (Replumaz et al., 2014)		Base is poorly distinguished from Anomaly IVc	Lower half of anomaly has southward dip	Anomaly has WNW-ESE linear trace that plunges ESE	Anomaly has a rounded isotropic shape with no indiation of trench orientation		Match between Vote Maps and individual tomography models supports the identificaiton of Anomaly V as a distinct anomaly			
	At any given point, Anomaly V has a vertical thickness of 400-500 km			NE portion of Anomaly V is not imaged by this model								
Anomaly VI	Multiple anomalies beneath north Tibetan Plateau and Central Asian Orogenic Belt Anomalies are distributed between 1000 km and 2900 km depth, mostly below 1500 km Depth and position of Anomaly VI suggests they relate to pre-Jurassic terrane assembly of the east Eurasian continent	Central China anomaly (Van der Meer et al., 2018)	**Anomaly VI is important for models of the pre-Jurassic accretion of terranes to the Central Asian Orogenic Belt and Tibetan Plateau. Anomaly VI is not required by our models for the India-Asia collision and is not investigated further.**									

Anomaly Ic has an east-dipping cylindrical geometry, visible between 250 and 700 km depth. The top and bottom surfaces of Anomaly Ic are indistinguishable from Anomaly Ia and IIb, respectively.

Anomaly Id is well-defined in the upper mantle and top of the lower mantle. It has a linear, steeply northeast dipping geometry that trends NW-SE, parallel the Sunda-Sumatra-Andaman trench from northeast India (94°E 24°N) to Sumatra (126°E 8°S) (Figs. 8–10, and Table 2). It is visible from 0 km to ~900 km depth (Fig. 8–10 and Table 2). In the northwest, Anomaly Id merges laterally with Anomalies Ia, Ib, and II. In the southeast, the base of Anomaly Id merges with the top of Anomaly III. A gap in Anomaly Id is present in all tomography models between 20°N and 5°N at ~500–900 km depth (Figs. 8a, 9b, 9d, 9e, 10). Above this depth, Anomaly Id forms a near continuous anomaly across its entire horizontal length.

5.2.1.1. Geological interpretations of Anomaly I. Anomaly Ia (Figs. 8, 20) is indicative of a steeply NE-dipping subducting slab from the northern edge of the Indian continent; this is consistent with observations from regional-scale tomography and receiver function studies (Fig. 21 - see section 5.5). Assumed sinking rates of 10 mm/yr and 20 mm/yr predict that Anomaly Ia subducted sometime between ~40–0 Ma or ~20–0 Ma, respectively (Table 2). It is unclear whether Anomaly Ia represents oceanic or continental lithosphere or a mix of the two. Parts of Anomaly Ia described here are equivalent to seismic anomalies described in previous work. This includes the *'CR anomaly'*, interpreted by Replumaz et al. (2014) as subducting Indian cratonic lithosphere, and the *'Burma anomaly'*, interpreted by van der Meer et al. (2018) and van Hinsbergen et al. (2019) as subducted Greater India continental lithosphere (Table 2).

Anomaly Ib is not formally identified as a subducted slab by previous studies (e.g. Van der Voo et al., 1999; Replumaz et al., 2010; Replumaz et al., 2014; van der Meer et al., 2018). Assumed sinking rates of 10 mm/yr and 20 mm/yr predict that Anomaly Ib subducted sometime between ~70–40 Ma or ~35–20 Ma, respectively (Table 2). The horizontally extensive geometry of Anomaly Ib satisfies two interpretations (Figs. 8, 20). Anomaly Ib may represent a subducted slab that has folded and stagnated within the MTZ as the overlying trench migrated in a NE-SW direction (e.g. Fig. 6d-f). Alternatively, part or all of Anomaly Ib may represent Indian and/or Asian subcontinental lithospheric mantle detached from the base of the Tibetan Plateau during or prior to the India-Asia collision (*s.l.*) via delamination, lithospheric dripping or some other abrasive mechanism (e.g. Houseman and Molnar, 1997; Göğüş et al., 2017; Kelly et al., 2019).

Anomaly Ic (Figs. 8, 20a-b) is consistent with a localized slab attached to the Indian continent. Assumed sinking rates of 10 mm/yr and 20 mm/yr predict that Anomaly Ic subducted sometime between ~70–0 Ma or ~35–0 Ma (Table 2). Anomaly Ic is equivalent to the previously defined *'HK anomaly'* (Hafkenscheid et al., 2006; Replumaz et al., 2014) and the *'Hindu Kush anomaly'* (van der Meer et al., 2018). Those studies suggest that this slab comprises oceanic lithosphere below 200 km depth and continental lithosphere above this depth (e.g. Kufner et al., 2016). We note that the structurally distinct appearance of Anomaly Ic may be due to the relatively denser array of seismic instrumentation of the overlying Hindu Kush and Pamir regions, and the higher concentration of deep earthquakes (>200 km) in this region, both of which improve the tomographic resolution.

Anomaly Id is interpreted as Indian plate oceanic lithosphere subducted into the Sunda-Sumatra-Andaman trench (Figs. 8–10). Assumed sinking rates of 10 mm/yr and 20 mm/yr predict that Anomaly Id subducted sometime between ~90–0 Ma or ~45–0 Ma (Table 2). The north and south portions of Anomaly Id are respectively equivalent to the '*Burma anomaly*' and '*Sunda anomaly*' of van der Meer et al. (2018) and the '*BU anomaly*' and '*AN anomaly*' of Replumaz et al. (2014). The gap in Anomaly Id below the Andaman Islands has been interpreted as a slab window (Figs. 8a, 9b, 9d, 9e, 10), produced by migration of the India-Asia plate boundary, which ruptured and dragged the northern portion of the slab northwards by >1000 km, during a period of strike-slip motion on the overlying plate boundary (e.g. Advokaat et al., 2018; van der Meer et al., 2018).

5.2.2. Anomaly II

Anomaly II strikes NW-SE in the MTZ and lower mantle beneath the Himalayan orogen and northern India (Fig. 8). The size and geometry of Anomaly II is best described as two connected anomalies (Table 2). Anomaly IIa is small, but well defined between 73°E 27°N and 87°E 28°N (Figs. 8–10, 13–20). Its top surface is imaged in the east at ~450–550 km depth and plunges to the west; the full linear trace is visible at ~700–-800 km depth (Figs. 9–10, Table 2). The base of Anomaly IIa is imaged at ~800–1000 km, where it widens and merges into the underlying Anomaly IIb. Anomaly IIb is visible over a larger horizontal area but is poorly defined and patchy in appearance; it is visible between 73°E, 27°N to 87°E, 28°N at a depth of 700–1100 km (Table 2), although its base may extend as deep as 1300 km (Figs. 8, 10–11, 13–20). From bottom to top, the overall geometry of Anomaly IIb transitions from a horizontal anomaly at its base into several localized pillars of seismically fast material, of which Anomaly IIa is the largest and most well defined (Figs. 13–20, Supplementary Materials 06). Anomaly IIa cannot be distinguished from the SL2013sv surface wave tomography model of Schaeffer and Lebedev (2013) (Figs. 9, 13–19), perhaps due to its relatively small size above 700 km depth.

5.2.2.1. Geological interpretations of Anomaly II. The geometry of Anomaly II suggests that it is a slab subducted from a SW migrating trench (Figs. 8, 20). The horizontal width of Anomaly IIb in a northeast-southwest direction suggests that it stagnated in the MTZ before sinking into the lower mantle (e.g. Fig. 6). Pillars of seismically fast materially protruding upwards from the base of Anomaly IIb may indicate that this slab sank unevenly into the lower mantle. Assumed sinking rates of 10 mm/yr and 20 mm/yr predict that Anomaly II subducted sometime between ~110–45 Ma or ~55–22 Ma, respectively (Table 2).

Anomaly IIa is equivalent to anomaly '*IV*' of Van der Voo et al. (1999) and the '*IN anomaly*' of Replumaz et al. (2014), which are interpreted as Indian continental lithosphere subducted between ~45–15 Ma. Anomaly IIb is equivalent to part of the *'AS anomaly'* of Replumaz et al. (2014), which is interpreted as Asian lithosphere subducted southward beneath north Qiantang during the Eocene. Hafkenscheid et al. (2006) interpreted Anomaly II (their '*anomaly Hi*') as subducted Neotethys oceanic lithosphere, which formed the back-arc to a Late Cretaceous intra-oceanic arc. Alternatively, van der Meer et al. (2018) and van Hinsbergen et al. (2019) interpret Anomaly II as oceanic lithosphere of the Greater India Basin (their '*Himalayas anomaly*') subducted beneath the GHS/THS microcontinent between 58 and 15 Ma.

5.2.3. Anomaly III

Anomaly III in the lower mantle is a well-defined fast anomaly observed beneath west India to Sumatra between 66°E 25°N and 105°E 0°N (Figs. 8, 10–11, 13–20, and Table 2). It is arguably the most robust anomaly considered by this study, based on the similarity of its size, depth and geometry displayed by all tomography models (Fig. 19). It is linear and steeply northeast-dipping anomaly with a NW-SE strike. The top of Anomaly III is imaged in the southeast at ~800 km depth beneath Sumatra and in the northwest at ~900 km depth beneath western India (Fig. 10); the full linear trace is visible at ~950–1000 km depth (Fig. 11). Below ~1100–1150 km depth, its NE-SW horizontal width increases downward. The base of Anomaly III is imaged at a depth of ~1600–1700 km (Figs. 13–20).

5.2.3.1. Geological interpretations of Anomaly III. Anomaly III (Figs. 8, 20) is consistent with subduction and slab-folding beneath an initially southwest-migrating, NW-SE striking trench that became stationary above the top of Anomaly III (e.g. Fig. 6a-c). Assumed sinking rates of 10 mm/yr and 20 mm/yr predict that Anomaly III subducted sometime between ~170–90 Ma or ~85–45 Ma, respectively (Table 2).

Anomaly III is equivalent to anomaly '*II*' of Van der Voo et al. (1999), the '*India anomaly*' of van der Meer et al. (2018), and the upper half of

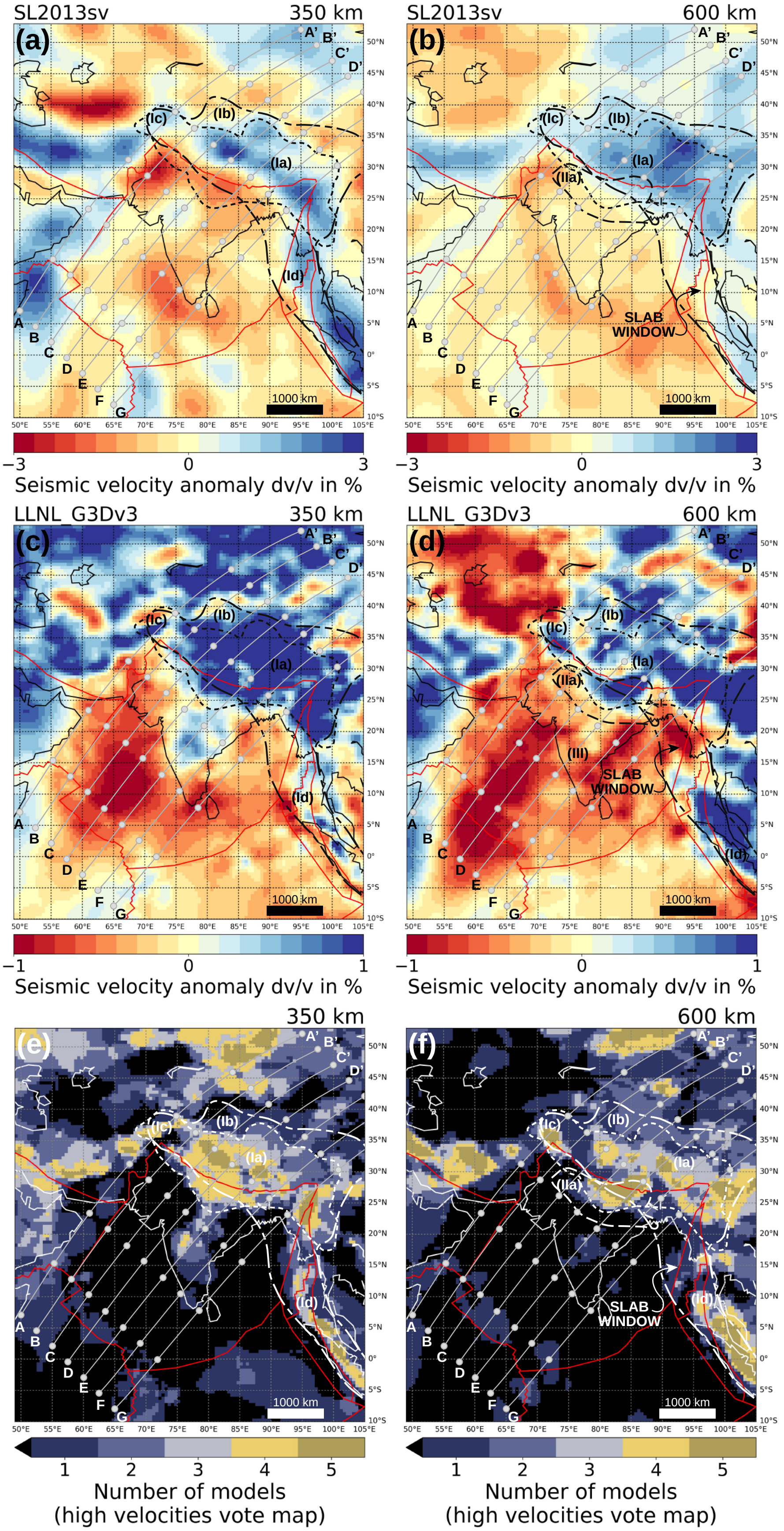

(*caption on next page*)

Fig. 9. Seismic tomographic images of subducted slabs beneath the Indian hemisphere at 350 km and 600 km depth. Present-day coastlines and plate boundaries drawn with black solid line and red solid line, respectively. Outlines of anomalies are drawn with dashed lines; reconstruction of India at 59 Ma drawn with solid dark grey line (see also Fig. 8). Major sutures drawn with light grey line (see also Fig. 1). Lines of section shown in Figs. 12–20 are drawn with solid grey lines. (a) 350 km and (b) 600 km depth slices from tomography model SL2013sv. (c) 350 km and (d) 600 km depth slices from tomography model LLNL_G3Dv3. (e) 350 km (f) and 600 km depth slices of Vote Maps for models SL2013sv, LLNL_G3Dv3, DETOX-P2, UU-P07 and MITP08. Contours on Vote maps show how many of the selected models identify a seismically fast anomaly (≥ +0.3%) at any given point on the map. See Shephard et al. (2017) for further details of Vote Maps. Depth slices and Vote Maps drawn using SubMachine (Hosseini et al., 2018). Georeferenced overlays (.kml, .kmz) and shapefiles of all points, lines, and polygons presented in our map figures are available for use and editing with global information system software (e.g. Google Earth, GPlates, ArcGIS) in Supplementary Materials 01 and 02.

the *'anomaly IC'* of Hafkenscheid et al. (2006) who interpret it as Neotethys oceanic lithosphere subducted beneath the Lhasa terrane between the Early Cretaceous to the Eocene. Alternatively, Replumaz et al. (2014) suggest that Anomaly III (equivalent to their '*TH anomaly'*) represents Neotethys oceanic lithosphere subducted beneath an intra-oceanic arc. All of these previous interpretations suggest that Anomaly III detached from the northern margin of the Indian continent in response to continental collision of India with Asia (Van der Voo et al., 1999; van der Meer et al., 2018) or an intra-oceanic arc (Replumaz et al., 2014). We note that the trace of this anomaly overlaps with the restored location of the Lhasa terrane at 20°N ± 4° at the onset of the Himalayan orogen (Fig. 8), based on palaeomagnetism and crustal shortening estimates from Tibet (e.g. Huang et al., 2015a; Li et al., 2015; Kapp and DeCelles, 2019).

5.2.4. Anomaly IV

Anomaly IV is a composite of three overlapping NW-SE striking anomalies beneath India and the western Indian Ocean (Fig. 8). These anomalies (IVa, IVb, IVc) are visible between 55°E 20°N and 87°E 7°S, and 750 km to 2000–2300 km depth and collectively dip northwards (Figs. 8–20, and Table 2). The size and geometry of Anomalies IVa, IVb, and IVc are poorly defined (Fig. 12–18) and highly variable between all tomography models (Fig. 19). Anomaly IVa is small and localized. It is not imaged by the MIT-P08 model and it is poorly imaged by all other P-wave models between 57°E, 0°N to 67°E, 17°N (Figs. 8, 10, 13–15, 19–20, and Table 2). It has a NE-SW linear trace that is visible from a depth of ~750 km to ~1000–1100 km depth where its base merges into the underlying Anomaly IVb (Table 2). Anomaly IVb is a north-dipping, NW-SE striking linear anomaly, poorly imaged between 55°E, 20°N to 87°E, 7°S at a depth of ~1000–1100 km to 1650–2000 km (Figs. 8, 11–20, and Table 2). The base of Anomaly IVb merges with the top of Anomaly IVc. Anomaly IVc is a wide, north-dipping, NW-SE striking linear anomaly that is poorly imaged between 60°E, 30°N to 90°E, 5°N at a depth of ~1400–1600 km to 2200–2300 km (Figs. 8, 12–20, and Table 2). The upper half of Anomaly IVc merges with parts of Anomalies III, IVb, and V (Figs. 12–19, Supplementary Materials 06).

5.2.4.1. Geological interpretations of Anomaly IV. The small, sub-horizontal geometry and linear NE-SW trace of Anomaly IVa (Figs. 10, 20b-d) suggests that this anomaly represents lithosphere either subducted from a NE-SW striking, stationary subduction zone or a NW-SE striking and NE-SW migrating subduction zone. Similarly, the geometries of Anomaly IVb and IVc suggest that they represent lithosphere subducted from one or two NW-SE striking and SE-migrating subduction zone(s) (Figs. 8, 20). The horizontal widths of Anomalies IVa, IVb, and IVc suggest that they stagnated and folded in the MTZ prior to sinking into the lower mantle (e.g. Fig. 6). Assumed sinking rates of 10 mm/yr and 20 mm/yr predict that: (1) Anomaly IVa subducted between ~110–75 Ma or ~55–37 Ma, respectively; (2) Anomaly IVb subducted sometime between ~200–100 Ma or ~100–50 Ma, respectively; and (3) Anomaly IVc subducted sometime between ~230–140 Ma or ~115–70 Ma, respectively (Table 2).

Hafkenscheid et al. (2006) identified Anomalies IVa, IVb, and southern part of IVc as a single anomaly (their *'anomaly IO'*), and identified the northern part of Anomaly IVc as the lower half of their *'anomaly IC'*. They interpreted these anomalies as part of the same Neotethys oceanic slab as Anomaly III (their *'anomaly IC'*).

Anomaly IVa is equivalent to the *'Carlsberg anomaly'* of Gaina et al. (2015) and van der Meer et al. (2018). van Hinsbergen et al. (2019) interpret the *'Carlsberg anomaly'* to originate from localized northwestward subduction of Neotethys oceanic lithosphere beneath the Arabian plate between the Late Cretaceous and Paleocene during the West India orogeny (e.g. Gnos et al., 1997; Gaina et al., 2015; van Hinsbergen et al., 2019).

Anomaly IVb is equivalent to the '*Maldives anomaly*' of van der Meer et al. (2018), who refrained from making a geological interpretation for the origin of this anomaly due to the unresolved debate over the location and timing of Jurassic-Cretaceous intra-ocean arcs in the Neotethys Ocean. Van der Voo et al. (1999) interpreted this anomaly (their anomaly '*III*') as Neotethys oceanic lithosphere subducted beneath an equatorial mid- to Late Cretaceous intra-oceanic arc.

Anomaly IVc has not been formally recognized as a distinct anomaly by previous studies, although it is partly equivalent to the lower portion of anomaly '*II*' of Van der Voo et al. (1999) who interpreted that anomaly as Neotethys oceanic lithosphere subducted beneath Lhasa during the Cretaceous.

Based on our own observations, we suggest that Anomaly IV represents one or more slabs subducted between the Jurassic to Cretaceous from one or more NW-SE striking and SW migrating intra-oceanic arcs in the Neotethys Ocean. However, the sizes and shapes of Anomalies IVa, IVb, and IVc are poorly constrained by all models (Figs. 12–18, Table 2) and resolution tests demonstrate that these anomalies derive from a region of low tomographic resolution (e.g. Amaru, 2007; Li et al., 2008; Simmons et al., 2012). Consequently, we argue that it is not (yet) possible to determine from tomographic imaging alone whether Anomaly IV represents three north-dipping slabs stacked atop of each other, or whether it represents one or two larger slabs.

5.2.5. Anomaly V

Anomaly V is relatively small and round in the lower mantle beneath the western Himalaya (Figs. 8, 11–16, 19–20). It is imaged between 73°E, 35°N to 91°E, 26°N at a depth range of 1200 km to ~1800–2000 km (Table 2). The size and geometry of Anomaly V is poorly constrained and varies between tomography models (Fig. 19) but appears to strike NW-SW and dip towards the SW; the top and bottom surfaces of Anomaly V deepen towards the SE, and its horizontal width increases with depth. In the west, the top of Anomaly V is indistinguishable from the base of Anomaly IIb (Figures13, 20b).

5.2.5.1. Geological interpretation of Anomaly V. Anomaly V is poorly defined and any geological interpretations based on its appearance are made with low confidence. Its geometry suggests that it represents lithosphere subducted from a NW-SE striking and NE migrating subduction zone. The eastward increase in depth of the top surface of Anomaly V may indicate that it detached earlier in the east than in the west. Its horizontal width suggests that it stagnated and folded in the MTZ prior to sinking into the lower mantle (e.g. Fig. 6). Assumed sinking rates of 10 mm/yr and 20 mm/yr predict that Anomaly V subducted between ~230–140 Ma or ~115–70 Ma, respectively (Table 2). Anomaly V is equivalent to the '*Nepal anomaly*' of van der Meer et al. (2018), anomaly '*I*' of Van der Voo et al. (1999), and '*anomaly PT*' of Hafkenscheid et al. (2006), which are all interpreted as Bangong-Tethys oceanic lithosphere subducted beneath Qiangtang during the Jurassic to Late Cretaceous. Alternatively, Replumaz et al., (2014) recognized Anomaly V as part of their '*AS anomaly*,' which

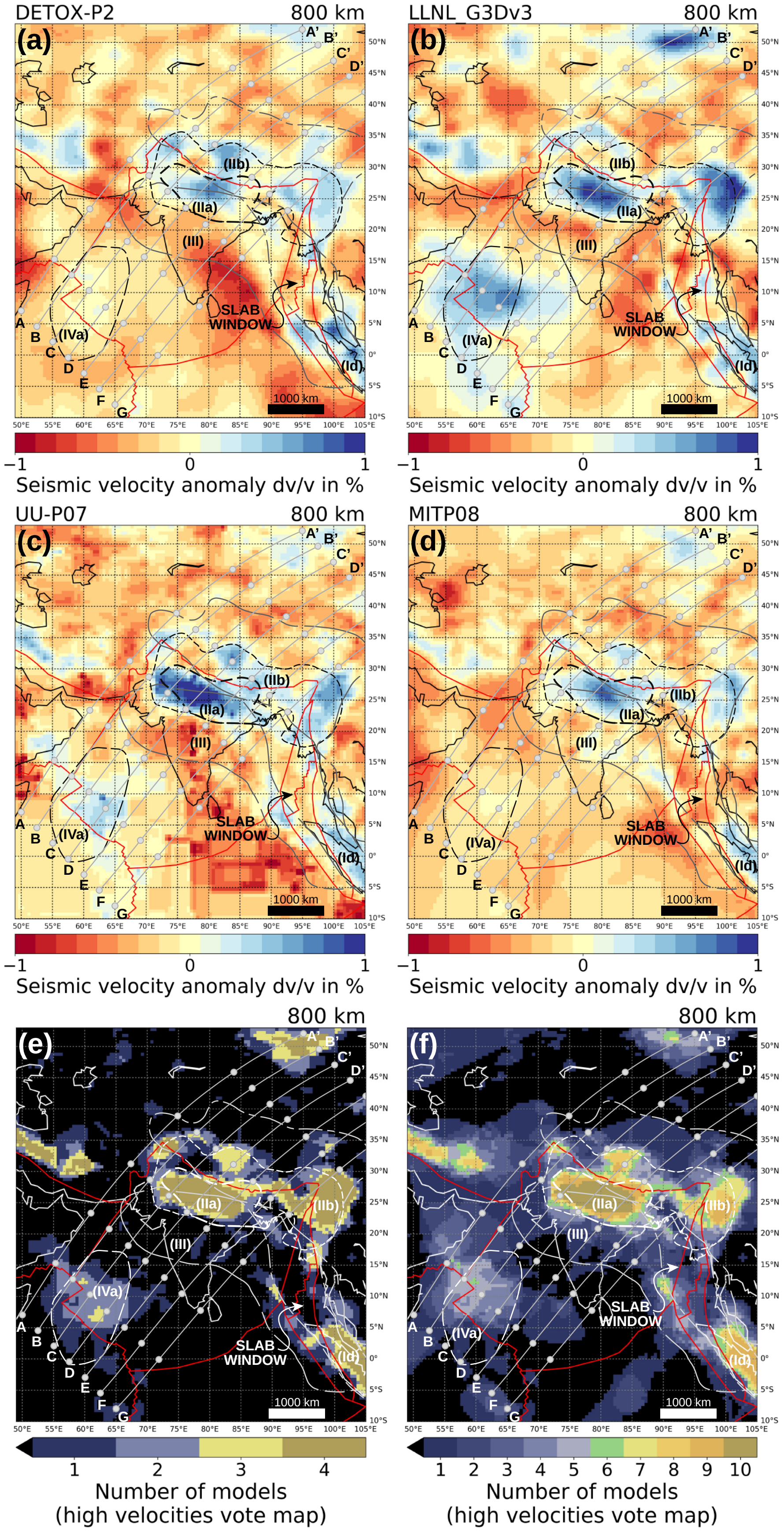

(caption on next page)

Fig. 10. Seismic tomographic images of subducted slabs beneath the Indian hemisphere at 800 km depth. See Fig. 9 for explanation of annotations and structures drawn over each depth slice. Depth slices shown for tomography models (a) DETOX-P2, (b) LLNL_G3Dv3, (c) UU-P07, and (d) MITP08. (e) Vote Map for models LLNL_G3Dv3, DETOX-P2, UU-P07 and MITP08. (f) Vote Map for P-wave models GyPSuM-P, HMSL-P06, PRIP05, SP12RTS-P, SPani-P, DETOX-P2, GAPP4, LLNL_G3Dv3, MITP08, UU-P07 (For model sources and details see Table 1). See Fig. 9 for further details.

they interpreted as Asian lithosphere subducted southward beneath Qiantang during the Eocene.

5.2.6. Anomaly VI

Anomaly VI represents a collection of deep anomalies in the lower mantle beneath the central and northern Tibetan plateau and the Central Asian orogenic belt (Figs. 12–20, Table 2). These anomalies form along a linear NW-SE strike between 1000 km and 2900 km depth although most are imaged below 1500 km depth (Fig. 20). Their depth and position suggest that they represent Paleotethys oceanic lithosphere subducted prior to the Jurassic during terrane accretion along the southern margin of Asia (e.g. Van der Meer et al., 2018; their '*Central China anomaly*'). As such, Anomaly VI is not directly relevant to the India-Asia collision and it is not discussed further; it is included for its relevance to pre-Jurassic models of the assembly of Asia and the Tibetan plateau.

5.3. Timing of the Himalayan orogeny and India-Asia collision

The timing of the India-Asia collision (*s.l.*) places an important constraint on the magnitude of convergence accommodated between India and Asia since the onset of collision (e.g. Ingalls et al., 2016; van Hinsbergen et al., 2019; Zhou and Su, 2019). There are several ways in which onset of the Himalayan orogeny (the India-Asia collision *s.l.*) can be constrained; from a plate kinematic perspective we wish to determine the earliest arrival of the Tethyan Himalaya passive margin into a subduction zone (e.g. Hu et al., 2016a). The oldest THS strata that contain Asia-derived sediments (based on UPb detrital zircon age populations) occur within the Paleocene Sangdanlin Formation (Saga section; DeCelles et al., 2014, Hu et al., 2015, Metcalf and Kapp, 2017), and Zongzhuo Formation (Gyangze section; Ding et al., 2005, Wu et al., 2014). Asia-derived zircons in those strata correlate with the Paleocene Quxia and Jialazi formations from the Xigaze forearc basin (Hu et al., 2016b). The Sangdanlin and Zongzhou formations and their correlative units have been interpreted as submarine fan deposits from a continental rise setting at the distal edge of Greater India; we thus follow previous studies that constrain the onset of the Himalayan orogeny at 59 ± 1 Ma, based on the youngest detrital zircon age of the Sangdanlin Formation (DeCelles et al., 2014; Wu et al., 2014; Hu et al., 2015; Hu et al., 2016b; Metcalf and Kapp, 2017).

The interpretation of collision at 59 ± 1 Ma requires the assumption that the Sangdanlin formation and correlative units were located at the distal edge of Greater India. This assumption is supported by a variety of bedrock datasets, which constrain the temporal evolution of uplift and deformation after 59 ± 1 Ma. Following the first arrival of Asian sediments on Greater India, the Xigaze forearc transitioned from a marine to non-marine depositional environment between 58 Ma and 54 Ma, with a cessation of sedimentation by ~51 Ma (Orme et al., 2015; Kapp and DeCelles, 2019). In the THS and GHS, the development and migration of a flexural bulge erosional unconformity at ~57–56 Ma is followed by the earliest deposition of shallow-marine Asia-derived sediments on the Tethyan Himalaya continental shelf between ~56–54 Ma, This is followed by a transition from shallow marine carbonates (53–54 Ma) to clastic sediments (53–50 Ma), and the end of marine sedimentation in many places along the Tethyan Himalaya margin by 50 Ma (Guillot et al., 2003; Green et al., 2008; Najman et al., 2010; Hu et al., 2015; Wang et al., 2015; Hu et al., 2016a; Najman et al., 2017; Searle, 2019). UHP/HP metamorphism of the THS is recorded in the NW Himalaya between ~56–43 Ma (de Sigoyer et al., 2000, Leech et al., 2005, Parrish et al., 2006, Donaldson et al., 2013, Rajkumar, 2015, Rehman et al., 2016, Bidgood et al., 2019a, 2019b), whereas the earliest prograde metamorphism within the GHS in the North Himalayan gneiss domes is recorded at ~56–54 Ma (Smit et al., 2014; Ding et al., 2016). The progression of these events supports the interpretation that collision (*s.l.*) occurred at ~59 Ma; we thus use this age to constrain the position of India at the onset of collision, based on plate reconstructions of the Indian and Atlantic oceans (see Section 5.4.).

In the case of the single subduction zone configuration, the onset of the Himalayan orogeny (the India-Asia collision *s.l.*) at 59 Ma is synonymous with the onset of the India-Asia collision *s.s.* (Hu et al., 2016a; Ingalls et al., 2016). In models with a double subduction zone configuration, the onset of the Himalayan orogeny at 59 Ma corresponds to collision of Greater India with a Neotethys intra-oceanic arc (e.g. Aitchison et al., 2007; Bouilhol et al., 2013; Replumaz et al., 2014); likewise, in models with a Greater India Basin reconstruction, the onset of the Himalayan orogeny at 59 Ma corresponds to collision between the GHS-THS microcontinent with the Asian active continental margin (van Hinsbergen et al., 2012; van Hinsbergen et al., 2019). The timing of the India-Asia collision *s.s.* in these latter two models is harder to constrain as in both cases, deformation and convergence following the onset of the Himalayan orogeny has been continuous up to the present day. Studies in favour of either of these two models often distinguish the India-Asia collision *s.l.* from the India-Asia collision *s.s.* in terms of an initial 'soft collision' (onset of the Himalayan orogeny) and subsequent 'hard collision' (onset of the India-Asia collision *s.s.*).

Models that favour a double subduction zone configuration constrain the timing of the India-Asia collision *s.s.* to ~45–40 Ma, based on: (1) a reduction in Indian plate velocity between ~50 Ma and ~40 Ma in response to 'hard collision' of India with Asia; (2) changes in pluton isotope geochemistry in the Kohistan and Ladakh blocks between at ~50 Ma and ~40 Ma, which become more evolved due to contamination from the Karakoram block and/or the subducting Indian lithosphere; (3) a change from calc-alkaline magmatism to alkaline magmatism in southern Tibet at ~40 Ma; and (4) an increase in zircon and monazite crystallization recorded in the Himalayan orogen after ~40 Ma (e.g. Bouilhol et al., 2013; Replumaz et al., 2014; Burg and Bouilhol, 2019; Jagoutz et al., 2019).

Models that favour the Greater India Basin reconstruction use similar concepts to constrain the timing of the India-Asia collision *s.s.* but constrain this event to ~30–20 Ma, based on (1) a reduction in Indian plate velocity at ~25–20 Ma; (2) the earliest metamorphism recorded in the LHS, interpreted as the onset of collision and accretion of the LHS to the GHS-THS microcontinent; (3) the absence of Eocene-Oligocene foreland basin strata; and (4) the onset of far-field deformation in Central Asia at ~25–20 Ma (e.g. van Hinsbergen et al., 2012; van Hinsbergen et al., 2019).

Given the variability of interpretations for the timing of the India-Asia collision *s.s.*, we present our plate kinematic framework for testing subduction zone configurations and Greater India reconstructions with respect to the onset of the Himalayan orogeny (i.e. the India-Asia collision *s.l.*), which is well constrained to 59 ± 1 Ma.

5.4. Locations of India and Asia at the onset of the India-Asia collision (s.l.)

For this study, the relative motions of India and the southern Asian margin must be reconstructed with respect to a fixed mantle reference frame so that plate boundaries, plate motions and surface deformation may be correlated with the absolute locations of subducted slabs (e.g. van der Meer et al., 2010; Torsvik and Cocks, 2017). To achieve this, we integrate our selected geological and geophysical datasets within an existing plate reconstruction model (i.e., our 'plate kinematic framework', provided by Müller et al., 2019) using the palaeo-global information system software, GPlates (Müller et al., 2018).

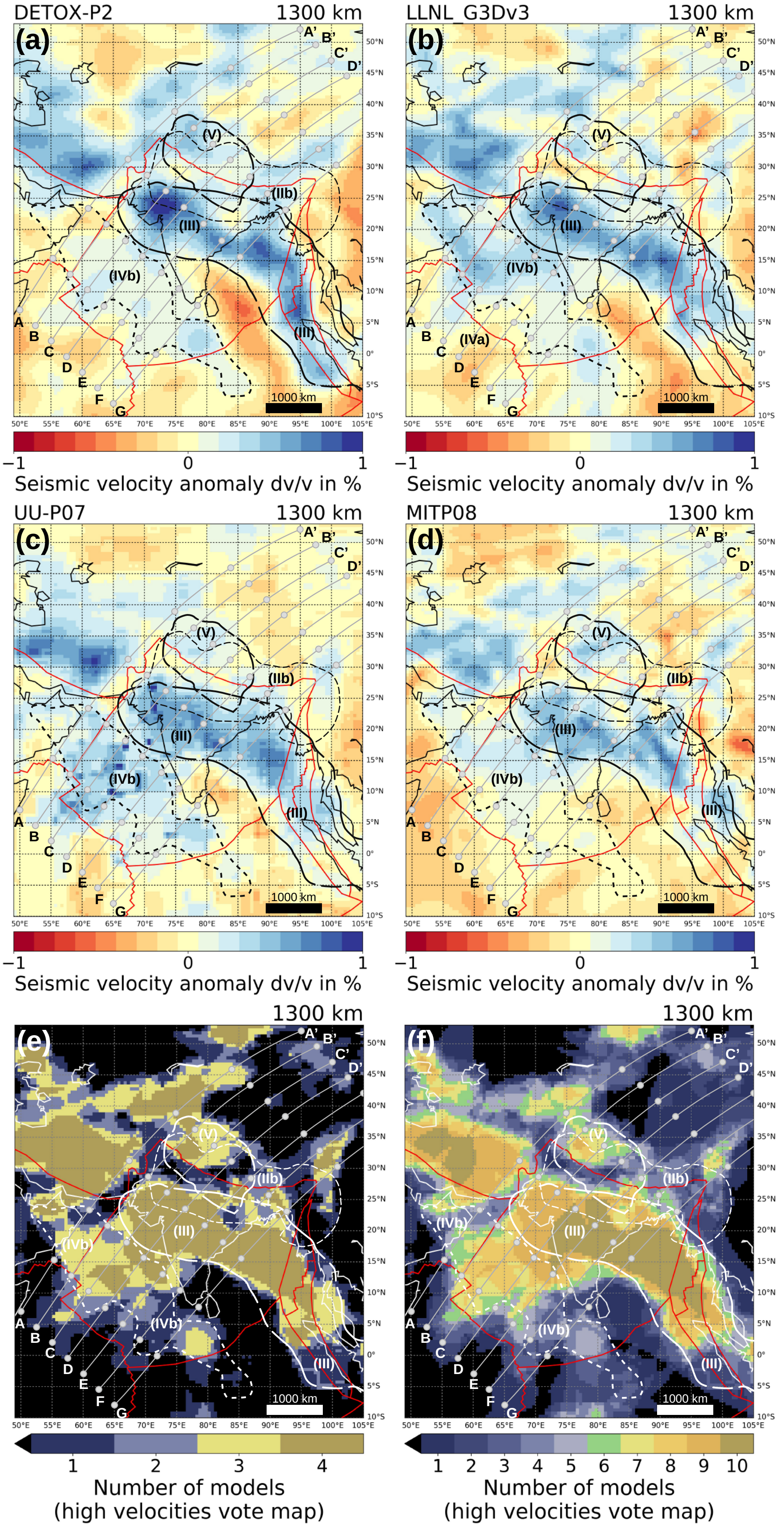

(*caption on next page*)

Fig. 11. Seismic tomographic images of subducted slabs beneath the Indian hemisphere at 1300 km depth. See Fig. 9 for explanation of annotations and structures drawn over each depth slice. Depth slices shown for tomography models (a) DETOX-P2, (b) LLNL_G3Dv3, (c) UU-P07, and (d) MITP08. (e) Vote Map for models LLNL_G3Dv3, DETOX-P2, UU-P07 and MITP08. (f) Vote Map for P-wave models GyPSuM-P, HMSL-P06, PRIP05, SP12RTS-P, SPani-P, DETOX-P2, GAPP4, LLNL_G3Dv3, MITP08, UU-P07 (For model sources and details, see Hosseini et al., 2018). See Fig. 9 for further details.

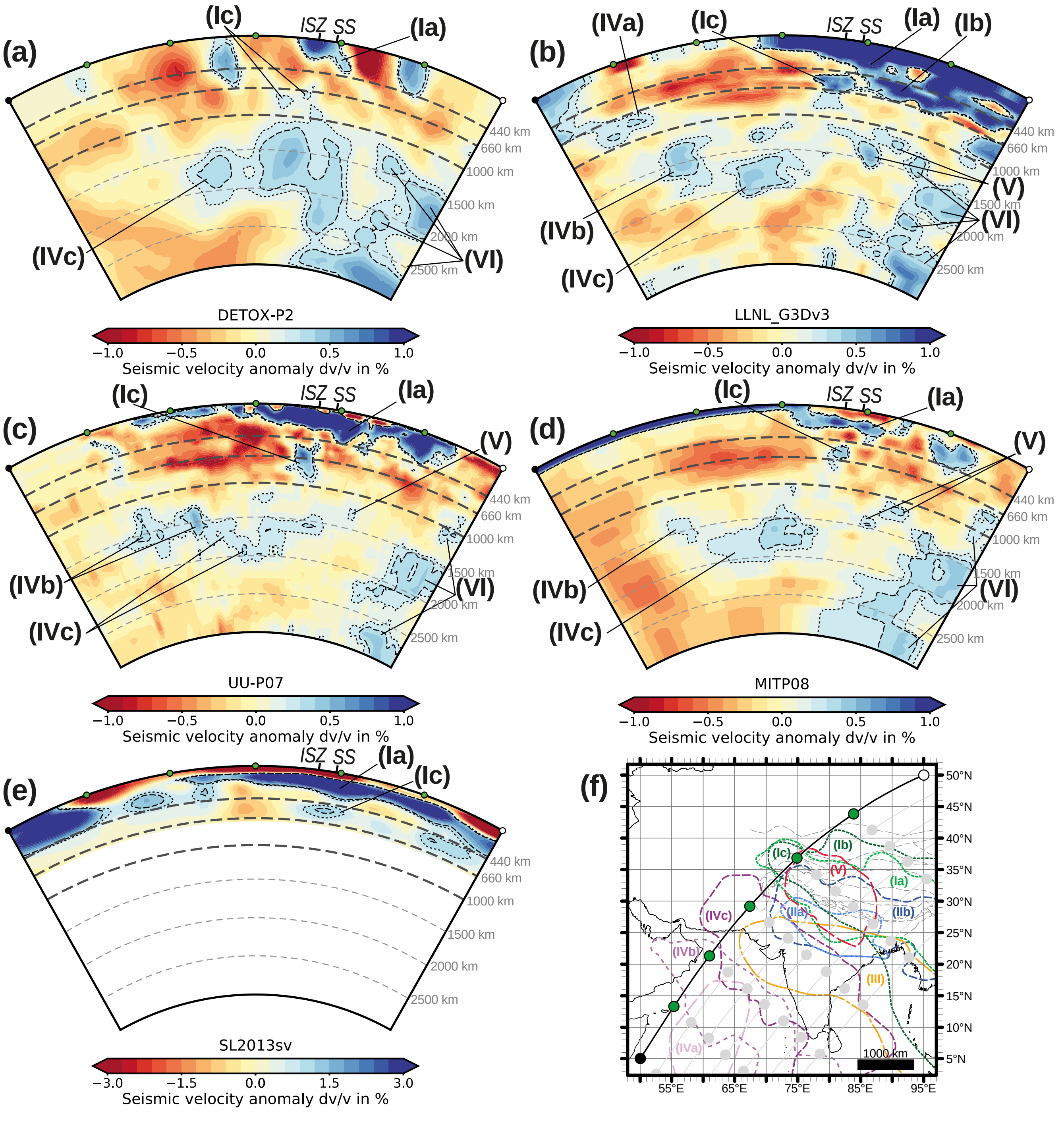

Fig. 12. Cross section A through seismic tomography models (a) DETOX-P2, (b) LLNL_G3Dv3, (c) UU-P07, (d) MITP08, and (e) SL2013sv3. Labels display positions of anomalies I to VI, marked on Figs. 8–11. Locations of specific surface structures are labelled: AFT – Altyn Tagh Fault; BN – Bangong-Nuijang suture; ISZ – Indus suture; J – Jinsha suture; K – Kunlun suture; MFT – Main Frontal thrust; SS – Shyok suture; see Figs. 1 and 2 for further reference. (f) Map trace of tomographic line of section, with geological structures and seismic tomography anomalies outlined. Location of cross section are displayed in Figs. 8–11. Cross sections drawn using SubMachine (Hosseini et al., 2018).

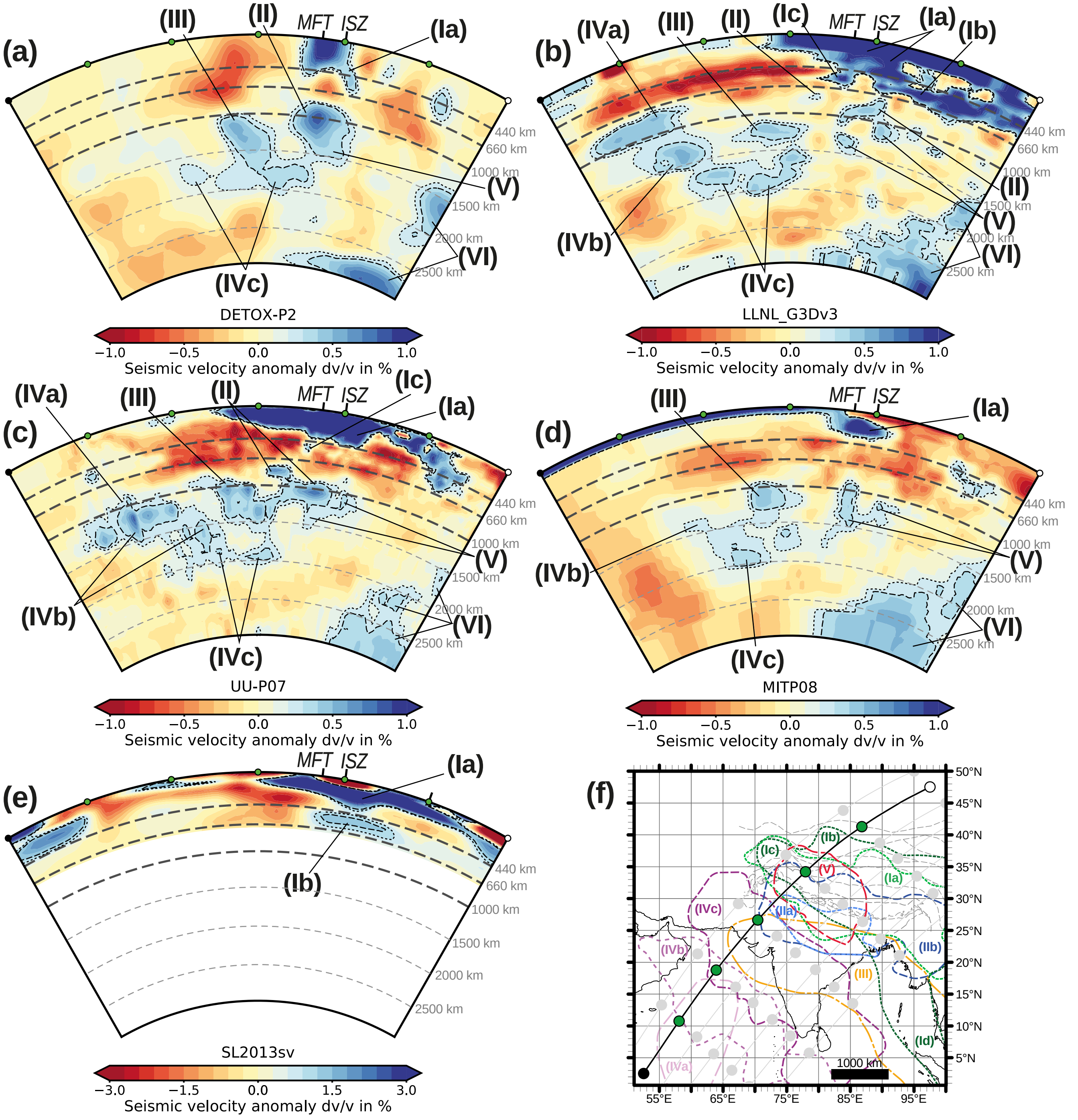

Fig. 13. Cross section B – see Fig. 12 for full figure caption.

5.4.1. Reconstruction of India at 59 Ma

We reconstruct plate motions using finite rotation poles from Müller et al. (2019), which are calculated from an 'optimized mantle reference frame,' based on joint global inversion of hotspot motions, slab geometries and locations, and lithospheric net rotation estimates (Tetley, 2018; Tetley et al., 2019). Fortunately, during the Cenozoic, the motion of India is tightly constrained by magnetic reversal isochrons within the Indian and Atlantic oceans, based on (1) global magnetic reversal picks (Seton et al., 2014) compiled by Müller et al. (2016); and (2) robustly defined hotspot tracks that lend a high degree of certainty to reference frames for plate restorations of 0–70 Ma (e.g. Torsvik et al., 2008; Doubrovine et al., 2012; Müller et al., 2019).

At 59 Ma, our reconstruction places the east and west syntaxes of India at 5.2°S and 2.5°N, respectively (Fig. 8). Alternative reference frames place the east and west syntaxes at comparable latitudes of 8°S to 11°S, and 3°N to 3°S, respectively (Fig. 8), although small shifts in longitude (0° to 6°) and latitude (1° to 5°) occur due to the manner in which different reference frames handle effects such as true polar wander, hotspot motion, longitudinal drift of Africa, and net lithospheric rotation (e.g. Shephard et al., 2012; Torsvik et al., 2012; Matthews et al., 2016).

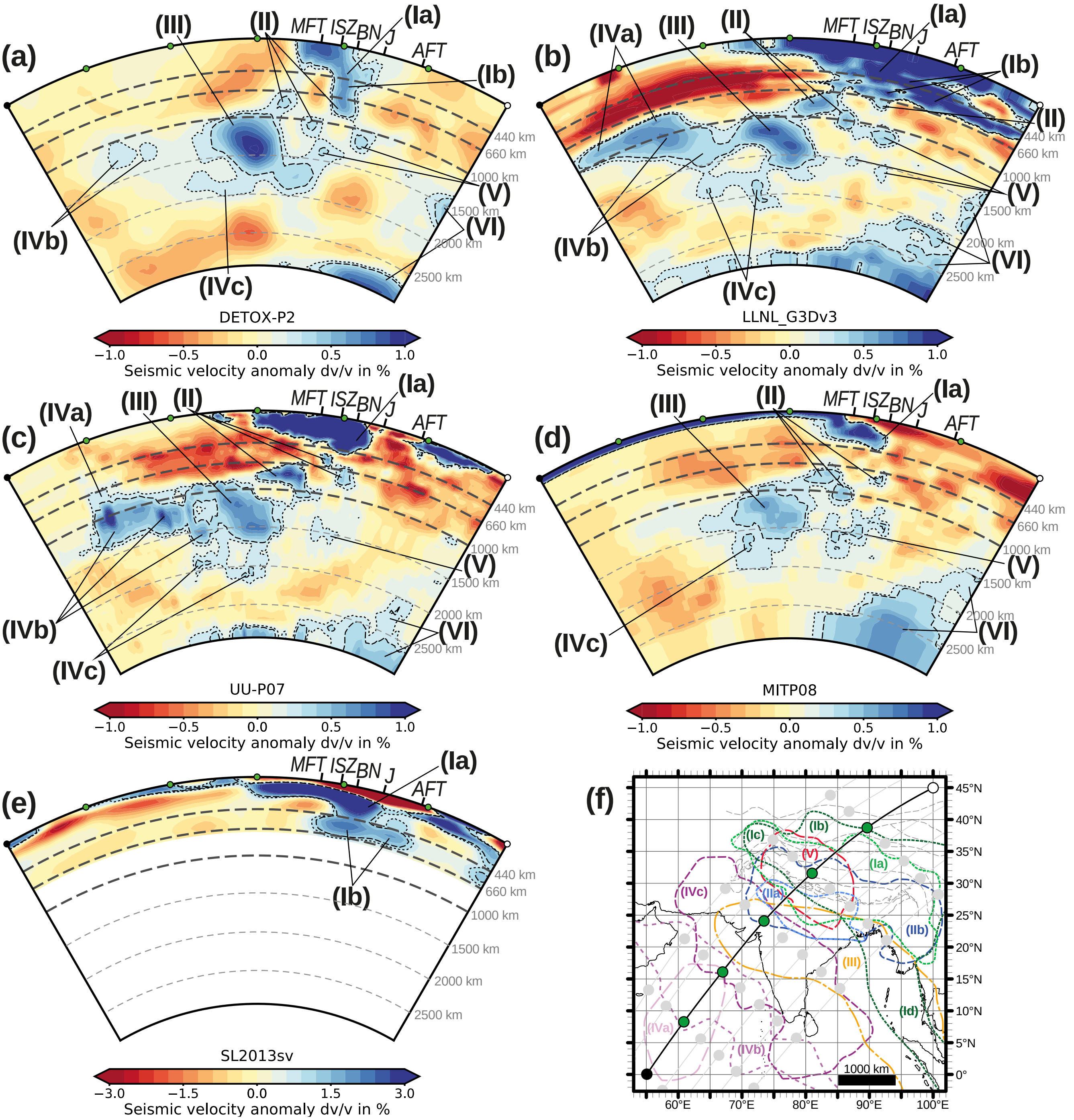

Fig. 14. Cross section C – see Fig. 12 for full figure caption.

5.4.2. Reconstruction of the Asian margin at 59 Ma

The location of the southern Asian margin cannot be determined from plate circuits, as the geological record of ocean spreading within the Tethys oceans has been subducted. Paleomagnetic data from the Linzizong volcanics place Lhasa at 20°N ± 4° between ~55–50 Ma (Fig. 8) (Huang et al., 2015a), which is in good agreement with other paleomagnetic studies (e.g. Lippert et al., 2014; Ma et al., 2014b; Huang et al., 2015b). This is consistent with estimates of ~1000 km of shortening within Asian crust across the Tibetan plateau since collision at 59 ± 1 Ma, and the location of a well-imaged linear seismic anomaly in the lower mantle beneath central India (our Anomaly III, Fig. 8) (Dupont-Nivet et al., 2010; van Hinsbergen et al., 2011a; Li et al., 2015; Kapp and DeCelles, 2019). We therefore locate the south Asian margin of the Lhasa terrane at 20°N at the onset of the India-Asia collision (*s.l.*).

5.5. Size and structure of Greater India preserved in the Himalaya-Tibet orogen

Greater India formed the northern passive margin of the Indian continent (Hu et al., 2016a; van Hinsbergen et al., 2019). It was subjected to several episodes of rifting and associated intra-plate magmatism during the Permian (e.g. Vannay and Spring, 1993; Chauvet et al., 2008), Triassic (e.g. Huang et al., 2018), and Early Cretaceous (e.g. Zhu et al., 2009a; Hu

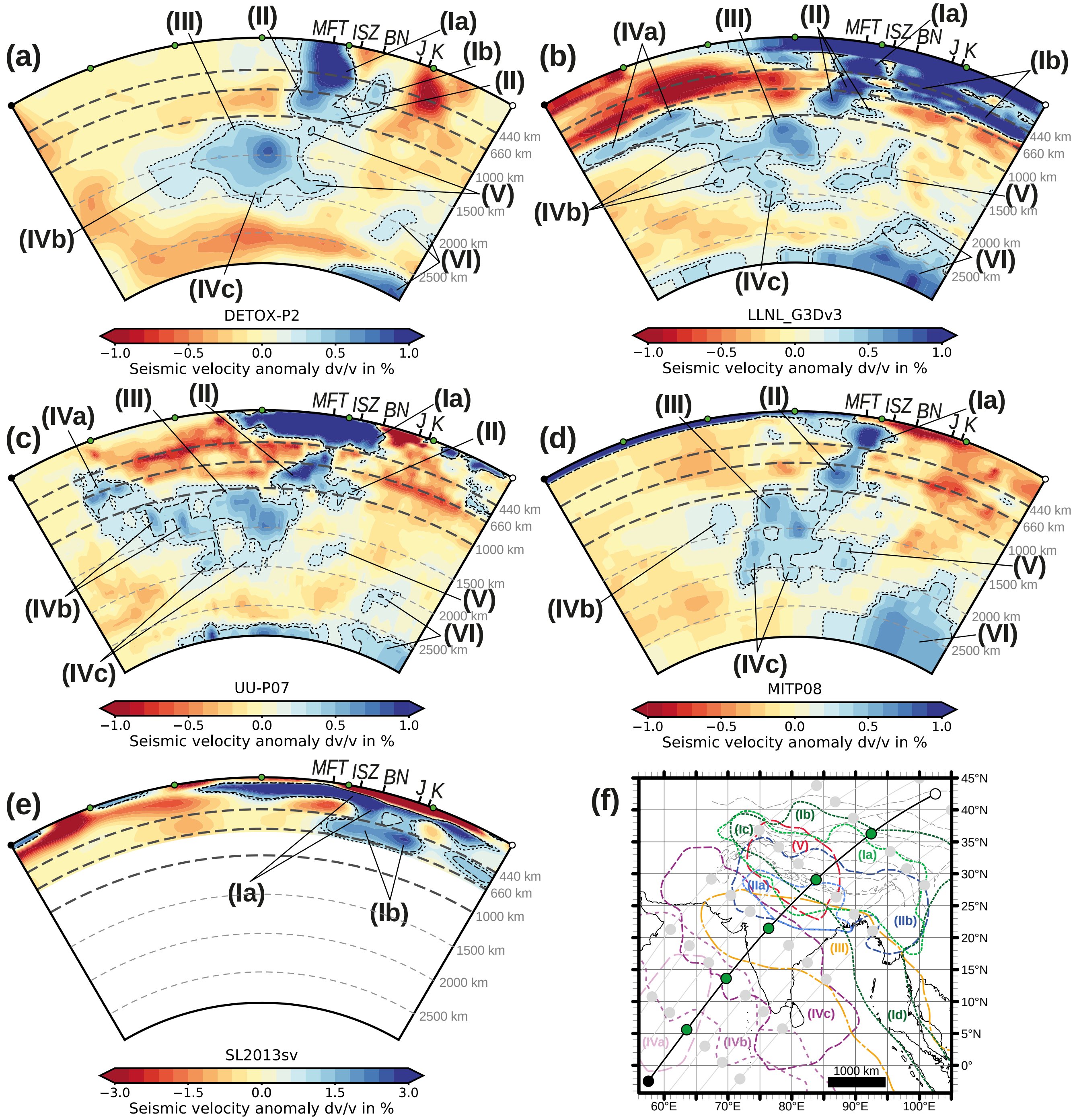

Fig. 15. Cross section D – see Fig. 12 for full figure caption.

et al., 2010; Liu et al., 2015; Chen et al., 2018). The maximum size of Greater India cannot exceed the distance between the Asian margin and the MBT at the onset of collision at 59 ± 1 Ma (Fig. 8). Further constraints on the size and geometry of Greater India are based on stratigraphic correlations, estimates of Indian crustal shortening within the Himalayan-Tibetan orogenic system, and subsurface imaging of Indian continental lithosphere beneath Tibet (Fig. 21).

5.5.1. The ‘suspect terrane’ hypothesis for the GHS-THS stratigraphy

The GHS and THS share several commonalities that distinguish them from the underlying LHS. Some authors view the GHS and THS as a single package of Neoproterozoic to Cenozoic strata, differentiated from each other only on a structural and metamorphic basis (see review of Martin, 2017b). The LHS (HFT-A, Fig. 1; Assemblage A of Martin, 2017b) is distinguished from GHS-THS strata (HFTB, Fig. 1; Assemblage B of Martin, 2017b) based on the age of their constituent sedimentary and igneous rocks and on SmNd isotopic compositions (Mottram et al., 2014; Martin, 2017b; Goscombe et al., 2018; Spencer et al., 2018). Based on these differences, and the structural isolation of GHS-THS from the LHS, Martin (2017b) argued that the post-Cretaceous GHS-THS strata fit the definition of a suspect terrane (Coney et al., 1980). This debate continues; for example, Dyck et al. (2019) argue that Paleoproterozoic gneiss mapped in the

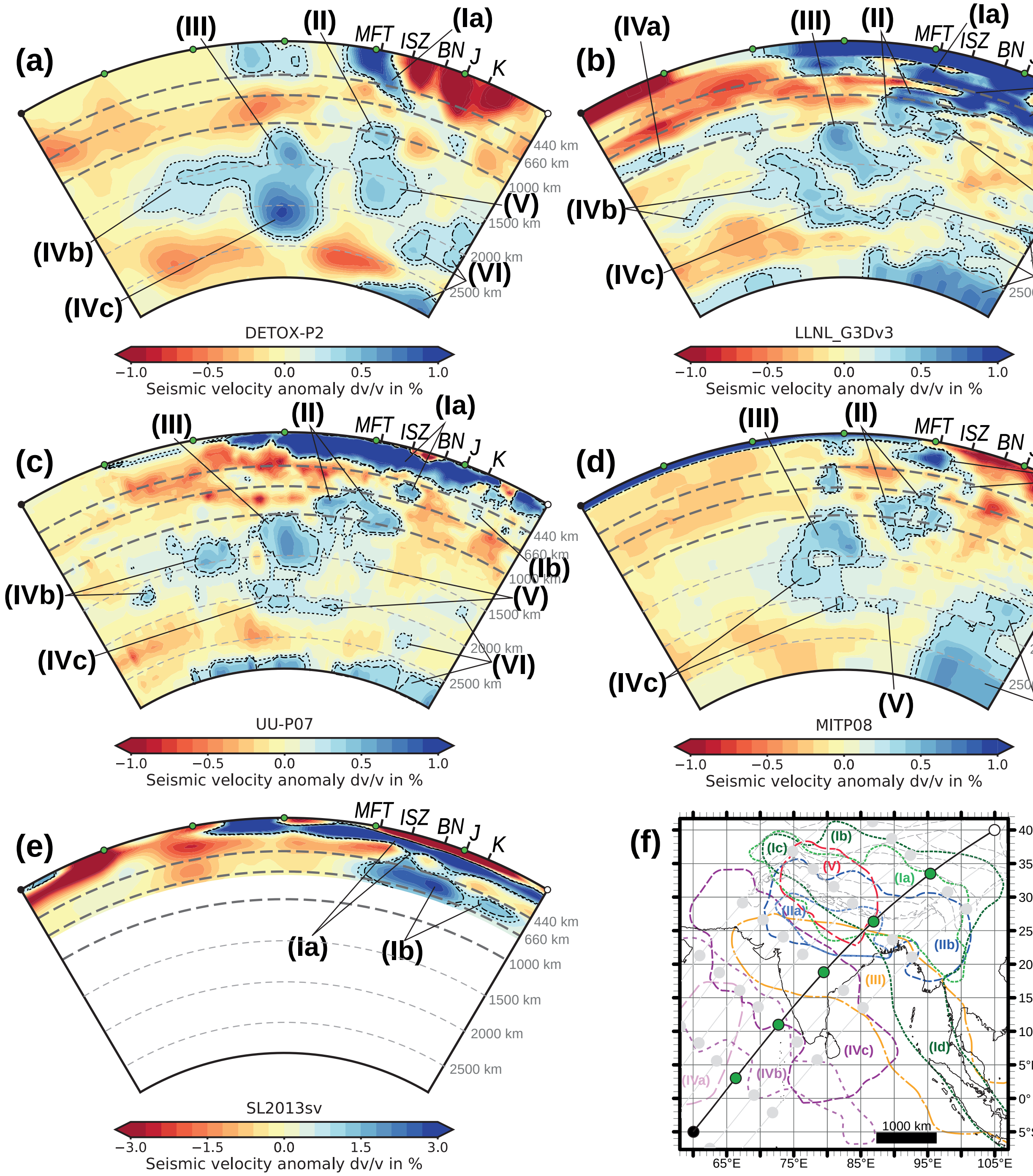

Fig. 16. Cross section E – see Fig. 12 for full figure caption.

basal section of the GHS in central Nepal correlates with similar-aged gneisses in the LHS, and that the GHS and LHS are therefore part of the same contiguous passive margin sequence.

5.5.2. Crustal shortening estimates

Table 3 presents a compilation of published shortening estimates from across the Himalayan orogen. Local minimum and maximum restored lengths of the LHS, GHS and THS are displayed on Fig. 21a (see Table 3 for references). Shortening estimates associated with deformation within the SHZ, LHS, and the underlying MFT range between 161 km to 522 km (Table 3). Displacement estimates along the overlying MCT range between 52 km to 259 km (Table 3). Shortening estimates along discrete brittle structure within the GHS range between 4 km to 75 km (Table 3). Shortening estimates for the THS and ISZ are sparse, but range between 85 km to 139 km, and 36 km to 120 km, respectively (Table 3). Excluding ductile shortening (which may be as high as 230 km in the GHS; Corrie and Kohn, 2011), the sum of the mean minimum and maximum shortening estimates from each unit gives an estimated total crustal shortening of 740 km to 608 km within Indian crustal units since the onset of collision at 59 ± 1 Ma. Locally restoring the estimated amounts of crustal shortening indicates that prior to collision, crustal units of Greater India extended ~900 km to ~750 km north of the MFT (Fig. 21a), which is in close

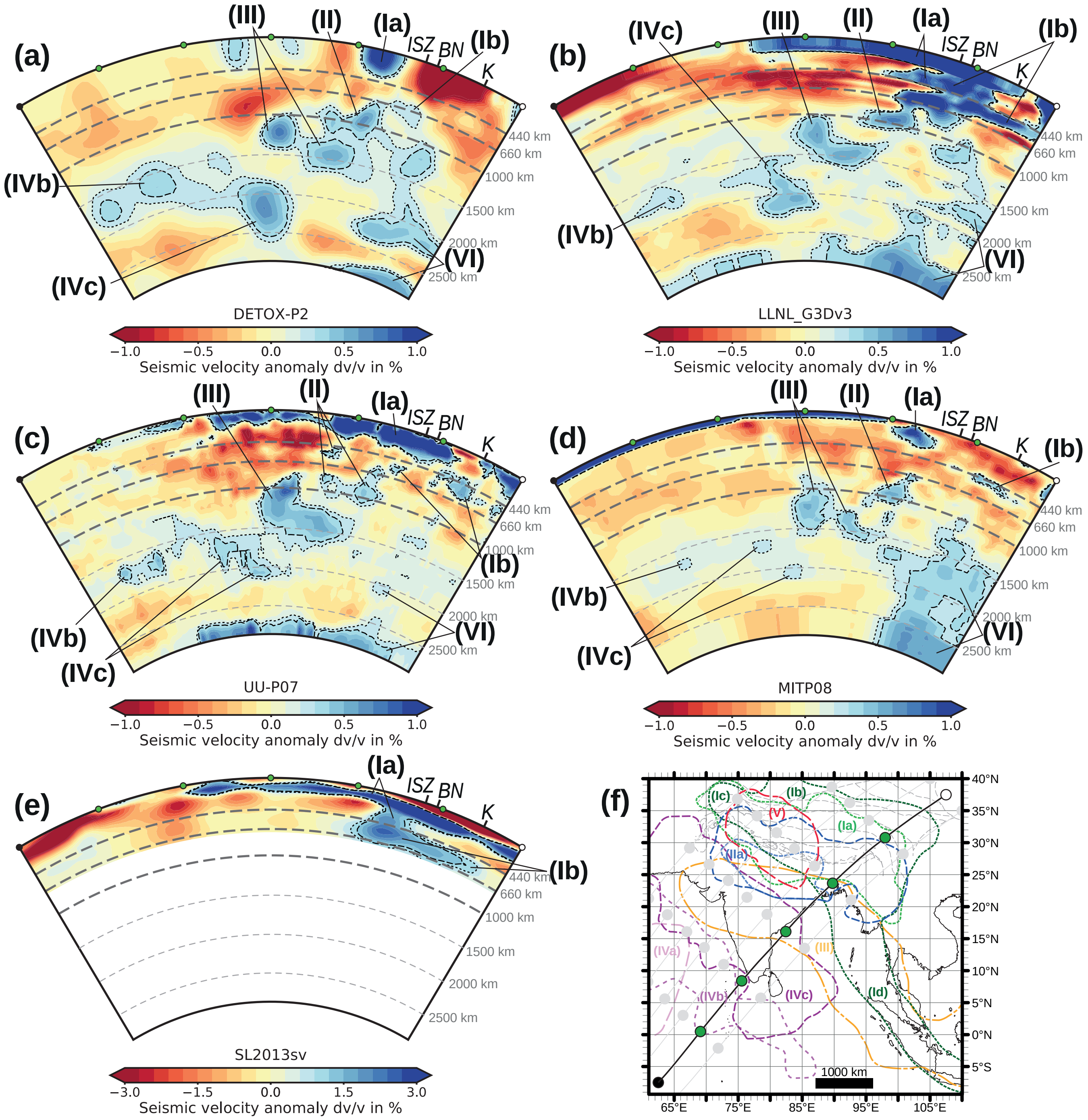

Fig. 17. Cross section F – see Fig. 12 for full figure caption.

agreement with previous estimates of total crustal shortening (e.g. Robinson et al., 2006; Guillot et al., 2008; Long et al., 2011), and estimates of the area of Indian lithosphere imaged beneath the Tibetan Plateau via geophysical techniques (see below). We note the remarkable consistency between the restored length of the LHS and the most northerly imaged India lower crust (red dots, Fig. 21a). These shortening estimates are also consistent with paleomagnetic datasets which suggest that edge of Greater India was located <1000 km beyond the MFT in the Early Cretaceous, prior to rifting from Gondwana (Huang et al., 2017a; Huang et al., 2017b; van Hinsbergen, 2019; van Hinsbergen et al., 2019), although this is disputed by Rowley (2019a, 2019b) who uses a less conventional statistical method for interpreting paleomagnetic data.

5.5.3. Subsurface images of Indian lower crust and lithosphere beneath Tibet

Table 4 collates the most northen longitudes, latitudes and depths at which the Indian lower crust, Indian lithosphere top surface, and Indian lithosphere-asthenosphere boundary (LAB) are imaged beneath Tibet, from a variety of different geophysical analyses. From west to east, receiver function studies suggest that Indian lower crust may be traced as far north as ~32° N to ~30° N at a depth range of ~50 km to ~90 km, detected by the granulite to eclogite transition imaged above the Indian continental Moho (Fig. 21a and Table 4) (Kind et al., 2002; Wittlinger et al., 2004; Nábělek et al., 2009; Xu et al., 2015; Shi et al., 2016; Xu et al., 2017). Likewise, receiver function studies suggest that the top surface of Indian lithospheric mantle and the LAB may be traced from west to east

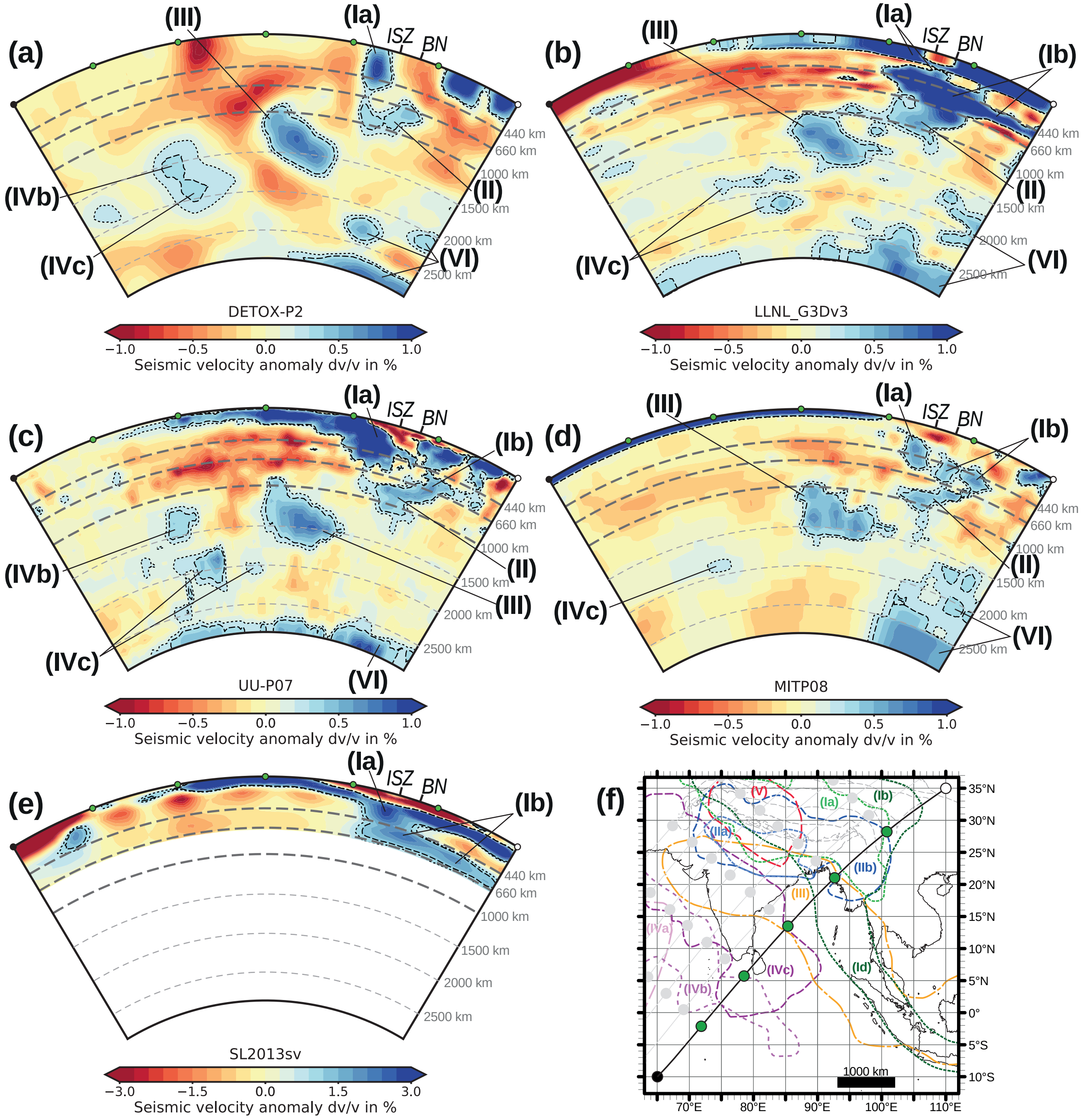

Fig. 18. Cross section G – see Fig. 12 for full figure caption.

as far north as ~35–33° N to ~32–31° N at respective depth ranges of ~80–200 km and ~200–250 km (Fig. 21a and Table 4) (Zhao et al., 2010; Xu et al., 2015; Shi et al., 2016; Xu et al., 2017).

Regional body-wave and surface-wave tomographic models suggest that the Indian lithosphere top surface extends northwards to at least ~32° N and in many places appears as far north as ~34–36° N at a depth range of ~100–400 km (Fig. 21a and Table 4) (He et al., 2010; Ceylan et al., 2012; Liang et al., 2012; Zhang et al., 2012b; Agius and Lebedev, 2013; Zhao et al., 2014; Zhang et al., 2015; Liang et al., 2016; Hearn et al., 2019). Some of these tomography-based studies image the Indian lithosphere, ~1° to ~2° latitude further north than receiver function studies for the same north-south transect (Table 4). Many of these tomography studies included structure-specific resolution tests with modified reference models to validate their interpretations and are thus considered robust (e.g. Liang et al., 2012; Zhao et al., 2014; Zhang et al., 2015; Liang et al., 2016). Regional tomographic studies also suggest that the Indian lithosphere is fragmented laterally, with east and west Tibet characterised by sub-horizontal underthrusting Indian lithosphere and central Tibet characterised by moderate to steeply subducting Indian lithosphere that may be traced into the mantle transition zone (Table 4) (e.g. Liang et al., 2016; Duan et al., 2017), as suggested by Anomaly Ia observed in the global tomography models SL2013sv (Fig. 21b) and LLNL-G3Dv3 (Figs. 21c).

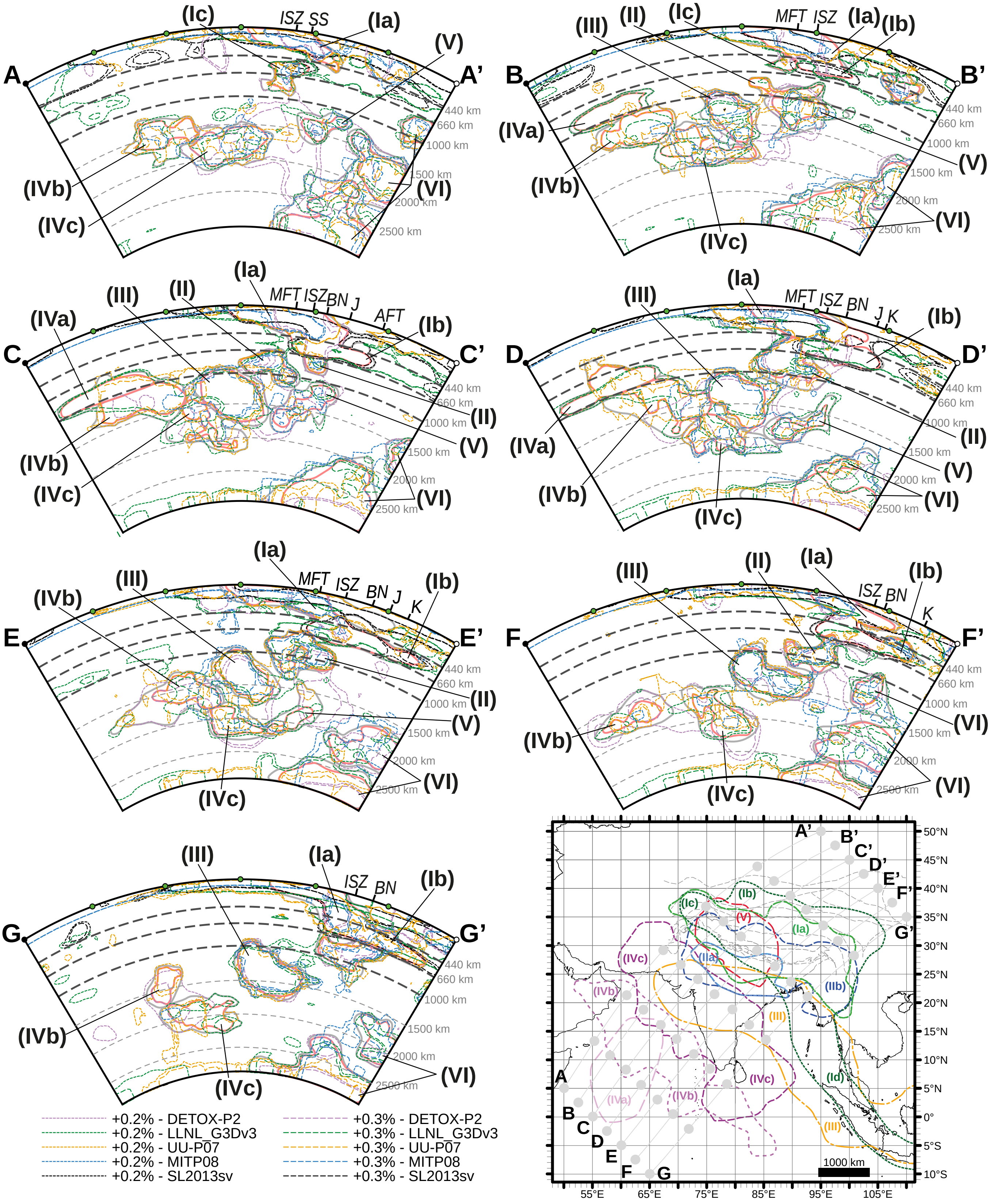

Fig. 19. Outlines of seismically fast anomalies, drawn from the +0.2% (short dashed line) and +0.3% (long dashed line) velocity contours of each tomography model (lines colour-coded by model) for cross sections A to G. For additional clarity, these cross sections are displayed without annotations, along with cross sections showing only +0.2%, and only +0.3% contours in Supplementary Materials 07.

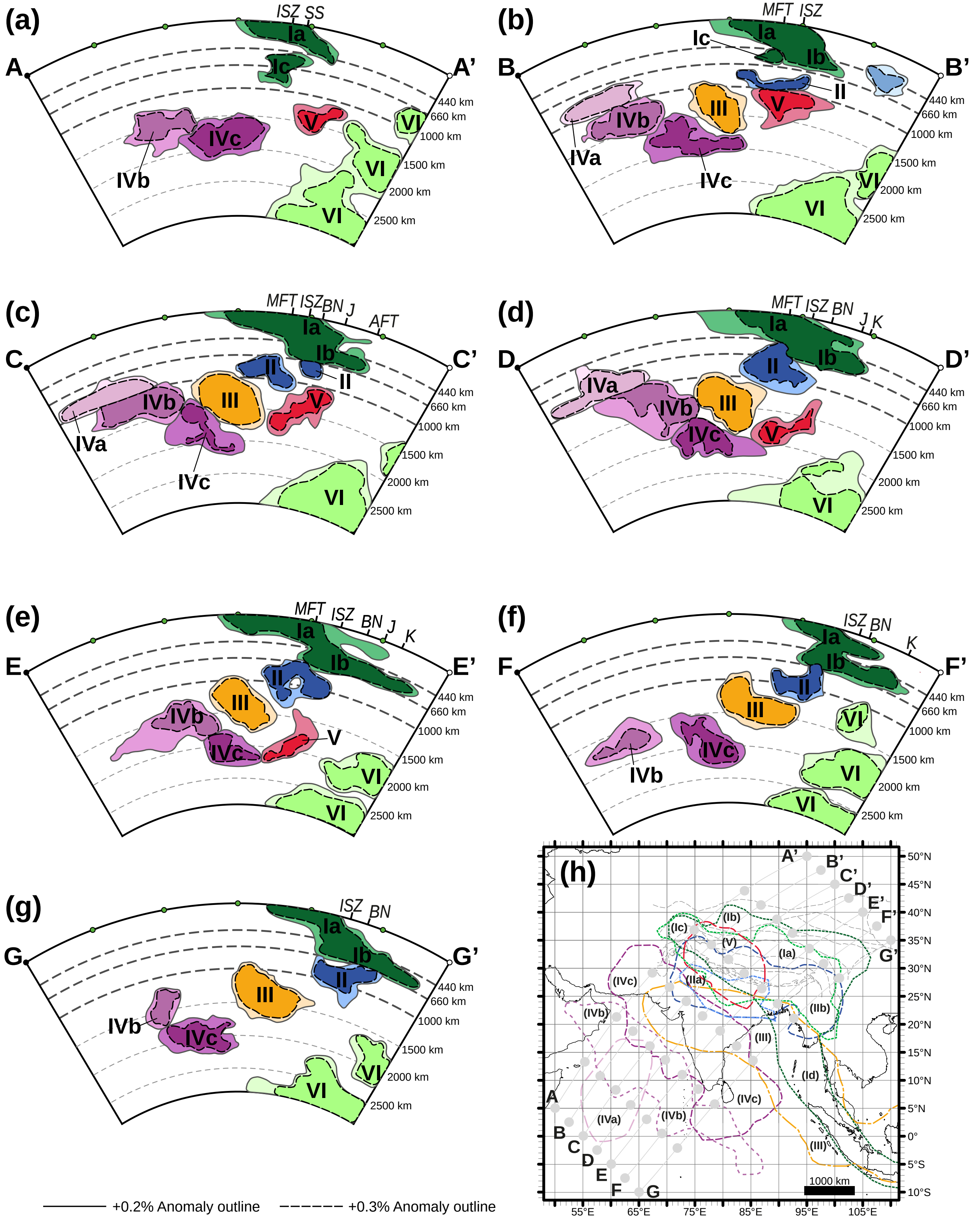

Fig. 20. Outlines of Anomalies I to VI based on the combined +0.2% (solid outline, faded colour) and +0.3% (dashed outline, bold colour) velocity contours from in Fig. 19, and as defined in Table 2.

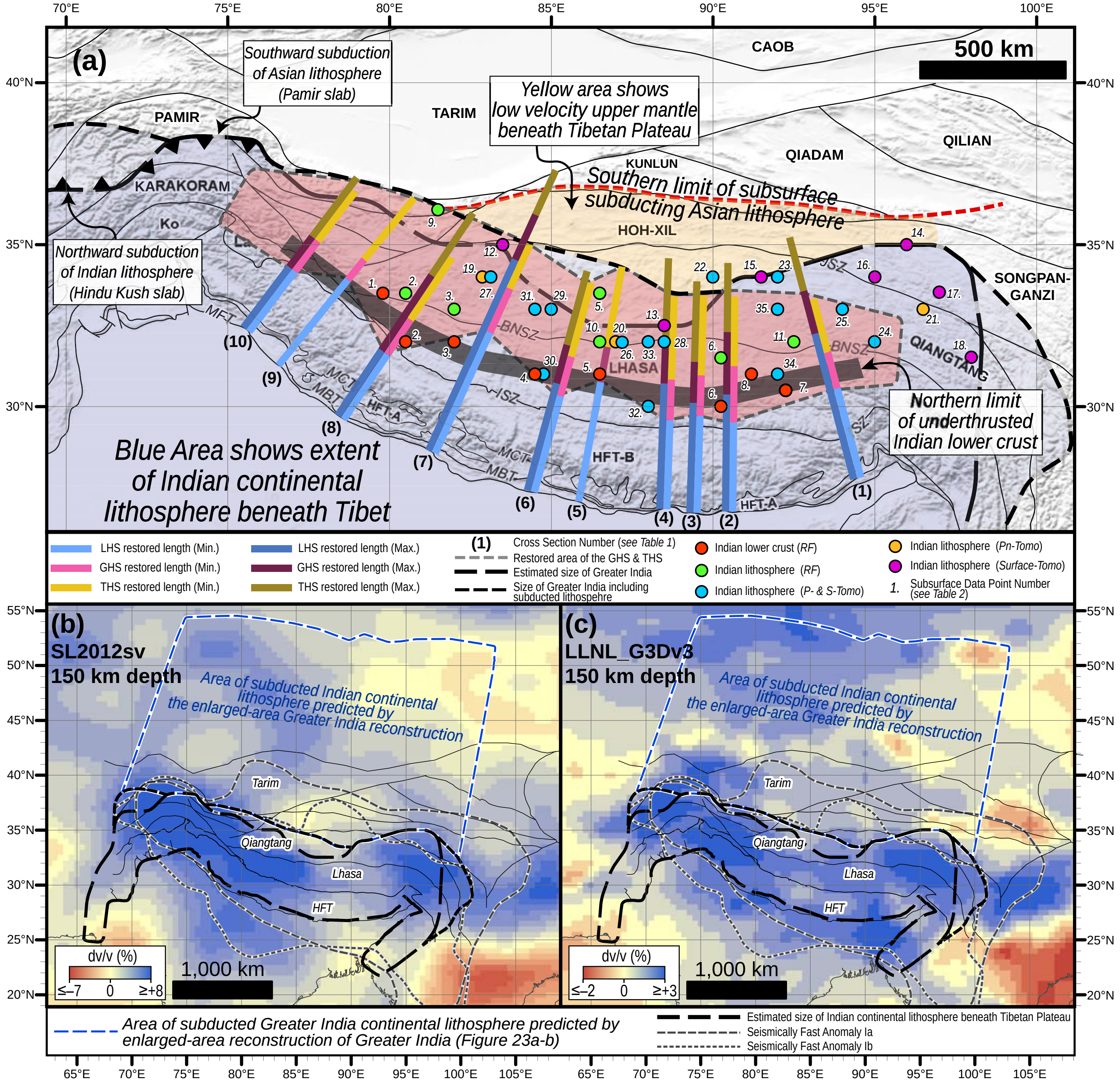

Fig. 21. (a-c) Spatial extent of underthrusted/subducted Indian lithosphere immediately beneath the Tibetan plateau, based on Himalayan crustal shortening estimates and geophysical subsurface imaging. (a) Blue shaded area with thick long-dashed line marks the edge of Indian continental lithosphere (Greater India) underlying the Tibetan plateau, estimated from geophysical datasets and cross section restorations. Thick short-dashed line shows extent of Indian continental lithosphere underlying the Tibetan plateau after vertical slabs of Indian lithosphere are unfolded to a horizontal position. Position and polarity of the Pamir and Hindu Kush subduction zones is based on Kufner et al. (2016). Red dashed line marks southern limit of southward subducting Asian continental lithosphere beneath the Tibetan Plateau; yellow area marks low seismic velocity zone in the upper mantle beneath the Tibetan Plateau (based on: Wittlinger et al., 1996, Liang et al., 2012, Zhang et al., 2012b, Zhao et al., 2014). Coloured circles show the positions at which the Indian crust and lithosphere are imaged beneath the Tibetan Plateau. Colours correspond to: red – Indian lower crust imaged via receiver function surveys; green – Indian lithosphere imaged via receiver function surveys; blue - Indian lithosphere imaged via P- and S-wave tomography; yellow - Indian lithosphere imaged via Pn-wave tomography; purple - Indian lithosphere imaged via surface-wave tomography. Numbers next to coloured circle can be matched to their data sources presented in Table 4. Thick semi-transparent solid line marks northern limit of Indian lower crust imaged beneath Tibet. NE-SW trending, light and dark coloured bars respectively show minimum and maximum restored lengths of the LHS (blue), GHS (purple), and the THS (yellow), determined from cross section restoration. Cross section numbers can be matched with their data sources in Table 3. Red shaded area with short-dashed line outlines approximate combined area of the restored GHS and THS. Abbreviations on underlying map are as in Figs. 1–2. (b-c) 150 km depth slice of tomography models (b) SL2013sv and (c) LLNL_G3Dv3. Estimated size of Greater India displayed by thick long-dashed line. Outline of seismically fast anomaly I is marked by thick grey dashed line. Estimated size of Indian continental crust and mantle lithosphere that must be removed via subduction to satisfy the enlarged-area Greater India reconstruction is outlined by blue dashed line, based on Fig. 23c. Georeferenced overlays (.kml, .kmz) and shapefiles of all points, lines, and polygons presented in our map figures are available for use and editing with global information system software (e.g. Google Earth, GPlates, ArcGIS) in Supplementary Materials 01 and 02.

Table 3

Crustal shortening estimates for Indian crustal units in the Himalayan orogen. Shortening estimates are graphically displayed in Fig. 21.

Location	Cross Section Number	SHZ + LHS				MCT		GHS				THS				ISZ				Source
		Shortening (km)		Restored length (km)		Shortening (km)		Shortening (km)		Restored length (km)		Shortening (km)		Restored length (km)		Shortening (km)		Restored length (km)		
		Max.	Min.	Max.	Min.	Max.	Min.	Max.	Min.	Max.	Min.	Max.	Min.	Max.	Min.	Max.	Min.	Max.	Min.	
West Arunachal Pradesh	1	308	–	751	565	140	–	67	–	–	–	–	–	–	–	–	–	–	–	Yin et al., 2010
Arunachal Himal	1	268	–	349	–	52	–	4	–	–	–	–	–	–	–	–	–	–	–	Ningthoujam et al., 2015
Bhutan	2	267	164	406	312	156	97	53	31	–	–	–	–	–	–	–	–	–	–	Long et al., 2011
West Bhutan	3	340–359	315–325	–	–	174–220	200	–	–	–	–	–	–	–	–	–	–	–	–	McQuarrie et al., 2014, Tobgay et al., 2012
Sikkim	4	253	–	312	–	249	–	–	–	–	–	139	133	–	–	–	–	–	–	Ratschbacher et al., 1994, Mitra et al., 2010
Darjeeling-Sikkim	4	363	–	–	–	101	–	–	–	–	–	–	–	–	–	–	–	–	–	Bhattacharyya et al., 2015
East Nepal	5	–	–	–	–	175	140	–	–	–	–	–	–	–	–	–	–	–	–	Schelling and Arita, 1991
East-Central Nepal	6	283.3	267.7	400	–	132–210	117–140	–	–	–	–	–	–	–	–	–	–	–	–	Schelling, 1992, Kohn et al., 2004, Khanal and Robinson, 2013
West-Central Nepal	6	243.5	208	335.5	300	127.5	105	–	–	138	116	–	–	–	–	–	–	–	–	Robinson and Martin, 2014
West Nepal – Kumaun India	7	372–522	322–374	450–710	490–493	125–245	111–157	75	8	300	–	–	–	400	–	–	–	–	–	Robinson et al., 2006, Robinson, 2008, Carosi et al., 2010, Robinson and McQuarrie, 2012, Mandal et al., 2019
Kumaun-Garhwal India	8	162	161	247	232	259	193	–	–	283	231	–	–	–	–	–	–	–	–	Srivastava and Mitra, 1994
Mt Kailas, Tibet	8	–	–	–	–	–	–	–	–	–	–	112	–	–	–	64	–	–	–	Murphy and Yin, 2003
Himachal Himal	9	326	–	306	–	181	–	–	–	–	–	–	–	–	–	–	–	–	–	Webb, 2013
Zanskar-Ladakh	10	–	–	–	–	–	–	–	–	–	–	87–126	85	–	–	36	–	–	–	Searle et al., 1987; Searle et al., 1990
Zanskar-Ladakh	10	–	–	–	–	–	–	–	–	–	–	87	85	–	–	–	–	–	–	Corfield and Searle, 2000, Steck et al., 1993
Generalized	–	–	–	–	–	–	–	–	–	–	–	–	–	–	–	120	100	–	–	Li et al., 2015
Mean	–	331	267	459	399	170	139	50	20	240	174	116	109	400	400	73	–	–	–	
Standard deviation	–	90	75	168	122	53	34	28	12	73	58	19	24	–	–	35	–	–	–	

Table 4
Depth and location of Indian lower crust and Indian lithosphere imaged directly beneath the Tibetan Plateau.

Method	Source	Data Point Number		Indian Lower Crust		Indian Lithosphere				
						Top of Lithosphere		LAB		
			Longitude	Latitude	Depth (km)	Latitude	Depth (km)	Latitude	Depth (km)	Notes
Receiver functions	Wittlinger et al., 2004	1	79.3° E to 80.3° E	33.5° N	90	–	–	–	–	–
	Xu et al., 2017	2	79.5° E to 81.5° E	32° N	50	33.5° N	80	32.5° N	200	–
		3	81° E to 83° E	32° N	50	33° N	80	32.5° N	200	–
	Nábělek et al., 2009	4	84° E to 85° E	31° N	80	–	–	–	–	–
	Xu et al., 2015	5	85° E to 88° E	31° N	60	33.5° N	80	–	–	–
	Shi et al., 2016	6	89° E to 91.5° E	30° N	90	31.5° N	150	–	–	–
		7	91.5° E to 93° E	30.5° N	70	30.5° N	150	–	–	Lithospheric mantle has detached from underplated indian lower crust above.
	Kind et al., 2002	8	81° E to 82° E	31° N	70	–	–	–	–	–
	Zhao et al., 2010	9	81° E to 82° E	–	–	–	–	35° N	200	LAB is subhorizontal. Significant anisotropy north of Indian LAB.
		10	86° E to 87° E	–	–	–	–	32° N	200	LAB dips northwards. MTZ is depressed north of 32° N. Significant anisotropy north of Indian LAB.
		11	90° E to 95° E	–	–	32° N	200	31° N	250	MTZ is depressed north of 31° N. Significant anisotropy north of Indian LAB.
	Duan et al., 2017	–	85° E to 93° E	–	–	–	–	–	–	MTZ depressed by 15–20 km, interpreted as subduction of Indian lithopshere into MTZ
Surface wave tomography	Agius and Lebedev, 2013	12	82° E to 85° E	–	–	35° N	150–300	–	–	–
		13	85° E to 92° E	–	–	32.5° N	150–300	–	–	–
		14	92° E to 100° E	–	–	36.5° N	150–300	–	–	–
	Ceylan et al., 2012	15	90° E to 94° E	–	–	34° N	100–300	33° N	100–300	Vertical Indian slab
		16	94° E to 96° E	–	–	34° N	100–150	34° N	150–200	Sub-horizontal Indian slab, slight southward dip
		17	96° E to 98° E	–	–	34° N to 33° N	100–150	34° N to 33° N	150–200	Sub-horizontal Indian slab, striking northwest-southeast, slight southward dip
		18	98° E	–	–	33° N to 30° N	100–300	33° N to 30° N	100–300	Vertical Indian slab, striking north-south
Pn tomography	Hearn et al., 2019	19	82° E to 84° E	–	–	34° N	–	–	–	–
		20	86° E to 88° E	–	–	32° N	–	–	–	–
		21	95° E to 98° E	–	–	33° N	–	–	–	–
P-wave tomography	He et al., 2010	22	88° E to 92° E	–	–	34° N	300	34° N	400	–
	Zhang et al., 2012a;	23	91° E to 93° E	–	–	34° N	100–200	33.5° N	200	
	Zhang et al., 2012b	24	94° E to 96° E	–	–	32° N	100–200	32° N	180	LAB is sub-horizontal
	Zhang et al., 2015	25	84° E to 86° E	–	–	33° N	100	33° N	250	Lithospheric mantle is sub-horizontal
		26	86° E to 88° E	–	–	32° N	250–300	32° N	350–450	–
	Zhao et al., 2014	27	82° E to 84° E	–	–	34° N	100	34° N	200–300	Lithospheric mantle is sub-horizontal
P- and S-wave tomography	Liang et al., 2012	28	85° E to 92° E	–	–	32° N	75–187	–	–	Low velocity zones between Himalaya and central Tibet interpreted as upwelling fluids or hot mantle through fragmented indian continental lithosphere
		29	92° E to 96° E	–	–	33° N	75–187	32° N	400	–
	Liang et al., 2016	30	83° E to 86° E	–	–	31° N	350	30° N	450	Northward dipping
		31	86° E to 90° E	–	–	30° N	400	30° N	500	Northward dipping
		32	91° E to 93° E	–	–	31° N	350	31° N	450	Northward dipping
		33	83° E to 86° E	–	–	33° N	250	33° N	350	Northern fragment of detached underthrusted indian lithopsphere
		34	86° E to 90° E	–	–	32° N	200	32° N	300	Northern fragment of detached underthrusted indian lithopsphere
		35	91° E to 93° E	–	–	33° N	250	33° N	250	Northern fragment of detached underthrusted indian lithopsphere

LAB - Lithosphere-Asthenospher Boundary; MTZ - Mantle Transition Zone

Beneath northern Tibet, some studies have proposed that Asian lithospheric mantle subducts southward beneath the Tibetan plateau as far south as the Qiangtang block (e.g. Tapponnier et al., 2001; Kind et al., 2002; Wittlinger et al., 2004; Kumar et al., 2006; Zhao et al., 2010; Replumaz et al., 2014). In the Pamir range, west of Tibet, both Indian and Asian continental lithosphere are imaged subducting to depths of at least 200 km (e.g. Wittlinger et al., 2004; Kufner et al., 2016). However, east of the Pamir range, a variety of P-, Pn-, S-, and surface-wave tomography models that include structure-specific resolution tests, do not observe subduction of Asian lithospheric mantle south of the Tarim basin, Kunlun range and Qaidam basin (red dashed line – Fig. 21a) (Ceylan et al., 2012; Liang et al., 2012; Zhang et al., 2012b; Zhao et al., 2014; Zhang et al., 2015; Liang et al., 2016; Hearn et al., 2019). Instead, these studies observe a region of low seismic velocity beneath central Qiangtang northwards to 36° N to 37° N, between the MTZ and ~50–100 km depth (yellow area – Fig. 21a). A comparison of global P- and surface-wave tomography models with this local tomography supports this observation (Fig. 21b-c, Supplementary Materials 06). Explanations for this low velocity zone continue to be debated, and include shear heating in a laterally east-west flowing mantle shear zone, mantle upwelling, and partial melting (e.g. Ceylan et al., 2012; Liang et al., 2012; Zhao et al., 2014; Zhang et al., 2015).

Our synthesis of geophysical studies (Table 4 and Fig. 21) indicates that the distance between the MBT (the southern limit of Greater India) and the most northerly imaged Indian lower crust ranges between 300 km to 420 km (red dots, and thick solid line, Fig. 21a), which is in excellent agreement with the restored length of LHS (blue bars, Fig. 21a). Similarly, the distance between the MBT and the leading edge of Indian continental lithospheric mantle beneath Tibet ranges between 360 km to 900 km (long-dashed line, and blue, green, orange, and purple spots, Fig. 21a), which is in good agreement with the total restored length of crustal units in the Himalaya (blue, red and brown bars, Fig. 21a). This suggests that the pre-deformed area of the LHS is balanced by the area of Indian lower crust and underlying continental mantle beneath southern Tibet, and that the pre-deformed area of all Indian crustal rocks within the Himalayan orogen is balanced by the area of all Indian lithosphere imaged in the upper mantle beneath the Tibetan plateau, and above the mantle transition zone. We use these constraints to define: (1) the pre-collisional width of the minimum-area Greater India restoration; (2) the area of subducted continental lithosphere predicted by the enlarged-area Greater India restorations (Fig. 21b-c); and (3) the area of the Greater India Basin.

6. Critical evaluation of subduction zone configurations and Greater India reconstructions for the India-Asia collision (*s.l.*)

In this section, we integrate datasets presented in Section 5 to test the validity of previously proposed subduction zone configurations (section 3.1) and Greater India reconstructions (section 3.2) for the India-Asia collision (*s.l.*) and post-Triassic evolution of the central Tethys oceans.

6.1. Viable post-Triassic subduction zone configurations for the central Tethys Oceans

Our synthesis of the bedrock record from the Tibetan Plateau (Section 5.1, Figs. 3, 7) can be integrated with our tomographic observations of seismically fast anomalies beneath the Indian hemisphere (-Section 5.2., Figs. 8, 20) to constrain the post-Triassic distribution of subduction zones in the central Tethys Oceans (Fig. 22). Assumptions used to interpret subduction zone and slab kinematics from seismic tomography are outlined in section 4.2. Sinking rate estimates (Table 5) for the tops of slabs assume that slab break-off is instantaneous unless otherwise stated; therefore, these rates are minimum estimates.

6.1.1. Bangong-Tethys subduction events

Bedrock constraints suggest that Early to Late Jurassic subduction of the Bangong-Tethys Ocean beneath the Qiangtang-Karakoram block and Lhasa block produced one or two slabs (BT Slab; Fig. 22), which broke off at ~130–110 Ma (Events: 51–53, 59–61, Fig. 3). If two slabs were produced, they may not be tomographically distinguishable from each other because of their close proximity to each other. Anomaly V (Fig. 20, 22a) is the best candidate for the Bangong-Tethys slab as all other slabs are either too shallow or too far south to remain consistent with the recorded Neotethys subduction events (see below). However, we note that the size and horizontal extent of Anomaly V is smaller than expected for this slab. A slab-break off event at ~130–110 Ma translates into a whole-mantle average sinking rate of 9.2–10.9 mm/yr for the top of Anomaly V (Table 5).

6.1.2. Neotethys subduction events

Bedrock constraints are consistent with either one, two, or three north-dipping subduction zones in the Neotethys Ocean (Fig. 7). This must include subduction beneath southern Lhasa between ~200–150 Ma and ~110–40 Ma, and subduction beneath one or two intra-oceanic arcs between ~165–110 Ma (Fig. 3), which may have remained active until ~90–80 Ma or ~60–50 Ma, depending on how one interprets the bedrock record of subduction and the palaeogeography of Greater India (Fig. 7). Integrating bedrock constraints with the mantle record yields the following subduction zone configurations:

6.1.2.1. ~200 Ma to ~166–150 Ma. Subduction beneath southern Lhasa (Gangdese arc) between ~200–150 Ma (Fig. 3) correlates with the deepest of the four anomalies, Anomaly IVc (Fig. 22a). A subduction initiation event at ~200 Ma translates into a whole-mantle average sinking rate of 11.0–11.5 mm/yr for the base of Anomaly IVc (Table 5).

During this timeframe, the Kohistan intra-oceanic arc may form the westward continuation of the Gangdese arc, or it may initiate south of the Gangdese arc in the Neotethys Ocean in the Late Jurassic (Fig. 22a-b, e). Likewise, the Spontang and Dras ophiolites may form in back arc setting between the Kohistan and Karakoram blocks, or they may form in a mid ocean-spreading ridge setting south or west of the Gangdese arc (Fig. 22a-b, e).

6.1.2.2. ~166–150 Ma to ~80 Ma. Three alternative scenarios (A, B-1, B-2) are proposed to explain the subduction zone configuration of the central Neotethys Ocean between ~166-150 Ma and ~80 Ma:

Scenario A (**Fig. 22**b-c): At ~166–150 Ma, the subduction zone located along the southern margin of Lhasa migrated southwest to an intra-oceanic setting via slab-roll back, resulting in the ~150–110 Ma magmatic gap on South Lhasa (N1 slab – Fig. 22a). This intra-oceanic arc comprised the Middle to Late Jurassic Naga, Kiogar, Luobusa, and Xiugugabu ophiolites, the Zedong arc, and the Kohistan arc (Events 19, 41, 43; Fig. 3). Oceanic lithosphere subducted beneath this South Neotethys intra-oceanic arc is defined by Anomalies IVc, IVb, and possibly IVa, the geometries of which are consistent with at least ~2000 km southwest trench migration (N1 slab – Figs. 20, 22a).

A second Neotethys intra-oceanic arc initiated at ~146–130 Ma, proximal to the southern margin of Lhasa (N2 slab – Fig. 22b). This intra-oceanic arc comprised the Xigaze, Sangsang, Spontang and Dras ophiolites (Events 37, 39, 42–45; Fig. 3). This satisfies, (1) the deposition of Lhasa-derived sediments of the Xigaze Group on top of the Xigaze and Sangsang ophiolites; and (2) the presence of metamorphic soles and melange units with SSZ compositions in the footwalls to the Xigaze, Sangsang and Dras ophiolites. Oceanic lithosphere subducted beneath this North Neotethys intra-oceanic arc is defined by Anomaly III (N2 slab – Fig. 20, 22b). Subduction initiation of this slab at ~146–-130 Ma yields a whole-mantle average sinking rate of 11.0–13.1 mm/yr for the base of Anomaly III (Table 5).

Both intra-oceanic arcs were active at least until ~120–110 Ma. Northward migration of the North Neotethys trench towards Lhasa (N2 slab – Fig. 22c) led to resumed magmatism along the Gangdese arc at ~110 Ma, and a cessation of intra-oceanic magmatism by ~80 Ma (Events 28, 37–46; Fig. 3).

The location and geometry of Anomaly IV (Fig. 20) does not permit northward migration of the South Neotethys intra-oceanic arc, meaning

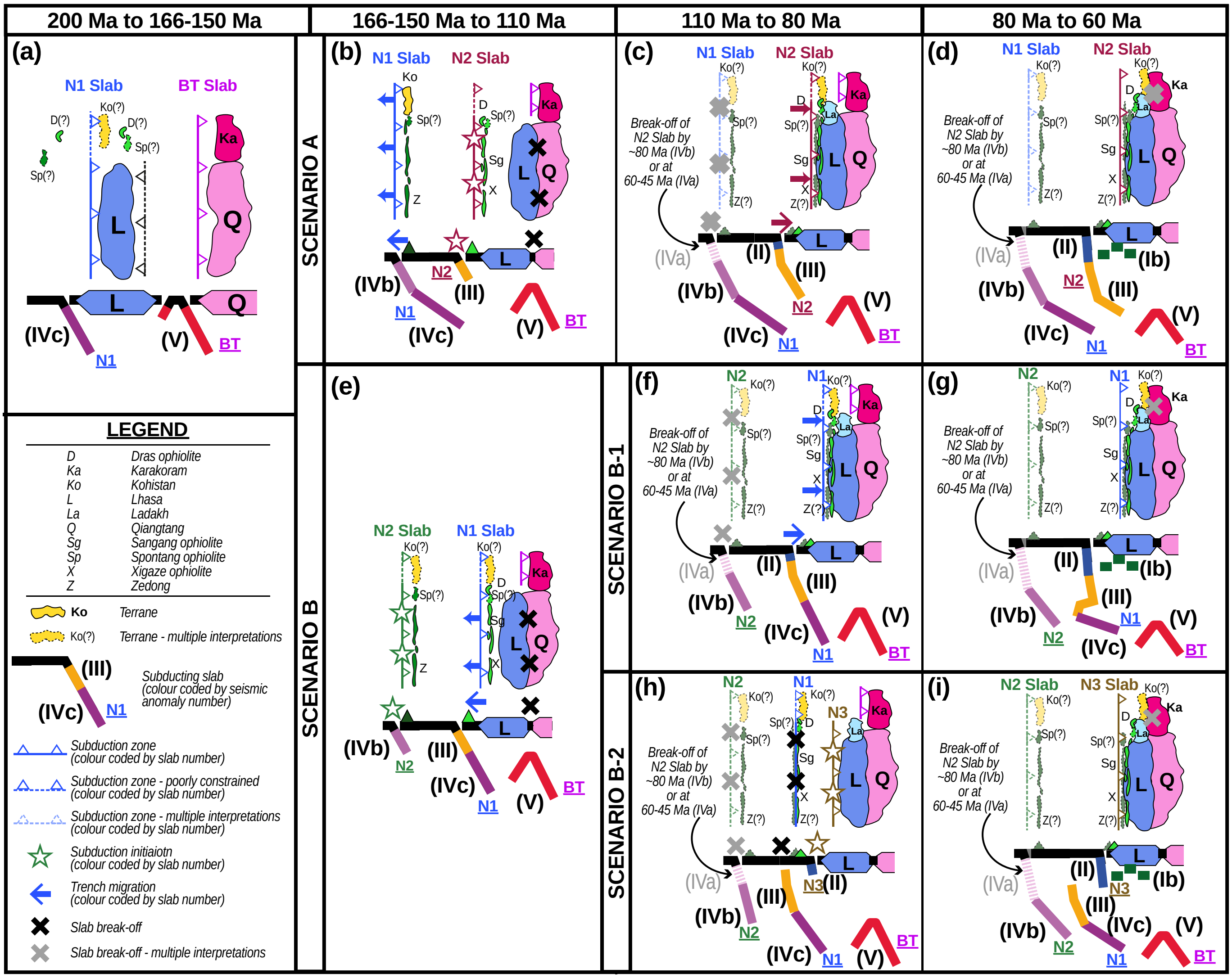

Fig. 22. Post-Triassic subduction zone configurations for the central Tethys Oceans based on integration of bedrock and mantle observations. (a-d) Scenario A. (e) Scenario B (f-g) Scenario B-1. (h-i) Scenario B-2.

that it must have terminated at a subequatorial latitude (Fig. 22c). If the Kohistan block is assumed to accrete to the Karakoram block by 80 Ma, then the South Neotethys intra-oceanic arc must have terminated by ~90 Ma, to allow it to migrate northward as an extinct arc. Cessation of subduction of the N1 slab at ~120–90 Ma (Fig. 22c) yields a whole-mantle average sinking rate of 8.3–12.2 mm/yr for the top of Anomaly IVb or 6.3–8.3 mm/yr for the top of Anomaly IVa, depending on which anomaly defines the top of this slab (Table 5). Alternatively, subduction beneath the South Neotethys intra-oceanic arc was still active at ~80 Ma, and Kohistan and Karakoram did not collide until the Cenozoic (Fig. 22c-d).

Scenario B (Fig. 22e-f, h): At ~166 Ma, the South Neotethys intra-oceanic arc initiated at a subequatorial latitude (N2 slab – Fig. 22e), and comprised the Middle to Late Jurassic Naga, Kiogar, Luobusa, and Xiugugabu ophiolites, the Zedong arc, and the Kohistan arc (Events 19, 41, 43; Fig. 3). Oceanic lithosphere subducted beneath this arc is defined by Anomaly IVb, and possibly IVa (N2 slab – Figs. 20, 22e-i); subduction initiation at ~166 Ma yields a whole-mantle average sinking rate of 9.9–12.0 mm/yr for the base of Anomaly IVb (Table 5).

At ~146–130 Ma, southward roll-back of the subduction zone bounding South Lhasa (N1 slab – Fig. 22e) led to intra-oceanic subduction and formation of the Xigaze and Sangsang ophiolites, and extensional deformation of Lhasa (Events 37, 39, 42–45, 48, 55; Fig. 3), which satisfies the same constraints from these ophiolites mentioned in Scenarios A. Lithosphere subducted beneath this North Neotethys intra-oceanic arc is defined by Anomalies III and IVc (N2 slab – Figs. 20, 22e-i). In this scenario, large gaps between these anomalies imply that the N2 slab is only partly imaged by the tomography models.

In Scenario B, the Spontang ophiolite may have been located in either of the intra-oceanic arcs (N1 or N2 slabs – Fig. 22e), whereas SSZ assemblages below the Dras ophiolite suggest that this formed part of the North Neotethys intra-oceanic arc (N1 slab – Fig. 22e). As with Scenario A, the South Neotethys intra-oceanic arc may terminate between ~120–90 Ma or remain active at 80 Ma. At ~110 Ma, two alternative situations are possible:

Scenario B-1 (Fig. 22f-g) is based on the premise that the ISZ only contains evidence for two distinct suture zones (Mahéo et al., 2004; Mahéo et al., 2006; Guilmette et al., 2009; Searle, 2019). Between ~110–80 Ma, northward migration of the North Neotethys intra-oceanic arc leads to a renewal of the Gangdese arc on Lhasa at ~110 Ma and a cessation of intra-oceanic arc magmatism between ~116–80 Ma (Fig. 22f). To the west, the transition from intra-oceanic to continental arc magmatism does not occur until ~80 Ma when the Ladakh batholith is emplaced (Events 28–30; Fig. 3). At ~80 Ma, continued subduction of the N2 slab beneath this arc is defined by Anomalies II, III, and IVc (Figs. 20, 22f).

Table 5
Slab sinking rate estimates determined for Anomalies I to V in Scenarios A, B-1 and B-2.

Anomaly	**Sinking Rate (mm/yr)**					
	Scenario A		Scenario B-1		Scenario B-2	
	Base of anomaly	Top of anomaly	Base of anomaly	Top of anomaly	Base of anomaly	Top of anomaly
II	Connected to III	10.0 to 18.3$^{\dagger(F)}$ 7.6 to 12.2$^{*(E)}$	10.0 to 11.8‡	*Same as Scenario A*	Connected to III	*Same as Scenario A*
III	11.0 to 13.1‡	Connected to II	Connected to IVc	10.0 to 14.4‡	Connected to IVc	Connected to II
IVa	12.3 to 16.9$^{*(D)}$ Connected to IVb$^{(B\text{ or }C)}$	13.6 to 16.7$^{*(D)}$ 12.7 to 16.7$^{\dagger(C)}$ 6.3 to 8.3$^{*(B)}$	*Same as Scenario A*		*Same as Scenario A*	
IVb	Connected to IVc	8.3 to 12.2$^{(A)}$	9.9 to 12.0‡	*Same as Scenario A*	9.9 to 12.0‡	*Same as Scenario A*
IVc	11.0 to 11.5‡	Connected to IVb	11.0 to 11.5‡	Connected to III	11.0 to 11.5‡	Connected to III
V	–	9.2 to 10.9‡	*Same as Scenario A*		*Same as Scenario A*	

*sinking rate estimates in a single subduction zone configuration at the on set of the India-Asia collision (*s.l.*)

†sinking rate estimates in a double subduction zone configuration at the on set of the India-Asia collision (*s.l.*)

‡sinking rate estimates consitent with both a single subduction zone configuration and a double subduction zone configuration at the on set of the India-Asia collision (s.l.)

A - Assumes IVb forms the top of the South Neotethys intra-oceanic arc (N1 Slab) which broke off at ~120–90 Ma

B - Assumes IVa forms the top of the South Neotethys intra-oceanic arc (N1 Slab) which broke off at ~120–90 Ma

C - Assumes IVa forms the top of the South Neotethys intra-oceanic arc (N1 Slab) which broke off at ~59–45 Ma

D - Assumes IVa subducted during the West India orogen

E - Assumes slab break-off at 59–45 Ma

F -Assumes slab break-off at 45–30 Ma

Scenario B-2 (Fig. 22 h-i) is designed to explain the overlap of 10–30 M.yr. of continental magmatism on the Gangdese arc and intra-oceanic magmatism recorded by the North Neotethys intra-oceanic arc between ~110–80 Ma. Subduction initiation along the south margin of Lhasa and Ladakh renews the Gangdese arc at ~110 Ma, defined by Anomaly II (N3 slab – Fig. 22 h), which yields a whole mantle average sinking rate of 10.0–11.8 mm/yr for its base. Meanwhile, the North Neotethys intra-oceanic arc remains active until ~110–80 Ma (Events 28, 37–46, 49; Fig. 3). Between ~100–80 Ma the North Neotethys intra-oceanic arc records deformation and cooling, in response to collision with either the extinct South Neotethys intra-oceanic arc, or the Gangdese arc (Events 28, 30, 38, 40, 46; Fig. 3). In this scenario, the ISZ must contain at least three different suture zones; currently there is evidence for only two sutures within the ISZ, although other studies have argued for more than two sutures (e.g. Guilmette et al., 2012; Hébert et al., 2012). Slab break-off from the North Neotethys intra-oceanic arc between ~110–80 Ma, yields a whole mantle average sinking rate of 10.0–14.4 mm/yr for the top of Anomaly III (Table 5).

6.1.2.3. ~80–30 Ma. If the South Neotethys intra-oceanic arc remained active until the India-Asia collision (*s.l.*), as argued for by Replumaz et al. (2014), Jagoutz et al. (2015), Burg and Bouilhol, 2019, and others, then the top of the N1 slab is defined by Anomaly IVa. This yields a whole-mantle average sinking rate of 12.7–16.7 mm/yr, for the top of Anomaly IVa, assuming break-off at ~59–45 Ma (Fig. 22d, g, i, Table 5) based on ages of UHP metamorphism in the THS. The West Pakistan ophiolites form part of the South Neotethys intra-oceanic at this time (Events 32–35; Fig. 3). However, this scenario conflicts with our synthesis of bedrock observations which suggest that (1) the Kohistan and Karakoram blocks collided at ~90–80 Ma; and (2) intra-oceanic arc magmatism east of Kohistan did not occur after ~110–80 Ma (see Section 5.1.).

Alternatively, if the south Neotethys intra-oceanic subduction zone terminated by ~80 Ma, then Anomaly IVa either represents the top of the N1 slab, or it represents a separate slab that subducted during the West India orogeny from ~81–65 Ma to ~55–45 Ma during collision of northwest India with the West Pakistan ophiolites and the Kabul block. In the case of the later, Anomaly IVa yields a whole-mantle average sinking rate of 12.3–16.9 mm/yr for its base and 13.6–16.7 mm/yr for its top (Table 5) (e.g. van der Meer et al., 2018; van Hinsbergen et al., 2019).

Between 80 and 59 Ma, subduction beneath southern Lhasa is defined either by Anomalies II and III (Scenario A, N2 slab – Fig. 22d), or by Anomalies II, III, and IVc (Scenario B-1, N2 slab – Fig. 22 g), or by Anomaly II (Scenario B-2, N3 slab – Fig. 22i). In either case, the top of this slab is defined by Anomaly II, which broke off at ~59–45 Ma or at ~45–30 Ma, depending on which Greater India reconstruction is favoured. These yield respective whole-mantle average sinking rates of 7.6–12.2 mm/yr, or 10.0–18.3 mm/yr (Table 5).

By assuming that the top of Anomaly II represents oceanic lithosphere that broke off from the continental margin of Greater India, it follows that Anomaly Ia, and perhaps some of Ib and Ic, represent subducted Indian continental lithosphere. To the east, Anomaly Id represents Indian oceanic lithosphere subducted beneath Myanmar and Sumatra prior to and during collision (*s.s.*), which may have provided the driving force for continental subduction. The lower portion of the Anomaly Id slab was probably connected to Anomaly II, prior to slab dragging. The horizontal width of Anomaly Ib is too large, too shallow and too far north to be explained in its entirety by a Neotethys subduction zone. Instead we propose that most of Anomaly Ib represents Asian and perhaps Indian continental lithosphere that delaminated or dripped into the MTZ, driven by convective removal or gravitational instability prior to and during collision (e.g. Houseman and Molnar, 1997; Hyndman, 2019; Kelly et al., 2019).

Scenarios A, and B-1 assume that Anomalies II and III represent the same slab (Fig. 22d, g); however, they are presently separated by ~1000-–2000 km horizontal distance. We thus propose that in those two scenarios, the slab defined by Anomaly II, ruptured from the underlying slab defined by Anomaly III during continental collision and was dragged ~1000-–2000 km northwards. This is consistent with (1) ~1000 km *syn*-collisional northward migration of the India-Asia plate boundary; and (2) the ~1000 km-wide gap in Anomaly Id (Fig. 8), interpreted as a slab window produced by northward slab dragging by previous studies (e.g. Advokaat et al., 2018; van der Meer et al., 2018).

6.1.3. Subduction zone configurations for the central Tethys Oceans and the India-Asia collision (s.l.)

Anomalies I, II, III, and IV are most consistently interpreted as subducted Neotethys oceanic lithosphere. In this scenarios their positions, which overlap in depth range but are located at different latitudes (Fig. 20), do not support Jurassic to Paleocene subduction of Neotethys oceanic lithosphere by a single subduction zone (i.e. Fig. 4a-c and model a➔b➔e➔i on Fig. 7 are not viable). Alternative scenarios in which some of these anomalies represent older oceanic lithosphere derived from the Bangong-Tethys or Paleotethys oceans may permit subduction of the Neotethys Ocean via a single subduction zone; however, at this time our integration of seismic tomographic observations and bedrock datasets do not support such models.

Our Scenarios A, B-1, and B-2, which are all permissible with respect to the bedrock and mantle record, argue that Anomalies I, II, III and IV equate to two or three slabs of Neotethys oceanic lithosphere. This implies that the ISZ contains more than one suture zone, which is consistent with the occurrence of SSZ ophiolites overlying metamorphic soles and melange units, which also have SSZ compositions (e.g. Mahéo et al., 2004; Mahéo et al., 2006; Guilmette et al., 2009; Hébert et al., 2012).

In all three of our scenarios, the south Neotethys intra-oceanic arc may or may not have been active after 80 Ma, and this is entirely dependent on which reconstruction of Greater India is chosen, as is discussed in Section 6.2. Scenarios A and B-1 are more viable than B-2 because the former require two suture zones in the ISZ, which is consistent with observations (e.g. Mahéo et al., 2004; Mahéo et al., 2006; Guilmette et al., 2009; Searle, 2019), whereas the latter requires three. From a geophysical perspective, Scenario A has a better fit with the geometries and locations of seismic anomalies than Scenario B. All scenarios produce acceptable sinking rate estimates, although we note that inscenarios which assume the N1 Slab broke off at ~120–90 Ma, more acceptable sinking rates are estimated by correlating the top of that slab with Anomaly IVb, rather than IVa (Table 5).

At present, the close agreement of Scenario A with both the mantle and bedrock records suggest that this is the most plausible post-Triassic subduction zone configuration for the central Tethys oceans. All of our scenarios contain uncertainty surrounding the tectonic and palaeogeographic evolution of the Kohistan and Karakoram blocks, the Dras arc, and the Spontang and Dras ophiolites, due to variations in how the bedrock record of these tectonic elements has been interpreted by previous studies (See section 5.1. and Supplementary Materials 03). Resolution of the debates surrounding these tectonic elements is a major challenge, but is needed in order to better constrain the most valid subduction zone configuration (s) for the central Tethys oceans. Despite their differences, Scenarios A and B place the same constraints on the subduction zone configuration of the Neotethys Ocean at the onset of the India-Asia collision (*s.l.*). Two distinct subduction zone configurations are possible at the onset of the India-Asia collision (*s.l.*) at 59 Ma:

6.1.3.1. Single subduction zone configuration for the India-Asia collision (s.l.). The single subduction zone configuration is defined by subduction of Neotethys oceanic beneath the Gangdese arc (e.g. Fig. 4d-f) and is consistent with our bedrock synthesis, which demonstrates a lack of direct evidence for intra-oceanic arc magmatism east of Kohistan, after ~110–80 Ma. This configuration assumes that the closure of the Shyok basin between Kohistan and Karakoram occurred at ~90–80 Ma. At the onset of collision (*s.l.*), this subduction zone was located above the present day locations of Anomaly III (Scenarios A and B-1; Fig. 22d, g) or Anomaly II (Scenario B-2; Fig. 22i); this is consistent with palaeomagnetic and crustal shortening constraints which place the southern Asian margin at 20°N ± 4° latitude (e.g. Huang et al., 2015a; Li et al., 2015; Kapp and DeCelles, 2019).

6.1.3.2. Double subduction zone configuration for the India-Asia collision (s.l.). This configuration assumes that the Gangdese arc (above Anomaly III or II), and the South Neotethys intra-oceanic arc (Anomaly IVa and IVb) were both active at the onset of collision (*s.l.*) (Fig. 4 g-i). Collision at ~59 Ma occurred between Greater India and the South Neotethys intra-oceanic arc, followed by collision with the Gangdese arc at ~45–30 Ma. This model contradicts our extensive list of observations that support accretion of Kohistan to Karakoram by ~80 Ma (section 5.1.1) and demonstrate an absence of post-80 Ma intra-oceanic arc magmatism west of Kohistan (section 5.1.2). Justification for this configuration derives from arguments in support of the minimum-area restoration of Greater India (see section 6.2), which may or may not outweigh arguments based on the bedrock record of magmatism and collision, given their uncertainty. Nevertheless, the distribution of seismically fast anomalies in the deep mantle is consistent with this configuration and yields acceptable sinking rates (Table 5).

The geometries and positions of the seismic anomalies allow for <1000 km of northeast-southwest migration of the trench above Anomalies II and III, and ~1000–2000 km of southwest migration of the trench above Anomaly IV (Figs. 8, 20). However, a lateral separation of >1000 km is maintained between the upper portions of Anomaly IV and Anomalies II and III. Consequently, these anomalies do not support a double subduction zone configuration in which the South Neotethys intra-oceanic arc migrates towards the Gangdese arc prior to collision (Fig. 4j-l) (e.g. Jagoutz et al., 2015). Therefore, we argue that double subduction does not provide an explanation for the rapid motion of India during the Late Cretaceous and Paleocene, as argued for by Jagoutz et al. (2015).

The anomalies are also hard to reconcile with a two-stage double subduction zone configuration (Fig. 4 m-o) (e.g. Hafkenscheid et al., 2006; Kapp and DeCelles, 2019). In that scenario, Anomaly IV defines a slab of Neotethys Ocean subducted beneath a southward migrating intra-oceanic arc comprising the Xigaze ophiolite and overlying Xigaze Group sediments that was active until collision at 59 Ma (Fig. 4 m). Neotethys Ocean in the back-arc of the south-migrating intra-oceanic arc is defined by Anomalies Id, II and III, which subducted beneath Lhasa from 59 Ma to ~40-30 Ma (Fig. 4n-o). This is problematic because it implies that only one subduction zone was active in the Neotethys Ocean prior to 59 Ma, which must have remained close to Lhasa until ~90–80 Ma in order to deposit Lhasa-derived sediments in the Xigaze Group forearc strata. This is inconsistent with paleomagnetic datasets, which argue for a subequatorial Neotethys subduction zone during the Early Cretacous (e.g. Klootwijk et al., 1984; Zaman and Torii, 1999; Ahmad et al., 2000; Khan et al., 2009). The assumption that Anomalies Id, II and III define a slab of Neotethys Ocean subducted between ~59 Ma and ~40–30 Ma is also inconsistent with previous studies which propose that the eastern portions of these anomalies are related to Mesozoic to recent subduction beneath Myanmar and Sumatra (e.g. Hall and Spakman, 2015; van der Meer et al., 2018). Furthermore, this scenario yields an extreme whole-mantle average sinking rate of 27.1–28.8 mm/yr for the base of Anomaly III, which far exceeds previous estimates of whole-mantle average rates, which range globally between ~10–20 mm/yr (e.g. Sigloch and Mihalynuk, 2013; Butterworth et al., 2014; Wu et al., 2016; van der Meer et al., 2018; Chen et al., 2019). We acknowledge that between 59 Ma and 40–30 Ma, India migrated northward at an average rate of ~107–85 mm/yr with respect to a fixed mantle, which is at least consistent with an anomalously high sinking rate. However, based on the remaining caveats outlined above, along with the absence of post-80 Ma intra-oceanic magmatism record in the bedrock record east of Kohistan, we propose that the combined bedrock and mantle record does not support the two-stage double subduction zone models (Fig. 4 m-o) of Kapp and DeCelles (2019) and Hafkenscheid et al. (2006).

6.2. Reconstructions of Greater India for models of the India-Asia collision (s.l.)

In this section, we test the various reconstructions of Greater India against the subduction zone configurations determined from Scenarios A and B-1, within a plate kinematic framework (Fig. 23). These tests allow us to critically evaluate tectonic models of the India-Asia collision (*s.l.*). Model strengths and weaknesses are summarized in Table 6. Georeferenced overlays (.kml, .kmz) and shapefiles of all points, lines, and polygons presented in our map figures are available for use and editing

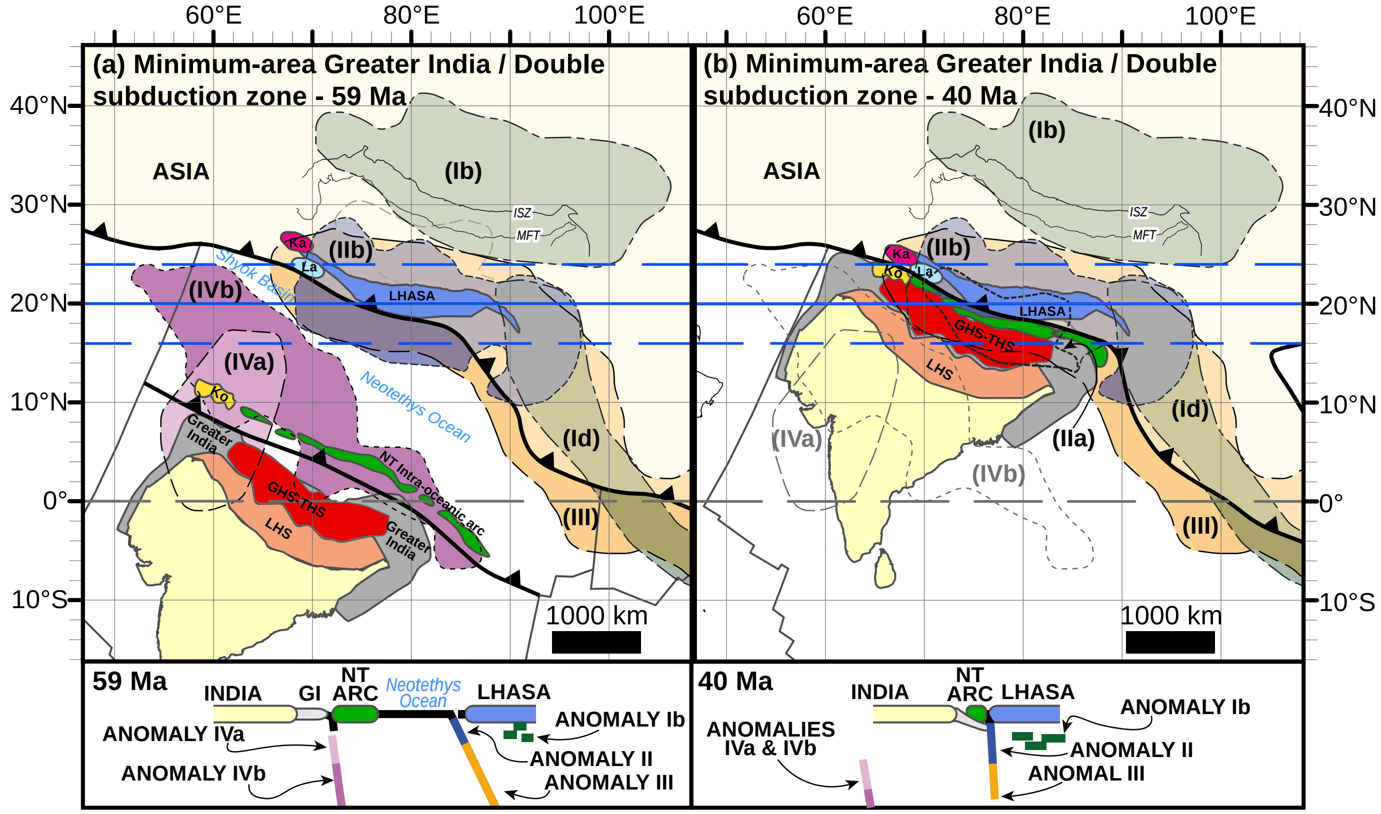

Figs. 23. Plate kinematic-based scenarios for the India-Asia collision based on integration of geological, geophysical and kinematic datasets. Position of India based on plate reconstruction model of (Müller et al., 2019). Thick blue lines mark paleolatitude of Lhasa block (solid lines) plus errors (dashed lines) at timing of collision. Size of Greater India imaged beneath present-day Tibetan plateau (dark grey shaded area), the undeformed Lesser Himalayan Sequence (LHS – orange shaded area) and the undeformed Greater Himalayan Sequence (GHS) and Tethyan Himalayan Sequence (THS) (red shaded area) are based on Fig. 21. Positions of seismically fast anomalies I to IV are based on Figs. 8–20. Present-day positions of the Main Frontal Thrust (MFT) and Indus Suture Zone (ISZ) marked by dark grey solid lines. Present-day coastline marked by thin light grey solid line. Abbreviations: Ka – Karakoram; Ko – Kohistan; La – Ladakh. (a-b) *Minimum-area Greater India reconstruction / double subduction zone configuration*: (a) Collision between India and the Neotethys (NT) intra-oceanic arc at 59 Ma. Kohistan block forms part of the intra-oceanic arc. Anomaly IV corresponds to Neotethys slab detached from Neotethys intra-oceanic arc following collision. (b) Collision between India and south-central Asian margin (Lhasa block) at 40 Ma. Anomalies II and III correspond to Neotethys slab detached from Gangdese arc on the Lhasa and Ladakh blocks. Collision between Kohistan and Karakoram blocks during closure of Shyok basin occurs at that time. (c-d) *Enlarged-area Greater India reconstruction / single subduction zone configuration*: (c) Collision between India and south Asian margin (Lhasa block) at 59 Ma. Anomalies II and III corresponds to Neotethys slab detached from Gangdese arc on the Lhasa, Ladakh and Kohistan blocks. Light grey shaded area marks size of Indian continental lithosphere that must be subducted completely. (d) Continued convergence and subduction of Indian continental lithosphere beneath Asia at 40 Ma. Anomaly II is dragged northwards during collision, which produces slab window in Anomaly Id (Figs. 8a, 9b, 9d, 9e, 10). Anomaly Ia and Ib correspond to subducted Indian continental lithosphere and delaminated Asian lithosphere. (e-f) *Greater India Basin reconstruction / single subduction zone configuration*: (e) Collision between the GHS-THS microcontinent block and south-central Asian margin (Lhasa block) at 59 Ma. GHS-THS block is separated from the rest of India by oceanic lithosphere of the Greater India Basin. Anomalies IIb and III correspond to Neotethys slab detached from Gangdese arc on the Lhasa, Ladakh and Kohistan blocks. (f) Collision of India with the GHS-THS block at 20 Ma. Anomaly IIa corresponds to subducted Greater India Basin oceanic lithosphere. Anomaly II is dragged northwards during collision, which produces slab window in Anomaly Id (Figs. 8a, 9b, 9d, 9e, 10). Anomaly Ia and Ib correspond to subducted Indian continental lithosphere and delaminated Asian lithosphere. Georeferenced overlays (.kml, .kmz) and shapefiles of all points, lines, and polygons presented in our map figures are available for use and editing with global information system software (e.g. Google Earth, GPlates, ArcGIS) in Supplementary Materials 01 and 02.

with global information system software (e.g. Google Earth, GPlates, ArcGIS) in Supplementary Materials 01 and 02.

6.2.1. Minimum-area Greater India reconstructions

Implementing the minimum-area reconstruction of Greater India (Fig. 5a) into a plate kinematic framework (Fig. 23a-b) at 59 Ma places the northern margin of Greater India at 0° N to 8° N, above Anomalies IVa and IVb, with ~2000 km of oceanic lithosphere between Greater India and the reconstructed Asian continental margin (Fig. 23a). This invokes a model of collision between India and an intra-oceanic arc located above Anomalies IVa and IVb at 59 Ma (Fig. 23a). Subduction of Neotethys oceanic lithosphere continued beneath the Asian continent until ~45–-30 Ma, when Greater India and Asia collided (*s.s.*) (Fig. 23b). This is consistent with the reduction in Indian plate velocity recorded at ~40 Ma (Fig. 3). The slab subducting beneath the Asian margin at that time is defined by Anomalies II and III (N2 slab – Fig. 22d, 23a-b). Assuming slab break-off occurred between ~45–30 Ma, this yields a whole-mantle average sinking rate of 10.0–18.3 mm/yr for the top of Anomaly II (Table 5).

6.2.1.1. Model strengths. (1) Models of the India-Asia collision (*s.l.*) with a minimum-area Greater India reconstruction and a double subduction zone configuration are consistent with bedrock evidence for more than one suture zone (i.e. closure of at least two oceans, separated by an intra-oceanic arc) within the ISZ (Table 6) (e.g. Mahéo et al., 2004; Mahéo et al., 2006; Guilmette et al., 2009; Guilmette et al., 2012; Hébert et al., 2012), and provides coherent explanations for all of the seismic anomalies except Anomaly IVa (see below). (2) This Greater India reconstruction is consistent with Indian crustal shortening estimates and the area of Indian lithosphere imaged beneath southern Tibet. It also produces a

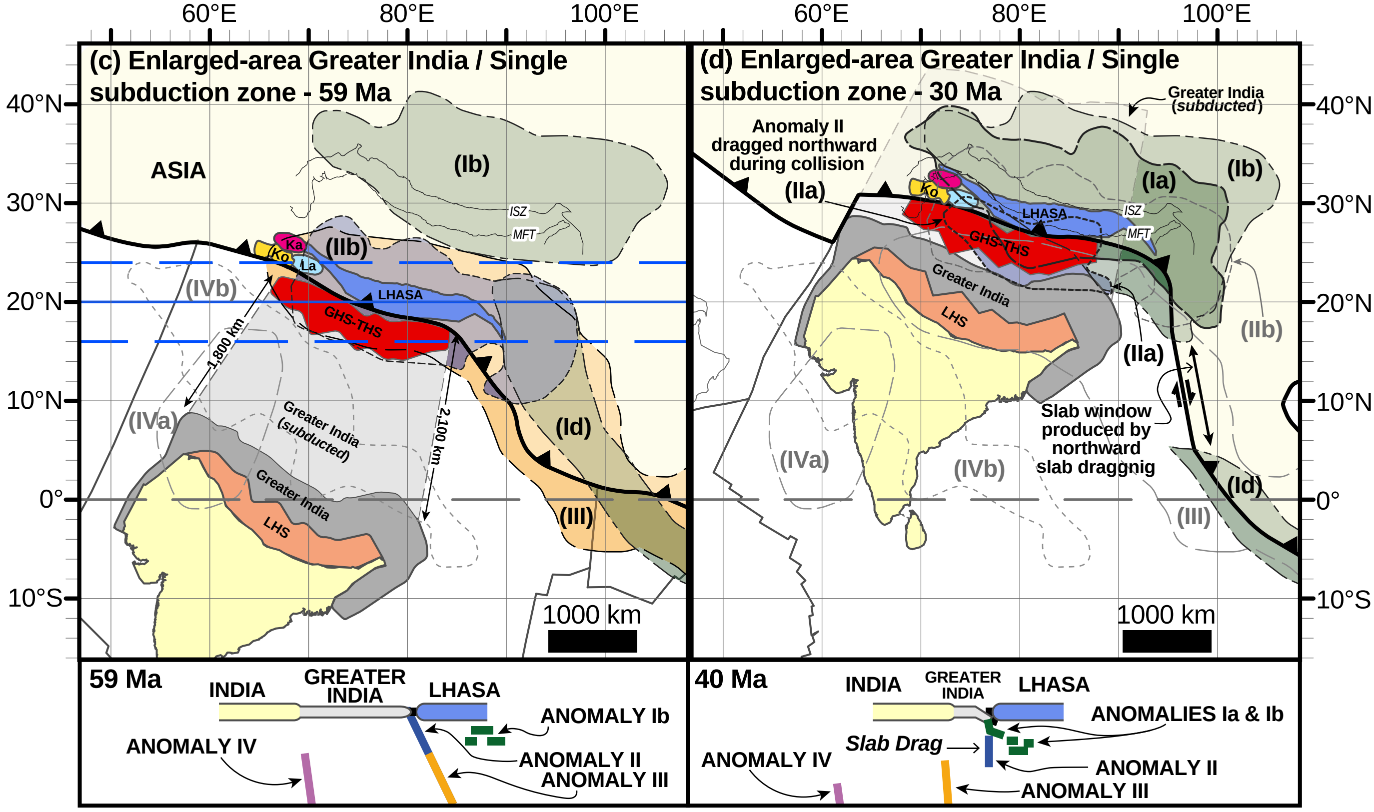

Figs. 23 (*continued*).

good fit with reconstructions of Gondwana, prior to rifting of India from Australia (Table 6). (3) Subequatorial restoration of the Neotethys intra-oceanic arc based on the location of Anomaly IV is consistent with palaeomagnetic analyses from Kohistan and Ladakh (e.g. Klootwijk et al., 1984, Zaman and Torii, 1999, Ahmad et al., 2000, Khan et al., 2009), and with the minimum-area restoration of Greater India (Figs. 21, 23a) (Table 6). (4) Soft arc-continent collision at 59 ± 1 Ma, followed by hard continent-continent collision at ~45–30 Ma is consistent with the restored location of the southern margin of Asia, decelerations in the India plate velocity (Fig. 3) and with temporal changes in the geochemical signatures of magmas emplaced into the Kohistan and Ladakh blocks (Table 6) (e.g. Bouilhol et al., 2013; Jagoutz et al., 2019).

6.2.1.2. Model weaknesses. (1) Models with a double subduction zone configuration, which assume that the northern subduction zone closed along the Shyok suture zone (e.g. Bouilhol et al., 2013; Burg and Bouilhol, 2019) are inconsistent with a wide array of bedrock data that supports collision between Kohistan and Karakoram at ~90–80 Ma (Fig. 3) (section 5.1.1) (Table 6). (2) With the exception of bedrock data from Kohistan and the West Pakistan ophiolites, there is no bedrock evidence for intra-oceanic arc magmatism recorded in the ISZ after ~116–80 Ma (Fig. 3) (Table 6). (3) This model lacks an explanation for Late Cretaceous sillimanite-grade metamorphism and associated orogenic deformation recorded by the Karakoram block (Table 6). (4) The presence of Lhasa-derived sediments in the Xigaze Group place the Xigaze forearc and underlying Xigaze ophiolite along the southern margin of Lhasa in the Early Paleocene. As such, the double subduction zone configuration must assume that deformation and uplift recorded by the Xigaze forearc between 58 and 51 Ma, occurred in response to long range stress-transfer from the South Neotethys intra-oceanic arc to the Gangdese arc at the onset of collision at 59 Ma (*s.l.*) (Table 6). (5) The lateral extent of Anomaly IVa is significantly less than required by this model, which must assume that the N1 slab is only partly imaged by the seismic tomography models (Table 6).

6.2.2. Enlarged-area Greater India reconstructions

Within our plate kinematic framework, the enlarged-area Greater India restoration has a pre-collisional northeast-southwest width of ~2500–3000 km (Fig. 23c), based on the locations of India and the southern Asian margin at 59 Ma. The area of Greater India preserved in the bedrock record has a pre-collisional northeast-southwest width of ≤900 km (Figs. 21, 23c); this implies that a slab of Greater India continental crust and lithospheric mantle ~2000 km by ~2500 km in area must have subducted into the mantle without subsequently returning to the bedrock record (Fig. 23c). A significant volume of the subducted Greater India lithosphere must, therefore, be represented by Anomalies Ia and Ib in the MTZ. This may be explained, either by a regular mode of subduction, or by underthrusting of Greater India beneath Tibet, followed by massive amounts of lithospheric delamination or dripping. Both explanations are consistent with the present-day subsurface structure of Indian continental lithosphere imaged beneath Tibet (section 5.6.3.; Fig. 21). Based on the absence of intra-oceanic arc magmatic rocks with ages younger than ~116–80 Ma, this model has no reason to invoke subequatorial intra-oceanic subduction of Neotethys oceanic lithosphere after 80 Ma.

6.2.2.1. Model strengths. (1) Models of the India-Asia collision (*s.l.*) with an enlarged-area Greater India reconstruction and a single subduction zone configuration, are the most consistent of all three models, with respect to timing constraints for intra-oceanic subduction and collision between India and Asia from the bedrock record (Table 6). (2) These models are consistent with the presence of Cretaceous Lhasa-derived sediments in the Xigaze forearc basin, and the uplift and abandonment this forearc between 58 and 51 Ma in response to collision between Greater India and Lhasa at ~59 Ma (Table 6). (3) This model provides coherent explanations for all of the seismic anomalies, with acceptable slab sinking rates and dynamics (Table 5).

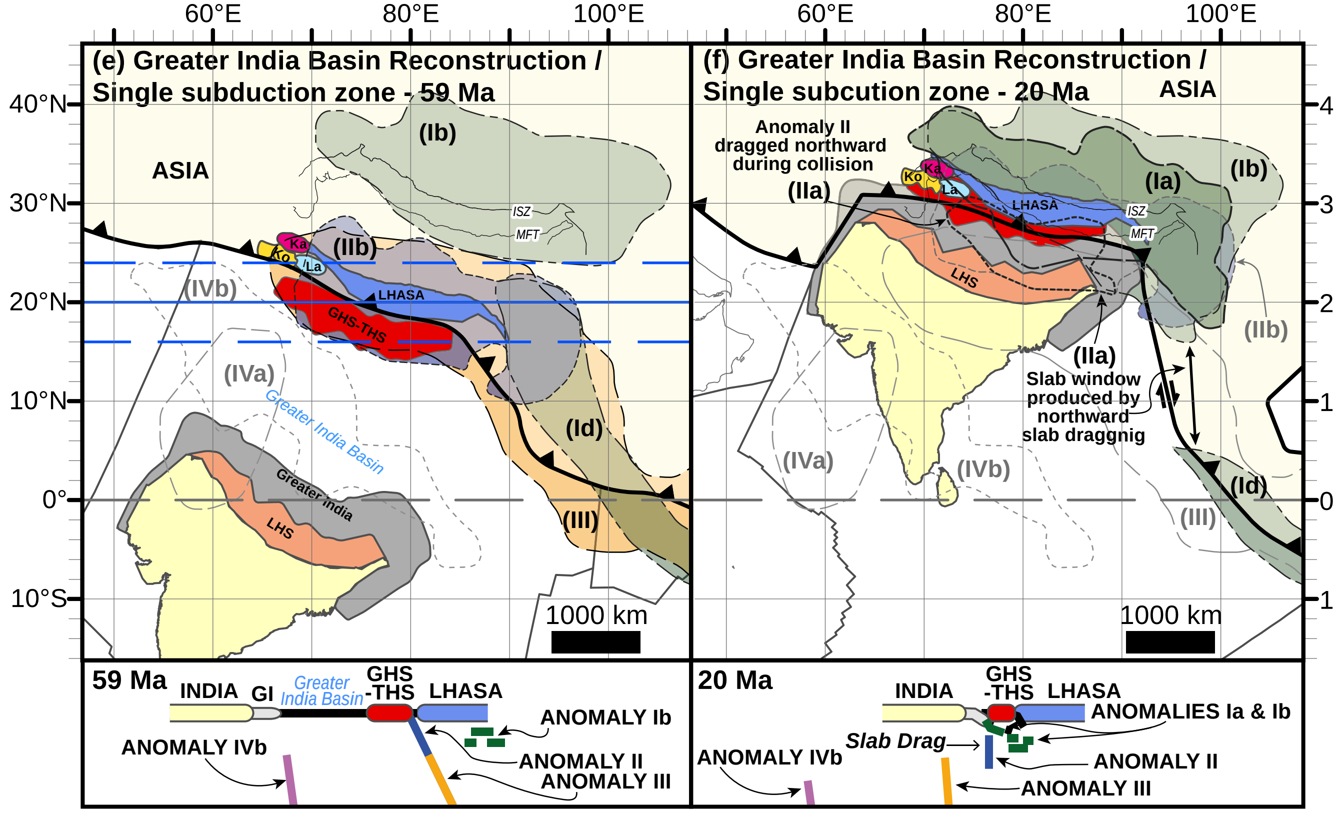

Figs. 23 (*continued*).

6.2.2.2. Model weaknesses. (1) The size of Greater India predicted by this model is significantly less than estimates from the bedrock record (Fig. 21, 23c), and from most paleomagnetic datasets (Table 6) (Huang et al., 2017a; Huang et al., 2017b). Recent work by Rowley (2019a) argues for the use of an alternative statistical method, which demonstrates that existing paleomagnetic data are consistent with the enlarged-area restoration, however, this method is currently disputed (Rowley, 2019b; van Hinsbergen, 2019). Furthermore, the reconstruction argued for by Rowley (2019a) produces a poor fit with the west Australian margin in reconstructions of Gondwana, prior to break-up (van Hinsbergen, 2019; van Hinsbergen et al., 2019). We suggest that this inconsistency may be reconciled if one invokes extension of Greater India, without ocean spreading after it rifted from Gondwana (Table 6) (2) This model requires complete subduction of a portion of continental lithosphere including its lower and middle crust and some if not all of its upper crust that was at least ~2000 km by ~2500 km in area (Figs. 21b-c, 23c); the feasibility of this remains disputed (Table 6), and is discussed further in section 6.2.2. (e.g. Rowley and Ingalls, 2017; van Hinsbergen et al., 2017).

6.2.3. Greater India Basin reconstructions

Van Hinsbergen et al. (2012), Van Hinsbergen et al. (2019)) developed the Greater India Basin hypothesis within a kinematic framework and our reconstruction is equivalent to their most recent model, but with the addition of interpretations for Anomalies Ib, IVb, and IVc. The Greater India Basin reconstruction may be applied to a single subduction zone configuration (Fig. 23e-f), in which the onset of the India-Asia collision (*s.l.*) at ~59 Ma is defined by collision between the GHS-THS microcontinent and the southern Asian continental margin. Applying the Greater India Basin reconstruction to models with a double subduction zone configuration produces a poor fit with the distribution of seismic anomalies, and requires unreasonably fast sinking rates.

Based on our synthesis of crustal shortening estimates and sub-surface imaging of Indian continental lithosphere (Fig. 21, Tables 3–4), our reconstruction assumes that the Greater India Basin has a northeast-southwest width of ~2000 km (Fig. 23e). The subducted Greater India Basin slab is assumed to be contiguous or near contiguous with the Neotethys slab subducted beneath the southern Asian margins, and is represented by some if not all of Anomaly II (Fig. 23f). Closure of the Greater India Basin during collision between the LHS margin of Greater India and the GHS-THS microcontinent occurred sometime between ~30–20 Ma; this yields an average sinking rate of 15.0–22.5 mm/yr for the top of Anomaly II, which is an acceptable rate for the upper mantle.

6.2.3.1. Model strengths. (1) The Greater India Basin reconstruction provides a coherent explanation for the India-Asia collision that is consistent with mantle tomography and plate kinematics, and does not require extreme magnitudes of continental subduction (Table 6) (e.g. van Hinsbergen et al., 2019). (2) This Greater India reconstruction is consistent with Indian crustal shortening estimates and the area of Indian lithosphere imaged beneath southern Tibet. It also produces a good fit with reconstructions of Gondwana, prior to rifting of India from Australia (Table 6). (3) These models are consistent with the presence of Cretaceous Lhasa-derived sediments in Xigaze forearc basin, and the uplift and abandonment of this forearc between 58 and 51 Ma in response to collision between THS units of Greater India and Lhasa at ~59 Ma (Table 6).

6.2.3.2. Model weaknesses. (1) This scenario implies that either subduction of the Greater India Basin was amagmatic, or that magmatism related to subduction of the Greater India Basin is recorded by Eocene-Oligocene adakitic assemblages in the Gangdese arc, located at least ~400–600 km inland of the south margin of the GHS-THS microcontinent (e.g. Searle et al., 2011; Guan et al., 2012; Ma et al., 2014a) (Table 6). (2) This hypothesis necessitates closure of the Greater India Basin between the GHS and LHS, which is presently defined by the MCT. The MCT forms a crustal scale shear zone that is traceable along the entire length of the Himalayan orogen (Fig. 3) and has been studied with field- and laboratory-based

Table 6
Model strengths and weaknesses from geological, geophysical, geodynamic, and plate kinematic perspectives.

Model	Geological perspective		Geophysical perspective		Geodynamic and plate kinematic perspectives		Further investigations & requirements for model validation
	Strengths	Weaknesses	Strengths	Weaknesses	Strengths	Weaknesses	
Enlarged-area Greater India reconstruction + single subduction zone configuration	Most consistent with timing constraints for inta-oceanic subduction and collision from the bedrock record out of all three models	The size of Greater India predicted by this model is significantly less than estimates from the bedrock record	Produced coherent explanation for all seismic anomalies	None	Produces acceptable sinking rate estimates for all slabs	Model require subduction of continental lithosphere (including its lower, middle ± upper crust) that was at least 2000 km × 2500 km in area	Mass balance of Himalaya-Tibet system and underlying upper mantle that accounts for relamination of Indian crust, delamination of Asian lithosphere and lateral flow of Asian continental crust
	Consistent with constraints from the Xigaze forearc, which argue for Thanetian to Ypresian collision between Greater India and Lhasa					Inconsistent with Mesozoic palaoemagnetic constraints from Greater India and reconstructions of Gondwana; requires continental extension of Greater India, withouth ocean spreading after break-up of Godwana	Composition, structure and thickness of pre-collisional Greater India Physics of subduction of continental lithosphere
Minimum-area Greater India reconstruction + double subduction zone configuration	ISZ contains bedrock evidence for more than one suture zone, supporting the existence of a Neotethys intra-oceanic arc, separate from the Gangdese arc	Inconsistent with bedrock evidence for closure and suturing of the Shyok Basin between Karakoram and Kohistan between 90 and 80 Ma	Produced coherent explanation for all seismic anomalies except Anomaly IVa	Anomaly IVa is smaller than required by this model; implies that this slab is only partly imaged by the tomography models	Produces acceptable sinking rate estimates for all slabs	Distribution of seismic anaomlies is inconsistent with two-stage double subduction configuration (e.g. Kapp and DeCelles, 2019)	Timing of collision between Kohistan and Karakoram blocks
	Explains variations in isotope geochemistry in igneous plutonic phases of the Kohistan arc	Ypresian uplift and abonandonment of Xigaze forearc located along the southern margin of Lhasa requires long-range stress transfer from South Neothethys intra-oceanic to Gangdese arc at that time			Consistent with equatorial paleo-latitudes estimated from paleomagnetic studies of the Kohistan block	Distribution of seismic anaomlies is inconsistent with northward migrating sub-equatorial subduction zone (e.g. Jagoutz et al., 2015)	Search for evidence of intra-oceanic arc magmatism between 110 and 80 Ma and 80–60 Ma
	The size of Greater India is supported by bedrock observations	Lack of intra-oceanic arc magmatic rocks with ages younger than 116–80 Ma			Produces a good fit with reconstructions of Gondwana, prior to rifting of India from Australia		Improved seismic tomographic imaging of central and southern Indian hemisphere mantle to improve geometric definition of subducted slabs, in particularl the lateral and vertical extents of Anomalies IVa and IVb
	The size of Greater India fits the location of the intra-oceanic subduction zone inferred from Anomaly IV	Does not provide an explanation for Late Cretaceous metamorphism and deformation recorded by the Karakoram block			Consistent with declaration of Indian plate between 50 Ma and 40 Ma due to later collision (s.s.) between Asian margin and India		
					Does not require extreme volume and duration of continental subduction		

(continued on next page)

Table 6 (*continued*)

Model	Geological perspective		Geophysical perspective		Geodynamic and plate kinematic perspectives		Further investigations & requirements for model validation
	Strengths	Weaknesses	Strengths	Weaknesses	Strengths	Weaknesses	
Greater india Basin reconstruction + single subduction zone configuration	Consistent with constraints from the Xigaze forearc, which argue for Thanetian to Ypresian collision between Greater India and Lhasa	The GHS and THS do not record any subduction-related magmatism during subduction of the Greater India Basin	Produced coherent explanation for all seismic anomalies	None	Produces a good fit with reconstructions of Gondwana, prior to rifting of India from Australia	Removal of the Greater Inida Basin suture and forearc stratigraphy requires prolonged subduction-erosion, which is inconsistent with the record of accretion recorded by metamorphism in the GHS since ~50 Ma	Mechanics of subduction-erosion and subduction-accretion in continental collisions and how these processes are recorded by the bedrock record
		Record of metamorphism in THS and GHS are best explained by progressive subduction-accretion, which is hard to reconcile with subduction-erosion of the Greater India Basin suture			Does not require extreme volume and duration of continental subduction		Invesitigation of subsurface lithosphereic structure of the Himalayan orogeny: is there evidence for a subducted forearc?
	The size of Greater India is supported by bedrock observations	No geological evidence for a suture between the GHS and LHS			Produces acceptable sinking rate estimates for all slabs		Irrefutable dismissal of other models

analyses for over 80 years (e.g. Larson et al., 2015; Martin, 2017a). There is no observable record of a suture zone existing between the GHS and LHS (e.g. Searle, 2019). Additionally, the thermal structure of the MCT, which emplaced high-grade metamorphic rocks over low-grade metamorphic rocks (e.g. Parsons et al., 2016b; Hunter et al., 2018), is contrary to the thermal structure of most, if not all other examples of suture zones that typically place low-grade metamorphic rocks over high-grade metamorphic rocks (e.g. Dewey, 1977; Parsons et al., 2018) (Table 6). Consequently, van Hinsbergen et al. (2019) proposed that the Greater India Basin suture and the Eocene-Oligocene Greater India Basin forearc and foreland basin were removed via subduction-erosion between ~50–30 Ma; this implies that the MCT thrusted the GHS over and beyond the Greater India Basin suture, which is inferred to presently reside in the subsurface beneath the Himalayan orogen or deeper in the upper mantle. Subduction-erosion along the Greater India Basin subduction zone requires out-of-sequence thrusting (e.g. Scholl and von Huene, 2007, 2010) within the GHS during the Eocene to Oligocene; however, this is hard to reconcile with metamorphic discontinuities within and between the THS, GHS and LHS that record near-continuous burial, underplating and accretion and of material via progressive in-sequence thrusting since ~56 Ma (see section 2.1) (Table 6).

6.3. Discussion: Summary of competing scenarios for the India-Asia collision and directions of future research

None of the available models (Fig. 23) provide an entirely satisfactory and coherent explanation for the India-Asia collision (*s.l.*) (Table 6). Studies that interpret their data in the context of, or in support of any one of the models presented above must be aware that in doing so, they implicitly accept some model assumptions that conflict with published datasets or with widely accepted geodynamic concepts.

Models with a minimum-area Greater India reconstruction and a double subduction zone configuration are hindered by disputed interpretations of the bedrock record of subduction, accretion and collision along the Indus and Shyok sutures (Table 6). The absence of post-80 Ma intra-oceanic arc magmatism east of Kohistan cannot be explained by subduction-erosion; this process only removes forearc material from the upper plate, as back-stepping of the subduction interface into the upper plate also results in back-stepping of the arc volcanic front (e.g. Isozaki et al., 2010; Scholl and von Huene, 2010). Additionally, these models predict that the top of the N1 slab is much larger than Anomaly IVa. Further investigations of this model should focus on, (1) an improved seismic tomographic resolution of the mantle beneath the central Indian Ocean to allow for more robust tests of the expected size, position and geometry of subducted slabs; (2) the disputed timing of collision between the Kohistan and Karakoram blocks and closure of the Shyok suture; (3) the cause of Late Cretaceous metamorphism and orogenic deformation recorded by the Karakoram block; and (4) the youngest occurrence of intra-oceanic arc magmatism recorded in the ISZ, east of the Kohistan and Ladakh blocks (Table 6). Validation of this last point would be aided by elucidation of the petrogenetic relationship between the Spontang ophiolite and overlying 'Spong arc' andesite, and robust evidence for, or against Late Cretaceous intra-oceanic magmatism along the Neotethys intra-oceanic arc.

Models with an enlarged-area Greater India reconstruction and a single subduction zone configuration fit the bedrock data but require an arguably unfeasible amount of continental subduction (Table 6). Validation of such models requires further investigation into the limits of continental subduction and confirmation that seismically fast material in the upper mantle and MTZ below the Tibetan plateau is Indian continental lithosphere (Table 6).

Models with a Greater India Basin reconstruction fit with most bedrock and mantle constraints, but require Late Cretaceous ocean spreading of the Greater India Basin between the GHS and LHS followed by the removal of all bedrock evidence for the Greater India Basin and its forearc and suture zone via subduction-erosion and out-of-sequence thrusting, on and below the ~2000 km long MCT (Table 6). Validation of this model would be aided by (1) geophysical observations of a buried or subducted Greater India Basin forearc or suture zone beneath the Himalayan orogen; and (2) a demonstration that the metamorphic record of the Himalayan orogen is consistent with subduction-erosion during subduction of Greater India Basin oceanic lithosphere between ~50 Ma and ~30–20 Ma.

6.4. Discussion: Cryptic suture zones & continental subduction

If the enlarged-area Greater India reconstruction is correct, then currently accepted rates of recycling of continental material into mantle, since the initiation of plate tectonics may be severely underestimated (e.g. Kawai et al., 2013). If the Greater India Basin reconstruction is correct, then this raises the possibility that many suture zones and closed oceans remain unidentified within the high-grade metamorphic belts of other collisional zones. We explore the validity of these geodynamic assumptions and their implications for our understanding of continental collision in more detail below.

6.4.1. A suture zone with no bedrock record?

The suggestion by van Hinsbergen et al. (2012, 2019) that a suture zone could form with no bedrock record of the former ocean to which it relates is not unrealistic. Whereas suture zones are commonly identified from the occurrence of accreted remnants of ophiolites and ocean plate stratigraphy scraped up from a subducting oceanic plate (e.g. Wahrhaftig, 1984; Kusky et al., 2013), these features need not always be present. Preservation of these oceanic lithologies requires accretion of lower-plate material to the upper plate during subduction, but not all subduction zones accrete material to the upper plate. A 'cryptic' suture zone may be formed if all oceanic crust and associated lithologies are removed from the bedrock record during subduction, for example via subduction-erosion (e.g. Burke et al., 1977; Dewey, 1977; Scholl and von Huene, 2007; Scholl and von Huene, 2010).

Approximately 75% of active subduction zones in the Pacific Ocean are currently in a mode of subduction-erosion, whereby upper plate material is accreted to the lower plate via out-of-sequence-thrusting (e.g. Scholl and von Huene, 2007; Scholl and von Huene, 2010; Stern, 2011). This can result in progressive removal of forearc and accretionary complexes from the bedrock record. Active examples include the Mariana-Izu-Bonin subduction system, the South American Cordillera, the Bismarck arc on Papua New Guinea and the Luzon arc on Taiwan (e.g. Abbott et al., 1994; Malavieille et al., 2002; McIntosh et al., 2005; Isozaki et al., 2010; Scholl and von Huene, 2010). In the case of the Luzon arc and Taiwan orogeny, the subducting South China Sea has dragged the Luzon forearc into the upper mantle beneath the Taiwan orogen, which has been identified via geophysical techniques (Malavieille et al., 2002; McIntosh et al., 2005; Camanni et al., 2016). Observations of such processes beg the question, 'what remnants of that subduction zone and suture zone will be preserved in bedrock record tens of millions of years from now?'

Ancient examples of suture zones characterized by subduction-erosion in the geological record include the Border Ranges Fault in Alaska (Clift et al., 2005), the Annieopsquotch Accretionary tract and Red Indian Line in Newfoundland (Zagorevski et al., 2007; Zagorevski et al., 2009), the Indus suture between the Kohistan arc and Indian continental crust (Burg, 2011), and parts of the Proterozoic Labrador trough and Cape Smith belt of the New Quebec and Ungava orogens (Burke et al., 1977). Large sections of these suture zones are devoid of remnants of the subducted oceanic lithosphere or forearc. They are identified from one or more of the following: (*1*) the presence of arc assemblages on one side of these structures signifying the former presence of a subduction zone, (*2*) the occurrence of oceanic lithologies located several hundred kilometres along strike of these structures, and/or (*3*) provenance-related arguments that indicate that rocks on either side of the suture are exotic with respect to each other. The examples outlined above demonstrate that in the absence of lithological evidence for a sutured subduction zone, suture zone identification should follow similar lines to the terrane hypothesis (Coney et al., 1980), whereby a suture zone is supported if it can be demonstrated that the structure in question separates two crustal blocks with different geological histories that invoke their separation via an ocean (e.g. Burke et al., 1977; Dewey, 1977; Coney et al., 1980).

With respect to the Greater India Basin hypothesis, the THS and GHS appear to fit the definition of a 'suspect terrane' (Coney et al., 1980; Martin, 2017b), which is consistent with the suggestion that the MCT represents the palaeo-plate boundary between the GHS and LHS. However, the situation implied by the Greater India Basin hypothesis is still unique; all of the above examples of active or ancient subduction-erosion correspond either to on-going subduction of ocean lithosphere or to collision of a continental block with an intra-oceanic arc. Neither of these situations are comparable to the tectonic setting of the Greater India Basin hypothesis for the India-Asia collision, in which a continental block collides with a continental arc. Furthermore, whilst the cases above demonstrate that it is possible to close parts of an ocean without preserving oceanic lithologies in the bedrock record, these examples still preserve some evidence of a former subduction zone, either in the presence of suprasubduction zone arc assemblages in the upper plate (e.g. Clift et al., 2005; Zagorevski et al., 2009; Burg, 2011), or by the presence of ophiolitic fragments and ocean plate stratigraphy identified hundreds of kilometres away from, but along strike of the suspected suture zone (e.g. Burke et al., 1977; Dewey, 1977). Interpretation of the MCT as a former suture zone is exceptional given that no suprasubduction zone arc assemblages, ophiolite fragments and ocean plate stratigraphy are reported along its entire length of over 2000 km.

Lastly, we note that the metamorphic history and thermal structure of the footwall and hanging wall of the MCT is atypical for that of a suture zone. This model implies that the Greater India Basin subduction zone must have been located to the south of the present-day GHS, which was able to thicken and heat up via in-sequence thrusting and accretion at mid-crustal depths, contemporaneous with subduction-erosion of Greater India Basin ocean plate stratigraphy and forearc assemblages via out-of-sequence thrusting (see section 2.1). Whilst such a system is conceivable (e.g. Gilotti et al., 2017), an explanation for the switching back and forth of the active subduction interface from out-of-sequence to in-sequence thrusting has not been proposed and there are no other past or present examples where these processes have been confidently identified.

The Greater India Basin hypothesis requires a complicated and perhaps exceptional set of circumstances to explain closure of the Greater India Basin and formation of its suture zone along the MCT. Despite these circumstances, the suggestion that subduction-erosion has removed the entire bedrock record of the Greater India Basin from the MCT remains permissible because in the current situation, the absence of evidence is indistinguishable from the evidence of absence. Further validation of this model may be sought from two perspectives: (1) This hypothesis may be tested via geophysical techniques to search for the subducted remnants of the Greater India forearc and foreland basin in the lithosphere and/or upper mantle beneath the Himalaya-Tibet orogenic system. Seismic velocity and gravity models for the Taiwan orogen suggest that it is possible to identify a subducted forearc via geophysical techniques (e.g. Malavieille et al., 2002; McIntosh et al., 2005; Camanni et al., 2016). To date, geophysical studies of the Himalayan orogen have not directly targeted this hypothesis. (2) Advancement of our understanding of the controls of subduction-erosion versus subduction-accretion, in-sequence versus out-of-sequence thrusting, and shear zone nucleation and abandonment would clarify whether the metamorphic record of the Himalayan orogen is consistent with subduction-erosion during closure of the Greater India Basin. Continued focus on these problems by on-going and future studies of the MCT and the record of crustal accretion and underplating within the Himalayan orogeny (e.g. Larson et al., 2015; Carosi et al., 2018; Goscombe et al., 2018; Waters, 2019) will improve our understanding of such processes and provide a robust test of the Greater India Basin hypothesis.

6.4.2. Wholesale subduction of continental crust and lithosphere?

Based on the uncertainty surrounding the Greater India Basin hypothesis and the difficulties associated with testing it, we consider whether the India–Asia collision can be better explained with the enlarged-area Greater India reconstruction, in which a portion of continental lithosphere (including its continental crust) ~2000 km by ~2500 km in area is subducted into the upper mantle and MTZ. If this model cannot viably explain the India–Asia collision, then that would offer a robust argument in favour of either the minimum-area Greater India reconstruction (i.e. a double subduction zone configuration at ~59 Ma) or the Greater India Basin reconstruction.

Diagnostic UHP minerals, such as coesite and diamond, preserved in exhumed continental terranes demonstrate that continental crust can experience minimum pressures of ~3–4 GPa during subduction (e.g. Chopin, 2003, Dobrzhinetskaya et al., 2011, Bidgood et al., 2019a, 2019b). Some studies have even reported evidence of coesite-to-stishovite transformation in metamorphosed continental crust (Liu et al., 2007; Liu et al., 2018); this is indicative of a minimum pressure of ~8.5–9 GPa, and requires subduction to at least ~250–300 km mantle depth, assuming a lithostatic pressure-to-depth conversion. Such examples also demonstrate that subducted continental crust may return to crustal depths (e.g. Ernst, 1999; Afonso and Zlotnik, 2011). Thermomechanical geodynamic modelling typically shows that the upper and middle continental crust is too buoyant to subduct (e.g. Agard et al., 2009; Capitanio et al., 2010); however, the properties of the modelled crust (e.g. volume, composition and strength) place some control over this (e.g. Palin et al., 2017). In contrast, sub-continental lithospheric mantle is negatively buoyant with respect to the asthenospheric mantle, as is mafic lower crust once it has undergone transformation to eclogite (e.g. Capitanio et al., 2010; Afonso and Zlotnik, 2011).

If continental crust is strongly coupled to its lithospheric mantle, the positive buoyancy of the upper and middle crust can stall subduction without forcing it to split from its underlying lower crust and mantle lithosphere (Afonso and Zlotnik, 2011). This typically results in detachment of the entire subducting oceanic lithosphere (i.e. slab break-off) and exhumation of the subducting continental lithosphere, as has been suggested for present-day subducted Indian lithosphere beneath the Hindu Kush region (Kufner et al., 2016). If the mechanical coupling between the upper, middle and lower continental crust and its lithospheric mantle is weak, the buoyant middle and upper crust is likely to split from the lower crust; this will allow the negative buoyancy of the lower crust and continental lithospheric mantle to sustain and even drive continental subduction and convergence after the initiation of continental collision (e.g. Capitanio et al., 2010, Afonso and Zlotnik, 2011). For example, shortening estimates from Australian upper crust in Timor suggests that it accreted and deformed during on-going subduction of 215–229 km (transport-parallel length) of its sub-continental lithospheric mantle beneath the Banda arc (Tate et al., 2015). This is consistent with geochemical signatures of lower crustal eclogite xenoliths reported from mid-ocean ridge and island arc basalts (Workman et al., 2004; Hanan et al., 2013). Likewise, in the western Pacific region, localized splitting of the 660 km discontinuity has been attributed to the transformation of jadeite to stishovite and calcium ferrite-type $NaAlSiO_4$ at ~22–23 GPa in continental crust trapped in the MTZ (Kawai and Tsuchiya, 2012; Kawai et al., 2013). Beneath the Tibetan plateau, thickening of the MTZ beneath Lhasa and Qiangtang has also been attributed to the presence of subducted and/or delaminated lithospheric mantle (Duan et al., 2017).

Thermodynamic modelling of pressure-dependent phase changes suggests that transformation of felsic crust to stishovite, K-hollandite (K-Al-silicate) and a Ca-Al-silicate phase (CAS) at ~7.7–9 GPa results in a net negative buoyancy with respect to the surrounding mantle. This pressure range is equivalent to ~250–300 km depth, assuming a lithostatic pressure-to-depth conversion. These silicate phases remain denser than the surrounding mantle down to the base of the MTZ where they become trapped due to the formation of denser Mg-perovskite and magnesiowustite in the underlying lower mantle (Afonso and Zlotnik, 2011; Kawai et al., 2013). Fig. 24 displays phase diagrams for average compositions of continental upper, middle and lower crust with variable volumes of mafic components (Rudnick and Gao, 2014; Hacker et al., 2015) at upper mantle pressures and temperatures. Each plot is colour-contoured to show relative density differences with respect to pyrolitic mantle (absolute densities are displayed in Supplementary Materials 08). Continental lower crust and the most mafic end-members of the middle crust (Figs. 24c-f) are dense enough to sink through the upper mantle at all pressures. Importantly, the continental upper crust and regular (less mafic) middle crust are dense enough to remain in the upper mantle, once they enter the stishovite stability field at ~7.7–9 GPa (Fig. 24a-b). This density increase is even greater within the hollandite stability field. As such, the stishovite-in and hollandite-in reaction curves represent an effective 'depth of no return' for middle and upper continental crust, as long any shallower portions of the slab do not pull it back to the surface (Afonso and Zlotnik, 2011; Kawai and Tsuchiya, 2013; Kawai et al., 2013).

Based on our density calculations (Fig. 24) and the current state-of-knowledge of continental subduction as outlined above, subduction of a large volume of Greater India continental lithosphere is plausible, as long as (1) the continental crust was thin enough and compositionally dense enough so as not to stall subduction and promote slab break-off or delamination; and (2) the mechanical coupling between the crust and lithospheric mantle was strong enough to resist detachment whilst it was at pressures of <7.7–9 GPa.

The crustal record of Greater India is at least consistent with this requirement: Greater India represents the northern passive margin of the Indian continental lithosphere and was subjected to rifting and associated intra-plate magmatism during the Permian, Triassic, and Early Cretaceous. Additionally, the high plate velocity of the Indian continent at the timing of collision (Fig. 3) would have promoted deep subduction of continental lithosphere, as the detachment of middle and upper continental crust during subduction is a time-dependent process (Afonso and Zlotnik, 2011). A potential modern analogue for the Greater India margin may be represented by the stretched and thinned continent crust of Zealandia, spanning >1000 km between mainland New Zealand and New Caledonian with a crustal thickness of ~10–20 km for much of its area (e.g. Segev et al., 2012; Laske et al., 2013). An upper-crustal thickness estimate of ~10 km for the THS in the Annapurna region (e.g. Godin, 2003) is at least comparable to Zealandia, although this would require Greater India to have had a relatively thin middle and lower crust (e.g. Guillot et al., 2008).

To summarize, the enlarged-area Greater India reconstruction requires wholesale subduction of a ~2000 km by ~2500 km area of continental lithosphere, including its lower and middle crust, and some if not all of its upper crust. Based on our current understanding (Fig. 24), this is entirely plausible, but requires specific circumstances relating to the composition and rheology of Greater India and the dynamics of the Indian plate, which are largely unconstrained and/or untested. Validation of this hypothesis would be aided by the following: (1) Improved understanding of the rheology, composition and thickness of Greater India lithosphere margin with respect to models of slab break-off and crustal delamination during subduction; and (2) Determination of the lithological properties of seismically fast material in the MTZ beneath Tibet, and an improved ability to geophysically discriminate between subducted continental and oceanic crust and lithospheric mantle (e.g. Kawai et al., 2013). The possibility that some or all of the missing Greater India middle and upper crust detached from its subducting lithospheric mantle and relaminated to the base of the Tibetan plateau (e.g. Hacker and Gerya, 2013) should also be investigated as a viable means to explain the India-Asia collision with an enlarged-area reconstruction of Greater India.

7. Summary and conclusions

With the recent development of user-friendly software for plate reconstruction modelling (GPlates, Müller et al., 2018) and graphical display of seismic tomography models (SubMachine, Hosseini et al., 2018), the integration of geological, geophysical and plate kinematic datasets should become standard, state-of-the-art procedure for the development of tectonic

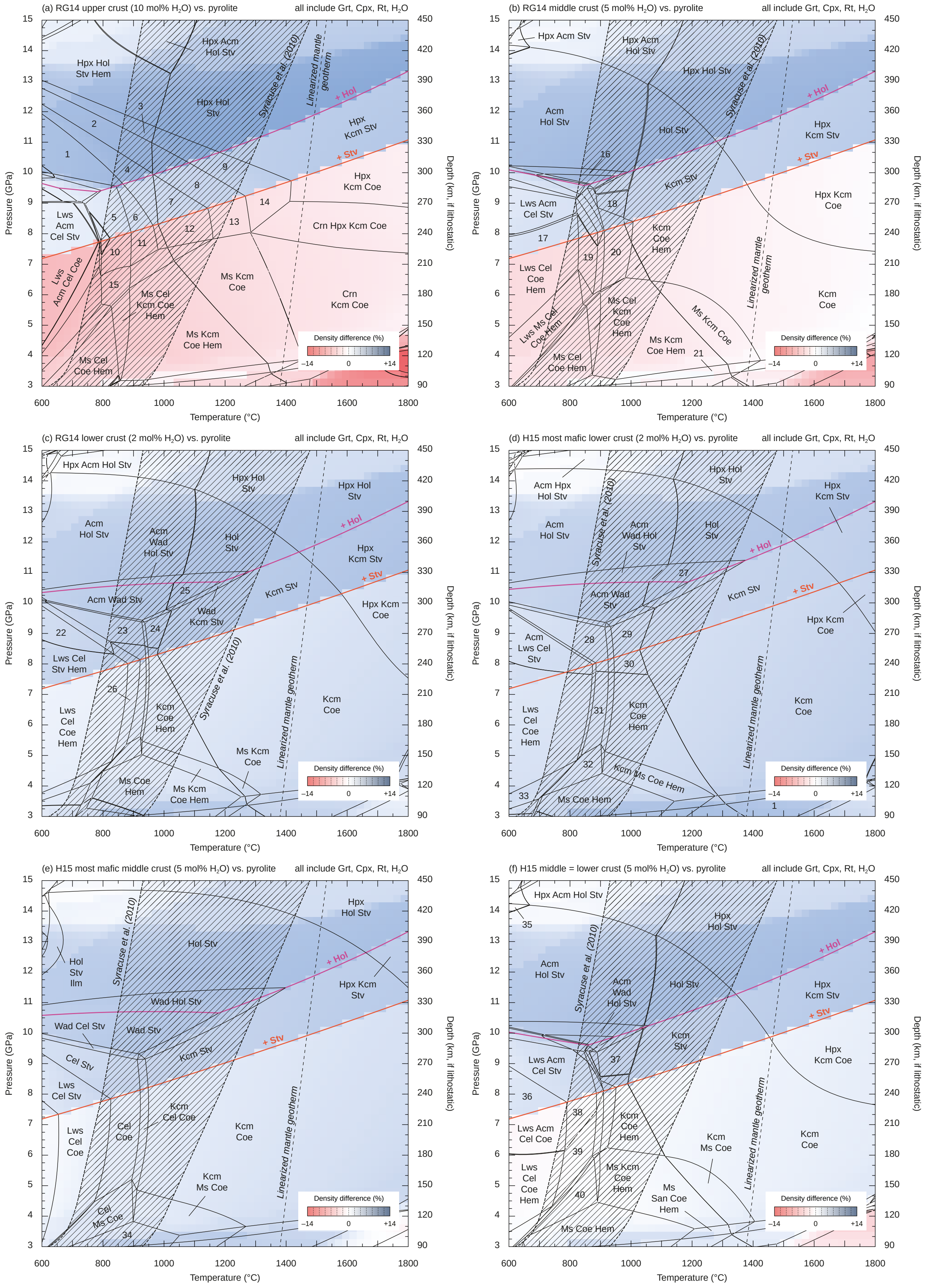

(caption on next page)

Fig. 24. Calculated pressure–temperature (*P–T*) pseudosections showing phase assemblages that would stabilize in average compositions of continental crust at upper mantle conditions (3–15 GPa), colour-contoured for relative density difference ($\Delta\rho$) with respect to pyrolytic mantle. Equivalent plots contoured for absolute density are displayed in Supplementary Materials 08. Note that in addition to the labelled phases listed in each stability field, all stability fields include garnet (Grt), clinopyroxene (Cpx), rutile (Rt) and water (H_2O). Percentage density difference at any given *P–T* point is calculated as follows: $100 \times [(\rho C - \rho M)/\rho M)]$, where ρC = density of the crustal component and ρM = density of mantle pyrolite. Stippled region marks the range of slab-top geotherms in modern-day subduction zones, as determined by Syracuse et al. (2010). Upper and lower limits of this envelope are projected linearly at $P > 8$ GPa, which lies outside of the limits considered in that study. Linearized mantle geotherm is from Holland et al. (2013) and represents the maximum temperatures that subducted material could reach at any given pressure, assuming heating of slab components by conduction only. (a) Rudnick and Gao (2014) upper crust composition (10 mol% H_2O); (b) Rudnick and Gao (2014) middle crust composition (5 mol% H_2O); (c) Rudnick and Gao (2014) lower crust composition (2 mol% H_2O); (d) Hacker et al. (2015) 'most mafic lower crust' (2 mol% H_2O); (e) Hacker et al. (2015) 'most mafic middle crust' (5 mol% H_2O); (f) Hacker et al. (2015) 'middle = lower crust' (i.e. a continental crust comprising only upper and lower compositions) (5 mol% H_2O). Phase abbreviations are as follows: Acm – acmite; Cpv – Ca-perovskite; Cel – celadonite; Coe – coesite; Cpx – clinopyroxene (diopside/omphacite/jadeite); Crn – corundum; Grt – garnet; H2O – water; Hem – hematite; Hol – hollandite; Hpx – high-pressure orthopyroxene; Ilm – ilmenite; Kcm – K-cymrite; Lws – lawsonite; Mpv – Mg-perovskite; Ms. – muscovite (phengite); Npv – Na-perovskite; Rt – rutile; San – sanidine; Stv – stishovite; Tpz – hydro-topaz; Wad – wadsleyite. Numbered fields contain the following assemblages (all including Grt, Cpx, Rt, and H_2O): 1 – Lws Hol Stv Hem; 2 – Hol Stv Hem Tpz; 3 – Hpx Hol Stv Hem Tpz; 4 – Lws Hol Stv Hem Tpz; 5 – Hpx Mpv Napv Kcm Stv; 6 – Hpx Napv Kcm Stv; 7 – Hpx Mpv Kcm Stv Tpz; 8 – Hpx Napv Kcm Stv Tpz; 9 – Hpx Kcm Stv Tpz; 10 – Hpx Mpv Napv Kcm Coe; 11 – Hpx Napv Kcm Coe; 12 – Hpx Mpv Kcm Coe Tpz; 13 – Hpx Napv Kcm Coe Tpz; 14 – Hpx Kcm Coe Tpz; 15 – Lws Ms. Cel Kcm Coe Hem; 16 – Acm Wad Hol Stv; 17 – Lws Cel Stv Hem; 18 – Kcm Stv Hem; 19 – Lws Coe Hem; 20 – Kcm Coe Hem Ms.; 21 – Ms. Kcm San Coe Hem; 22 – Cpv Hpx Npv Kcm Stv; 23 – Hpx Npv Kcm Stv; 24 – Hpx Kcm Stv Hem; 25 – Acm Wad Kcm Stv; 26 – Cpv Lws Cel Coe Hem; 27 – Wad Hol Stv; 28 – Cpv Hpx Npv Kcm Stv; 29 – Acm Kcm Stv; 30 – Acm Kcm Coe; 31 – Lws Kcm Cel Coe Hem; 32 – Lws Ms. Kcm Cel Coe Hem; 33 – Lws Ms. Cel Coe Hem; 34 – Cel Kcm Ms. Coe; 35 – Acm Stv; 36 – Lws Acm Cel Stv ($-H_2O$); 37 – Acm Kcm Stv; 38 – Lws Acm Cel Coe; 39 – Lws Cel Coe Hem; 40 – Ms. Cel Coe Hem.

---

models of regional geological events. This process enables the development of a tectonic model within a plate kinematic framework by which, we mean a tectonic model that considers constraints from the bedrock and mantle record in the context of past and present motions and distributions of tectonic plates. We have applied this approach to test the validity of competing subduction zone configurations and Greater India restorations, for models of the India-Asia collision (*s.l.*) and the post-Triassic evolution of the central Tethys oceans.

By integrating seismic tomography of subducted lithosphere in the deep mantle with the bedrock record of subduction and accretion from the Tibetan plateau, we have tested five previously proposed subduction zone configurations for the post-Triassic evolution of the central Tethys oceans. Our analysis concludes that seismically fast anomalies beneath the Indian hemisphere correspond to: (1) Bangong-Tethys oceanic lithosphere (our Anomaly V) subducted from one of two subduction zones on the north and south respective margins of the Lhasa and Qiangtang blocks; (2) Neotethys oceanic lithosphere subducted from two or three subduction zones, one located along the southern Lhasa block and one or two located at intra-oceanic settings between Lhasa and Greater India (our Anomalies II, III, and IV); (3) Subducted Indian continental lithosphere and/or delaminated Indian and/or Asian continental lithosphere in the upper mantle and mantle transition zone (MTZ) beneath the Tibetan plateau (our Anomaly I).

Our observations and interpretations are inconsistent with models, which assume that the entire central Neotethys Ocean was consumed by a single subduction zone along the southern margin of Lhasa (e.g. Gansser, 1966; Hu et al., 2016a). This implies that the Indus Suture Zone contains the sutures of at least two Neotethys subduction zones. The geometries of the seismic anomalies are also inconsistent with, (1) double subduction zone configurations which require northward migration of the southern Neotethys subduction zone during the Late Cretaceous to Eocene (Jagoutz et al., 2015); and (2) two-stage double subduction zone configurations in which the northern Neotethys subduction zone migrated southwards and collided with Greater India, which was followed by initiation of a second subduction zone along southern Lhasa (e.g. Hafkenscheid et al., 2006; Kapp and DeCelles, 2019). Instead, our constraints are compatible with our proposed scenarios A, B-1, and B-2, in which the southern subduction zone is fixed at subequatorial latitudes in the Cretaceous. Variations between these scenarios relate to differences in slab migrations, subduction initiation and slab break-off events, which occur prior to ~80 Ma. After ~80 Ma and leading up to the India-Asia collision at ~59 Ma, Scenarios A, B-1, and B-2 have comparable subduction zone configurations. These scenarios yield whole-mantle average sinking rates of ~8–18 mm/yr. Scenario A provides the most consistent explanation for both bedrock and mantle observations.

Our three viable subduction zone scenarios constrain two possible subduction zone configurations for the onset of the India-Asia collision (*s.l.*) at ~59 Ma. The *single subduction zone configuration* assumes one subduction zone active along the southern margin of Lhasa at ~59 Ma. The *double subduction zone configuration* assumes one subduction zone along the southern margin Lhasa, and a second, stationary or southward migrating, intra-oceanic subduction zone at a subequatorial latitude at ~59 Ma. Based on our synthesis of bedrock observations, justification for the double subduction zone configuration is entirely based on which palaeogeographic reconstruction of Greater India is favoured.

At the onset of the India-Asia collision at ~59 Ma, northern India was located at the equator, whilst the southern Asian contiental margin resided at 20° N ± 4°, along the southern edge of the Lhasa block. These constraints, combined with our assessment of viable subduction zone scenarios, allow for three distinct reconstructions of Greater India, each of which yields a distinct tectonic model for the India-Asia collision (*s.l.*).

The 'minimum-area' restoration of Greater India invokes a double subduction zone configuration in which India collides with a south Neotethys intra-oceanic arc at ~59 Ma, before colliding with Asia, at ~45–30 Ma. This model produces a good spatial fit between Greater India and seismic Anomaly IV at 59 Ma, and provides explanations for variations in the Indian plate velocity and pluton isotope geochemistry on the Kohistan and Ladakh blocks. However, it is inconsistent with (1) bedrock evidence for collision between Kohistan and Karakoram by 80 Ma; (2) the lack of direct observations of post-80 Ma intra-oceanic magmatism east of Kohistan; and (3) sedimentary and geochronological constraints from the Xigaze forearc and from the ISZ south of Ladakh. This model also predicts that the south Neotethys intra-oceanic slab is much larger than its seismic anomaly indicates (Anomaly IV). Nevertheless, this model cannot be ruled out because the uncertainties surrounding the interpretation of the bedrock record of subduction and accretion in the ISZ and the Kohistan, Karakoram and Ladakh blocks are still large.

The 'enlarged-area' restoration of Greater India assumes that Greater India had a pre-collisional north-south width (present-day coordinates) of ~2500–3000 km, and requires wholesale subduction of a ~2000 km by ~2500 km area of Greater India lithosphere, which includes its lower and middle crust and some if not all of its upper crust. Current understanding of continental subduction, combined with our own density calculations for subducted continental crust at upper mantle conditions, demonstrates that this extreme magnitude of continental subduction is at least plausible, but requires the composition, strength and rheology of the Greater India continental lithosphere to satisfy a specific set of geological criteria (e.g. thin middle and upper continental crust; strong coupling between lower, middle and upper crust and lithospheric mantle; more mafic composition of upper and middle crust), which remain largely unconstrained and untested. Importantly, this model implies that global rates and volumes of continental subduction since the initiation of plate tectonics may be severely underestimated. There is also on-going dispute over how well this restoration of Greater India fits with reconstructions of Gondwana, which are more consistent with the other two Greater India reconstructions.

The 'Greater India Basin' reconstruction was designed in a kinematic framework and is therefore consistent with all kinematic and mantle constraints and most if not all bedrock constraints. This model assumes that the boundary between the GHS and LHS, defined by the Main Central thrust (MCT), represents the palaeo-plate boundary along which the Greater India Basin closed. However, there is no bedrock evidence for a suture zone or Eocene-Oligocene forearc and foreland basin strata reported anywhere along this structure. Consequently, this model invokes substantial subduction-erosion which thrusted the Greater India Basin foreland and forearc basins, beneath, and hinterland-ward of the GHS. When compared to other examples of subduction-erosion, the complete absence of bedrock evidence for a suture zone between the GHS and LHS is unprecedented, but not implausible. However, it is hard to reconcile with the metamorphic record of the THS, GHS, and LHS, which records near-continuous accretion and underplating since ~56 Ma, which must have occurred contemporaneously with, and up-section of subduction-erosion of the Greater India Basin forearc and foreland basin. This model implies that the geological signatures of suture zones are not fully understood, and that other cryptic suture zones and closed oceans may remain unidentified within the high-grade metamorphic belts of other collisional zones.

Our review and analysis demonstrates that none of the current models for the India-Asia collision (*s.l.*), are entirely satisfactory. Resolution of this on-going debate requires further investigation of the following: (1) the timing of collision between the Karakoram and Kohistan blocks and closure of the Shyok suture; (2) the cause of Late Cretaceous metamorphism recorded by the Karakoram and Lhasa blocks; (3) structural, petrogenetic, and palaeogeographic links between the Kohistan block, the Dras-Nindam forearc, the Ladakh batholith, and the Lhasa block; (4) evidence for or against post-80 Ma intra-oceanic magmatism in the Indus suture zone, east of Kohistan; (5) the record of accretion and underplating recorded by the THS, GHS, LHS and MCT, and its compatibility with models of subduction-erosion of the Greater India Basin forearc; (6) the pre-collisional restoration of Greater India prior to break-up of Gondwana, and its fit with western Australia and the surrounding continental blocks; (7) the composition, structure and rheology of Greater India crust and lithosphere and their mechanical limits of continental subduction; (8) new seismic tomography models of the Indian hemisphere with improved resolution beneath the Indian Ocean, to advance our understanding of mantle structure beneath this region and provide a better test of competing subduction zone configurations of the central Tethys oceans; (9) geophysical tests of the hypothesis that the Greater India Basin forearc was subducted beneath the Himalaya-Tibet orogenic system; and (10) the lithological properties of seismically fast material within the mantle transition zone beneath Tibet, and a means to distinguish between subducted oceanic and continental lithosphere.

Additional references cited in supplementary materials

Abrajevitch et al., 2005
Allemann, 1979
Anczkiewicz et al., 2000
Bailey, 2014
Baxter et al., 2011
Booth et al., 2004
Bouilhol et al., 2011
Burg et al., 1998
Casnedi et al., 1978
Chan et al., 2007a
Chan et al., 2007b
Chen et al., 2006
Chu et al., 2006
Chung et al., 2009
Chung et al., 2005
Coulon et al., 1986
Dai et al., 2011
Debon, 1995
Debon et al., 1986
DeCelles et al., 2007
Deschamps and Lallemand, 2003
Ding and Lai, 2003
Dong et al., 2006
Ducea et al., 2003
Foster et al., 2002
Foster et al., 2004
Fraser et al., 2001
Garzanti et al., 2018
Geng et al., 2006
Gnos et al., 2001
Gnos et al., 1998
GSC Geological Survey of China & CIGMR Chengdu, 2004
Guynn et al., 2006
Hacker et al., 2000
He et al., 2007
Hu et al., 2004
Huang et al., 2015c
Jagoutz et al., 2009
Jain and Singh, 2008
Kakar et al., 2014
Kang et al., 2009
Kapp et al., 2003
Khan et al., 1996
Khan et al., 2007
Le Fort et al., 1983
Lee et al., 2012
Lee et al., 2009
Leier et al., 2007
Li et al., 2008
Liang et al., 2004
Mahar et al., 2014
Mahar et al., 2016
Maluski and Matte, 1984
Marcoux et al., 1987
McDermid et al., 2002
Miller et al., 2000
Parrish and Tirrul, 1989
Pearce, 2008
Petterson, 2010
Petterson and Windley, 1985
Pudsey, 1985
Pudsey, 2009
Rehman et al., 2011
Resing et al., 2011
Rex et al., 1988
Reynolds et al., 1983
Robertson, 2000
Robinson et al., 2004
Sarwar, 1992
Schaltegger et al., 2002
Schärer et al., 1990
Schwab et al., 2004
Searle and Treloar, 2010
Searle et al., 1990b
Searle et al., 2011a
Sen et al., 2018

Sharma et al., 1978
Shi, 2007
Singh et al., 2007
St-Onge et al., 2010
Streule et al., 2009
Thanh et al., 2010
Thanh et al., 2012
Treloar and Izatt, 1993
Treloar et al., 1989
Volkmer et al., 2007
Wang et al., 2008
Wang et al., 1987
Wang et al., 2000
Wang et al., 2006
Wartho et al., 2009
Wei et al., 2006
Wen et al., 2008
Wilson, 1989
Woelki et al., 2018
Wu et al., 2010
Xia et al., 2011
Xia et al., 2008
Xiang et al., 2005
Xie et al., 2002a
Xie et al., 2002b
Xiong et al., 2011
Xu et al., 1985
Yin and Grant-Mackie, 2005
Yamamoto and Nakamura, 2000
Yang et al., 2004
Zagorevski and van Staal, 2015
Zaman et al., 2013
Zeitler, 1985
Zhang et al., 2007a
Zhang et al., 2007b
Zhang, 2000
Zhang et al., 2002
Zhang et al., 2004
Zhang et al., 2010
Zhao et al., 2008
Zhiqiang et al., 2010
Zhiqiang et al., 2008
Zhong et al., 2006
Zhou et al., 2004
Zhou et al., 2002
Zhou et al., 2010
Zhou et al., 2008
Zhu et al., 2008
Ziabrev et al., 2003
Zyabrev et al., 1989

Declaration of Competing Interest

The authors declare that they have no known competing financial interests or personal relationships that could have appeared to influence the work reported in this paper.

Acknowledgements

We thank Thomas Garth, Aaron Martin, Yani Najman, Mike Searle, Cees van Staal, John Wakabayashi, Dave Waters and Alex Zagorevski for insightful discussion during the initial write-up of this manuscript. We thank reviewers Stephan Guillot, Paul Kapp and Eduardo Garzanti, and assistant editor Douwe van Hinsbergen, who provided helpful reviews which improved our manuscript. This research was funded by the European Research Council (ERC) under the European Union's Horizon 2020 research and innovation program (grant agreement 639003 “DEEP TIME”), and by a Philip Leverhulme Prize of the Leverhulme Trust.

Appendix A. Supplementary data

Supplementary data to this article can be found online at https://doi.org/10.1016/j.earscirev.2020.103084.

References

Abbott, L.D., Silver, E.A., Galewsky, J., 1994. Structural evolution of a modern arc-continent collision in Papua New Guinea. Tectonics 13, 1007–1034.

Abrajevitch, A.V., Ali, J.R., Aitchison, J.C., Badengzhu, A., Davis, A.M., Liu, J., Ziabrev, S.V., 2005. Neotethys and the India–Asia collision: Insights from a palaeomagnetic study of the Dazhuqu ophiolite, southern Tibet. Earth and Planetary Science Letters 233, 87–102.

Advokaat, E., van Hinsbergen, D., Spakman, W., 2018. Dragging and segmentation of the Burma and Sunda slabs caused by increasing curvature of the Sunda Trench. EGU General Assembly Conference Abstracts 7103.

Afonso, J.C., Zlotnik, S., 2011. The subductability of continental lithosphere: the before and after story. In: Brown, D., Ryan, P.D. (Eds.), Arc-Continent Collision. Springer Berlin Heidelberg, Berlin, Heidelberg, pp. 53–86.

Agard, P., Yamato, P., Jolivet, L., Burov, E., 2009. Exhumation of oceanic blueschists and eclogites in subduction zones: timing and mechanisms. Earth Sci. Rev. 92, 53–79.

Agius, M.R., Lebedev, S., 2013. Tibetan and Indian lithospheres in the upper mantle beneath Tibet: evidence from broadband surface-wave dispersion. Geochem. Geophys. Geosyst. 14, 4260–4281.

Agrusta, R., Goes, S., van Hunen, J., 2017. Subducting-slab transition-zone interaction: Stagnation, penetration and mode switches. Earth Planet. Sci. Lett. 464, 10–23.

Ahmad, M.N., Yoshida, M., Fujiwara, Y., 2000. Paleomagnetic study of Utror volcanic formation: remagnetizations and postfolding rotations in Utror area, Kohistan arc, northern Pakistan. Earth, Planets and Space 52, 425–436.

Ahmed, Z., 1993. Leucocratic rocks from the Bela ophiolite, Khuzdar District, Pakistan. Geol. Soc. Lond., Spec. Publ. 74, 89–100.

Aitchison, J.C., Ali, J.R., Davis, A.M., 2007. When and where did India and Asia collide? J. Geophys. Res. Solid Earth 112, B05423.

Aitchison, J.C., Badengzhu Davis, A.M., Liu, J., Luo, H., Malpas, J.G., McDermid, I.R.C., Wu, H., Ziabrev, S.V., Zhou, M.-F., 2000. Remnants of a Cretaceous intra-oceanic subduction system within the Yarlung–Zangbo suture (southern Tibet). Earth Planet. Sci. Lett. 183, 231–244.

Allemann, F., 1979. Time of emplacement of the Zhob Valley ophiolites and Bela ophiolites, Baluchistan (preliminary report). *Geodynamics of Pakistan*. Geological Survey of Pakistan, Quetta, pp. 215–242.

Amaru, M., 2007. Global Travel Time Tomography with 3-D Reference Models. Utrecht University, PhD Thesis.

Ambrose, T.K., Larson, K.P., Guilmette, C., Cottle, J.M., Buckingham, H., Rai, S., 2015. Lateral extrusion, underplating, and out-of-sequence thrusting within the Himalayan metamorphic core, Kanchenjunga, Nepal. Lithosphere 7, 441–464.

An, W., Hu, X., Garzanti, E., BouDagher-Fadel, M.K., Wang, J., Sun, G., 2014. Xigaze forearc basin revisited (South Tibet): provenance changes and origin of the Xigaze ophiolite. GSA Bull. 126, 1595–1613.

Anczkiewicz, R., Burg, J.P., Villa, I.M., Meier, M., 2000. Late Cretaceous blueschist metamorphism in the Indus Suture Zone, Shangla region, Pakistan Himalaya. Tectonophysics 324, 111–134.

Bailey, E.A., 2014. Testing models of ultra-fast India-Asia convergence: new paleomagnetic results from Ladakh, Western Himalaya. BSc Honors Thesis. Massachusetts Institute of Technology, MA, USA.

Bao, P., Su, L., Wang, J., Zhai, Q., 2013. Study on the tectonic setting for the ophiolites in Xigaze, Tibet. Acta Geol. Sin. 87, 395–425 English Edition.

Baxter, A.T., Aitchison, J.C., Ali, J.R., Zyabrev, S.V., 2010. Early cretaceous radiolarians from the Spongtang massif, Ladakh, NW India: implications for Neo-Tethyan evolution. J. Geol. Soc. 167, 511–517.

Baxter, A.T., Aitchison, J.C., Zyabrev, S.V., 2009. Radiolarian age constraints on Mesotethyan ocean evolution, and their implications for development of the Bangong–Nujiang suture, Tibet. J. Geol. Soc. 166, 689–694.

Baxter, A.T., Aitchison, J.C., Zyabrev, S.V., Ali, J.R., 2011. Upper Jurassic radiolarians from the Naga Ophiolite, Nagaland, northeast India. Gondwana Research 20, 638–644.

Beaumont, C., Jamieson, R.A., Nguyen, M.H., Lee, B., 2001. Himalayan tectonics explained by extrusion of a low-viscosity crustal channel coupled to focused surface denudation. Nature 414, 738–742.

Beck, R.A., Burbank, D.W., Sercombe, W.J., Khan, A.M., Lawrence, R.D., 1996. Late cretaceous ophiolite obduction and Paleocene India-Asia collision in the westernmost Himalaya. Geodin. Acta 9, 114–144.

Bédard, É., Hébert, R., Guilmette, C., Lesage, G., Wang, C.S., Dostal, J., 2009. Petrology and geochemistry of the Saga and Sangsang ophiolitic massifs, Yarlung Zangbo Suture Zone, Southern Tibet: evidence for an arc–back-arc origin. Lithos 113, 48–67.

Bhattacharyya, K., Mitra, G., Kwon, S., 2015. Geometry and kinematics of the Darjeeling–Sikkim Himalaya, India: implications for the evolution of the Himalayan fold-thrust belt. J. Asian Earth Sci. 113, 778–796.

Bhutani, R., Pande, K., Venkatesan, T.R., 2009. 40Ar–39Ar dating of volcanic rocks of the Shyok suture zone in north–west trans-Himalaya: implications for the post-collision evolution of the Shyok suture zone. J. Asian Earth Sci. 34, 168–177.

Bidgood, A., Parsons, A.J., Lloyd, G.E., Waters, D., Goddard, C., 2019a. EBSD analysis of palisade quartz textures: implications for coesite-quartz transformation, Tso Morari dome, Himalaya. International Eclogites Conference 2019, Petrozavodsk, Russia.

Bidgood, A., Waters, D., Searle, M.P., 2019b. Prograde UHP metamorphism in felsic and mafic lithologies and clues to pre-Himalayan metamorphism in the Tso Morari dome, Ladakh, Himalaya. International Eclogites Conference 2019, Petrozavodsk, Russia.

Booth, A.L., Zeitler, P.K., Kidd, W.S., Wooden, J., Liu, Y., Idleman, B., Hren, M., Chamberlain, C.P., 2004. U-Pb zircon constraints on the tectonic evolution of southeastern Tibet, Namche Barwa area. American Journal of Science 304, 889–929.

Borneman, N.L., Hodges, K.V., Soest, M.C., Bohon, W., Wartho, J.-A., Cronk, S.S., Ahmad, T., 2015. Age and structure of the Shyok suture in the Ladakh region of northwestern India: Implications for slip on the Karakoram fault system. Tectonics 34, 2011–2033.

Bouilhol, P., Jagoutz, O., Hanchar, J.M., Dudas, F.O., 2013. Dating the India–Eurasia collision through arc magmatic records. Earth Planet. Sci. Lett. 366, 163–175.

Bouilhol, P., Schaltegger, U., Chiaradia, M., Ovtcharova, M., Stracke, A., Burg, J.-P., Dawood, H., 2011. Timing of juvenile arc crust formation and evolution in the Sapat Complex (Kohistan–Pakistan). Chemical Geology 280, 243–256.

Braden, Z., Godin, L., Cottle, J.M., 2017. Segmentation and rejuvenation of the Greater Himalayan sequence in western Nepal revealed by in situ U–Th/Pb monazite petrochronology. Lithos 284-285, 751–765.

Buchs, N., Epard, J.-L., Müntener, O., 2018. U-Pb zircon ages from a suprasubduction zone ophiolite, Nidar, NW Himalaya, India: Incipient arc magmatism in fore-arc oceanic crust. In: Hetényi, G., Guillermin, Z., Jordan, M., Raymond, G., Subedi, S., Buchs, N., Robyr, M., JL, E. (Eds.), Himalaya-Karakorum-Tibet Workshop 2018. Lausanne, Switzerland.

Buckman, S., Aitchison, J.C., Nutman, A.P., Bennett, V.C., Saktura, W.M., Walsh, J.M.J., Kachovich, S., Hidaka, H., 2018. The Spongtang Massif in Ladakh, NW Himalaya: An early cretaceous record of spontaneous, intra-oceanic subduction initiation in the Neotethys. Gondwana Res. 63, 226–249.

Burg, J.-P., 2011. The Asia–Kohistan–India collision: review and discussion. Arc-Continent Collision. Springer Berlin Heidelberg, Berlin, Heidelberg, pp. 279–309.

Burg, J.P., Bodinier, J.L., Chaudhry, S., Hussain, S., Dawood, H., 1998. Infra-arc mantle-crust transition and intra-arc mantle diapirs in the Kohistan Complex (Pakistani Himalaya): Petro-structural evidence. Terra Nova 10, 74–80.

Burg, J.P., Chen, G.M., 1984. Tectonics and structural zonation of southern Tibet, China. Nature 311, 219–223.

Burg, J.-P., Bouilhol, P., 2019. Timeline of the South-Tibet--Himalayan belt: the geochronological record of subduction, collision, and underthrusting from zircon and monazite U-Pb ages. Can. J. Earth Sci. 56 (12), 1318–1332.

Burg, J.P., Brunel, M., Gapais, D., Chen, G.M., Liu, G.H., 1984. Deformation of leucogranites of the crystalline Main Central Sheet in southern Tibet (China). J. Struct. Geol. 6, 535–542.

Burke, K., Dewey, J.F., Kidd, W.S.F., 1977. World distribution of sutures — the sites of former oceans. Tectonophysics 40, 69–99.

Butterworth, N.P., Talsma, A.S., Müller, R.D., Seton, M., Bunge, H.P., Schuberth, B.S.A., Shephard, G.E., Heine, C., 2014. Geological, tomographic, kinematic and geodynamic constraints on the dynamics of sinking slabs. J. Geodyn. 73, 1–13.

Camanni, G., Alvarez-Marron, J., Brown, D., Ayala, C., Wu, Y.-M., Hsieh, H.-H., 2016. The deep structure of south-Central Taiwan illuminated by seismic tomography and earthquake hypocenter data. Tectonophysics 679, 235–245.

Capitanio, F.A., Morra, G., Goes, S., Weinberg, R.F., Moresi, L., 2010. India–Asia convergence driven by the subduction of the Greater Indian continent. Nat. Geosci. 3, 136–139.

Carosi, R., Montomoli, C., Iaccarino, S., Massonne, H.-J., Rubatto, D., Langone, A., Gemignani, L., Visonà, D., 2016. Middle to late Eocene exhumation of the Greater Himalayan Sequence in the Central Himalayas: progressive accretion from the Indian plate. GSA Bull. 128, 1571–1592.

Carosi, R., Montomoli, C., Iaccarino, S., Visonà, D., 2018. Structural evolution, metamorphism and melting in the Greater Himalayan Sequence in central-western Nepal. Geol. Soc. Lond., Spec. Publ. 483, 305–323.

Carosi, R., Montomoli, C., Langone, A., Turina, A., Cesare, B., Iaccarino, S., Fascioli, L., Visonà, D., Ronchi, A., Rai, S.M., 2015. Eocene partial melting recorded in peritectic garnets from kyanite-gneiss, Greater Himalayan Sequence, central Nepal. Geol. Soc. Lond., Spec. Publ. 412, 111–129.

Carosi, R., Montomoli, C., Rubatto, D., Visonà, D., 2010. Late Oligocene high-temperature shear zones in the core of the Higher Himalayan Crystallines (Lower Dolpo, western Nepal). Tectonics 29, TC4029.

Casnedi, R., Desio, A., Forcella, F., Nicoletti, M., Petrucciani, C., 1978. Absolute age of some granitoid rocks between Hindu Raj and Gilgit River (Western Karakorum). Atti della Accademia Nazionale dei Lincei. Classe di Scienze Fisiche, Matematiche e Naturali. Rendiconti 64, 204–210.

Catlos, E.J., Harrison, T.M., Kohn, M.J., Grove, M., Ryerson, F.J., Manning, C.E., Upreti, B.N., 2001. Geochronologic and thermobarometric constraints on the evolution of the Main Central Thrust, Central Nepal Himalaya. J. Geophys. Res. 106, 16177–16204.

Ceylan, S., Ni, J., Chen, J.Y., Zhang, Q., Tilmann, F., Sandvol, E., 2012. Fragmented Indian plate and vertically coherent deformation beneath eastern Tibet. J. Geophys. Res. 117, B11303.

Chan, G.H.N., Aitchison, J.C., Crowley, Q.G., Horstwood, M.S.A., Searle, M.P., Parrish, R.R., Chan, J.S.-L., 2015. U–Pb zircon ages for Yarlung Tsangpo suture zone ophiolites, southwestern Tibet and their tectonic implications. Gondwana Res. 27, 719–732.

Chan, G.H.N., Crowley, Q., Searle, M.P., Aitchison, J.C., Horstwood, M., 2007a. U–Pb zircon ages of the Yarlung Zangbo suture zone ophiolites, south Tibet. 22nd Himalaya–Karakoram–Tibet Workshop, Hong Kong, China.

Chan, G.H.N., Searle, M.P., Aitchison, J.C., Ma, G.S.K., 2007b. Geochemistry and tectonic significance of peridotites from the Kiogar ophiolite, SW Tibet. Geochimica et Cosmochimica Acta 71 (Supplement), 159.

Chauvet, F.o., Lapierre, H., Bosch, D., Guillot, S.p., Mascle, G., Vannay, J.-C., Cotten, J., Brunet, P., Keller, F., 2008. Geochemistry of the Panjal Traps basalts (NW Himalaya): records of the Pangea Permian break-up. Bulletin de la Société Géologique de France 179, 383–395.

Chen, S.-S., Fan, W.-M., Shi, R.-D., Liu, X.-H., Zhou, X.-J., 2018. 118–115 Ma magmatism in the Tethyan Himalaya igneous province: Constraints on early cretaceous rifting of the northern margin of Greater India. Earth Planet. Sci. Lett. 491, 21–33.

Chen, Y.-W., Wu, J., Suppe, J., 2019. Southward propagation of Nazca subduction along the Andes. Nature 565, 441–447.

Chen, Y., Zhang, K., Yang, Z., Luo, T., 2006. Discovery of a complete ophiolite section in the Jueweng area, Nagqu County, in the central segment of the Bangong Co–Nujiang junction zone, Qinghai–Tibet Plateau. Geological Bulletin of China 25, 694–699.

Chiu, H.-Y., Chung, S.-L., Wu, F.-Y., Liu, D., Liang, Y.-H., Lin, I.J., Iizuka, Y., Xie, L.-W., Wang, Y., Chu, M.-F., 2009. Zircon U–Pb and Hf isotopic constraints from eastern Transhimalayan batholiths on the precollisional magmatic and tectonic evolution in southern Tibet. Tectonophysics 477, 3–19.

Chopin, C., 2003. Ultrahigh-pressure metamorphism: tracing continental crust into the mantle. Earth Planet. Sci. Lett. 212, 1–14.

Chu, M.F., Chung, S.L., Song, B., Liu, D., O'Reilly, S.Y., Pearson, N.J., Ji, J., Wen, D.J., 2006. Zircon U-Pb and Hf isotope constraints on the Mesozoic tectonics and crustal evolution of southern Tibet. Geology 34, 745–748.

Chung, S.-L., Chu, M.-F., Ji, J., O'Reilly, S.Y., Pearson, N.J., Liu, D., Lee, T.-Y., Lo, C.-H., 2009. The nature and timing of crustal thickening in Southern Tibet: Geochemical and zircon Hf isotopic constraints from postcollisional adakites. Tectonophysics 477, 36–48.

Chung, S.-L., Chu, M.-F., Zhang, Y., Xie, Y., Lo, C.-H., Lee, T.-Y., Lan, C.-Y., Li, X., Zhang, Q., Wang, Y., 2005. Tibetan tectonic evolution inferred from spatial and temporal variations in post-collisional magmatism. Earth-Science Reviews 68, 173–196.

Čížková, H., Bina, C.R., 2013. Effects of mantle and subduction-interface rheologies on slab stagnation and trench rollback. Earth Planet. Sci. Lett. 379, 95–103.

Čížková, H., Bina, C.R., 2019. Linked influences on slab stagnation: Interplay between lower mantle viscosity structure, phase transitions, and plate coupling. Earth Planet. Sci. Lett. 509, 88–99.

Clennett, E., Sigloch, K., Mihalynuk, M.G., Seton, M., Müller, D., 2019. A Quantitative Tomotectonic Plate Reconstruction of Western North America and the Eastern Pacific Basin. AGU Fall Meeting 2019, San Francisco, CA, USA.

Clift, P.D., Hannigan, R., Blusztajn, J., Draut, A.E., 2002. Geochemical evolution of the Dras–Kohistan Arc during collision with Eurasia: evidence from the Ladakh Himalaya, India. Island Arc 11, 255–273.

Clift, P.D., Pavlis, T., DeBari, S.M., Draut, A.E., Rioux, M., Kelemen, P.B., 2005. Subduction erosion of the Jurassic Talkeetna-Bonanza arc and the Mesozoic accretionary tectonics of western North America. Geology 33, 881–884.

Coney, P.J., Jones, D.L., Monger, J.W.H., 1980. Cordilleran suspect terranes. Nature 288, 329–333.

Corfield, R.I., Searle, M.P., 2000. Crustal shortening estimates across the north Indian continental margin, Ladakh, NW India. Geol. Soc. Lond., Spec. Publ. 170, 395–410.

Corfield, R.I., Searle, M.P., Pedersen, R.B., 2001. Tectonic setting, Origin, and Obduction history of the Spontang Ophiolite, Ladakh Himalaya, NW India. J. Geol 109, 715–736.

Corrie, S.L., Kohn, M.J., 2011. Metamorphic history of the central Himalaya, Annapurna region, Nepal, and implications for tectonic models. GSA Bull. 123, 1863–1879.

Cottle, J.M., Larson, K.P., Kellett, D.A., 2015. How does the mid-crust accommodate deformation in large, hot collisional orogens? A review of recent research in the Himalayan orogen. J. Struct. Geol. 78, 119–133.

Coulon, C., Maluski, H., Bollinger, C., Wang, S., 1986. Mesozoic and cenozoic volcanic rocks from central and southern Tibet:39Ar-40Ar dating, petrological characteristics and geodynamical significance. Earth and Planetary Science Letters 79, 281–302.

Dai, J., Wang, C., Hébert, R., Li, Y., Zhong, H., Guillaume, R., Bezard, R., Wei, Y., 2011. Late Devonian OIB alkaline gabbro in the Yarlung Zangbo Suture Zone: Remnants of the Paleo-Tethys? Gondwana Research 19, 232–243.

Dai, J., Wang, C., Polat, A., Santosh, M., Li, Y., Ge, Y., 2013. Rapid forearc spreading between 130 and 120Ma: evidence from geochronology and geochemistry of the Xigaze ophiolite, southern Tibet. Lithos 172–173, 1–16.

de Sigoyer, J., Chavagnac, V.r., Blichert-Toft, J., Villa, I.M., Luais, B.a., Guillot, S.p., Cosca, M., Mascle, G., 2000. Dating the Indian continental subduction and collisional thickening in the northwest Himalaya: Multichronology of the Tso Morari eclogites. Geology 28, 487–490.

Debon, F., 1995. Incipient India-Eurasia collision and plutonism: the Lower Cenozoic Batura granites (Hunza Karakorum, North Pakistan). Journal of the Geological Society 152, 785–795.

Debon, F., Le Fort, P., Dautel, D., Sonet, J., Zimmermann, J.L., 1987. Granites of western Karakorum and northern Kohistan (Pakistan): A composite mid-cretaceous to upper cenozoic magmatism. Lithos 20, 19–40.

Debon, F., Zimmermann, J.-L., Bertrand, J.-M., 1986. Le granite du Baltoro (batholite axial du Karakorum, nord Pakistan): une intrusion subalcaline d'âge Miocène Supérieur. *Comptes rendus de l'Académie des sciences*. Série 2, Mécanique, Physique, Chimie, Sciences de l'univers, Sciences de la Terre 303, 462–468.

DeCelles, P.G., Gehrels, G.E., Quade, J., Ojha, T.P., 1998. Eocene-early Miocene foreland basin development and the history of Himalayan thrusting, western and Central Nepal. Tectonics 17, 741–765.

DeCelles, P.G., Kapp, P., Ding, L., Gehrels, G.E., 2007. Late Cretaceous to middle Tertiary basin evolution in the central Tibetan Plateau: Changing environments in response to tectonic partitioning, aridification, and regional elevation gain. GSA Bulletin 119, 654–680.

DeCelles, P.G., Kapp, P., Gehrels, G.E., Ding, L., 2014. Paleocene-Eocene foreland basin evolution in the Himalaya of southern Tibet and Nepal: Implications for the age of initial India-Asia collision. Tectonics 33, 824–849.

Deschamps, A., Lallemand, S., 2003. Geodynamic setting of Izu-Bonin-Mariana boninites. In: Later, R.D., Leat, P.T. (Eds.), *Intra-Oceanic Subduction Systems: Tectonic and Magmatic Processes*. Geological Society of London Special Publications, 219, pp. 163–185.

Dewey, J.F., 1977. Suture zone complexities: A review. Tectonophysics 40, 53–67.

Dhuime, B., Bosch, D., Garrido, C.J., Bodinier, J.-L., Bruguier, O., Hussain, S.S., Dawood, H., 2009. Geochemical architecture of the lower- to middle-crustal section of a paleo-island Arc (Kohistan complex, Jijal–Kamila Area, Northern Pakistan): implications for the evolution of an oceanic subduction zone. J. Petrol. 50, 531–569.

Ding, L., Kapp, P., Wan, X., 2005. Paleocene–Eocene record of ophiolite obduction and initial India-Asia collision, south central Tibet. Tectonics 24, TC3001.

Ding, L., Lai, Q., 2003. New geological evidence of crustal thickening in the Gangdese block prior to the Indo-Asian collision. Chinese Science Bulletin 48, 1604–1610.

Ding, H., Zhang, Z., Dong, X., Tian, Z., Xiang, H., Mu, H., Gou, Z., Shui, X., Li, W., Mao, L., 2016. Early Eocene (c. 50 Ma) collision of the Indian and Asian continents: constraints from the North Himalayan metamorphic rocks, southeastern Tibet. Earth Planet. Sci. Lett. 435, 64–73.

Dobrzhinetskaya, L., Faryad, S.W., Wallis, S., Cuthbert, S., 2011. Ultrahigh-Pressure Metamorphism: 25 Years after the Discovery of Coesite and Diamond. Elsevier, p. 696.

Domeier, M., Doubrovine, P.V., Torsvik, T.H., Spakman, W., Bull, A.L., 2016. Global correlation of lower mantle structure and past subduction. Geophys. Res. Lett. 43, 4945–4953.

Donaldson, D.G., Webb, A.A.G., Menold, C.A., Kylander-Clark, A.R.C., Hacker, B.R., 2013. Petrochronology of Himalayan ultrahigh-pressure eclogite. Geology 41, 835–838.

Dong, Y.H., Xu, J.F., Zeng, Q.G., Wang, Q., Mao, G.Z., Li, J., 2006. Is there a Neo-Tethy's subduction record earlier than arc volcanic rocks in the Sangri Group? Acta Petrologica Sinica 22, 661–668.

Doubrovine, P.V., Steinberger, B., Torsvik, T.H., 2012. Absolute plate motions in a reference frame defined by moving hot spots in the Pacific, Atlantic, and Indian oceans. J. Geophys. Res. 117, B09101.

Duan, Y., Tian, X., Liang, X., Li, W., Wu, C., Zhou, B., Iqbal, J., 2017. Subduction of the Indian slab into the mantle transition zone revealed by receiver functions. Tectonophysics 702, 61–69.

Dubois-Côté, V., Hébert, R., Dupuis, C., Wang, C.S., Li, Y.L., Dostal, J., 2005. Petrological and geochemical evidence for the origin of the Yarlung Zangbo ophiolites, southern Tibet. Chem. Geol. 214, 265–286.

Ducea, M.N., Lutkov, V., Minaev, V.T., Hacker, B., Ratschbacher, L., Luffi, P., Schwab, M., Gehrels, G.E., McWilliams, M., Vervoort, J., Metcalf, J., 2003. Building the Pamirs: The view from the underside. Geology 31, 849–852.

Dunlap, W.J., Wysoczanski, R., 2002. Thermal evidence for early cretaceous metamorphism in the Shyok suture zone and age of the Khardung volcanic rocks, Ladakh, India. J. Asian Earth Sci. 20, 481–490.

Dupont-Nivet, G., Lippert, P.C., Van Hinsbergen, D.J.J., Meijers, M.J.M., Kapp, P., 2010. Palaeolatitude and age of the Indo–Asia collision: palaeomagnetic constraints. Geophys. J. Int. 182, 1189–1198.

Dyck, B., St-Onge, M., Searle, M.P., Rayner, N., Waters, D., Weller, O.M., 2019. Protolith lithostratigraphy of the Greater Himalayan Series in Langtang, Nepal: implications for the architecture of the northern Indian margin. Geol. Soc. Lond., Spec. Publ. 483, 281–304.

Dziewonski, A.M., Anderson, D.L., 1981. Preliminary reference Earth model. Phys. Earth Planet. Inter. 25, 297–356.

Einsele, G., Liu, B., Dürr, S., Frisch, W., Liu, G., Luterbacher, H.P., Ratschbacher, L., Ricken, W., Wendt, J., Wetzel, A., Yu, G., Zheng, H., 1994. The Xigaze forearc basin: evolution and facies architecture (cretaceous, Tibet). Sediment. Geol. 90, 1–32.

Ernst, W.G., 1999. Metamorphism, partial preservation, and exhumation of ultrahigh-pressure belts. Island Arc 8, 125–153.

Forsyth, D., Uyeda, S., 1975. On the Relative Importance of the Driving forces of Plate Motion. Geophys. J. R. Astron. Soc. 43, 163–200.

Foster, G., Gibson, H.D., Parrish, R., Horstwood, M., Fraser, J., Tindle, A., 2002. Textural, chemical and isotopic insights into the nature and behaviour of metamorphic monazite. Chemical Geology 191, 183–207.

Foster, G., Parrish, R.R., Horstwood, M.S.A., Chenery, S., Pyle, J., Gibson, H.D., 2004. The generation of prograde P–T–t points and paths; a textural, compositional, and chronological study of metamorphic monazite. Earth and Planetary Science Letters 228, 125–142.

Foulger, G.R., Panza, G.F., Artemieva, I.M., Bastow, I.D., Cammarano, F., Evans, J.R., Hamilton, W.B., Julian, B.R., Lustrino, M., Thybo, H., Yanovskaya, T.B., 2013. Caveats on tomographic images. Terra Nova 25, 259–281.

Fraser, J.E., Searle, M.P., Parrish, R.R., Noble, S.R., 2001. Chronology of deformation, metamorphism, and magmatism in the southern Karakoram Mountains. GSA Bulletin 113, 1443–1455.

Fuchs, G., 1982. The geology of western Zanskar. Jahrb. Geol. Bundesanst. 125, 1–50.

Gaetani, M., Garzanti, E., Jadoul, F., Nicora, A., Tintori, A., Pasini, M., Khan, K.S.A., 1990. The North Karakorum side of the Central Asia geopuzzle. GSA Bull. 102, 54–62.

Gaetani, M., Jadoul, F., Erba, E., Garzanti, E., 1993. Jurassic and cretaceous orogenic events in the North Karakoram: age constraints from sedimentary rocks. In: Treloar, P.J., Searle, M.P. (Eds.), Himalayan Tectonics. Geological Society of London, Special Publication 74, pp. 39–52.

Gaina, C., van Hinsbergen, D.J.J., Spakman, W., 2015. Tectonic interactions between India and Arabia since the Jurassic reconstructed from marine geophysics, ophiolite geology and seismic tomography. Tectonics 34, 875–906.

Gansser, A., 1966. The Indian Ocean and the Himalayas, a geological interpretation: Eclogae Geol. Eclogae Geol. Helv. 67, 479–507.

Garnero, E.J., McNamara, A.K., Shim, S.-H., 2016. Continent-sized anomalous zones with low seismic velocity at the base of Earth's mantle. Nat. Geosci. 9, 481–489.

Garzanti, E., Radeff, G., Malusà, M.G., 2018. Slab breakoff: A critical appraisal of a geological theory as applied in space and time. Earth-Science Reviews 177, 303–319.

Geng, Q., Pan, G., Wang, L., Zhu, D., Liao, Z., 2006. Isotopic geochronology of the volcanic rocks from the Yeba Formation in the Gangdise zone, Xizang. Sedimentary Geology and Tethyan Geology 26, 1–7.

Gibbons, A.D., Zahirovic, S., Müller, R.D., Whittaker, J.M., Yatheesh, V., 2015. A tectonic model reconciling evidence for the collisions between India, Eurasia and intra-oceanic arcs of the central-eastern Tethys. Gondwana Res. 28, 451–492.

Gilotti, J., Mcclelland, W., van Staal, C., Petrie, M., 2017. Detrital zircon evidence for eclogite formation by basal subduction erosion—An example from the Yukon-Tanana composite arc, Canadian Cordillera. Geol. Soc. Am. Spec. Pap. 526, 173–189.

Gnos, E., Immenhauser, A., Peters, T., 1997. Late cretaceous/early Tertiary convergence between the Indian and Arabian plates recorded in ophiolites and related sediments. Tectonophysics 271, 1–19.

Gnos, E., Khan, M., Khan, A., Mahmood, K., Villa, I.M., 2001. Age and tectonic setting of the Ras Koh ophiolites, Pakistan. Acta Mineralogica Pakistanica 11, 105–118.

Gnos, E., Khan, M., Mahmood, K., Khan, A.S., Shafique, N.A., Villa, I.M., 1998. Bela oceanic lithosphere assemblage and its relation to the Reunion hotspot. Terra Nova 10, 90–95.

Godin, L., 2003. Structural evolution of the Tethyan sedimentary sequence in the Annapurna area, Central Nepal Himalaya. J. Asian Earth Sci. 22, 307–328.

Godin, L., Harris, L.B., 2014. Tracking basement cross-strike discontinuities in the Indian crust beneath the Himalayan orogen using gravity data – relationship to upper crustal faults. Geophys. J. Int. 198, 198–215.

Goes, S., Agrusta, R., Van Hunen, J., Garel, F., 2017. Subduction-transition zone interaction: A review. Geosphere 13, 644–664.

Goes, S., Capitanio, F.A., Morra, G., 2008. Evidence of lower-mantle slab penetration phases in plate motions. Nature 451, 981.

Göğüş, O.H., Pysklywec, R.N., Şengör, A.M.C., Gün, E., 2017. Drip tectonics and the enigmatic uplift of the Central Anatolian Plateau. Nat. Commun. 8, 1538.

Goscombe, B., Gray, D., Foster, D.A., 2018. Metamorphic response to collision in the Central Himalayan Orogen. Gondwana Res. 57, 191–265.

Grand, S.P., van der Hilst, R.D., Widiyantoro, S., 1997. High resolution global tomography: a snapshot of convection in the Earth. Geol. Soc. America Today 7 (4), 1–7.

Green, O.R., Searle, M.P., Corfield, R.I., Corfield, R.M., 2008. Cretaceous-tertiary carbonate platform evolution and the age of the india-asia collision along the Ladakh Himalaya (Northwest India). J. Geol 116, 331–353.

GSC (Geological Survey of China) & CIGMR (Chengdu, 2004. Institute of Geology and Mineral Resources). Geological map of Tibet (China) and adjacent areas (1: 1,500,000) with an explanation. Chengdu Cartographic Press Chengdu.

Guan, Q., Zhu, D.-C., Zhao, Z.-D., Dong, G.-C., Zhang, L.-L., Li, X.-W., Liu, M., Mo, X.-X., Liu, Y.-S., Yuan, H.-L., 2012. Crustal thickening prior to 38Ma in southern Tibet: evidence from lower crust-derived adakitic magmatism in the Gangdese Batholith. Gondwana Res. 21, 88–99.

Guillot, S., Replumaz, A., 2013. Importance of continental subductions for the growth of the Tibetan plateau. Bulletin de la Société Géologique de France 184, 199–223.

Guillot, S., Garzanti, E., Baratoux, D., Marquer, D., Mahéo, G., de Sigoyer, J., 2003. Reconstructing the total shortening history of the NW Himalaya. Geochem. Geophys. Geosyst. 4 (7), 1064.

Guillot, S., Mahéo, G., de Sigoyer, J., Hattori, K.H., Pêcher, A., 2008. Tethyan and Indian subduction viewed from the Himalayan high- to ultrahigh-pressure metamorphic rocks. Tectonophysics 451, 225–241.

Guilmette, C., Hébert, R., Dostal, J., Indares, A., Ullrich, T., Bédard, É., Wang, C., 2012. Discovery of a dismembered metamorphic sole in the Saga ophiolitic mélange, South Tibet: assessing an early cretaceous disruption of the Neo-Tethyan supra-subduction zone and consequences on basin closing. Gondwana Res. 22, 398–414.

Guilmette, C., Hébert, R., Wang, C., Villeneuve, M., 2009. Geochemistry and geochronology of the metamorphic sole underlying the Xigaze Ophiolite, Yarlung Zangbo Suture Zone, South Tibet. Lithos 112, 149–162.

Guynn, J.H., Kapp, P., Pullen, A., Heizler, M., Gehrels, G., Ding, L., 2006. Tibetan basement rocks near Amdo reveal "missing" Mesozoic tectonism along the Bangong suture, central Tibet. Geology 34, 505–508.

Hacker, B.R., Gerya, T.V., 2013. Paradigms, new and old, for ultrahigh-pressure tectonism. Tectonophysics 603, 79–88.

Hacker, B.R., Gnos, E., Ratschbacher, L., Grove, M., McWilliams, M., Sobolev, S.V., Wan, J., Zhenhan, W., 2000. Hot and Dry Deep Crustal Xenoliths from Tibet. Science 287, 2463–2466.

Hacker, B.R., Kelemen, P.B., Behn, M.D., 2015. Continental lower Crust. Annu. Rev. Earth Planet. Sci. 43, 167–205.

Hafkenscheid, E., Wortel, M.J.R., Spakman, W., 2006. Subduction history of the Tethyan region derived from seismic tomography and tectonic reconstructions. J. Geophys. Res. 111, B08401.

Hall, R., Spakman, W., 2015. Mantle structure and tectonic history of SE Asia. Tectonophysics 658, 14–45.

Hanan, B.B., Blichert-Toft, J., Hemond, C., Sayit, K., Agranier, A., Graham, D.W., Albarède, F., 2013. Pb and Hf isotope variations along the Southeast Indian Ridge and the dynamic distribution of MORB source domains in the upper mantle. Earth Planet. Sci. Lett. 375, 196–208.

He, S., Kapp, P., DeCelles, P.G., Gehrels, G.E., Heizler, M., 2007. Cretaceous–Tertiary geology of the Gangdese Arc in the Linzhou area, southern Tibet. Tectonophysics 433, 15–37.

He, R., Zhao, D., Gao, R., Zheng, H., 2010. Tracing the Indian lithospheric mantle beneath central Tibetan Plateau using teleseismic tomography. Tectonophysics 491, 230–243.

Hearn, T.M., Ni, J.F., Wang, H., Sandvol, E.A., Chen, Y.J., 2019. Depth dependent Pn velocities and configuration of Indian and Asian lithosphere beneath the Tibetan Plateau. Geophys. J. Int. 217, 179–189.

Hébert, R., Bezard, R., Guilmette, C., Dostal, J., Wang, C.S., Liu, Z.F., 2012. The Indus–Yarlung Zangbo ophiolites from Nanga Parbat to Namche Barwa syntaxes, southern Tibet: first synthesis of petrology, geochemistry, and geochronology with incidences on geodynamic reconstructions of Neo-Tethys. Gondwana Res. 22, 377–397.

Herren, E., 1987. Zanskar shear zone: Northeast-southwest extension within the higher Himalayas (Ladakh, India). Geology 15, 409–413.

Heuberger, S., Schaltegger, U., Burg, J.-P., Villa, I.M., Frank, M., Dawood, H., Hussain, S., Zanchi, A., 2007. Age and isotopic constraints on magmatism along the Karakoram-Kohistan Suture Zone, NW Pakistan: evidence for subduction and continued convergence after India-Asia collision. Swiss J. Geosci. 100, 85–107.

Hildebrand, R.S., 2009. Did westward subduction cause cretaceous-tertiary orogeny in the North American Cordillera? Geological Society of America Special Paper 457, p. 71

Hodges, K.V., 2000. Tectonics of the Himalaya and southern Tibet from two perspectives. GSA Bull. 112, 324–350.

Holland, T.J.B., Hudson, N.F.C., Powell, R., Harte, B., 2013. New thermodynamic models and calculated phase equilibria in NCFMAS for basic and ultrabasic compositions through the transition zone into the uppermost lower mantle. J. Petrol. 54, 1901–1920.

Honegger, K., Dietrich, V., Frank, W., Gansser, A., Thöni, M., Trommsdorff, V., 1982. Magmatism and metamorphism in the Ladakh Himalayas (the Indus-Tsangpo suture zone). Earth Planet. Sci. Lett. 60, 253–292.

Honegger, K., Le Fort, P., Mascle, G., Zimmermann, J.-L., 1989. The blueschists along the Indus Suture Zone in Ladakh, NW Himalaya. J. Metamorph. Geol. 7, 57–72.

Hosseini, K., Sigloch, K., 2015. Multifrequency measurements of core-diffracted P waves (Pdiff) for global waveform tomography. Geophys. J. Int. 203, 506–521.

Hosseini, K., Matthews, K.J., Sigloch, K., Shephard, G.E., Domeier, M., Tsekhmistrenko, M., 2018. SubMachine: Web-based Tools for Exploring Seismic Tomography and Other Models of Earth's Deep Interior. Geochem. Geophys. Geosyst. 19, 1464–1483.

Hosseini, K., Sigloch, K., Tsekhmistrenko, M., Zaheri, A., Nissen-Meyer, T., Igel, H., 2020. Global mantle structure from multi-frequency tomography using P, PP and P-diffracted waves. Geophys. J. Int. 220, 96–141.

Houseman, G.A., Molnar, P., 1997. Gravitational (Rayleigh–Taylor) instability of a layer with non-linear viscosity and convective thinning of continental lithosphere. Geophys. J. Int. 128, 125–150.

Houser, C., Masters, G., Shearer, P., Laske, G., 2008. Shear and compressional velocity models of the mantle from cluster analysis of long-period waveforms. Geophys. J. Int. 174, 195–212.

Hsü, K.J., Guitang, P., Sengör, A.M.C., 1995. Tectonic evolution of the Tibetan Plateau: A working hypothesis based on the archipelago model of orogenesis. Int. Geol. Rev. 37, 473–508.

Hu, X., Garzanti, E., Moore, T., Raffi, I., 2015. Direct stratigraphic dating of India-Asia collision onset at the Selandian (middle Paleocene, 59 ± 1 Ma). Geology 43, 859–862.

Hu, X., Garzanti, E., Wang, J., Huang, W., An, W., Webb, A., 2016a. The timing of India-Asia collision onset – Facts, theories, controversies. Earth Sci. Rev. 160, 264–299.

Hu, X., Jansa, L., Chen, L., Griffin, W.L., O'Reilly, S.Y., Wang, J., 2010. Provenance of lower cretaceous Wölong Volcaniclastics in the Tibetan Tethyan Himalaya: Implications for the final breakup of Eastern Gondwana. Sediment. Geol. 223, 193–205.

Hu, X., Wang, J., BouDagher-Fadel, M., Garzanti, E., An, W., 2016b. New insights into the timing of the India–Asia collision from the Paleogene Quxia and Jialazi formations of the Xigaze forearc basin, South Tibet. Gondwana Res. 32, 76–92.

Hu, D., Wu, Z., Jiang, W., Ye, P., 2004. P-T-t path of mafic granulite metamorphism in northern Tibet and its geodynamical implications. Acta Geologica Sinica-English Edition 78, 155–165.

Huang, W., Dupont-Nivet, G., Lippert, P.C., Hinsbergen, D.J.J., Dekkers, M.J., Waldrip, R., Ganerød, M., Li, X., Guo, Z., Kapp, P., 2015a. What was the Paleogene latitude of the Lhasa terrane? A reassessment of the geochronology and paleomagnetism of Linzizong volcanic rocks (Linzhou basin, Tibet). Tectonics 34, 594–622.

Huang, W., Dupont-Nivet, G., Lippert, P.C., van Hinsbergen, D.J.J., Dekkers, M.J., Guo, Z., Waldrip, R., Li, X., Zhang, X., Liu, D., Kapp, P., 2015b. Can a primary remanence be retrieved from partially remagnetized Eocence volcanic rocks in the Nanmulin Basin (southern Tibet) to date the India-Asia collision? J. Geophys. Res. 120, 42–66.

Huang, W., Lippert, P.C., Jackson, M.J., Dekkers, M.J., Zhang, Y., Li, J., Guo, Z., Kapp, P., van Hinsbergen, D.J.J., 2017a. Remagnetization of the Paleogene Tibetan Himalayan carbonate rocks in the Gamba area: Implications for reconstructing the lower plate in the India-Asia collision. J. Geophys. Res. 122, 808–825.

Huang, W., Lippert, P.C., Zhang, Y., Jackson, M.J., Dekkers, M.J., Li, J., Hu, X., Zhang, B., Guo, Z., van Hinsbergen, D.J.J., 2017b. Remagnetization of carbonate rocks in southern Tibet: Perspectives from rock magnetic and petrographic investigations. J. Geophys. Res. 122, 2434–2456.

Huang, Y., Cao, H.-W., Li, G.-M., Brueckner, S.M., Zhang, Z., Dong, L., Dai, Z.-W., Lu, L., Li, Y.-B., 2018. Middle–late Triassic bimodal intrusive rocks from the Tethyan Himalaya in South Tibet: Geochronology, petrogenesis and tectonic implications. Lithos 318–319, 78–90.

Huang, W., van Hinsbergen, D.J.J., Maffione, M., Orme, D.A., Dupont-Nivet, G., Guilmette, C., Ding, L., Guo, Z., Kapp, P., 2015c. Lower Cretaceous Xigaze ophiolites formed in the Gangdese forearc: Evidence from paleomagnetism, sediment provenance, and stratigraphy. Earth and Planetary Science Letters 415, 142–153.

Hunter, N.J.R., Weinberg, R.F., Wilson, C.J.L., Luzin, V., Misra, S., 2018. Microscopic anatomy of a "hot-on-cold" shear zone: Insights from quartzites of the Main Central Thrust in the Alaknanda region (Garhwal Himalaya). GSA Bull. 130, 1519–1539.

Hyndman, R.D., 2019. Mountain building orogeny in precollision hot backarcs: north American Cordillera, India-Tibet, and Grenville Province. J. Geophys. Res. Solid Earth 124, 2057–2079.

Iaccarino, S., Montomoli, C., Carosi, R., Massonne, H.-J., Langone, A., Visonà, D., 2015. Pressure–temperature–time–deformation path of kyanite-bearing migmatitic paragneiss in the Kali Gandaki valley (Central Nepal): Investigation of late Eocene–early Oligocene melting processes. Lithos 231, 103–121.

Ingalls, M., Rowley, D.B., Currie, B., Colman, A.S., 2016. Large-scale subduction of continental crust implied by India–Asia mass-balance calculation. Nat. Geosci. 9, 848–853.

Isozaki, Y., Aoki, K., Nakama, T., Yanai, S., 2010. New insight into a subduction-related orogen: A reappraisal of the geotectonic framework and evolution of the Japanese Islands. Gondwana Res. 18, 82–105.

Jagoutz, O., Bouilhol, P., Schaltegger, U., Müntener, O., 2019. The isotopic evolution of the Kohistan Ladakh arc from subduction initiation to continent arc collision. Geol. Soc. Lond., Spec. Publ. 483, 165–182.

Jagoutz, O.E., Burg, J.-P., Hussain, S., Dawood, H., Pettke, T., Iizuka, T., Maruyama, S., 2009. Construction of the granitoid crust of an island arc part I: geochronological and geochemical constraints from the plutonic Kohistan (NW Pakistan). Contributions to Mineralogy and Petrology 158, 739–755.

Jagoutz, O., Royden, L., Holt, A.F., Becker, T.W., 2015. Anomalously fast convergence of India and Eurasia caused by double subduction. Nat. Geosci. 8, 475–478.

Jain, A.K., Singh, S., 2008. Tectonics of the southern Asian Plate margin along the Karakoram Shear Zone: Constraints from field observations and U–Pb SHRIMP ages. Tectonophysics 451, 186–205.

Ji, W.-Q., Wu, F.-Y., Chung, S.-L., Li, J.-X., Liu, C.-Z., 2009. Zircon U–Pb geochronology and Hf isotopic constraints on petrogenesis of the Gangdese batholith, southern Tibet. Chem. Geol. 262, 229–245.

Johnston, S.T., 2008. The Cordilleran Ribbon continent of North America. Annu. Rev. Earth Planet. Sci. 36, 495–530.

Kakar, M.I., Collins, A.S., Mahmood, K., Foden, J.D., Khan, M., 2012. U-Pb zircon crystallization age of the Muslim Bagh ophiolite: Enigmatic remains of an extensive pre-Himalayan arc. Geology 40, 1099–1102.

Kakar, M.I., Kerr, A.C., Mahmood, K., Collins, A.S., Khan, M., McDonald, I., 2014. Supra-subduction zone tectonic setting of the Muslim Bagh Ophiolite, northwestern Pakistan: Insights from geochemistry and petrology. Lithos 202–203, 190–206.

Kang, Z., Xu, J., Wang, B., Dong, Y., Wang, S., Chen, J., 2009. Geochemistry of Cretaceous volcanic rocks of Duoni Formation in northern Lhasa block: discussion of tectonic setting. Earth Science-Journal of China University of Geosciences 34, 89–104.

Kapp, P., DeCelles, P.G., 2019. Mesozoic–Cenozoic geological evolution of the Himalayan-Tibetan orogen and working tectonic hypotheses. Am. J. Sci. 319, 159–254.

Kapp, P., DeCelles, P.G., Gehrels, G.E., Heizler, M., Ding, L., 2007. Geological records of the Lhasa-Qiangtang and Indo-Asian collisions in the Nima area of Central Tibet. GSA Bull. 119, 917–933.

Kapp, P., Murphy, M.A., Yin, A., Harrison, T.M., Ding, L., Guo, J., 2003. Mesozoic and Cenozoic tectonic evolution of the Shiquanhe area of western Tibet. Tectonics 22 (4), 1029.

Kapp, P., Yin, A., Harrison, T.M., Ding, L., 2005. Cretaceous-Tertiary shortening, basin development, and volcanism in central Tibet. GSA Bull. 117, 865–878.

Kawai, K., Tsuchiya, T., 2012. High-P, T phase relations in the NaAlSi2O6 system from first principles computation. Phys. Chem. Miner. 39, 305–310.

Kawai, K., Tsuchiya, T., 2013. First-principles study on the high-pressure phase transition and elasticity of KAlSi3O8 hollandite. Am. Mineral. 98, 207–218.

Kawai, K., Yamamoto, S., Tsuchiya, T., Maruyama, S., 2013. The second continent: Existence of granitic continental materials around the bottom of the mantle transition zone. Geosci. Front. 4, 1–6.

Kellett, D.A., Cottle, J.M., Larson, K.P., 2019. The South Tibetan Detachment System: history, advances, definition and future directions. Geol. Soc. Lond., Spec. Publ. 483, 377–400.

Kellett, D.A., Cottle, J.M., Smit, M., 2014. Eocene deep crust at Ama Drime, Tibet: early evolution of the Himalayan orogen. Lithosphere 6, 220–229.

Kelly, S., Beaumont, C., Butler, J.P., 2019. Inherited terrane properties explain enigmatic post-collisional Himalayan-Tibetan evolution. Geology. 48, 8–14.

Kennett, B.L.N., Engdahl, E.R., 1991. Traveltimes for global earthquake location and phase identification. Geophys. J. Int. 105, 429–465.

Kennett, B.L.N., Engdahl, E.R., Buland, R., 1995. Constraints on seismic velocities in the Earth from traveltimes. Geophys. J. Int. 122, 108–124.

Khan, T., Asif Khan, M., Qasim Jan, M., Naseem, M., 1996. Back-arc basin assemblages in Kohistan, Northern Pakistan. Geodinamica Acta 9, 30–40.

Khan, M., Kerr, A.C., Mahmood, K., 2007. Formation and tectonic evolution of the Cretaceous–Jurassic Muslim Bagh ophiolitic complex, Pakistan: Implications for the composite tectonic setting of ophiolites. Journal of Asian Earth Sciences 31, 112–127.

Khan, S.D., Walker, D.J., Hall, S.A., Burke, K.C., Shah, M.T., Stockli, L., 2009. Did the Kohistan-Ladakh island arc collide first with India? Did Kohistan collide first with India? GSA Bull. 121, 366–384.

Khanal, S., Robinson, D.M., 2013. Upper crustal shortening and forward modeling of the Himalayan thrust belt along the Budhi-Gandaki River, Central Nepal. Int. J. Earth Sci. 102, 1871–1891.

Kind, R., Yuan, X., Saul, J., Nelson, D., Sobolev, S.V., Mechie, J., Zhao, W., Kosarev, G., Ni, J., Achauer, U., Jiang, M., 2002. Seismic Images of crust and upper mantle beneath Tibet: evidence for Eurasian Plate subduction. Science 298, 1219–1221.

Klootwijk, C., Sharma, M.L., Gergan, J., Shah, S.K., Tirkey, B., 1984. The Indus-Tsangpo suture zone in Ladakh, northwest Himalaya: further palaeomagnetic data and implications. Tectonophysics 106, 215–238.

Koelemeijer, P., Ritsema, J., Deuss, A., van Heijst, H.-J., 2016. SP12RTS: a degree-12 model of shear- and compressional-wave velocity for Earth's mantle. Geophys. J. Int. 204, 1024–1039.

Kohn, M.J., 2008. P-T-t data from central Nepal support critical taper and repudiate large-scale channel flow of the Greater Himalayan Sequence. GSA Bull. 120, 259–273.

Kohn, M.J., Wieland, M.S., Parkinson, C.D., Upreti, B.N., 2004. Miocene faulting at plate tectonic velocity in the Himalaya of central Nepal. Earth Planet. Sci. Lett. 228, 299–310.

Kufner, S.-K., Schurr, B., Sippl, C., Yuan, X., Ratschbacher, L., Akbar, A.S.O.M., Ischuk, A., Murodkulov, S., Schneider, F., Mechie, J., Tilmann, F., 2016. Deep India meets deep

Asia: Lithospheric indentation, delamination and break-off under Pamir and Hindu Kush (Central Asia). Earth Planet. Sci. Lett. 435, 171–184.

Kumar, S., Bora, S., Sharma, U.K., Yi, K., Kim, N., 2017. Early cretaceous subvolcanic calc-alkaline granitoid magmatism in the Nubra-Shyok valley of the Shyok Suture Zone, Ladakh Himalaya, India: evidence from geochemistry and U–Pb SHRIMP zircon geochronology. Lithos 277, 33–50.

Kumar, P., Yuan, X., Kind, R., Ni, J., 2006. Imaging the colliding Indian and Asian lithospheric plates beneath Tibet. J. Geophys. Res. 111, B06308.

Kusky, T.M., Windley, B.F., Safonova, I., Wakita, K., Wakabayashi, J., Polat, A., Santosh, M., 2013. Recognition of ocean plate stratigraphy in accretionary orogens through Earth history: A record of 3.8 billion years of sea floor spreading, subduction, and accretion. Gondwana Research 24 (2), 501–547.

Larson, K.P., Cottle, J.M., 2015. Initiation of crustal shortening in the Himalaya. Terra Nova 27, 169–174.

Larson, K.P., Ambrose, T.K., Webb, A.A.G., Cottle, J.M., Shrestha, S., 2015. Reconciling Himalayan midcrustal discontinuities: the Main Central thrust system. Earth Planet. Sci. Lett. 429, 139–146.

Laske, G., Masters, G., Ma, Z., Pasyanos, M., 2013. Update on CRUST1. 0—A 1-degree global model of Earth's crust. Geophys. Res. Abstr, 2013. EGU General Assembly Vienna, Austria, 2658.

Laskowski, A.K., Kapp, P., Vervoort, J.D., Ding, L., 2016. High-pressure Tethyan Himalaya rocks along the India-Asia suture zone in southern Tibet. Lithosphere 8, 574–582.

Le Fort, P., 1975. Himalayas: the collided range. Present knowledge of the continental arc. Am. J. Sci. 275, 1–44.

Le Fort, P., Michard, A., Sonet, J., Zimmermann, I., 1983. Petrography, geochemistry and geochronology of some samples from the Karakorum Axial Batholith (northern Pakistan). Granites of Himalayas, Karakorum and Hindu Kush. Institute of Geology, Punjab University, Lahore, pp. 377–388.

Lee, H.-Y., Chung, S.-L., Ji, J., Qian, Q., Gallet, S., Lo, C.-H., Lee, T.-Y., Zhang, Q., 2012. Geochemical and Sr–Nd isotopic constraints on the genesis of the Cenozoic Linzizong volcanic successions, southern Tibet. Journal of Asian Earth Sciences 53, 96–114.

Lee, H.-Y., Chung, S.-L., Lo, C.-H., Ji, J., Lee, T.-Y., Qian, Q., Zhang, Q., 2009. Eocene Neotethyan slab breakoff in southern Tibet inferred from the Linzizong volcanic record. Tectonophysics 477, 20–35.

Leech, M.L., Singh, S., Jain, A.K., Klemperer, S.L., Manickavasagam, R.M., 2005. The onset of India–Asia continental collision: early, steep subduction required by the timing of UHP metamorphism in the western Himalaya. Earth Planet. Sci. Lett. 234, 83–97.

Leier, A.L., Kapp, P., Gehrels, G.E., DeCelles, P.G., 2007. Detrital zircon geochronology of Carboniferous–Cretaceous strata in the Lhasa terrane. Southern Tibet. Basin Research 19, 361–378.

Lekic, V., Cottaar, S., Dziewonski, A., Romanowicz, B., 2012. Cluster analysis of global lower mantle tomography: A new class of structure and implications for chemical heterogeneity. Earth and Planetary Science Letters 357, 68–77.

Li, C., van der Hilst, R.D., Engdahl, E.R., Burdick, S., 2008. A new global model for P wave speed variations in Earth's mantle. Geochem. Geophys. Geosyst. 9, Q05018.

Li, Y., Wang, C., Dai, J., Xu, G., Hou, Y., Li, X., 2015. Propagation of the deformation and growth of the Tibetan–Himalayan orogen: A review. Earth Sci. Rev. 143, 36–61.

Li, S.-M., Wang, Q., Zhu, D.-C., Stern, R.J., Cawood, P.A., Sui, Q.-L., Zhao, Z., 2018. One or two early cretaceous Arc Systems in the Lhasa Terrane, Southern Tibet. J. Geophys. Res. Solid Earth 123, 3391–3413.

Li, J., Xia, B., Liu, L., Xu, L., He, G., Wang, H., Zhang, Y.-Q., Yang, Z., 2008. SHRIMP U-Pb zircon dating of diabase in the La'nga Co ophiolite, Burang, Tibet, China, and its geological significance. Geological Bulletin of China 27, 1739–1743.

Li, S., Yin, C., Guilmette, D., Din, L., Zhanga, J., 2019. Birth and demise of the Bangong-Nujiang Tethyan Ocean: a review from the Gerze area of Central Tibet. Earth-Sci. Rev. 198, 102907.

Liang, X., Chen, Y., Tian, X., Chen, Y.J., Ni, J., Gallegos, A., Klemperer, S.L., Wang, M., Xu, T., Sun, C., Si, S., Lan, H., Teng, J., 2016. 3D imaging of subducting and fragmenting Indian continental lithosphere beneath southern and Central Tibet using body-wave finite-frequency tomography. Earth Planet. Sci. Lett. 443, 162–175.

Liang, Y., Chung, S., Liu, D., O'Reilly, S., Chu, M., Ji, J., Song, B., Pearson, N., 2004. Detrital zircon study along the Tsangpo River, SE Tibet. AGU Fall Meeting 2004, San Francisco, CA, USA.

Liang, X., Sandvol, E., Chen, Y.J., Hearn, T., Ni, J., Klemperer, S., Shen, Y., Tilmann, F., 2012. A complex Tibetan upper mantle: A fragmented Indian slab and no south-verging subduction of Eurasian lithosphere. Earth Planet. Sci. Lett. 333–334, 101–111.

Linner, M., Fuchs, G., Koller, F., Thöni, M., 2001. The Nidar Ophiolite within the Indus Suture Zone in eastern Ladakh—a marginal basin ophiolite from the Jurassic–cretaceous boundary. J. Asian Earth Sci. 19, 39.

Lippert, P.C., van Hinsbergen, D.J.J., Dupont-Nivet, G., 2014. Early cretaceous to present latitude of the central proto-Tibetan Plateau: A paleomagnetic synthesis with implications for Cenozoic tectonics, paleogeography, and climate of Asia. In: Nie, J., Horton, B.K., Hoke, G.D. (Eds.), Toward an Improved Understanding of Uplift Mechanisms and the Elevation History of the Tibetan Plateau. 507. Geological Society of America, pp. 1–21.

Liu, L., Zhang, J.-F., Cao, Y.-T., Green, H.W., Yang, W.-Q., Xu, H.-J., Liao, X.-Y., Kang, L., 2018. Evidence of former stishovite in UHP eclogite from the South Altyn Tagh, western China. Earth Planet. Sci. Lett. 484, 353–362.

Liu, L., Zhang, J., Green, H.W., Jin, Z., Bozhilov, K.N., 2007. Evidence of former stishovite in metamorphosed sediments, implying subduction to >350 km. Earth Planet. Sci. Lett. 263, 180–191.

Liu, Z., Zhou, Q., Lai, Y., Qing, C., Li, Y., Wu, J., Xia, X., 2015. Petrogenesis of the early cretaceous Laguila bimodal intrusive rocks from the Tethyan Himalaya: implications for the break-up of Eastern Gondwana. Lithos 236–237, 190–202.

Long, S., McQuarrie, N., Tobgay, T., Grujic, D., 2011. Geometry and crustal shortening of the Himalayan fold-thrust belt, eastern and central Bhutan. GSA Bull. 123, 1427–1447.

Ma, L., Wang, B.-D., Jiang, Z.-Q., Wang, Q., Li, Z.-X., Wyman, D.A., Zhao, S.-R., Yang, J.-H., Gou, G.-N., Guo, H.-F., 2014a. Petrogenesis of the Early Eocene adakitic rocks in the Napuri area, southern Lhasa: Partial melting of thickened lower crust during slab break-off and implications for crustal thickening in southern Tibet. Lithos 196-197, 321–338.

Ma, Y., Yang, T., Yang, Z., Zhang, S., Wu, H., Li, H., Li, H., Chen, W., Zhang, J., Ding, J., 2014b. Paleomagnetism and U-Pb zircon geochronology of lower cretaceous lava flows from the western Lhasa terrane: New constraints on the India-Asia collision process and intracontinental deformation within Asia. J. Geophys. Res. 119, 7404–7424.

Maffione, M., van Hinsbergen, D.J.J., Koornneef, L.M.T., Guilmette, C., Hodges, K., Borneman, N., Huang, W., Ding, L., Kapp, P., 2015. Forearc hyperextension dismembered the south Tibetan ophiolites. Geology 43, 475–478.

Mahar, M.A., Mahéo, G., Goodell, P.C., Pavlis, T.L., 2014. Age and origin of post collision Baltoro granites, south Karakoram, North Pakistan: Insights from in-situ U–Pb, Hf and oxygen isotopic record of zircons. Lithos 205, 341–358.

Mahar, M.A., Mahéo, G., Goodell, P.C., Pavlis, T.L., 2016. Timing and origin of migmatitic gneisses in south Karakoram: Insights from U–Pb, Hf and O isotopic record of zircons. Journal of Asian Earth Sciences 120, 1–16.

Mahéo, G., Bertrand, H., Guillot, S., Villa, I.M., Keller, F., Capiez, P., 2004. The South Ladakh ophiolites (NW Himalaya, India): an intra-oceanic tholeiitic arc origin with implication for the closure of the Neo-Tethys. Chem. Geol. 203, 273–303.

Mahéo, G., Fayoux, X., Guillot, S., Garzanti, E., Capiez, P., Mascle, G., 2006. Relicts of an intra-oceanic arc in the Sapi-Shergol mélange zone (Ladakh, NW Himalaya, India): implications for the closure of the Neo-Tethys Ocean. J. Asian Earth Sci. 26, 695–707.

Mahmood, K., Boudier, F., Gnos, E., Monié, P., Nicolas, A., 1995. 40Ar/39Ar dating of the emplacement of the Muslim Bagh ophiolite, Pakistan. Tectonophysics 250, 169–181.

Malavieille, J., Lallemand, S.E., Dominguez, S., Deschamps, A., Lu, C.-Y., Liu, C.-S., 2002. Arc-Continent Collision in Taiwan: New Marine Observations and Tectonic Evolution. Geology and geophysics of an arc-continent collision, Taiwan 358. Geological Society of America, pp. 189–213.

Malpas, J., Zhou, M.-F., Robinson, P.T., Reynolds, P.H., 2003. Geochemical and geochronological constraints on the origin and emplacement of the Yarlung Zangbo ophiolites, Southern Tibet. Geol. Soc. Lond., Spec. Publ. 218, 191–206.

Maluski, H., Matte, P., 1984. Ages of Alpine tectonometamorphic events in the northwestern Himalaya (northern Pakistan) by 39Ar/40Ar method. Tectonics 3, 1–18.

Mandal, S., Robinson, D.M., Kohn, M.J., Khanal, S., Das, O., 2019. Examining the tectonostratigraphic architecture, structural geometry, and kinematic evolution of the Himalayan fold-thrust belt, Kumaun, northwest India. Lithosphere 11, 414–435.

Marcoux, J., Girardeau, J., Fourcade, E., Bassoullet, J.-P., Philip, J., Jaffrezo, M., Xuchang, X., Chengfa, C., 1987. Geology and biostratigraphy of the Jurassic and lower cretaceous series to the north of the Lhasa Block. Geodinamica Acta 1, 313–325.

Martin, A.J., 2017a. A review of definitions of the Himalayan Main Central Thrust. Int. J. Earth Sci. 106, 2131–2145.

Martin, A.J., 2017b. A review of Himalayan stratigraphy, magmatism, and structure. Gondwana Res. 49, 42–80.

Matthews, K.J., Maloney, K.T., Zahirovic, S., Williams, S.E., Seton, M., Müller, R.D., 2016. Global plate boundary evolution and kinematics since the late Paleozoic. Glob. Planet. Chang. 146, 226–250.

McDermid, I.R.C., Aitchison, J.C., Davis, A.M., Harrison, T.M., Grove, M., 2002. The Zedong terrane: A Late Jurassic intra-oceanic magmatic arc within the Yarlung–Tsangpo suture zone, southeastern Tibet. Chemical Geology 187, 267–277.

McIntosh, K., Nakamura, Y., Wang, T.K., Shih, R.C., Chen, A., Liu, C.S., 2005. Crustal-scale seismic profiles across Taiwan and the western Philippine Sea. Tectonophysics 401, 23–54.

McQuarrie, N., Tobgay, T., Long, S.P., Reiners, P.W., Cosca, M.A., 2014. Variable exhumation rates and variable displacement rates: Documenting recent slowing of Himalayan shortening in western Bhutan. Earth Planet. Sci. Lett. 386, 161–174.

Metcalf, K., Kapp, P., 2017. The Yarlung suture mélange, Lopu Range, southern Tibet: Provenance of sandstone blocks and transition from oceanic subduction to continental collision. Gondwana Res. 48, 15–33.

Miller, C., Schuster, R., Klotzli, U., Frank, W., Grasemann, B., 2000. Late Cretaceous-Tertiary magmatic and tectonic events in the Transhimalaya batholith (Kailas area, SW Tibet). Schweizerische Mineralogische und Petrographische Mitteilungen 80, 1–20.

Mitra, G., Bhattacharyya, K., Mukul, M., 2010. The lesser Himalayan Duplex in Sikkim: Implications for variations in Himalayan shortening. J. Geol. Soc. India 75, 289–301.

Monger, J.W.H., Gibson, H.D., 2019. Mesozoic-Cenozoic deformation in the Canadian Cordillera: The record of a "Continental Bulldozer"? Tectonophysics 757, 153–169.

Montelli, R., Nolet, G., Dahlen, F.A., Masters, G., 2006. A catalogue of deep mantle plumes: new results from finite-frequency tomography. Geochem. Geophys. Geosyst. 7, Q11007.

Mottram, C.M., Cottle, J.M., Kylander-Clark, A.R.C., 2019. Campaign-style U-Pb titanite petrochronology: along-strike variations in timing of metamorphism in the Himalayan metamorphic core. Geosci. Front. 10, 827–847.

Mottram, C.M., Warren, C.J., Regis, D., Roberts, N.M.W., Harris, N.B.W., Argles, T.W., Parrish, R.R., 2014. Developing an inverted Barrovian sequence; insights from monazite petrochronology. Earth Planet. Sci. Lett. 403, 418–431.

Müller, R.D., Cannon, J., Qin, X., Watson, R.J., Gurnis, M., Williams, S., Pfaffelmoser, T., Seton, M., Russell, S.H.J., Zahirovic, S., 2018. GPlates: building a virtual earth through deep time. Geochem. Geophys. Geosyst. 19, 2243–2261.

Müller, R.D., Royer, J.-Y., Lawver, L.A., 1993. Revised plate motions relative to the hotspots from combined Atlantic and Indian Ocean hotspot tracks. Geology 21, 275–278.

Müller, D., Seton, M., Zahirovic, S., Williams, S.E., Matthews, K.J., Wright, N.M., Shephard, G.E., Maloney, K.T., Barnett-Moore, N., Hosseinpour, M., Bower, D.J., Cannon, J., 2016. Ocean Basin Evolution and Global-Scale Plate Reorganization events since Pangea Breakup. Annu. Rev. Earth Planet. Sci. 44, 107–138.

Müller, R.D., Zahirovic, S., Williams, S.E., Cannon, J., Seton, M., Bower, D.J., Tetley, M., Heine, C., Le Breton, E., Liu, S., Russell, S.H.J., Yang, T., Leonard, J., Gurnis, M., 2019.

A global plate model including lithospheric deformation along major rifts and orogens since the Triassic. Tectonics 38, 1884–1907. https://doi.org/10.1029/2018TC005462.

Murphy, M.A., Yin, A., 2003. Structural evolution and sequence of thrusting in the Tethyan fold-thrust belt and Indus-Yalu suture zone, southwest Tibet. GSA Bull. 115, 21–34.

Murphy, M.A., Yin, A., Harrison, T.M., Dürr, S.B., C., Z., Ryerson, F.J., Kidd, W.S.F., W., X., Z., X., 1997. Did the Indo-Asian collision alone create the Tibetan plateau? Geology 25, 719–722.

Nábělek, J., Hetényi, G., Vergne, J., Sapkota, S., Kafle, B., Jiang, M., Su, H., Chen, J., Huang, B.-S., 2009. Underplating in the Himalaya-Tibet collision zone revealed by the Hi-CLIMB experiment. Science 325, 1371–1374.

Najman, Y., Appel, E., Boudagher-Fadel, M., Bown, P., Carter, A., Garzanti, E., Godin, L., Han, J., Liebke, U., Oliver, G., Parrish, R., Vezzoli, G., 2010. Timing of India-Asia collision: geological, biostratigraphic, and palaeomagnetic constraints. J. Geophys. Res. Solid Earth 115, B12416.

Najman, Y., Jenks, D., Godin, L., Boudagher-Fadel, M., Millar, I., Garzanti, E., Horstwood, M., Bracciali, L., 2017. The Tethyan Himalayan detrital record shows that India–Asia terminal collision occurred by 54 Ma in the Western Himalaya. Earth Planet. Sci. Lett. 459, 301–310.

Nelson, J., Colpron, M., Israel, S., 2013. The Cordillera of British Columbia, Yukon, and Alaska: tectonics and metallogeny. Tectonics, Metallogeny, and Discovery: The North American Cordillera and Similar Accretionary Settings: Society of Economic Geologists Special Publication. 17, pp. 53–109.

Nicolas, A., Girardeau, J., Marcoux, J., Dupre, B., Xibin, W., Yougong, C., Haixiang, Z., Xuchang, X., 1981. The Xigaze ophiolite (Tibet): a peculiar oceanic lithosphere. Nature 294, 414–417.

Ningthoujam, P.S., Dubey, C.S., Lolee, L.K., Shukla, D.P., Naorem, S.S., Singh, S.K., 2015. Tectonic studies and crustal shortening across Easternmost Arunachal Himalaya. J. Asian Earth Sci. 111, 339–349.

Niu, Y., 2018. Origin of the LLSVPs at the base of the mantle is a consequence of plate tectonics – A petrological and geochemical perspective. Geosci. Front. 9, 1265–1278.

Obayashi, M., Yoshimitsu, J., Nolet, G., Fukao, Y., Shiobara, H., Sugioka, H., Miyamachi, H., Gao, Y., 2013. Finite frequency whole mantle P wave tomography: Improvement of subducted slab images. Geophys. Res. Lett. 40, 5652–5657.

Orme, D.A., Laskowski, A.K., 2016. Basin Analysis of the Albian–Santonian Xigaze Forearc, Lazi Region, South-Central Tibet. J. Sediment. Res. 86, 894–913.

O'Neill, C., Müller, D., Steinberger, B., 2005. On the uncertainties in hot spot reconstructions and the significance of moving hot spot reference frames. Geochem. Geophys. Geosyst. 6, Q04003.

Orme, D.A., Carrapa, B., Kapp, P., 2015. Sedimentology, provenance and geochronology of the upper Cretaceous–lower Eocene western Xigaze forearc basin, southern Tibet. Basin Res. 27, 387–411.

Palin, R.M., Reuber, G.S., White, R.W., Kaus, B.J.P., Weller, O.M., 2017. Subduction metamorphism in the Himalayan ultrahigh-pressure Tso Morari massif: An integrated geodynamic and petrological modelling approach. Earth Planet. Sci. Lett. 467, 108–119.

Palin, R.M., Searle, M.P., Waters, D.J., Horstwood, M.S.A., Parrish, R.R., 2012. Combined thermobarometry and geochronology of peraluminous metapelites from the Karakoram metamorphic complex, North Pakistan; New insight into the tectonothermal evolution of the Baltoro and Hunza Valley regions. J. Metamorph. Geol. 30, 793–820.

Parrish, R.R., Gough, S.J., Searle, M.P., Waters, D.J., 2006. Plate velocity exhumation of ultrahigh-pressure eclogites in the Pakistan Himalaya. Geology 34, 989–992.

Parrish, R.R., Tirrul, R., 1989. U-Pb age of the Baltoro granite, northwest Himalaya, and implications for monazite U-Pb systematics. Geology 17, 1076–1079.

Parsons, A.J., Ferré, E.C., Law, R.D., Lloyd, G.E., Phillips, R.J., Searle, M.P., 2016a. Orogen-parallel deformation of the Himalayan midcrust: Insights from structural and magnetic fabric analyses of the Greater Himalayan Sequence, Annapurna-Dhaulagiri Himalaya, Central Nepal. Tectonics 35, 2515–2537.

Parsons, A.J., Law, R.D., Lloyd, G.E., Phillips, R.J., Searle, M.P., 2016b. Thermo-kinematic evolution of the Annapurna-Dhaulagiri Himalaya, Central Nepal: the composite orogenic system. Geochem. Geophys. Geosyst. 17, 1511–1539.

Parsons, A.J., Phillips, R.J., Lloyd, G.E., Law, R.D., Searle, M.P., Walshaw, R.D., 2016c. Mid-crustal deformation of the Annapurna-Dhaulagiri Himalaya, Central Nepal: An atypical example of channel flow during the Himalayan orogeny. Geosphere 12, 985–1015.

Parsons, A.J., Zagorevski, A., Ryan, J.J., McClelland, W.C., van Staal, C.R., Coleman, M.J., Golding, M.L., 2018. Petrogenesis of the Dunite Peak ophiolite, south-central Yukon, and the distinction between upper-plate and lower-plate settings: A new hypothesis for the late Paleozoic–early Mesozoic tectonic evolution of the Northern Cordillera. GSA Bull. 131, 274–298.

Pearce, J.A., 2008. Geochemical fingerprinting of oceanic basalts with applications to ophiolite classification and the search for Archean oceanic crust. Lithos 100, 14–48.

Pedersen, R.B., Searle, M.P., Corfield, R.I., 2001. U–Pb zircon ages from the Spontang Ophiolite, Ladakh Himalaya. J. Geol. Soc. 158, 513–520.

Petterson, M.G., 2010. A Review of the geology and tectonics of the Kohistan island arc, north Pakistan. *In:* Kusky, T. M., Zhai, M.-G. & Xiao, W. (eds.) *The Evolving Continents: Understanding Processes of Continental Growth.* Geological Society Special Publication. 338, 287-327. In: Kusky, T.M., Zhai, M.-G., Xiao, W. (Eds.), The Evolving Continents: Understanding Processes of Continental Growth. Geological Society of London, Special Publication 338, pp. 287–327.

Petterson, M.G., Windley, B.F., 1985. RbSr dating of the Kohistan arc-batholith in the Trans-Himalaya of north Pakistan, and tectonic implications. Earth and Planetary Science Letters 74, 45–57.

Petterson, M.G., Windley, B.F., 1992. Field relations, geochemistry and petrogenesis of the cretaceous basaltic Jutal dykes, Kohistan, northern Pakistan. J. Geol. Soc. 149, 107–114.

Phillips, R.J., Searle, M.P., Parrish, R.R., 2013. The geochemical and temporal evolution of the continental lithosphere and its relationship to continental-scale faulting: the Karakoram Fault, eastern Karakoram, NW Himalayas. Geochem. Geophys. Geosyst. 14, 583–603.

Pudsey, C., 1985. Cretaceous Aptian/Albian age for island-arc volcanics, Kohistan, North Pakistan. Geology of Western Himalayas 150–168.

Pudsey, C.J., 2009. The Northern Suture, Pakistan: margin of a Cretaceous island arc. Geological Magazine 123, 405–423.

Rajkumar, A., 2015. Prograde Histories in High-P to Ultra-High-P Metamorphic Rocks from Tibet and Northern India. Doctor of Philosophy. The University of Sydney.

Ratschbacher, L., Frisch, W., Liu, G., Chen, C., 1994. Distributed deformation in southern and western Tibet during and after the India-Asia collision. J. Geophys. Res. Solid Earth 99, 19917–19945.

Ravikant, V., Wu, F.-Y., Ji, W.-Q., 2009. Zircon U–Pb and Hf isotopic constraints on petrogenesis of the Cretaceous–Tertiary granites in eastern Karakoram and Ladakh, India. Lithos 110, 153–166.

Raz, U., Honegger, K., 1989. Magmatic and tectonic evolution of the Ladakh Block from field studies. Tectonophysics 161, 107–118.

Rehman, H.U., Lee, H.-Y., Chung, S.-L., Khan, T., O'Brien, P.J., Yamamoto, H., 2016. Source and mode of the Permian Panjal Trap magmatism: evidence from zircon U–Pb and Hf isotopes and trace element data from the Himalayan ultrahigh-pressure rocks. Lithos 260, 286–299.

Rehman, H.U., Seno, T., Yamamoto, H., Khan, T., 2011. Timing of collision of the Kohistan–Ladakh Arc with India and Asia: Debate. Island Arc 20, 308–328.

Replumaz, A., Negredo, A.M., Guillot, S., Villaseñor, A., 2010. Multiple episodes of continental subduction during India/Asia convergence: Insight from seismic tomography and tectonic reconstruction. Tectonophysics 483, 125–134.

Replumaz, A., Capitanio, F.A., Guillot, S., Negredo, A.M., Villaseñor, A., 2014. The coupling of Indian subduction and Asian continental tectonics. Gondwana Res. 26, 608–626.

Resing, J.A., Rubin, K.H., Embley, R.W., Lupton, J.E., Baker, E.T., Dziak, R.P., Baumberger, T., Lilley, M.D., Huber, J.A., Shank, T.M., Butterfield, D.A., Clague, D.A., Keller, N.S., Merle, S.G., Buck, N.J., Michael, P.J., Soule, A., Caress, D.W., Walker, S.L., Davis, R., Cowen, J.P., Reysenbach, A.-L., Thomas, H., 2011. Active submarine eruption of boninite in the northeastern Lau Basin. Nature Geoscience 4, 799–806.

Reuber, I., 1989. The Dras arc: two successive volcanic events on eroded oceanic crust. Tectonophysics 161, 93–106.

Reuber, I., Montigny, R., Thuizat, R., 1989. K/Ar ages of ophiolites and arc volcanics of the Indus suture zone : clues on the early evolution of Neotethys. Eclogae Geol. Helv. 82, 699–715.

Rex, A.J., Searle, M.P., Tirrul, R., Crawford, M.B., Prior, D.J., Rex, D.C., Barnicoat, A., Bertrand, J., Shackleton, R.M., Dewey, J.F., Windley, B.F., 1988. The geochemical and tectonic evolution of the central Karakoram, North Pakistan. Philosophical Transactions of the Royal Society of London. Series A, Mathematical and Physical Sciences 326, 229–255.

Reynolds, P.H., Brookfield, M.E., McNutt, R.H., 1983. The age and nature of Mesozoic-Tertiary magmatism across the Indus Suture Zone in Kashmir and Ladakh (N. W. India and Pakistan). Geologische Rundschau 72, 981–1003.

Ribe, N.M., Stutzmann, E., Ren, Y., van der Hilst, R., 2007. Buckling instabilities of subducted lithosphere beneath the transition zone. Earth Planet. Sci. Lett. 254, 173–179.

Ritsema, J., McNamara, A.K., Bull, A.L., 2007. Tomographic filtering of geodynamic models: Implications for model interpretation and large-scale mantle structure. J. Geophys. Res. Solid Earth 112, B01303.

Robertson, A.H.F., 2000. Formation of melanges in the Indus Suture Zone, Ladakh Himalaya by successive subduction-related, collisional and post-collisional processes during Late Mesozoic-Late Tertiary time. In: Khan, M.A., Treloar, P.J., Searle, M.P., Jan, M.Q. (Eds.), Tectonics of the Nanga Parbat Syntaxis and the Western Himalaya. Geological Society of London, Special Publication 170, pp. 333–374.

Robertson, A., Degnan, P., 1994. The Dras arc complex: lithofacies and reconstruction of a late cretaceous oceanic volcanic arc in the Indus Suture Zone, Ladakh Himalaya. Sediment. Geol. 92, 117–145.

Robinson, D.M., 2008. Forward modeling the kinematic sequence of the central Himalayan thrust belt, western NepalHimalayan thrust belt, western Nepal. Geosphere 4, 785–801.

Robinson, A.C., 2009. Geologic offsets across the northern Karakorum fault: Implications for its role and terrane correlations in the western Himalayan-Tibetan orogen. Earth Planet. Sci. Lett. 279, 123–130.

Robinson, D.M., Martin, A.J., 2014. Reconstructing the Greater Indian margin: A balanced cross section in Central Nepal focusing on the Lesser Himalayan duplex. Tectonics 33, 2143–2168.

Robinson, D.M., McQuarrie, N., 2012. Pulsed deformation and variable slip rates within the central Himalayan thrust belt. Lithosphere 4, 449–464.

Robinson, P.T., Bai, W.-J., Malpas, J., Yang, J.-S., Zhou, M.-F., Fang, Q.-S., Hu, X.-F., Cameron, S., Staudigel, H., 2004. Ultra-high pressure minerals in the Luobusa Ophiolite, Tibet, and their tectonic implications. In: Malpas, J., Fletcher, C.J.N., Ali, J.R., Aitchison, J.C. (Eds.), Aspects of the Tectonic Evolution of China. Geological Society of London, Special Publications 226, pp. 247–271.

Robinson, D.M., DeCelles, P.G., Copeland, P., 2006. Tectonic evolution of the Himalayan thrust belt in western Nepal: Implications for channel flow models. GSA Bull. 118, 865–885.

Rolland, Y., Pêcher, A., Picard, C., 2000. Middle cretaceous back-arc formation and arc evolution along the Asian margin: the Shyok Suture Zone in northern Ladakh (NW Himalaya). Tectonophysics 325, 145–173.

Rowley, D.B., 2019a. Comparing paleomagnetic study means with apparent wander paths: a case study and paleomagnetic test of the greater India versus greater Indian basin hypotheses. Tectonics 38, 722–740.

Rowley, D.B., 2019b. Reply to comment on 'comparing paleomagnetic study means with apparent Wander Paths: a case study and paleomagnetic test of the greater India versus greater Indian Basin hypotheses. Tectonics 38, 4521–4524. https://doi.org/10.1029/2019TC005740.

Rowley, D., Ingalls, M., 2017. Reply to 'unfeasible subduction?'. Nat. Geosci. 10, 879–880.

Rudnick, R.L., Gao, S., 2014. Composition of the continental crust. Treatise on Geochemistry, 2nd edition 3. Elsevier, pp. 1–64.

Sarwar, G., 1992. Tectonic setting of the Bela Ophiolites, southern Pakistan. Tectonophysics 207, 359–381.

Schaeffer, A.J., Lebedev, S., 2013. Global shear speed structure of the upper mantle and transition zone. Geophys. J. Int. 194, 417–449.

Schaltegger, U., Zeilinger, G., Frank, M., Burg, J.P., 2002. Multiple mantle sources during island arc magmatism: U-Pb and Hf isotopic evidence from the Kohistan arc complex, Pakistan. Terra Nova 14, 461–468.

Schärer, U., Copeland, P., Harrison, T.M., Searle, M.P., 1990. Age, Cooling History, and Origin of Post-Collisional Leucogranites in the Karakoram Batholith; A Multi-System Isotope Study. The Journal of Geology 98, 233–251.

Schärer, U., Hamet, J., Allègre, C.J., 1984. The Transhimalaya (Gangdese) plutonism in the Ladakh region: a UPb and RbSr study. Earth Planet. Sci. Lett. 67, 327–339.

Schelling, D., 1992. The tectonostratigraphy and structure of the eastern Nepal Himalaya. Tectonics 11, 925–943.

Schelling, D., Arita, K., 1991. Thrust tectonics, crustal shortening, and the structure of the far-eastern Nepal Himalaya. Tectonics 10, 851–862.

Scholl, D.W., von Huene, R., 2007. Crustal recycling at modern subduction zones applied to the past—issues of growth and preservation of continental basement crust, mantle geochemistry, and supercontinent reconstruction. Geol. Soc. America Memoirs 200, 9–32.

Scholl, D.W., von Huene, R., 2010. Subduction zone recycling processes and the rock record of crustal suture zones. Can. J. Earth Sci. 47, 633–654.

Schwab, M., Ratschbacher, L., Siebel, W., McWilliams, M., Minaev, V., Lutkov, V., Chen, F., Stanek, K., Nelson, B., Frisch, W., Wooden, J.L., 2004. Assembly of the Pamirs: Age and origin of magmatic belts from the southern Tien Shan to the southern Pamirs and their relation to Tibet. Tectonics 23, TC4002.

Searle, M.P., Treloar, P.J., 2010. Was Late Cretaceous–Paleocene obduction of ophiolite complexes the primary cause of crustal thickening and regional metamorphism in the Pakistan Himalaya? In: Kusky, T.M., Zhai, M.-G., Xiao, W. (Eds.), The Evolving Continents: Understanding Processes of Continental Growth. Geological Society of London, Special Publications 338, pp. 345–359

Searle, M.P., Rex, A.J., Tirrul, R., Rex, D.C., Barnicoat, A., Windley, B.F., 1989. Metamorphic, magmatic, and tectonic evolution of the Central Karakoram in the Biafo-Baltoro-Hushe regions of northern Pakistan. In: Malinconico, J.L.L., Lillie, R.J. (Eds.), Tectonics of the Western Himalayas. 232. Geological Society of America, pp. 47–73.

Searle, M.P., Windley, B.F., Coward, M.P., Cooper, D.J.W., Rex, A.J., Rex, D., Tingdong, L., Xuchang, X., Jan, M.Q., Thakur, V.C., Kumar, S., 1987. The closing of Tethys and the tectonics of the Himalaya. GSA Bull. 98, 678–701.

Searle, M.P., Pickering, K.T., Cooper, D.J.W., 1990a. Restoration and evolution of the intermontane Indus molasse basin, Ladakh Himalaya, India. Tectonophysics 174, 301–314.

Searle, M.P., Parrish, R.R., Tirrul, R., Rex, D.C., 1990b. Age of crystallization and cooling of the K2 gneiss in the Baltoro Karakoram. Journal of the Geological Society 147, 603–606.

Searle, M.P., 2019. Timing of subduction initiation, arc formation, ophiolite obduction and India–Asia collision in the Himalaya. Geol. Soc. Lond., Spec. Publ. 483, 19–37.

Searle, M., Corfield, R.I., Stephenson, B.E.N., McCarron, J.O.E., 1997. Structure of the North Indian continental margin in the Ladakh–Zanskar Himalayas: implications for the timing of obduction of the Spontang ophiolite, India–Asia collision and deformation events in the Himalaya. Geol. Mag. 134, 297–316.

Searle, M.P., Hacker, B.R., 2019. Structural and metamorphic evolution of the Karakoram and Pamir following India–Kohistan–Asia collision. Geol. Soc. Lond., Spec. Publ. 483, 555–582.

Searle, M.P., Crawford, M.B., Rex, A.J., 2011a. Field relations, geochemistry, origin and emplacement of the Baltoro granite, Central Karakoram. Transactions of the Royal Society of Edinburgh: Earth Sciences 83, 519–538.

Searle, M.P., Elliott, J.R., Phillips, R.J., Chung, S.L., 2011b. Crustal–lithospheric structure and continental extrusion of Tibet. J. Geol. Soc. 168, 633–672.

Searle, M.P., Parrish, R.R., Thow, A.V., Noble, S.R., Phillips, R.J., Waters, D.J., 2010. Anatomy, age and evolution of a collisional mountain belt: the Baltoro granite batholith and Karakoram Metamorphic complex, Pakistani Karakoram. J. Geol. Soc. 167, 183–202.

Segev, A., Rybakov, M., Mortimer, N., 2012. A crustal model for Zealandia and Fiji. Geophys. J. Int. 189, 1277–1292.

Sen, K., Adlakha, V., Singhal, S., Chaudhury, R., 2018. Migmatization and intrusion of "S-type" granites in the trans-Himalayan Ladakh Magmatic Arc of north India and their bearing on Indo-Eurasian collisional tectonics. Geological Journal 53, 1543–1556.

Şengör, A.M.C., Natal'in, B., 1996. Paleotectonics of Asia: Fragments of a syn thesis. In: Yin, A., Harrison, T.M. (Eds.), The Tectonic Evolution of Asia. Cambridge Univeristy Press, Cambridge, UK, pp. 486–640.

Seton, M., Müller, R.D., Zahirovic, S., Gaina, C., Torsvik, T., Shephard, G., Talsma, A., Gurnis, M., Turner, M., Maus, S., Chandler, M., 2012. Global continental and ocean basin reconstructions since 200Ma. Earth Sci. Rev. 113, 212–270.

Seton, M., Whittaker, J.M., Wessel, P., Müller, R.D., DeMets, C., Merkouriev, S., Cande, S., Gaina, C., Eagles, G., Granot, R., Stock, J., Wright, N., Williams, S.E., 2014. Community infrastructure and repository for marine magnetic identifications. Geochem. Geophys. Geosyst. 15, 1629–1641.

Sharma, K., Sinha, A., Bagdasarian, G., Gukasian, R., 1978. K/Ar dating of the Dras Volcanics, Shyok Volcanics and the Ladakh Granite, Ladakh, Northwest Himalaya. Himalayan Geology 8, 288–295.

Shephard, G.E., Bunge, H.P., Schuberth, B.S.A., Müller, R.D., Talsma, A.S., Moder, C., Landgrebe, T.C.W., 2012. Testing absolute plate reference frames and the implications for the generation of geodynamic mantle heterogeneity structure. Earth Planet. Sci. Lett. 317–318, 204–217.

Shephard, G.E., Matthews, K.J., Hosseini, K., Domeier, M., 2017. On the consistency of seismically imaged lower mantle slabs. Sci. Rep. 7, 10976.

Shi, R., 2007. SHRIMP dating of the Bangong Lake SSZ-type ophiolite: Constraints on the closure time of ocean in the Bangong Lake-Nujiang River, northwestern Tibet. Chinese Science Bulletin 52, 936–941.

Shi, D., Zhao, W., Klemperer, S.L., Wu, Z., Mechie, J., Shi, J., Xue, G., Su, H., 2016. West–east transition from underplating to steep subduction in the India–Tibet collision zone revealed by receiver-function profiles. Earth Planet. Sci. Lett. 452, 171–177.

Sigloch, K., Mihalynuk, M.G., 2013. Intra-oceanic subduction shaped the assembly of Cordilleran North America. Nature 496, 50–56.

Sigloch, K., Mihalynuk, M.G., 2017. Mantle and geological evidence for a late Jurassic–cretaceous suture spanning North America. GSA Bull. 129, 1489–1520.

Sigloch, K., McQuarrie, N., Nolet, G., 2008. Two-stage subduction history under North America inferred from multiple-frequency tomography. Nat. Geosci. 1, 458–462.

Simmons, N.A., Forte, A.M., Boschi, L., Grand, S.P., 2010. GyPSuM: A joint tomographic model of mantle density and seismic wave speeds. J. Geophys. Res. Solid Earth 115, B12310.

Simmons, N.A., Myers, S.C., Johannesson, G., Matzel, E., 2012. LLNL-G3Dv3: Global P wave tomography model for improved regional and teleseismic travel time prediction. J. Geophys. Res. Solid Earth 117, B10302.

Singh, S., Kumar, R., Barley, M.E., Jain, A.K., 2007. SHRIMP U–Pb ages and depth of emplacement of Ladakh Batholith, Eastern Ladakh, India. J. Asian Earth Sci. 30, 490–503.

Sinha Roy, S., 1976. A possible Himalayan microcontinent. Nature 263, 117–120.

Smit, M.A., Hacker, B.R., Lee, J., 2014. Tibetan garnet records early Eocene initiation of thickening in the Himalaya. Geology 42, 591–594.

Spakman, W., Chertova, M.V., van den Berg, A., van Hinsbergen, D.J.J., 2018. Puzzling features of western Mediterranean tectonics explained by slab dragging. Nat. Geosci. 11, 211–216.

Spencer, C.J., Dyck, B., Mottram, C.M., Roberts, N.M.W., Yao, W.-H., Martin, E.L., 2018. Deconvolving the pre-Himalayan Indian margin – Tales of crustal growth and destruction. Geosci. Front. 10, 863–872.

Srivastava, P., Mitra, G., 1994. Thrust geometries and deep structure of the outer and lesser Himalaya, Kumaon and Garhwal (India): Implications for evolution of the Himalayan fold-and-thrust belt. Tectonics 13, 89–109.

Stampfli, G.M., Borel, G.D., 2004. The TRANSMED transects in space and time: constraints on the paleotectonic evolution of the Mediterranean domain. In: Cavazza, W., Roure, F., Spakman, W., Stampfli, G.M., Ziegler, P.A. (Eds.), The TRANSMED Atlas. The Mediterranean Region from Crust to Mantle: Geological and Geophysical Framework of the Mediterranean and the Surrounding Areas. Springer, Berlin Heidelberg, pp. 53–80.

Staples, R.D., Gibson, H.D., Colpron, M., Ryan, J.J., 2016. An orogenic wedge model for diachronous deformation, metamorphism, and exhumation in the hinterland of the northern Canadian Cordillera. Lithosphere 8, 165–184.

Steck, A., Spring, L., Vannay, J.-C., Masson, H., Bucher, H., Stutz, E., Marchant, R., Tieche, J.-C., 1993. The tectonic evolution of the Northwestern Himalaya in eastern Ladakh and Lahul, India. In: Treloar, P.J., Searle, M.P. (Eds.), Himalayan Tectonics. Geological Society of London, Special Publication 74, pp. 265–276.

Steinberger, B., Torsvik, T.H., Becker, T.W., 2012. Subduction to the lower mantle – a comparison between geodynamic and tomographic models. Solid Earth 3, 415–432.

Stern, C.R., 2011. Subduction erosion: rates, mechanisms, and its role in arc magmatism and the evolution of the continental crust and mantle. Gondwana Res. 20, 284–308.

Stern, R.J., Bloomer, S.H., 1992. Subduction zone infancy: examples from the Eocene Izu-Bonin-Mariana and Jurassic California arcs. GSA Bull. 104, 1621–1636.

Stern, R.J., Gerya, T., 2018. Subduction initiation in nature and models: A review. Tectonophysics. 746, 173–198.

St-Onge, M.R., Rayner, N., Searle, M.P., 2010. Zircon age determinations for the Ladakh batholith at Chumathang (Northwest India): Implications for the age of the India–Asia collision in the Ladakh Himalaya. Tectonophysics 495, 171–183.

St-Onge, M.R., Searle, M.P., Wodicka, N., 2006. Trans-Hudson Orogen of North America and Himalaya-Karakoram-Tibetan Orogen of Asia: Structural and thermal characteristics of the lower and upper plates. Tectonics 25, TC4006.

Streule, M.J., Phillips, R.J., Searle, M.P., Waters, D.J., Horstwood, M.S.A., 2009. Evolution and chronology of the Pangong Metamorphic Complex adjacent to the Karakoram Fault, Ladakh: constraints from thermobarometry, metamorphic modelling and U–Pb geochronology. Journal of the Geological Society 166, 919–932.

Streule, M.J., Strachan, R.A., Searle, M.P., Law, R.D., 2010. Comparing Tibet-Himalayan and Caledonian crustal architecture, evolution and mountain building processes. Geol. Soc. Lond., Spec. Publ. 335, 207–232.

Syracuse, E.M., van Keken, P.E., Abers, G.A., 2010. The global range of subduction zone thermal models. Phys. Earth Planet. Inter. 183, 73–90.

Tapponnier, P., Zhiqin, X., Roger, F., Meyer, B., Arnaud, N., Wittlinger, G., Jingsui, Y., 2001. Oblique stepwise rise and growth of the Tibet Plateau. Science 294, 1671–1677.

Tate, G.W., McQuarrie, N., van Hinsbergen, D.J.J., Bakker, R.R., Harris, R., Jiang, H., 2015. Australia going down under: quantifying continental subduction during arc-continent accretion in Timor-Leste. Geosphere 11, 1860–1883.

Tesoniero, A., Auer, L., Boschi, L., Cammarano, F., 2015. Hydration of marginal basins and compositional variations within the continental lithospheric mantle inferred from a new global model of shear and compressional velocity. J. Geophys. Res. Solid Earth 120, 7789–7813.

Tetley, M.G., 2018. Constraining Earth's Plate Tectonic Evolution through Data Mining and Knowledge Discovery. PhD. The University of Sydney.

Tetley, M.G., Williams, S.E., Gurnis, M., Flament, N., Müller, R.D., 2019. Constraining absolute plate motions since the Triassic. J. Geophys. Res. Solid Earth 124, 7231–7258. https://doi.org/10.1029/2019JB017442.

Thanh, N.X., Itaya, T., Ahmad, T., Kojima, S., Ohtani, T., Ehiro, M., 2010. Mineral chemistry and K–Ar ages of plutons across the Karakoram fault in the Shyok-Nubra confluence of northern Ladakh Himalaya, India. Gondwana Research 17, 180–188.

Thanh, N.X., Rajesh, V.J., Itaya, T., Windley, B., Kwon, S., Park, C.-S., 2012. A Cretaceous forearc ophiolite in the Shyok suture zone, Ladakh, NW India: Implications for the tectonic evolution of the Northwest Himalaya. Lithos 155, 81–93.

Tobgay, T., McQuarrie, N., Long, S., Kohn, M.J., Corrie, S.L., 2012. The age and rate of displacement along the Main Central Thrust in the western Bhutan Himalaya. Earth Planet. Sci. Lett. 319–320, 146–158.

Torsvik, T.H., Cocks, L.R.M., 2017. The integration of palaeomagnetism, the geological record and mantle tomography in the location of ancient continents. Geol. Mag. 156, 242–260.

Torsvik, T.H., Müller, R.D., Van der Voo, R., Steinberger, B., Gaina, C., 2008. Global plate motion frames: Toward a unified model. Rev. Geophys. 46, RG3004.

Torsvik, T.H., Van der Voo, R., Preeden, U., Mac Niocaill, C., Steinberger, B., Doubrovine, P.V., van Hinsbergen, D.J.J., Domeier, M., Gaina, C., Tohver, E., Meert, J.G., McCausland, P.J.A., Cocks, L.R.M., 2012. Phanerozoic polar wander, palaeogeography and dynamics. Earth Sci. Rev. 114, 325–368.

Treloar, P.J., Izatt, C.N., 1993. Tectonics of the Himalayan collision between the Indian Plate and the Afghan Block: a synthesis. In: Treloar, P.J., Searle, M.P. (Eds.), Himalayan Tectonics. Geological Society of London, Special Publications 74, pp. 69–87.

Treloar, P.J., Petterson, M.G., Jan, M.Q., Sullivan, M.A., 1996. A re-evaluation of the stratigraphy and evolution of the Kohistan arc sequence, Pakistan Himalaya: implications for magmatic and tectonic arc-building processes. J. Geol. Soc. 153, 681–693.

Treloar, P.J., Rex, D.C., Guise, P.G., Coward, M.P., Searle, M.P., Windley, B.F., Petterson, M.G., Jan, M.Q., Luff, I.W., 1989. K-Ar and Ar-Ar geochronology of the Himalayan collision in NW Pakistan: Constraints on the timing of suturing, deformation, metamorphism and uplift. Tectonics 8, 881–909.

van der Hilst, R.D., Widiyantoro, S., Engdahl, E.R., 1997. Evidence for deep mantle circulation from global tomography. Nature 386, 578–584.

van der Meer, D.G., Spakman, W., van Hinsbergen, D.J.J., Amaru, M.L., Torsvik, T.H., 2010. Towards absolute plate motions constrained by lower-mantle slab remnants. Nat. Geosci. 3, 36–40.

van der Meer, D.G., van Hinsbergen, D.J.J., Spakman, W., 2018. Atlas of the underworld: Slab remnants in the mantle, their sinking history, and a new outlook on lower mantle viscosity. Tectonophysics 723, 309–448.

Van der Voo, R., Spakman, W., Bijwaard, H., 1999. Tethyan subducted slabs under India. Earth Planet. Sci. Lett. 171, 7–20.

van Hinsbergen, D.J.J., 2019. Comment on 'comparing paleomagnetic study means with Apparent Wander Paths: A case study and paleomagnetic test of the greater India versus greater Indian basin hypotheses' by David B, Rowley. Tectonics 38. https://doi.org/10.1029/2019TC005525.

van Hinsbergen, D.J.J., Kapp, P., Dupont-Nivet, G., Lippert, P.C., DeCelles, P.G., Torsvik, T.H., 2011a. Restoration of Cenozoic deformation in Asia and the size of Greater India. Tectonics 30, TC5003.

van Hinsbergen, D.J.J., Lippert, P.C., Dupont-Nivet, G., McQuarrie, N., Doubrovine, P.V., Spakman, W., Torsvik, T.H., 2012. Greater India Basin hypothesis and a two-stage Cenozoic collision between India and Asia. Proc. Natl. Acad. Sci. 109, 7659–7664.

van Hinsbergen, D.J.J., Lippert, P.C., Huang, W., 2017. Unfeasible subduction? Nat. Geosci. 10, 878–879.

van Hinsbergen, D.J.J., Lippert, P.C., Li, S., Huang, W., Advokaat, E.L., Spakman, W., 2019. Reconstructing Greater India: Paleogeographic, kinematic, and geodynamic perspectives. Tectonophysics 760, 69–94.

van Hinsbergen, D.J.J., Steinberger, B., Doubrovine, P.V., Gassmöller, R., 2011b. Acceleration and deceleration of India-Asia convergence since the Cretaceous: Roles of mantle plumes and continental collision. J. Geophys. Res. Solid Earth 116, B06101.

van Staal, C.R., Zagorevski, A., McClelland, W.C., Escayola, M.P., Ryan, J.J., Parsons, A.J., Proenza, J., 2018. Age and setting of Permian Slide Mountain terrane ophiolitic ultramafic-mafic complexes in the Yukon: Implications for late Paleozoic-early Mesozoic tectonic models in the northern Canadian Cordillera. Tectonophysics 744, 458–483.

Vannay, J.C., Spring, L., 1993. Geochemistry of the continental basalts within the Tethyan Himalaya of Lahul-Spiti and SE Zanskar, northwest India. Geol. Soc. Lond., Spec. Publ. 74, 237–249.

Volkmer, J.E., Kapp, P., Guynn, J.H., Lai, Q., 2007. Cretaceous-Tertiary structural evolution of the north central Lhasa terrane. Tibet. Tectonics 26, TC6007.

Wahrhaftig, C., 1984. Structure of the Marin Headlands block, California: A progress report. In: Blake, M.C.J. (Ed.), Franciscan Geology of Northern California. 43. Pacific Section S.E.P.M., pp. 31–50.

Walsh, J.M.J., Buckman, S., Nutman, A.P., Zhou, R., 2019. Age and provenance of the Nindam Formation, Ladakh, NW Himalaya: evolution of the intraoceanic dras arc before collision with India. Tectonics 38, 3070–3096.

Wang, W.-L., Aitchison, J.C., Lo, C.-H., Zeng, Q.-G., 2008. Geochemistry and geochronology of the amphibolite blocks in ophiolitic mélanges along Bangong-Nujiang suture, central Tibet. Journal of Asian Earth Sciences 33, 122–138.

Wang, X., Bao, P., Deng, W., Wang, F., 1987. Xigaze (Tibet) Ophiolite, Beijing, China. Geological publishing house.

Wang, J.-G., Hu, X.-M., BouDagher-Fadel, M., Wu, F.-Y., Sun, G.-Y., 2015. Early Eocene sedimentary recycling in the Kailas area, southwestern Tibet: implications for the initial India–Asia collision. Sediment. Geol. 315, 1–13.

Wang, J.-G., Hu, X., Garzanti, E., An, W., Liu, X.-C., 2017. The birth of the Xigaze forearc basin in southern Tibet. Earth Planet. Sci. Lett. 465, 38–47.

Wang, C., Liu, Z., Hébert, R., 2000. The Yarlung–Zangbo paleo-ophiolite, southern Tibet: implications for the dynamic evolution of the Yarlung–Zangbo Suture Zone. Journal of Asian Earth Sciences 18, 651–661.

Wang, R., Xia, B., Zhou, G., Zhang, Y., Yang, Z., Li, W., Wei, D., Zhong, L., Xu, L., 2006. U-Pb ages of zircons from the gabbro in Jiding ophiolite. Tibet. Chinese Science Bulletin 51, 114–117.

Wang, J.M., Zhang, J.J., Wang, X.X., 2013. Structural kinematics, metamorphic P–T profiles and zircon geochronology across the Greater Himalayan crystalline complex in south-central Tibet: implication for a revised channel flow. J. Metamorph. Geol. 31, 607–628.

Wartho, J.A., Rex, D.C., Guise, P.G., 2009. Excess argon in amphiboles linked to greenschist facies alteration in the Kamila Amphibolite Belt, Kohistan island arc system, northern Pakistan: insights from 40Ar/39Ar step-heating and acid leaching experiments. Geological Magazine 133, 595–609.

Waters, D.J., 2019. Metamorphic Constraints on the Tectonic Evolution of the High Himalaya in Nepal: the Art of the Possible. Geological Society of London, Special Publications 483, pp. 325–375 Special Publications. SP483-2018-187.

Webb, A.A.G., 2013. Preliminary balanced palinspastic reconstruction of Cenozoic deformation across the Himachal Himalaya (northwestern India). Geosphere 9, 572–587.

Wei, Z., Xia, B., Zhang, Y., Wang, R., Yang, Z., Wei, D., 2006. SHRIMP zircon dating of diabase in the Xiugugabu ophiolite in Tibet and its geological implications. Geotectonica et Metallogenia 30, 93–97.

Weinberg, R.F., Dunlap, W.J., Whitehouse, M., 2000. New field, structural and geochronological data from the Shyok and Nubra valleys, northern Ladakh: linking Kohistan to Tibet. Geol. Soc. Lond., Spec. Publ. 170, 253–275.

Wen, D.-R., Liu, D., Chung, S.-L., Chu, M.-F., Ji, J., Zhang, Q., Song, B., Lee, T.-Y., Yeh, M.-W., Lo, C.-H., 2008. Zircon SHRIMP U–Pb ages of the Gangdese Batholith and implications for Neotethyan subduction in southern Tibet. Chemical Geology 252, 191–201.

White, L.T., Ahmad, T., Ireland, T.R., Lister, G.S., Forster, M.A., 2011. Deconvolving episodic age spectra from zircons of the Ladakh Batholith, northwest Indian Himalaya. Chem. Geol. 289, 179–196.

Wilson, B.M., 1989. Igneous petrogenesis: a global tectonic approach. Springer Science & Business Media, p. 466.

Wittlinger, G., Masson, F., Poupinet, G., Tapponnier, P., Mei, J., Herquel, G., Guilbert, J., Achauer, U., Guanqi, X., Danian, S., Lithoscope Kunlun, T., 1996. Seismic tomography of northern Tibet and Kunlun: evidence for crustal blocks and mantle velocity contrasts. Earth Planet. Sci. Lett. 139, 263–279.

Wittlinger, G., Vergne, J., Tapponnier, P., Farra, V., Poupinet, G., Jiang, M., Su, H., Herquel, G., Paul, A., 2004. Teleseismic imaging of subducting lithosphere and Moho offsets beneath western Tibet. Earth Planet. Sci. Lett. 221, 117–130.

Woelki, D., Regelous, M., Haase, K.M., Romer, R.H.W., Beier, C., 2018. Petrogenesis of boninitic lavas from the Troodos Ophiolite, and comparison with Izu–Bonin–Mariana fore-arc crust. Earth and Planetary Science Letters 498, 203–214.

Workman, R.K., Hart, S.R., Jackson, M., Regelous, M., Farley, K.A., Blusztajn, J., Kurz, M., Staudigel, H., 2004. Recycled metasomatized lithosphere as the origin of the Enriched Mantle II (EM2) end-member: Evidence from the Samoan Volcanic Chain. Geochem. Geophys. Geosyst. 5, Q04008.

Wu, F.-Y., Ji, W.-Q., Liu, C.-Z., Chung, S.-L., 2010. Detrital zircon U–Pb and Hf isotopic data from the Xigaze fore-arc basin: Constraints on Transhimalayan magmatic evolution in southern Tibet. Chemical Geology 271, 13–25.

Wu, F.-Y., Ji, W.-Q., Wang, J.-G., Liu, C.-Z., Chung, S.-L., Clift, P.D., 2014. Zircon U–Pb and Hf isotopic constraints on the onset time of India-Asia collision. Am. J. Sci. 314, 548–579.

Wu, J., Suppe, J., Lu, R., Kanda, R., 2016. Philippine Sea and East Asian plate tectonics since 52 Ma constrained by new subducted slab reconstruction methods. J. Geophys. Res. Solid Earth 121, 4670–4741.

Xia, B., Li, J., Xu, L., Wang, R., Yang, Z., 2011. Sensitive High Resolution Ion Micro-Probe U-Pb Zircon Geochronology and Geochemistry of Mafic Rocks from the Pulan-Xiangquanhe Ophiolite, Tibet: Constraints on the Evolution of the. Neo-tethys. Acta Geologica Sinica - English Edition 85, 840–853.

Xia, B., Xu, L., Wei, Z., Zhang, Y., Wang, R., Li, J., Wang, Y., 2008. SHRIMP zircon dating of gabbro from the Donqiao ophiolite in Tibet and its geological implications. Acta Geologica Sinica 82, 528–531.

Xiang, S., Zeren, Z., Tian, L., Zhu, Y., Ma, X., Lu, Y., 2005. Geological report and map of the Jiali region (1: 250,000). Geol. Survey of China.

Xie, G., Zou, A., Yuan, J., Li, X., Tang, F., 2002a. Geological report and map of the Bangdo region (1: 250,000). Geol. Survey of China.

Xie, G.G., Zou, A.J., Yuan, J.Y., Liao, S.P., Li, X.Y., 2002b. Geological report and map of the Comai (1: 250,000). Geol. Survey of China 375.

Xiong, F.H., Yang, J.S., Liang, F.H., Ba, D.Z., Zhang, J., Xu, X.Z., Li, Y., Liu, Z., 2011. Zircon U-Pb ages of the Dongbo ophiolite,inthe western Yariung Zangbo sature zone and their geological significance. Acta Petrologica Sinica 27, 3223–3238.

Xu, R.-H., Sch, xe, rer, U., All, xe, gre, C.J., 1985. Magmatism and Metamorphism in the Lhasa Block (Tibet): A Geochronological Study. The Journal of Geology 93, 41–57.

Xu, Q., Zhao, J., Yuan, X., Liu, H., Pei, S., 2015. Mapping crustal structure beneath southern Tibet: Seismic evidence for continental crustal underthrusting. Gondwana Res. 27, 1487–1493.

Xu, Q., Zhao, J., Yuan, X., Liu, H., Pei, S., 2017. Detailed configuration of the underthrusting Indian lithosphere beneath Western Tibet revealed by receiver function images. J. Geophys. Res. Solid Earth 122, 8257–8269.

Yakovlev, P.V., Clark, M.K., 2014. Conservation and redistribution of crust during the Indo-Asian collision. Tectonics 33, 1016–1027.

Yamamoto, H., Kobayashi, K., Nakamura, E., Kaneko, Y., Kausar, A.B., 2005. U-Pb Zircon Dating of Regional Deformation in the lower Crust of the Kohistan Arc. Int. Geol. Rev. 47, 1035–1047.

Yin, J., Grant-Mackie, J.A., 2005. Late Triassic-Jurassic bivalves from volcanic sediments of the Lhasa block, Tibet. New Zealand Journal of Geology and Geophysics 48, 555–577.

Yin, A., Harrison, T.M., 2000. Geologic Evolution of the Himalayan-Tibetan Orogen. Annu. Rev. Earth Planet. Sci. 28, 211–280.

Yamamoto, H., Nakamura, E., 2000. Timing of magmatic and metamorphic events in the Jijal complex of the Kohistan arc deduced from Sm-Nd dating of mafic granulites. In: Asif Khan, M., Treloar, P.J., Searle, M.P., Qasim Jan, M. (Eds.), Tectonics of the Nanga Parbat Syntaxis and the Western Himalaya. Geological Society of London, Special Publications 170, pp. 313–319.

Yang, D.M., He, Z.H., Zheng, C.Q., Wang, T.W., 2004. Zircon SHRIMP U-Pb dating of Dezong granitoid gneisses and its geological implications in Menba Area, Tibet. Journal of Jilin University Earth Scienc 34, 12–22.

Yin, A., Dubey, C.S., Kelty, T.K., Webb, A.A.G., Harrison, T.M., Chou, C.Y., Célérier, J., 2010. Geologic correlation of the Himalayan orogen and Indian craton: part 2. Structural geology, geochronology, and tectonic evolution of the Eastern Himalaya. GSA Bull. 122, 360–395.

Young, A., Flament, N., Maloney, K., Williams, S., Matthews, K., Zahirovic, S., Müller, R.D., 2018. Global kinematics of tectonic plates and subduction zones since the late Paleozoic Era. Geosci. Front. 10, 989–1013.

Zagorevski, A., van Staal, C.R., 2015. Discussion on 'The sole of an ophiolite: the Ordovician Bay of Islands Complex, Newfoundland. Journal of the Geological Society 172, 519–521.

Zagorevski, A., Lissenberg, C.J., van Staal, C.R., 2009. Dynamics of accretion of arc and backarc crust to continental margins: Inferences from the Annieopsquotch accretionary tract, Newfoundland Appalachians. Tectonophysics 479, 150–164.

Zagorevski, A., van Staal, C.R., McNicoll, V.J., 2007. Distinct taconic, salinic, and acadian deformation along the Iapetus suture zone, newfoundland Appalachians. Can. J. Earth Sci. 44, 1567–1585.

Zahirovic, S., Matthews, K.J., Flament, N., Müller, R.D., Hill, K.C., Seton, M., Gurnis, M., 2016. Tectonic evolution and deep mantle structure of the eastern Tethys since the latest Jurassic. Earth Sci. Rev. 162, 293–337.

Zaman, H., Otofuji, Y., Khan, S.R., Ahmad, M.N., 2013. New paleomagnetic results from the northern margin of the Kohistan Island Arc. Arabian J. Geosciences 6, 1041–1054.

Zaman, H., Torii, M., 1999. Palaeomagnetic study of cretaceous red beds from the eastern Hindukush ranges, northern Pakistan: palaeoreconstruction of the Kohistan–Karakoram composite unit before the India–Asia collision. Geophys. J. Int. 136, 719–738.

Zeitler, P.K., 1985. Cooling history of the NW Himalaya, Pakistan. Tectonics 4, 127–151.

Zeng, X.-W., Wang, M., Fan, J.-J., Li, C., Xie, C.-M., Liu, Y.-M., Zhang, T.-Y., 2018. Geochemistry and geochronology of gabbros from the Asa Ophiolite, Tibet: Implications for the early cretaceous evolution of the meso-tethys ocean. Lithos 320–321, 192–206.

Zhang, H.F., Xu, W.C., Guo, J.Q., Zong, K.Q., Cai, H.M., Yuan, H.L., 2007a. Zircon U-Pb and Hf isotopic composition of deformed granite in the southern margin of the Gangdese belt, Tibet: Evidence for early Jurassic subduction of Neo-Tethyan oceanic slab. Acta Petrologica Sinica 23, 1347–1353.

Zhang, Y., Zhang, K., Li, B., Wang, Y., Wei, Q., Tang, X., 2007b. Zircon SHRIMP U-Pb geochronology and petrogenesis of the plagiogranites from the Lagkor Lake ophiolite, Gerze, Tibet, China. Chinese Science Bulletin 52, 651–659.

Zhang, K.J., 2000. Cretaceous palaeogeography of Tibet and adjacent areas (China): tectonic implications. Cretaceous Research 21, 23–33.

Zhang, K.-J., Xia, B., Liang, X., 2002. Mesozoic–Paleogene sedimentary facies and paleogeography of Tibet, western China: tectonic implications. Geological Journal 37, 217–246.

Zhang, K.-J., Xia, B.-D., Wang, G.-M., Li, Y.-T., Ye, H.-F., 2004. Early Cretaceous stratigraphy, depositional environments, sandstone provenance, and tectonic setting of central Tibet, western China. GSA Bulletin 116, 1202–1222.

Zhang, K.-J., Xia, B., Zhang, Y.-X., Liu, W.-L., Zeng, L., Li, J.-F., Xu, L.-F., 2014. Central Tibetan Meso-Tethyan oceanic plateau. Lithos 210-211, 278–288.

Zhang, K.-J., Zhang, Y.-X., Tang, X.-C., Xia, B., 2012a. Late Mesozoic tectonic evolution and growth of the Tibetan plateau prior to the Indo-Asian collision. Earth Sci. Rev. 114, 236–249.

Zhang, Z.M., Zhao, G.C., Santosh, M., Wang, J.L., Dong, X., Liou, J.G., 2010. Two stages of granulite facies metamorphism in the eastern Himalayan syntaxis, south Tibet: petrology, zircon geochronology and implications for the subduction of Neo-Tethys and the Indian continent beneath Asia. Journal of Metamorphic Geology 28, 719–733.

Zhang, H., Zhao, D., Zhao, J., Liu, H., 2015. Tomographic imaging of the underthrusting Indian slab and mantle upwelling beneath Central Tibet. Gondwana Res. 28, 121–132.

Zhang, H., Zhao, D., Zhao, J., Xu, Q., 2012b. Convergence of the Indian and Eurasian plates under eastern Tibet revealed by seismic tomography. Geochem. Geophys. Geosyst. 13, Q06W14.

Zhao, J., Yuan, X., Liu, H., Kumar, P., Pei, S., Kind, R., Zhang, Z., Teng, J., Ding, L., Gao, X., Xu, Q., Wang, W., 2010. The boundary between the Indian and Asian tectonic plates below Tibet. Proc. Natl. Acad. Sci. 107, 11229–11233.

Zhao, J., Zhao, D., Zhang, H., Liu, H., Huang, Y., Cheng, H., Wang, W., 2014. P-wave tomography and dynamics of the crust and upper mantle beneath western Tibet. Gondwana Res. 25, 1690–1699.

Zhao, T.-P., Zhou, M.-F., Zhao, J.-H., Zhang, K.-J., Chen, W.E.I., 2008. Geochronology and geochemistry of the c. 80 Ma Rutog granitic pluton, northwestern Tibet: implications for the tectonic evolution of the Lhasa Terrane. Geological Magazine 145, 845–857.

Zhiqiang, K., Jifeng, X., Baodi, W., Jianlin, C., 2010. Qushenla Formation volcanic rocks in north Lhasa block: Products of Bangong Co-Nujiang Tethy's southward subduction. Acta Petrologica Sinica 26, 3106–3116.

Zhiqiang, K., Jifeng, X., Yanhui, D., Baodi, W., 2008. Cretaceous volcanic rocks of Zenong Group in north-middle Lhasa block: products of southward subducting of the Slainajap Ocean? Acta Petrologica Sinica 24, 303–314.

Zhong, L.F., Xia, B., Zhou, G.Q., Zhang, Y.Q., Wang, R., Wei, D.L., Yang, Z.Q., 2006. SHRIMP age determination of Diabase in Luobusa ophiolite, southern Xizang (Tibet). Geological Review 52, 224–229.

Zhou, S., Mo, X., Dong, G., Zhao, Z., Qiu, R., Guo, T., Wang, L., 2004. 40Ar-39Ar geochronology of Cenozoic Linzizong volcanic rocks from Linzhou Basin, Tibet, China, and their geological implications. Chinese Science Bulletin 49, 1970–1979.

Zhou, S., Mo, X., Mahoney, J.J., Zhang, S., Guo, T., Zhao, Z., 2002. Geochronology and Nd and Pb isotope characteristics of gabbro dikes in the Luobusha ophiolite. Tibet. Chinese Science Bulletin 47, 143–146.

Zhou, S., Mo, X., Niu, Y., Qiu, R., Zhao, Z., Xie, G., Sun, K., 2010. The distribution of the Linzizong sequences along the Indo-Asian collision belt. AGU Fall Meeting, San Francisco, CA, USA.

Zhou, J., Su, H., 2019. Site and timing of substantial India-Asia collision inferred from crustal volume budget. Tectonics 38, 2275–2290.

Zhou, C., Zhu, D., Zhao, Z., Xu, J., Wang, L., Chen, H., Xie, L., Dong, G., Zhou, S., 2008. Petrogenesis of Daxiong pluton in western Gangdese, Tibet: Zircon U-Pb dating and Hf isotopic constraints. Acta Petrologica Sinica 24, 348–358.

Zhu, D.-C., Chung, S.-L., Mo, X.-X., Zhao, Z.-D., Niu, Y., Song, B., Yang, Y.-H., 2009a. The 132 Ma Comei-Bunbury large igneous province: Remnants identified in present-day southeastern Tibet and southwestern Australia. Geology 37, 583–586.

Zhu, D.-C., Mo, X.-X., Niu, Y., Zhao, Z.-D., Wang, L.-Q., Liu, Y.-S., Wu, F.-Y., 2009b. Geochemical investigation of early cretaceous igneous rocks along an east–west traverse throughout the central Lhasa Terrane, Tibet. Chem. Geol. 268, 298–312.

Zhu, D.C., Pan, G.T., Wang, L.Q., Mo, X.X., Zhao, Z.D., Zhou, C.Y., Liao, Z.L., Dong, G.C., Yuan, S.H., 2008. Tempo-spatial variations of Mesozoic magmatic rocks in the Gangdise belt, Tibet, China, with a discussion of geodynamic setting-related issues. Geological Bulletin of China 27, 1535–1550.

Zhu, D.-C., Wang, Q., Chung, S.-L., Cawood, P.A., Zhao, Z.-D., 2018. Gangdese Magmatism in Southern Tibet and India–Asia Convergence since 120 Ma. Geological Society, London Special Publications, 483, SP483.14.

Zhuang, G., Najman, Y., Tian, Y., Carter, A., Gemignani, L., Wijbrans, J., Jan, M.Q., Khan, M.A., 2018. Insights into the evolution of The Hindu Kush-Kohistan-Karakoram from modern river sand detrital geo- and thermochronological studies. J. Geol. Soc. 175, 934–948 jgs2018–007.

Ziabrev, S.V., Aitchison, J.C., Abrajevitch, A.V., Zhu, B., Davis, A.M., Luo, H., 2003. Precise radiolarian age constraints on the timing of ophiolite generation and sedimentation in the Dazhuqu terrane, Yarlung–Tsangpo suture zone. Tibet. Journal of the Geological Society 160, 591–599.

Ziabrev, S.V., Kojima, S., Ahmad, T., 2008. Radiolarian biostratigraphic constraints on the generation of the Nidar ophiolite and the onset of Dras arc volcanism: tracing the evolution of the closing Tethys along the Indus–Yarlung–Tsangpo suture. Stratigraphy 5, 99–112.

Zyabrev, S., Aitchison, J., Davis, A., Luo, H., Malpas, J., 1989. Radiolarian biostratigraphy of supra-ophiolite sequences in the Xigaze area, Yarlung-Tsangpo suture, Southern Tibet (preliminary report). Radiolaria 17, 13–19.